



The  
University  
Of  
Sheffield.

# Quantitative Thermography and Image Quality in Additive Manufacturing of Metals

by:  
Leigh Stanger

A thesis submitted in partial fulfilment of the requirements for the degree of  
Doctor of Philosophy

The University of Sheffield  
Faculty of Engineering  
Department of Electronic and Electrical Engineering

Submitted  
November 2020

# CONTENTS

---

Contents.....	2
Acknowledgments .....	7
Abstract.....	8
Outputs .....	9
Publications.....	9
Publications in submission.....	9
Conference presentations .....	9
Nomenclature .....	10
Symbols.....	10
Abbreviations.....	12
Physical constants.....	14
Thesis overview.....	15
Motivation .....	15
Aims and objectives .....	15
Thesis structure .....	16
1. Introduction .....	17
1.1 Introduction to thermography.....	17
1.1.1 Challenges in thermography .....	18
1.2 Introduction to additive manufacturing .....	19
1.3 Standardisation and measurement science.....	20
1.4 Radiation thermometry & thermography in literature.....	21
1.4.1 David P DeWitt (USA).....	21
1.4.2 Measurement standards laboratory (NZ) .....	22
1.4.3 <b>BIPM</b> working group for non-contact thermometry .....	22
1.4.4 National Physical Laboratory (UK) .....	22
1.4.5 National Institute of Standards and Technology (USA) .....	23
1.4.6 Other work pertinent to this thesis .....	24
1.5 Thermography for the additive manufacture of metals in literature .....	25
1.5.1 Imperial College London (UK) .....	25
1.5.2 Technical University of Munich (Germany) .....	26
1.5.3 National Institute of Standards and Technology (USA) .....	26
1.5.4 The University of Texas El Paso.....	27
1.5.5 Other work pertinent to this thesis .....	28
1.5.6 <b>IR</b> imaging for process control / defect detection.....	28

1.6	Conclusions .....	29
1.7	References .....	29
2.	Theory .....	34
2.1	Surface to surface radiation transfer .....	35
2.1.1	Geometric considerations.....	35
2.1.2	Radiation terms.....	37
2.1.3	Collection of radiation onto a detector .....	39
2.1.4	Emissivity, emission and reflection .....	44
2.2	Blackbody radiation .....	47
2.2.1	Blackbody cavities .....	47
2.2.2	Planck's law .....	48
2.2.3	The spectral integral measurement equation .....	50
2.2.4	Alternative forms and approximations of Planck's law .....	51
2.2.5	Illustrative example.....	56
2.2.6	Comparison of models .....	58
2.3	Thermographic instruments .....	60
2.3.1	Photon transducers.....	60
2.3.2	Dark and flat-field corrections .....	62
2.3.3	Noise .....	63
2.3.4	Exposure and rolling shutter .....	63
2.3.5	Sampling and Fourier analysis.....	65
2.3.6	Data handling .....	69
2.4	Imaging and image processing.....	70
2.4.1	Optical transfer functions .....	70
2.4.2	Measurement field of view .....	72
2.4.3	Targets.....	72
2.4.4	Image processing .....	76
2.5	References .....	81
3.	Experimental methods.....	84
3.1	Blackbody reference .....	84
3.1.1	Radiometric calibration.....	86
3.1.2	Thermal field mapping methods.....	87
3.2	Characterisation targets.....	88
3.2.1	Five-bar transmission target .....	90
3.2.2	Knife edge target.....	90
3.2.3	Aperture targets.....	91

3.2.4	Aerosol jet printed checkerboard targets.....	92
3.3	<b>IR</b> image acquisition in an <b>AM</b> process .....	93
3.3.1	BeAM Magic 2.0, <b>DED-LB/M</b> – Chapter 4.....	93
3.3.2	Renishaw SLM 125, <b>PBF-LB/M</b> – Chapter 5 .....	96
3.3.3	Laser Additive Manufacturing Process Replicator – Chapter 6 .....	98
	References .....	102
4.	Low cost thermography metrology in commercial directed energy deposition additive manufacturing.....	104
4.1	Preparation of the PiCam system .....	105
4.2	Calibration & characterisation .....	105
4.2.1	Radiometric calibration.....	105
4.2.2	Spectral responsivity .....	106
4.2.3	Standard thermographic performance metrics .....	106
4.2.4	Spatial transfer function characterisation .....	107
4.3	Calibration & characterisation results .....	109
4.3.1	Blackbody calibration.....	109
4.3.2	Spectral responsivity .....	110
4.3.3	Noise equivalent temperature difference .....	110
4.3.4	Modulation transfer function .....	110
4.4	Thermography of steady state DED-LB/M results .....	111
4.4.1	Instantaneous field of view.....	112
4.4.2	Insufficient laser filtering & mosaic response.....	112
4.4.3	Freezing plateau as a radiometric fixed point .....	113
4.4.4	Melt pool as a function of linear energy density .....	113
4.5	Conclusions .....	115
4.6	References .....	115
5.	Spatially resolved high dynamic range thermography in commercial powder bed fusion additive manufacturing.....	117
5.1	Characterisation analysis .....	119
5.1.1	<b>PSF</b> determination.....	119
5.2	<b>IR AM</b> data analysis .....	128
5.2.1	Mean thermal field .....	128
5.2.2	Thermal field model.....	128
5.3	Assessment of deconvolution methods.....	129
5.3.1	Thermal field model.....	130
5.4	Characterisation results .....	131

5.4.1	<b>IFOV</b> measurement .....	131
5.4.2	Blackbody calibration .....	131
5.4.3	<b>PSF</b> measurement .....	132
5.4.4	Comparison of thermal field measurement methods .....	133
5.5	Results of thermography of AM in a modified commercial machine .....	135
5.5.1	Mean radiance field .....	137
5.5.2	Measurement of the thermal field .....	137
5.6	Conclusions .....	139
5.7	References .....	140
6.	Spatiotemporally resolved quantitative thermography in powder bed fusion process replication .....	141
6.1	Characterisation analysis .....	143
6.1.1	Spectral characteristics .....	143
6.1.2	Noise .....	143
6.1.3	Geometric transforms.....	145
6.1.4	Scatter effect, <b>SSE</b> .....	146
6.1.5	Correcting for the pixel <b>ESF</b> .....	147
6.1.6	Measurement field of view ( <b>MFOV</b> ).....	148
6.2	Uncertainty .....	149
6.2.1	Calibration function uncertainty.....	150
6.2.2	Scene dependent uncertainty.....	151
6.2.3	Spatial measurement uncertainty .....	151
6.2.4	Components not considered.....	152
6.3	Characterisation results .....	153
6.3.1	Radiometric calibration.....	153
6.3.2	<b>IFOV</b> .....	153
6.3.3	<b>PSF</b> .....	153
6.3.4	<b>MFOV</b> and Measurement resolution.....	155
6.3.5	Direct measurement of a normal distribution.....	156
6.3.6	Geometric transform .....	157
6.4	Thermography of <b>AM/M</b> replicator results .....	158
6.4.1	Spatter.....	159
6.4.2	Signal to noise ratio and exposure time .....	159
6.4.3	Cooling rates (temporal) .....	160
6.4.4	Thermal gradients (spatial) .....	161
6.5	Conclusions .....	162

6.6	References .....	163
7.	Summary & conclusions.....	164
7.1	Summary .....	164
7.2	Conclusions .....	166
7.2.1	On quantitative thermography .....	166
7.2.2	On thermography in additive manufacturing .....	168
7.3	Further work .....	170
7.4	References .....	170
8.	Appendices.....	171
8.1	Estimating error by Taylor expansion .....	171
8.2	Area of section created by a line intersecting with a rectangle .....	171
8.3	Two wavelength systems, colour/radiance temperature and effective wavelength .....	174

## ACKNOWLEDGMENTS

---

Without the help and support of my peers, friends and family this journey would have never happened. The support offered by my supervisor Jon Willmott and our academic group: Nicholas Boone, Matthew Davies, Matthew Grainger, Andrew Heeley, Matthew Hobbs, Tom Rockett & Mary Stuart, has allowed the work in this thesis to happen. I have enjoyed spending time with this group of intelligent and engaging people. The supportive and creative environment has developed my confidence as a researcher. Many other people have helped this work come together. I would like to thank the group out of Harwell for presenting me with the opportunity to be involved in some truly fascinating scientific endeavours. I would also like to thank the Materials Science department at the University of Sheffield for their patience and helpful attitude. All of these groups have contributed to improving the quality of this work.

I would also like to take this opportunity to thank my partner Penelope for supporting me through this experience and for working hard to accommodate the commitment required for the undertaking of a PhD. I would like to thank my two young children Lilly & Eric. Without whom life during these years would not have been so full of joy and the wonder of discovery that children bring, even though they probably did not contribute to the quality of the thesis. Finally, I would like to thank my parents-in-law for reading my thesis and providing valuable non-technical feedback.

## ABSTRACT

---

This thesis presents work on quantitative thermography in the additive manufacturing of metals process. The work is motivated by a need for accurate, spatiotemporally resolved measurements of the thermal fields near the heat source, which is usually 50-500  $\mu\text{m}$  in size. This level of detail requires a high spatial sampling rate, which can be provided by near infrared sensitive silicon-based instruments. The high spatial sampling rate means that the resolution of the instruments is limited by the imaging components. The imaging performance is characterised by the spatial transfer function.

In this work three distinct silicon based thermographic instruments were designed and constructed. The three instruments were trialled in additive manufacturing of metals applications. The three trials were: a low-cost smart-phone-sensor system used on a commercial direct energy deposition machine; a high-performance sensor system with a telephoto lens used on a modified commercial machine; and a high performance, high magnification system used on a custom built process replicator. The performance of the three systems for their applications was assessed.

The three instruments have provided valid research data which paves the way for future studies using these technologies. The instrument used for thermography on the process replicator could resolve previously unseen levels of thermal detail in the process, having an instantaneous field of view of 3  $\mu\text{m}$ . The measurement field of view of this instrument was found to be a circle of 130  $\mu\text{m}$  diameter. The cooling rates in the process replicator for the alloy (Ti-6-4), were measured to be 0.06-0.14  $^{\circ}\text{C} \mu\text{s}^{-1}$ , which is consistent with literature for this material.

The spatial transfer function of the instruments was calculated using methods developed for this thesis. Measurements of the spatial transfer function were used to reconstruct the thermal fields and a method for validating the reconstruction was devised. A reconstruction method devised for this work was found to outperform the standard reconstruction methods used in literature, for scenes similar to those found in the additive manufacture of metals.

## OUTPUTS

---

### PUBLICATIONS

Stanger, L.R., Wilkes, T.C., Boone, N.A., McGonigle, A.J.S., Willmott, J.R., 'Thermal Imaging Metrology with a Smartphone Sensor'. *Sensors*, 2018. **18**(7): p. 2169.

Wilkes, T.C., Stanger, L.R., Willmott, J.R., Pering, T.D., McGonigle, A.J.S., England, R.A., 'The Development of a Low-Cost, Near Infrared, High-Temperature Thermal Imaging System and Its Application to the Retrieval of Accurate Lava Lake Temperatures at Masaya Volcano, Nicaragua.' *Remote Sensing*, 2018. **10**(3): p. 450.

Pering, T.D., Ilanko, T., Wilkes, T.C., England, R.A., Silcock, S.R., Stanger, L.R., Willmott, J.R., Bryant, R.G., McGonigle, A.J.S., 'A Rapidly Convecting Lava Lake at Masaya Volcano, Nicaragua'. *Frontiers in Earth Science*, 2019. **6**(241).

Stuart, M.B., Stanger L.R., Hobbs, M.J., Pering, T.D., Thio, D., McGonigle, A.J.S., Willmott, J.R., 'Low-Cost Hyperspectral Imaging System: Design and Testing for Laboratory-Based Environmental applications'. *Sensors*, 2020. **20**(11): p. 3293.

### PUBLICATIONS IN SUBMISSION

Stanger, L.R., Rockett T., Davies, M., Lyle, A., Anderson, M., Todd, I., Basoalto, H., Willmott, J.R., 'Reconstruction of microscopic thermal fields from oversampled infrared images in Laser based powder bed fusion' *IEEE Transactions on Instrumentation and Measurement*, Manuscript number: TIM-20-01623.

Stuart, M.B., McGonigle, A.J.S., Stanger L.R., Zhou, C., Pering, T.D., Willmott, J.R., 'Hyperspectral Imaging with a Smartphone'. *Sensors*, Manuscript ID: sensors-969501.

Ahmed, F.F., Clark S.J., Leung, C.L.A., Stanger, L.R., Willmott, J.R., Marussi, S., Honkimaki, V., Haynes, N., Lee, P.D., Zurob, H.S., Phillon. A.B., 'Achieving homogeneity in a high-Fe  $\beta$ -Ti alloy laser-printed from elemental powders'. *Acta Materialia*,

### CONFERENCE PRESENTATIONS

High Temperature Near Infrared Thermal Microscopy for Selective Laser Melting Additive Manufacturing (Talk), given by Leigh Stanger at: TEMPMEKO 2019, XIV International Symposium on Temperature and Thermal Measurements in Science and Industry, 10<sup>th</sup>-14<sup>th</sup> June 2019, Chengdu, China.

Quantitative thermography of glass casting using characterised low-cost short-wave Infrared Sensors (Poster), presented at: 14<sup>th</sup> Quantitative Infrared Thermography conference, 25<sup>th</sup>-29<sup>th</sup> July 2018, Berlin, Germany.

Volcano Monitoring with Smartphone Sensors (Talk), given by Leigh Stanger at: IOP Instrumentation for Combustion and Environmental Sensing workshop, 25<sup>th</sup> June 2019, University of Manchester, Manchester UK.

## NOMENCLATURE

SYMBOLS		
Symbol	Description	Unit
$\alpha$	Absorptivity	-
$\beta$	Optical transmission	Fractional transmission
$\varepsilon$	Emissivity	-
$\theta$	Zenith angle	Radians
$\kappa$	Sensitivity factor	Units of measurand $\cdot$ units of component <sup>-1</sup>
$\lambda$	Wavelength	$\mu\text{m}$
$\lambda_0$	Mean wavelength (of distribution)	$\mu\text{m}$
$\lambda_{\text{bar}}$	Repeat length – bar target	m
$\Delta\lambda$	Spectral width (of distribution)	$\mu\text{m}$
$\Lambda$	Effective wavelength	$\mu\text{m}$
$\mu_i$	$i^{\text{th}}$ moment (of distribution)	-
$\nu$	Frequency of a photon	$\text{s}^{-1}$
$\xi$	Filter function	Fractional
$\rho$	Reflectivity	Fractional
$\sigma_x$	Standard deviation in quantity $x$	Same unit as $x$
$\phi$	Azimuth angle	Radians
$\Phi$	Radiant flux	W
$\Phi_{BB}$	Blackbody flux	W
$\Phi_\lambda$	Spectral flux	$\text{W} \cdot \mu\text{m}^{-1}$
$\Phi_\gamma$	Photon flux	Photons $\cdot \text{s}^{-1}$
$\Omega$	Solid angle	sr
$\Omega_{AS}$	Solid angle subtended by aperture stop from measurement spot	sr
$\Omega_{FS}$	Solid angle subtended by aperture stop, from field stop surface	sr
$A$	Generic scalar coefficient	-
$A_i$	$i^{\text{th}}$ Sakuma-Hattori coefficient	-
$A_\Omega$	Area of sphere segment	$\text{m}^2$
$A_{AS}$	Area of aperture stop	$\text{m}^2$
$A_{FS}$	Area of field stop	$\text{m}^2$
$B_i$	$i^{\text{th}}$ order polynomial coefficient	-
$c_l$	Intercept of knife edge line	Pixel
$D_{FS}$	Characteristic length of field stop	m
$d_{\text{slit}}$	Slit width	m
$dA'$	Area of a surface	$\text{m}^2$
$dA$	Projected area of a surface	$\text{m}^2$
$E$	Irradiance	$\text{W} \cdot \text{m}^{-2}$
$E_{te}$	Etendue	$\text{m}^2 \cdot \text{sr}$
$E_{te\infty}$	Etendue at infinity focus	$\text{m}^2 \cdot \text{sr}$
$E_\gamma$	Energy of a photon	J
$\mathcal{F}$ ( $\mathcal{F}^{-1}$ )	Fourier transform (inverse)	-
$F\#$	F number	-
$F_s$	General sample frequency	Sampling Unit <sup>-1</sup>
$F_x, F_y$	Spatial sample frequency	$\text{m}^{-1}$ or Pixel <sup>-1</sup>

$F_t$	Temporal sample frequency	Hz, $s^{-1}$ or fps (frames per second)
$F_\gamma$	Photon frequency	Hz or $s^{-1}$
$F_{SS}$	Super-sampled frequency	Pixel $^{-1}$
$F_{bar}$	Spatial frequency – bar target	$m^{-1}$ or lppmm (line pairs per mm)
$f_L$	Focal length	m
$f_{BB,i}$	Blackbody response model	Typically: DL
$f_{weight}$	Weighting function	-
$G$	Gain	DL Electron $^{-1}$
<b>H</b>	Cartesian to homogenous coordinates transform	-
<b>H<math>^{-1}</math></b>	Homogenous to 2d Cartesian Coordinates transform	-
$H$	Linear energy density	J · m $^{-1}$
$I$	Radiant intensity	W · sr $^{-1}$
$I_{BB}$	Blackbody intensity	W · sr $^{-1}$
$I_\lambda$	Spectral intensity	W · sr $^{-1}$ · $\mu\text{m}^{-1}$
$I_\gamma$	Photon intensity	photons · s $^{-1}$ · sr $^{-1}$ · $\mu\text{m}^{-1}$
$k$	Coverage factor	$\sigma$
$L$	Radiance	W · m $^{-2}$ · sr $^{-1}$ (*projected)
$L_{BB}$	Blackbody radiance	W · m $^{-2}$ · sr $^{-1}$ (*projected)
$L_\lambda$	Spectral radiance	W · m $^{-2}$ · sr $^{-1}$ · $\mu\text{m}^{-1}$ (*projected)
$L_\gamma$	Photon radiance	Photons · s $^{-1}$ · m $^{-2}$ · sr $^{-1}$ · $\mu\text{m}^{-1}$ (*projected)
$M_{ag}$	Magnification	-
$M(-)$	Radiant exitance	W · m $^{-2}$
$M_{BB}(-)$	Blackbody exitance	W · m $^{-2}$
$M_\lambda(-)$	Spectral exitance	W · m $^{-2}$ · $\mu\text{m}^{-1}$
$M_\gamma(-)$	Photon exitance	Photons · s $^{-1}$ · m $^{-2}$
$m_l$	Gradient of knife edge line	Pixel · Pixel $^{-1}$
$N_\gamma$	Number of photons	Photons
$N_{e^-}$	Number of electrons (charge carriers)	Electrons
$N_{Abel}$	Number of coefficients in the Pretzier inverse Abel transform	-
$N_{pix}$	Number of pixels in <i>PSF</i> kernel	-
$N_{Sub}$	Number of sub-pixel evaluation points	-
$n$	Refractive index	-
$\mathbf{P}_{sc}$	Position of camera in scene coordinates (vector)	m
$QE$	Quantum Efficiency	Electrons Photon $^{-1}$
$QE^*$	Filtered Quantum efficiency	Electrons Photon $^{-1}$
$r_{AS} \approx r_{WD}$	Distance from measurement spot to Field stop $\approx$ working distance	m
$r_{FS} \approx r_{im}$	Distance from field stop to aperture stop $\approx$ image distance	m
$S$	Signal reported by an instrument	Typically: DL
$\tilde{S}$	Scene	Radiance or $^\circ\text{C}$

$\hat{S}$	Signal reported by an instrument in frequency space	Complex; Magnitude: DL, Phase: m or s
$S_{raw}$	Un-pre-processed image	DL
$T$	Thermodynamic temperature	K or °C
$T^*$	Effective temperature	K or °C
$T_{BB}$	Blackbody temperature	K or °C
$T_{90}$	Traceable calibration temperature	K or °C
$T_{peak}$	Peak measured temperature	K or °C
$T_{Rad}$	Radiance temperature	K or °C
$T_F$	As a general operator	-
$T_F$ ( <i>PSF</i> )	impulse response function	-
$\hat{T}_F$ ( <i>OTF</i> )	In spatial frequency space	-
$ \hat{T}_F $ ( <i>MTF</i> )	Magnitude – in $F_x$ space	-
$\Delta t$	Integration / exposure time	s
$U_x$ (k=y)	Standard Uncertainty in quantity $x$ , with coverage factor k=y	Same as $x$
$v$	velocity	$m \cdot s^{-1}$
$W_0$	Filter parameter - cutoff	pixel <sup>-1</sup>
$W_\sigma$	Filter parameter – roll off	pixel <sup>-1</sup>
$x$	Position of a point (vector)	m
$x, y, z$	Cartesian spatial coordinates Image space	m or pixels
$\tilde{x}, \tilde{y}, \tilde{z}$	Cartesian spatial coordinates Scene space	m
$z_{Extrema}$	Turning point in the <i>PSF</i> ( $Z$ )	mm
$\phi_{ap}$	Aperture diameter	m

## ABBREVIATIONS

Abbreviation	Name	Description
<i>AM</i>	Additive Manufacturing	A manufacturing method opposed to the standard subtractive techniques of machining
<i>ADC</i>	Analogue to Digital Converter	Electronic component which converts analogue signals from a transducer into a digital format
<i>BIPM</i>	International Bureau of Weights and Measures	International framework organisation for universal homogenisation of measurement
<i>BRDF</i>	Bi-directional Reflection Distribution Function	Property of a surface which determines reflection characteristics
<i>CCD</i>	Charge Coupled Device	Alternative <i>FPA</i> technology Largely replaced by <i>CMOS</i>
<i>CCT-WG-NCTh</i>	Constate Committee for Thermometry, Working Group for Non-Contact Thermometry	Committee out of the <i>BIPM</i> which oversees metrology related to non-contact measurement of temperature
<i>CFD</i>	Computational Fluid Dynamics	Computational model solved across surfaces
<i>CMOS</i>	Complementary Metal Oxide Semiconductor	Dominant <i>FPA</i> technology since the turn of the millennium
<i>CTF</i>	Contrast Transfer Function	Transfer function of a binary bar target
<i>DED</i>	Direct Energy Deposition	A method of <i>AM</i>
<i>DL</i>	Digital Levels	Unit reported by digital camera
<i>EE</i>	Enclosed Energy	Fraction of energy originating from a finite area

<i>ESF</i>	Edge Spread Function	Transfer function of a step function
<i>ESRF</i>	European Synchrotron Research Facility	Synchrotron research facility, Grenoble, France
<i>ESRF1</i>	<i>ESRF</i> Beam time April 2018	First experimental session, <i>ESRF</i> facility
<i>ESRF2</i>	<i>ESRF</i> Beam time June 2018	Second experimental session, <i>ESRF</i> facility
<i>Exp Fit</i>	Exponential <i>PSF</i> decay fit	Literature model for <i>PSF</i> decay at large $r$
<i>FEA</i>	Finite Element Analysis	Computational model solved at nodes
<i>(i)FFT</i>	(inverse) Fast Fourier Transform	Implementation of a discrete (inverse) Fourier transform
<i>FPA</i>	Focal Plane Array	Multi-element sensor in a staring imager system
<i>FWHM</i>	Full Width at Half Maximum	A measure of the width of a distribution
<i>FOV</i>	Field Of View	Projection of the sensitive area onto the scene
<i>IFOV</i>	Instantaneous Field of View	<i>FOV</i> of a single element in an imager
<i>IR</i>	Infrared Radiation	Electromagnetic radiation adjacent to visible with lower energy
<i>IRT</i>	Infrared Radiation Thermometer	Instrument, usually single pixel, which utilises Infrared radiation to measure surface $T$
<i>ITS-90</i>	International Temperature Scale of 1990	Accepted definition of temperature used in the SI
<i>LAMPRIi</i>	Laser Additive Manufacturing Process Replicator Mark ii	Custom test facility for multimodal imaging of <i>PBF-LB</i>
<i>LSF</i>	Line Spread Function	Transfer function of the optics in one dimension expressed in sample space
<i>MFOV</i>	Measurement Field Of View	The <i>FOV</i> required for a given <i>EE</i>
<i>MRTD</i>	Minimum Resolvable Temperature Difference	Temperature resolution performance metric for thermographic instruments
<i>MTF</i>	Modulation Transfer Function	Magnitude of the <i>OTF</i> in $F_x$ representation
<i>NETD</i>	Noise Equivalent Temperature Difference	Noise performance metric for thermographic instruments
<i>NIR</i>	Near Infrared Radiation	Part of the electromagnetic spectrum just outside the visible, on the long-wavelength side
<i>NIST</i>	National Institute of Standards and Technology	The <i>NMI</i> of the United States of America
<i>NMI</i>	National Measurement Institute	National institution responsible for maintenance and dissemination of the <i>SI</i>
<i>NPL</i>	National Physical Laboratory	The <i>NMI</i> of the United Kingdom
<i>NUC</i>	Non-Uniformity Correction	Correction to homogenise the response of an imager to a uniform scene
<i>OTF</i>	Optical Transfer Function	Spatial transfer function expressed in frequency space
<i>PBF</i>	Powder Bed Fusion	A method of <i>AM</i>
<i>PSF</i>	Point Spread Function	Impulse response function expressed in sample space
<i>PTB</i>	Physikalisch-Technische Bundesanstalt	The <i>NMI</i> of Germany
<i>rms</i>	Root mean squared	A measure of the noise in variable $x$
<i>ROI</i>	Region Of Interest	Sub-section of an image
<i>SEE</i>	Standard Error of Estimate	A measure of the goodness of fit of a curve
<i>SI</i>	Système International	International System of Units
<i>SRF</i>	Slit Response Function	Transfer function of a single finite-width slit

<i>SSE</i>	Size of Source Effect	Long distance scatter metric for an optical system
<i>TFOV</i>	Total Field Of View	Extent of the <i>FOV</i> of all elements of an imaging system
<i>3G Fit</i>	3 term Gaussian Fit	Literature method for <i>ESF</i> to <i>PSF</i> conversion
<i>-EB</i>	Electron Beam	Utilisation of an electron beam as a heat source for <i>AM</i>
<i>-LB</i>	Laser Beam	Utilisation of a laser as a heat source for <i>AM</i>
<i>/M</i>	Of metals	Standardised abbreviation for specifying <i>AM</i> method as applied to metals

#### PHYSICAL CONSTANTS

Symbol	Name	Value	Unit
$k_B$	Boltzmann constant <sup>1</sup>	$1.380649 \times 10^{-23}$	$J \cdot K^{-1}$
$c (\approx c_0)$	Speed of light (in a vacuum <sup>1</sup> )	$n \times c_0$ (299792458)	$m \cdot s^{-1}$
$h$	Planks constant <sup>1</sup>	$6.62607015 \times 10^{-34}$	$J \cdot s^{-1}$
$c_1 = 2\pi hc^2$	First radiation constant <sup>1</sup>	$3.741771 \times 10^{-16}$	$W \cdot m^2$
$c_2 = hc/k_B$	Second radiation constant <sup>1</sup>	$1.438776877 \times 10^{-2}$	$m \cdot K$
$b(c_3)$	Wien $\lambda$ displacement law constant <sup>1</sup> (A.K.A third radiation constant)	$2.897771955 \times 10^{-3}$	$m \cdot K$
$\sigma$	Stephan-Boltzmann constant <sup>1</sup>	$5.670374419 \times 10^{-8}$	$W \cdot m^{-2} \cdot K^{-4}$

<sup>1</sup>Exactly defined physical constants of nature. Tiesinga, E., et al., *2018 CODATA recommended values*. 2019, National Institute of Standards and Technology.: National Institute of Standards and Technology

# THESIS OVERVIEW

---

## MOTIVATION

The two major motivations for this work are: improved characterisation of thermal imaging systems, and better understanding of the additive manufacture of metals. Improving the characterisation is motivated by a desire to see rigorous metrological practices applied to radiometric thermography. Standard metrological practices are not well documented or developed in this field. This thesis aims to address one aspect of this problem, which is the spatial transfer function of the imaging system. The spatial transfer function is usually ill defined due to practical limitations of extended area imaging systems.

Improvements in thermal imaging can lead to better understanding and process control of the additive manufacture of metals. Better understanding of the additive manufacturing process can enhance part performance and drive a fundamental shift in the manufacture of metal parts for high value applications. High speed quantitative thermography provides a promising tool to achieve this aim. The challenge addressed here is to establish a rigorously sound metrological link between the captured infrared images and the thermal fields in the process. There are many research groups working on modelling the process, but there is a lack of validation. Validation of these models by accurate measurement of the spatiotemporally resolved thermal fields, would give confidence that the process has been fully captured by the models, leading to improved part performance and reduced variability.

## AIMS AND OBJECTIVES

The main aim of this thesis is to create an accurate radiometric thermography instrument. This is a problem with many aspects, any one of which deserves its own research agenda. It is the objective of this work to improve understanding of the spatial transfer function. This can be achieved by creating an accurate spatial transfer function characterisation method. The next objective is to use this measurement to devise an accurate thermal field reconstruction algorithm. Such algorithms are often referenced and applied in literature without validation, which leads to the next *important* objective: to devise and apply a validation framework for thermal field reconstruction algorithms.

The second aim is to apply quantitative thermography in the field of additive manufacturing. The objective is to devise, set up and use suitable instruments for monitoring multiple additive manufacturing processes. This includes three distinct approaches. Firstly, to assess a low-cost monitoring system, making use of the open source Raspberry PI platform. Secondly, to use a state-of-the-art instrument to capture process data from a modified commercial additive manufacturing machine, which provides an ideal opportunity to compare thermal field reconstruction methods. Thirdly and finally, to look at the process in a level of detail not possible in commercial applications using a custom-designed test rig. This contributes to a multi-million-pound advancement project by setting up a high-speed, high spatial resolution thermography system, to capture hitherto unprecedented levels of detail of the additive manufacturing process.

## THESIS STRUCTURE

In chapter 1 an introduction to the field of radiometric thermography and additive manufacturing of metals is given. The contemporary landscape of quantitative thermography is then laid out. As this field has many applications, the area of fundamental metrology is prioritised. The application of quantitative thermography to additive manufacturing of metals is a very active research area. The work of authors or institutions which are considered to be of the highest quality, or most influential, are discussed in this chapter.

In chapter 2 the theoretical basis required for an appreciation of the workings of a radiometric thermography system is explained. It is the hope of the author that this chapter presents a good foundation for any researcher wishing to embark on the journey toward quantitative radiometric thermography. The mathematics of a geometric transform, used to project an image onto a tilted plane, are presented here. The theory in this chapter is referenced in later chapters where necessary.

Chapter 3 contains the practical aspects of the work carried out in this thesis. This chapter aims to provide the information necessary for a well-equipped researcher to reproduce the work contained herein. It is the aim of the author to also share some of the more important practical lessons learned throughout the course of the PhD. Three methods of mapping images to thermal fields in the scene are presented: direct mapping and two reconstruction methods which are *regularised deconvolution* and *model deconvolution* (the second being an original method devised by the author).

Chapter 4 introduces the use of a novel, low-cost, accessible imaging system, and a procedure to characterise and validate the system as a thermographic instrument. A well-established method for characterising the spatial transfer function of the instrument is adapted to fit into the Fourier framework. The system is used in an additive manufacturing of metals setting and its suitability for the application is discussed.

Chapter 5 presents the characterisation and use of a cutting-edge thermographic system designed for this work. Modifications to a contemporary method of spatial transfer function measurement (slanted knife edge) are described. A validation method is developed for assessing the accuracy of thermal field mapping methods. The three thermal field mapping methods described in chapter 3 are compared. The three methods are applied to data acquired from a modified commercial additive manufacturing of metals machine. The performance of the reconstructions and the quality of the data are discussed.

Chapter 6 presents the characterisation and use of a third, custom-designed thermographic instrument. The instrument was used in a unique, cutting-edge additive manufacturing test environment. This environment was designed for simultaneous in-operando thermographic and x-ray imaging of the additive manufacturing process. Performance of the geometric correction method developed in chapter 2 is assessed. Sources of uncertainty and their quantification are discussed, and an uncertainty budget is constructed. Methods for using the spatial transfer function measurement to determine the measurement field of view of the instrument are presented and discussed. Deconvolution, geometric projection and conversion to surface temperature are applied to exemplar datasets from the additive manufacturing experiments. Results gained from these experiments are assessed and compared to literature.

Chapter 7 draws together the results of the work presented in this thesis and discusses conclusions which can be drawn. Finally, this chapter also provides ideas for future projects which could be undertaken, using the contents of this thesis as a foundation.

# 1. INTRODUCTION

---

This thesis investigates the use of radiometric (light measuring) thermographic (temperature mapping) instruments to measure surface temperature, as applied to the contemporary industrial process of Additive manufacturing of metals (*AM/M*). This chapter provides a brief overview of the topics of radiometric thermography and its application to the field of *AM/M*. The landscape of literature in the two linked, but distinct fields of study is then laid out. Finally, conclusions which can be drawn from literature and gaps in field are discussed.

## 1.1 INTRODUCTION TO THERMOGRAPHY

Thermography is the measurement of distribution of temperature. The term usually pertains to two-dimensional maps (images) of the spatial distributions of thermal fields. The dimension of time is often included in these measurements, and this three-dimensional data (2 space and 1 time) is the commonly accepted definition of thermography. Modern digital imaging and sensor technology allows previously inaccessible thermographic measurements to be made.

Temperature is a critical state variable in many industrial processes, and much effort is expended to measure and control it across a wide variety of industrial sectors and applications. The most developed form of thermometry is contact thermometry [1], in which a sensor (transducer) is brought into thermal equilibrium with the object to be measured. Contact thermometry is usually the most reliable and accurate way to measure the temperature of a system. Contact thermometry is not always convenient or possible in many situations [2].

The most common form of non-contact thermometry is infrared radiation thermometry, with the most common implementation of this being direct measurement of the radiance (brightness) of a surface. Infrared Radiation Thermometers (*IRT*s) usually measure the radiance of a single small area of a surface, and use this measurement along with some assumptions about the surface to infer a surface temperature.

A radiometric thermographic system can be conceptualised as a series of *IRT*s each pointed at a small surface area, and are often sold as such [3]. It will be shown throughout this thesis that significant care must be applied before assuming that the image presented by a thermographic instrument provides a true representation of the thermal field it is viewing.

Since the 19<sup>th</sup> century the measurement of the power in infrared radiation has been of interest to physicists and engineers [4]. The radiation emitted by objects (electromagnetic spectrum), existing in our observable surroundings, covers many orders of magnitude in energy and wavelength. Each of these energy scales is of interest for different applications. Figure 1.1-1 shows the small portion of the electromagnetic spectrum pertinent to this work, which is termed Infrared Radiation (*IR*). This translates as lower than red, because the radiation has less energy than the red end of the visible spectrum.

The main advances in *IR* thermography technology in the 20<sup>th</sup> century have often been driven by military applications [5-8]. Military applications make use of both long-wave *IR* for low temperatures, such as searching for body temperatures close to ambient surroundings, and short-wave/near *IR* for high temperature applications such as tracking the hot exhaust of rockets or jets. In recent decades, medical applications have found use for the longer wavelength (lower temperature thermography) [9, 10]. In addition, some industries have adopted thermography for process monitoring [11-13], and in the non-destructive testing of parts to find subsurface defects [14, 15], which usually requires an active pulsed heat input.

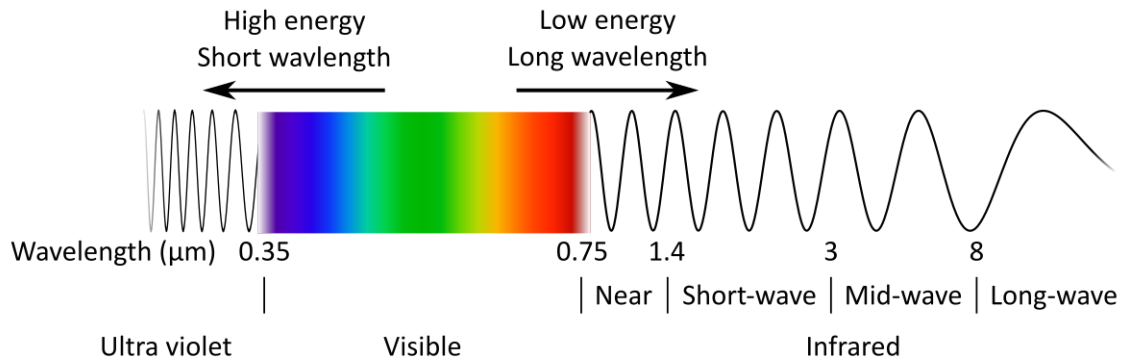


Figure 1.1-1 A portion of the electromagnetic spectrum. The wavelength range of interest for this work is the near infrared. The wavelength scale is not linear.

### 1.1.1 Challenges in thermography

Measuring temperature using radiometry can be very accurate. Radiometric measurement is used to interpolate the currently recognised international temperature scale at high temperatures. This kind of metrological application relies on a tightly controlled set of experimental parameters. It is difficult, if not impossible, to translate that level of accuracy to real world measurement applications. The main source of uncertainty in any radiometric measurement of temperature is likely to be the emissive properties of the surface itself. These emissive properties are usually covered by the catch all term: *emissivity*.

Accurate measurement of the emissivity of a surface is not trivial in any situation. Measuring the emissivity in an identical situation to that found in a temperature measurement in the field is even more challenging. Uncertainty in the emissivity is a most significant problem for very low emissivity surfaces, such as liquid metals where variations will have a large fractional effect on the amount of light emitted by a surface (radiance). It is a continual problem for any radiation thermometry application that the emissivity is, in general, unknown. A weakness of this work is that it relies on literature values of emissivity for any quantitative measurements of surface temperature.

In some measurement situations radiation reflected from the surface forms a significant fraction of the signal. This can include reflections of the ambient background, or specific hot objects, such as the sun. This problem in radiation thermometry is not prevalent in *AM*. This is due to the nature and location of the hot surface under inspection.

Another significant source of uncertainty is in the radiometric measurement itself. The main contribution of this thesis to the field, is the characterisation of the transfer function of the thermographic instrument. This is the ability of the instrument to make a *resolved* measurement of the scene under inspection. The term *resolved* is investigated and its exact meaning in the field of thermography is explored later in the work. Characterisation of the transfer function is also used to improve on the native performance of the instrument by image processing. The effects of this improvement are investigated in chapter 5.

The chosen application is thermographic measurement of the additive manufacturing (*AM*) of metals. The challenges specific to this application mainly relate to the use of a localised high-power heat source in these processes. This usually takes the form of a laser beam or an electron beam. Process efficiency demands the most rapid transition from feedstock to part. This is often achieved by using the highest available power, moving at the fastest possible speed. The requirement being to input enough energy to drive the feedstock through the phase transitions into the final printed part. The situation is hence a rapidly moving and localised heat source which imparts large spatial and temporal gradients in the feedstock and part. Assessment of the ability of a thermographic instrument to fully resolve these spatiotemporally localised thermal fields is an aim of this thesis.

The *AM* application is in some ways extremely challenging, but also does not include some of the problems which are prevalent in other applications. The aspects of *AM/M* which make quantitative thermography easier are the high temperatures and isolated thermal fields present in the process. One advantage of the high temperatures is the freedom to use mature, short wavelength sensor technologies, namely Silicon (Si).

The focus of this thesis is on characterising and improving the spatial aspects of thermal field measurement. This is primarily achieved by measuring and accounting for the spatial (as opposed to temporal) impulse response function of the instrument. For reasons of convention the term Point Spread Function (*PSF*) will be used to describe this property of the device. Its exact meaning and definition will be discussed in section 2.4. Another important development of this thesis is the concept of the Measurement Field Of View (*MFOV*) which determines how large a uniform region must be before the instrument can make an accurate measure of its temperature.

## 1.2 INTRODUCTION TO ADDITIVE MANUFACTURING

*AM/M*, especially of superalloys, is a very active area of contemporary research [16]. There are many methodologies which fall under the category *AM* of metals. For this thesis two of the widely used methods will be investigated:

- Laser-based Powder Bed Fusion of metals (*PBF-LB/M*)
- Laser-based Directed Energy Deposition of Metals (*DED-LB/M*).

(Abbreviations as per BS EN ISO/ASTM 52911-1:2019[17] and latest draft version of BS EN ISO/ASTM 52900:2017[18]). *PBF-LB/M* is often referred to by one of its alternative abbreviations (trade names), Selective Laser Melting (SLM), Selective Laser Sintering (SLS), Laser-based Powder Bed Fusion (LPBF) or Powder Bed Laser Fusion (PBLF). The basic principles of *PBF-LB* & *DED-LB* are illustrated in *Figure 1.2-1*.

A recent review of *AM* [19] for the aviation industry put *PBF* & *DED* as the primary *AM* technologies, and also the best placed for future integration into aviation supply chains. An introductory text to the field of *PBF-LB/M* is a published adaptation of a thesis by Yadroitsev (2009)[20]. This work gives a good balance of the basic theoretical aspects of a moving heat source interacting with the powder, supported by data and pictures of melt tracks taken from real machines.

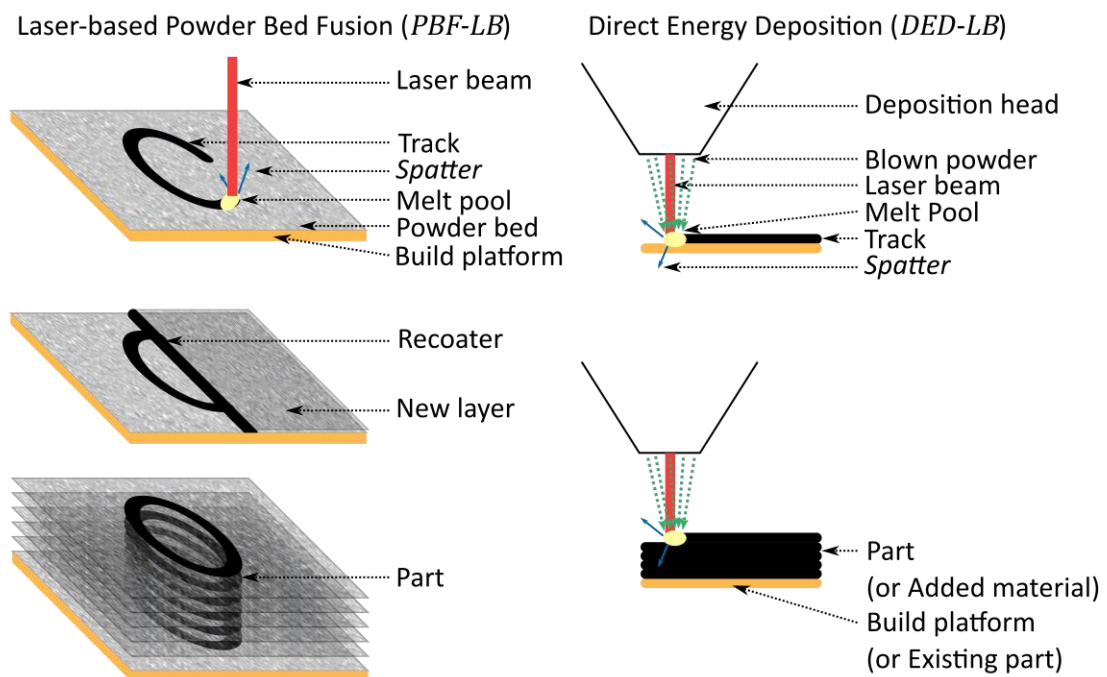


*Figure 1.2-1 PBF can create very complex high precision geometries with no additional time or machining work, DED can be used to repair or add to existing geometries and can be used to create large parts.*

### 1.3 STANDARDISATION AND MEASUREMENT SCIENCE

Standards and other internationally recognised documents provide a good framework which can be used to carry out research, and act as common points of reference for discussion. In addition to standards, other internationally accepted definitions allow measurements of ground truths to be compared. The pertinent standards and internationally accepted definitions are given in Table 1.3-1.

Temperature is defined in the System International (*SI*) [21] using a combination of the definition of energy, and the definition of Boltzmann's constant. This definition has only recently been adopted [22]. Until 2019 the Temperature scale was defined by the triple point of water, a physical phenomenon. In alignment with the other quantities in the *SI*, the definition was changed to be based on universal physical constants [23]. At the time of writing the internationally recognised temperature scale is the *international temperature scale of 1990 (ITS-90)* [24]. The *ITS-90* provides a methodology for universal standardisation of the realisation of a temperature scale. Above the freezing point of silver the *ITS-90* is realised by comparative radiation thermometry with fixed point cells of known phase transition temperature [25]. The National Metrology Institutes (*NMIs*) of countries around the world use the *ITS-90* to ensure that a temperature, as measured in one country, would be measured at that same temperature in any country.

There are two main groups of English language standards for the field of thermography and *AM*. In the USA the American Society for Testing and Materials (*ASTM*) produces the relevant standards. In Europe the British Standards (*BS*), European Standards (*EN*), and international standards (*ISO*) are closely aligned. The pertinent European standards for radiation thermometry are in the field of temperature measurement [26], and Industrial process control devices [27, 28]. From the USA a standalone test methods standard for *IRT*s [29] provides a useful source of performance metrics. In the field of thermography the most helpful source of standardisation in Europe comes under in the field of non-destructive testing [30-32].

*AM* is a relatively immature, and fast-moving discipline, therefore standards are being revised on a regular basis. It is useful to use *BS 52900:2017* [18] for a standardised vocabulary. This standard has an updated form in the draft phase at the time of writing. For the specific *flavours* of *AM*, *BS 52911-1:2019* covers *PBF-LB/M*, and *ASTMs: F3187 – 16* covers *DED-LB/M*.

Table 1.3-1 Pertinent international definitions and standards

ref	Institution	Standard Reference	Pertinent content
<b>Temperature scale</b>			
[21]	BIPM	The <i>SI</i>	Definition of temperature.
[24]	BIPM	<i>ITS-90</i>	Realisation of international temperature scale.
[25]	BIPM	Guide to the realisation of <i>ITS-90: Radiation Thermometry</i>	The role of IRTs in <i>ITS-90</i> and interpolation of calibration points for <i>IRT</i> s.
<b>Infrared radiation thermometry</b>			
[26]	BSi	BS 1041-5: 1989	Radiometric terms, operating principles of <i>IRT</i> s, calibration of <i>IRT</i> s.
[27]	BSi	DD IEC/TS 62492-1:2008	Lexicon of radiation thermometry, calculation of uncertainty.
[28]	BSi	PD IEC/TS 62492-2:2013	Characterisation and calibration methodologies.
[29]	ASTM	E1256-17	Characterisation and calibration methodologies.
<b>Thermography</b>			
[30]	BSi	BS ISO 10878:2013	Lexicon of thermography.
[31]	BSi	BS ISO 10880:2017	Important specifications for use in given application.
[32]	BSi	BS ISO 18251-1:2017	Performance metrics.
[33]	BSi	BS ISO 18434-1-2008	Lexicon, introduction to thermographic techniques.
<b>Imaging</b>			
[34]	BSi	BS ISO 12233:2017	Image quality characterisation methodologies.
<b>AM</b>			
[18]	BSi	BS EN ISO/ASTM 52900:2017	Lexicon of <i>AM</i> .
[17]	BSi	BS EN ISO/ASTM 52911-1:2019	Operating principles & lexicon of <i>PBF-LB/M</i> .
[35]	ASTM	F3187-16	Operating principles & lexicon of <i>DED/M</i> .

## 1.4 RADIATION THERMOMETRY & THERMOGRAPHY IN LITERATURE

In this section the most pertinent works in the field of quantitative thermography are described, these works are not restricted to the field of *AM*. The aim is to provide a resource for a reader wishing to enter the world of radiation thermometry and become familiar with the theory, technology, challenges and the state of the art.

### 1.4.1 David P DeWitt (USA)

DeWitt co-authored the most significant book in the field of radiation thermometry [36]. He has also published research papers and conference proceedings on the subject [37, 38]. Dewitt also made significant contributions to radiometric volumes, of the ubiquitous thermophysical properties, reference database compiled by Toulekain [39]. Although it is now dated, his work, in collaboration with others, constitutes the main source for reliable theoretically based understanding of the radiometric measurement of temperature used in this thesis.

#### 1.4.2 Measurement standards laboratory (NZ)

A large portion of the influential work over the last few decades in the field of quantitative radiation thermometry has come from the *NMI* of New Zealand, mainly headed by Peter Saunders and Rod White [11, 25, 40-46].

Yoon et al (2017)[25] has already been mentioned, and forms the link between the *ITS-90* and radiation thermometry. Saunders & Edgar (2009)[40] and Saunders (2011)[41], deal with correcting single pixel Infrared Radiation Thermometer (*IRT*) measurements, to account for the Size of Source Effect (*SSE*-see section 2.4) of the device. Saunders & Edgar (1999)[42] deals with the correction of thermal images captured with a camera, to account for the blur inherent in the instrument. The pair used a pinhole to measure the *PSF* of the instrument. They also used a technique by Ricolfi & Wang (1993)[47] to characterise the *SSE* of their thermographic instrument. In this work they showed that although the *PSF* can be partially corrected, other effects which contribute to the *SSE* are harder to remove, and careful optical design is required to minimize reflections and scattering in the optics.

In Saunders & White (2013)[43] the pair expose the dangers of closed box optical systems. The work shows that the *etendue* (see section 2.1.3) of the optical system changes with focus, making up to 20 % difference to the measured radiance. Saunders (2011)[44] is one of a number of works by the author which deal with uncertainties, and their propagation, in the radiometric measurement of temperature. Saunders & White (2003)[45] and Saunders (1997)[46] deal with the physical basis for the interpolation equations (see Section 2.2) used in radiation thermometry. The work provides insight into the different forms of interpolation equations, and how they can be used in relation to the spectral characteristics of a radiometric instrument used to measure temperature. The application-focused book 'Radiation Thermometry: Fundamentals and applications in the Petrochemical Industry' Saunders (2007)[11] forms a good introduction for researchers wishing to implement radiometric measurements of temperature.

#### 1.4.3 *BIPM* working group for non-contact thermometry (Worldwide)

The *BIPM* has a bank of consultative committees for the different measurement quantities in the *SI*. The committee relevant to temperature measurement is the consultative committee for thermometry (*CCT*), within this committee are several working groups of internationally recognized experts. The group most relevant to this thesis is the 'working group for non-contact Thermometry' (*WG-NCTh*) (formerly known as working group 5). The *CCT-WG-NCTh* has produced a number of useful documents mainly concerned with primary and calibration chain thermometry [25, 48, 49]. It is good practice to try to utilise documents of this type to inform metrology practices, so that work can be compared across the world. Yoon et al (2003)[25] has already been mentioned. Fischer et al (2003)[49] and Saunders et al (2008)[49] deal with the identification and quantification of uncertainties in a measurement of temperature by radiometric means. These works are mainly concerned with measuring and transferring calibrations via blackbody cavities and fixed points, but the work on uncertainty quantisation is useful to understand the sources of error in all radiometric temperature measurement systems.

#### 1.4.4 National Physical Laboratory (UK)

Work by the temperature and humidity group of the National Physical Laboratory includes a book by Coates and Lowe (2017)[50] on the theory of radiation thermometry. The publications pertinent to this work deal with the metrology of thermography [51-55]. Whittam et al (2014) [51] provides a comparison between some commercial thermography systems. The *SSE* and non-uniformity of the systems were found to make the uncertainty in temperature measurement larger than that stated by the manufacturer. McMillan et al (2018)[52] highlight the significant effect *SSE* has on uncertainty in small scale quantitative thermography. The work also proposes a method of non-uniformity correction

which relaxes the requirement for strict uniformity of the calibration target, similar to a method used at *PTB* [56].

Machin et al (2009)[53] elucidate the steps required to make a thermal measurement using a thermographic system truly quantitative in the metrological sense, including accreditation and traceability. Robinson et al (2017)[54] implement a geometric model of a scene in 3d to inform the expected reflection contributions to thermal measurements. This is implemented at a large-scale space simulating vacuum facility, where the radiative properties and temperature of devices is critical.

McEvoy et al 2012[55] surveyed 15 *NMIs* about the state of their thermographic testing facilities. They identified 6 fields which they felt were important for thermographic system characterisation (distinct from *IRT*s), these are laid out in Table 1.4-1. The survey also included a feedback category where the surveyed *NMIs* could specify any other services they thought pertinent, these are under the category 'other'. The work found that most European *NMIS* did not offer accredited calibration and characterisation services specifically tailored to thermographic instruments.

Table 1.4-1 Thermographic instrument characterisation facilities at European *NMIs*

Calibration methodology	Radiometric blackbody calibration.
Size of source effect	Aperture test or similar (see section 2.4.3).
Distance effect	Focus effects (see section 2.1.3).
Field uniformity	Non uniformity correction.
Environmental effects	Effect of ambient temperature, humidity etc.
Emissivity correction	Validity of the systems inbuilt emissivity correction.
Other	
Short term stability	Testing the stability over a period of one day.
Commonly used metrics ( <i>MRTD</i> , <i>NETD</i> etc.)	Industrially relevant performance metrics.

#### 1.4.5 National Institute of Standards and Technology (USA)

The National Institute of Standards and Technology (*NIST*) is a large organisation, and many individual groups within it have worked on quantitative thermography [57-65]. Lane et al (2013)[57] is probably the paper which has singularly had the most significant influence on this thesis. The calibration and measurement procedures for the instrument used in the publication are laid out in a *NIST* report by Lane & Whintont (2015)[58]. The publication and report form the best guidance found on preparing a radiometric imaging system for use as a quantitative thermographic instrument. The experimental procedures laid out in the report form the experimental basis which is built on in later chapters. The paper lays out a framework for estimating the uncertainty of the thermographic temperature measurement of a highly magnified metal cutting scene. The work found that the spatial transfer function of the instrument can be the largest source of uncertainty in this kind of application. The work by Lane et al builds on previous work by Whintont & Heigel [59-62] on the same application.

Envall et al (2009)[63] present a suite of characterisation tools for measurement of *SSE* in radiometric devices. The main focus of this is to determine the *SSE* of metrological *IRT*s. The work touches on the measurement of *SSE* in radiometric imaging instruments, citing the following work by Zong et al.

Work by Zong et al (2007)[64] was patented in 2008[65]. This work uses the spatial *PSF* measured by a small diameter aperture scene (see section 2.4.3). The aperture is moved around the Total Field Of View (*TFOV*) of the instrument to characterise the *SSE* in all parts of the image. The patent deals with the numerical application of the correction matrix derived from this characterisation to a measured image.

#### 1.4.6 Other work pertinent to this thesis

Fuwen et al (2018)[66] compare two deconvolution methodologies, they state a doubling in spatial resolution over direct measurements of temperature using regularised deconvolution and blind deconvolution. The work is aimed at the field of biomedical sciences. The best results were obtained with a blind deconvolution (estimated *PSF*) algorithm, which was tuned to the given scene. The work talks about the ringing effect encountered during this work.

Rozanski (2014)[67] compares 4 methodologies (*IFOV*,  $CTF = 0.5$ , *LSF* peak at 0.4 of max and  $MTF = 0.5$  (see later chapters for descriptions of these quantities)) for measuring the geometric resolution of scanning thermographic instruments. Empirical relationships between the methods are developed rather than decomposing each of them to a single framework, which, in the case of this work, is the Fourier analysis framework.

Masaoka et al (2014)[68] modified the slanted knife edge methodology presented in BS ISO 12233:2017[34] for finding the *PSF*, to fit a chosen functional form (model) directly to the step response function. Fitting the model directly to the step response function has the advantages of reducing noise in the final *PSF* measurement, but has the limitation that the validity of the model is not known a priori.

Pospíšil et al (2005)[69] used random (white) spatial noise scenes which contain all resolvable spatial frequencies to measure the spatial transfer function of a video camera system. This method has merit because it can measure all frequencies with a small amount of processing. It is the opinion of the author that a method like this could be used, but to characterise the whole position dependent transfer function of the instrument, not just the average across the entire *TFOV*.

Estrieau & Magnan (2003)[70] compare frequency response function measurement made using the slanted knife edge method in BS ISO 12233:2017[34], with spatial response measured using sinusoidally varying targets for Si sensors. Estrieau & Magnan (2003)[70] conclude that the results of the two methods are very similar and that the slanted knife edge methodology is superior due to its simplified experimental setup.

Du & Voss (2004)[71] measured the *PSF* of a Si based imaging system using a collimated laser source. The pair highlight the importance of consideration of the *PSF* to maintain radiometric calibration. The pair show that the radiance of an object in one part of the scene will affect radiometric measurement of other components of the scene for a significant distance (compared with the width of the peak of the *PSF*) from the original object.

## 1.5 THERMOGRAPHY FOR THE ADDITIVE MANUFACTURE OF METALS IN LITERATURE

There are two main modes of imaging for thermography of the melt pool in laser-based *AM/M*, co-axial and off-axial, see Figure 1.5-1. The co-axial methods usually provide a smaller *TFOV*, but the *TFOV* is always centred on the region of the build where the most significant thermal processes are occurring.

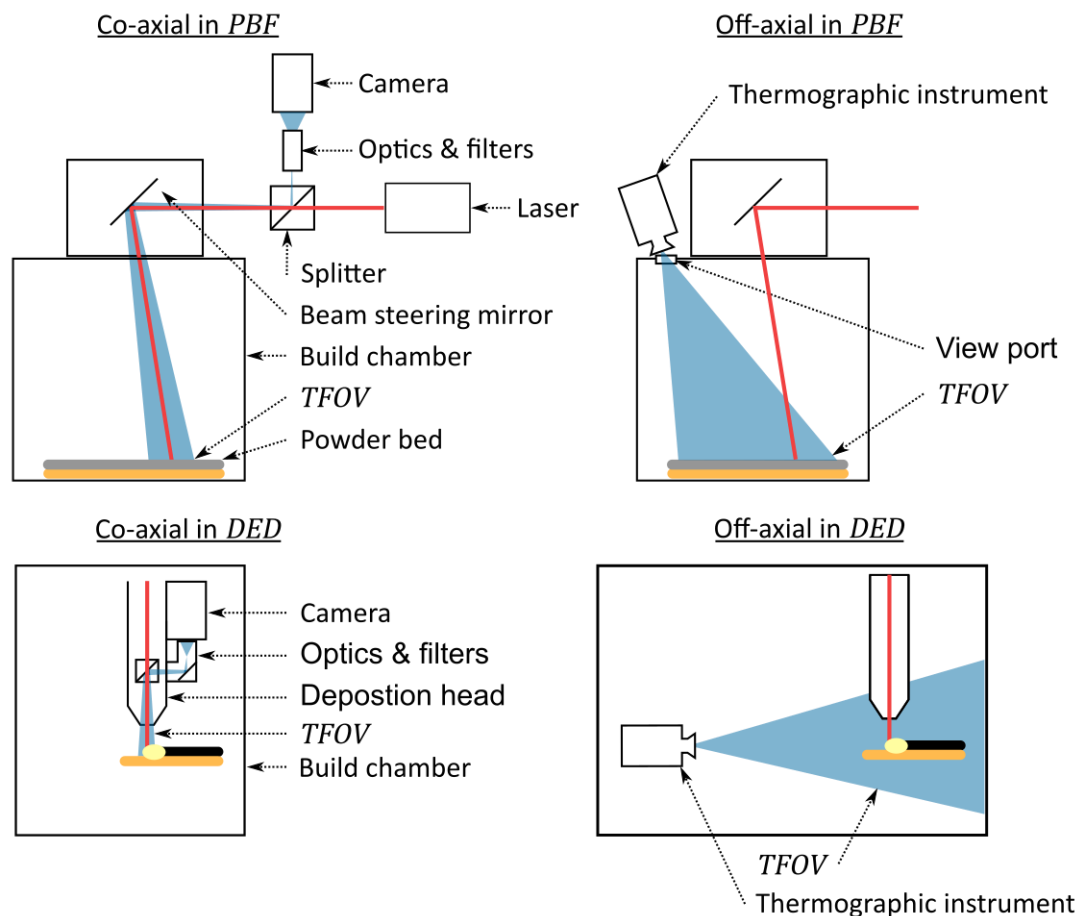


Figure 1.5-1 The two main options for thermography in AM of metals for the two AM methodologies investigated in this work.

### 1.5.1 Imperial College London (UK)

A Group based at Imperial College London have recently worked on thermography for *AM/M* [72, 73]. In Hooper (2018)[72] a two colour, high speed, coaxial system was developed using a pair of Si Photron *CMOS* cameras (Photron Ltd., Tokyo, Japan) to monitor melt pool temperatures in a modified commercial *PBF-LB/M* machine. The methodology was validated by laser-heating the tip of a type C Tungsten-Rhenium thermocouple. The spatial resolution was reported as 20  $\mu\text{m}$ , at a sample frequency of 100 kHz. The two wavelengths chosen were at 0.7  $\mu\text{m}$  and 0.95  $\mu\text{m}$ .

A two-colour system removes the sensitivity of the measurand (ratio) to factors which linearly scale the signal (see Appendix 8.3). The group assumed that the emissivity was identical at the two wavelengths (grey body). The *effective wavelength* [74] (Eq 8.3-4) of the system used is 2.67  $\mu\text{m}$ , giving it a sensitivity to temperature three times lower than a single waveband radiometric temperature measurement system operating at 0.9  $\mu\text{m}$ . The problems of multi wavelength radiometric temperature measurement are well known [37, 74, 75], mainly concerning the validity of the emissivity relation used. It is also pointed out in Yamada (2015) [75] that any hot objects within the *MFOV* of the pixels will result in a large temperature error, which is likely to be the case in the region

surrounding the heat source and on the periphery of the melt pool for this work. The very large thermal gradients present in this work will also mean that, if the *MFOV* is different in each channel, the peak radiance measured will be different in each channel, leading to significant errors in the measured peak temperature. The uncertainty of the measurements is not quantified. The author estimates that a 5-20 % error in ratio could be expected close to the laser spot, this would generate a 48-192 °C error in the measure Temperature at 2000 °C (Eq 2.2-24).

In Williams et al (2019) [73] the same coaxial system as in Hooper (2018) [72] was used to measure the size of the melt pool and amount of spatter generated throughout a build. In addition to the two-colour system, a long wavelength 7.5-13 µm FLIR camera was used to monitor the cooling rates of the parts in between the layers. The longer wavelength camera had a  $\sim 1 \text{ mm}^2$  *IFOV* with no mention of the *MFOV*, it is expected that due to the small temperature gradients across the parts in the inter-layer cooling phase, this distinction is unlikely to contribute a large error to their estimates of temperature. An in-situ characterisation of the effective emissivity of the printed part and the powder was performed using a single embedded type K, Nickel-Chromium thermocouple. The thermocouple was used to infer a surface temperature, but no uncertainty in this inference was included. The main aim of this work was to explore the relation between the temperature of the part just before the next layer started (dwell temperature), and the material properties. The dwell temperature varies with the time between layers and the geometry of the already printed part, which affects the heatsinking properties. The work found correlation between porosity and dwell temperature.

### 1.5.2 Technical University of Munich (Germany)

A group operating out of the *AM* lab of the Institute for machine tools and industrial management, have worked on thermal monitoring of *PBF-LB/M* [76-78]. Krauss et al(2012)[76] introduce a thermographic system based on an uncooled microbolometer array operating at 8-14 µm. The system was attached to an EOS 270 *PBF-LB/M* machine (EOS GmbH, Krailling, Germany). The *TFOV* of the system covered the entire powder bed. The resolution of the instrument is quoted as 250 µm, and a time constant of 5-15 ms which is insufficient to resolve the melt pool during a normal *PBF-LB/M* process. The group concentrate on looking at the cooling rate of the part after the laser has moved on, due to cited experimental difficulties all temperatures used are in terms of radiance temperature (emissivity assumed to be unity).

Krauss et al(2014)[77] and Krauss et al (2015)[78] use the previously described microbolometer array system as a process monitoring tool to investigate the effect of cooling rates on part performance, concentrating on how the geometry affects the thermal diffusivity of the part.

### 1.5.3 National Institute of Standards and Technology (USA)

*NIST* has invested a significant amount of resources into thermography for *AM/M* over the past decade [79-86]. Mani et al(2017)[79] reviews the measurement needs for process control in *PBF/M*. The work identifies peak temperature and temperature gradients in the melt pool as key process signatures, which can be used as parameters in real time process control. Peak temperature is important because it determines the alloy composition of the printed part, the rate of vaporisation of the alloy components is heavily correlated with the peak temperature reached. The thermal gradients during cooling significantly affect the crystal growth of the material and will have a strong influence on the material properties of the final printed part. The work calls for more effort to be put into quantifying the uncertainty in melt pool monitoring, to allow comparison between the work of different groups.

The *AM* bench marking test series [80] provides a resource for researchers in the field to access experimental data collected from a variety of sources. The data is curated by a committee chaired out

of *NIST* and is available for public access. The *AM* bench marking test series is under development as a resource at the time of writing.

Moylan et al (2014)[81] introduces *NIST*'s approach to developing their *IR* thermography experimental methodologies. They review the previous literature and assert that *IR* thermography plays an important role in process control and measurement.

Heigel, Lane & Moylan(2016)[82] look at the large-area emissive properties of metal parts printed with different print parameters. This work is mainly concerned with lower temperature, large area, part monitoring thermographic systems. These systems can look at the bulk temperature of the part as the print develops and does not assist understanding of the emissive properties in the kind of small-scale thermography attempted in this work. They show that the 'roughness' of the print affects the emissive properties of the surface.

Lane et al(2016)[83] introduce the thermographic facilities focused on *AM* at *NIST*. The work shows a similar knife edge *PSF* measurement to that utilised in this work based on work in another field [87]. It shows how difficult the emissivity is to measure, and that it is a large component of the uncertainty in measured thermal fields. The work also highlights the problems with image analysis in the presence of many confounding radiance sources, namely the spatter, and reflection of the spatter from the surface. The work found that the system had insufficient spatiotemporal resolution to capture the dynamics of the process.

Heigel & Lane (2017)[84] use a 1.35 – 1.6  $\mu\text{m}$  thermographic system, with a 40  $\mu\text{s}$  integration time and a *IFOV* of 36  $\mu\text{m}$  in the laser travel direction. They assess how the melt pool changes in the presence or absence of powder in the print. The Pair highlight the difficulty in making accurate radiometric measurements of temperature in the presence of metal powder which causes spatter and uneven print surfaces. One of the advantages of using longer-wavelength thermographic systems than the ones used in this thesis, is the ability to measure the lower temperatures below the freezing point of the metal, this advantage is offset by the almost certain saturation of the device at the very hot part of the print (adjacent to the laser) and the low pixel count (spatial sampling rate) that most longer wavelength systems have.

Lane et al(2017)[85] use a slanted knife edge to compare the spatial resolution performance in terms of frequency response function, of two thermographic instruments to be used for *AM* work at *NIST*. The work uses precision pinhole apertures to simulate the small, isolated high-radiance scenes found in *PBF*. The work notes the importance of reflections between the optical elements in the instrument and how offsets in these reflections affect the rotation symmetry of the *PSF*.

As part of the *AM* bench marking test series[80], Heigel et al (2020)[86] compared the cooling rates and melt pool lengths for IN625 overhanging and solid builds. They used a high speed InSb based instrument operating in the wavelength range: 1.35-1.6  $\mu\text{m}$ , with an *IFOV* of 34 by 52  $\mu\text{m}$  and an exposure time of 40  $\mu\text{s}$ . The wavelength range used means that the instrument was limited to a radiance temperature range of 500-1100  $^{\circ}\text{C}$  which is relatively narrow but does allow measurement of the initial solid cooling rate which is of importance to the material properties of the printed part.

#### 1.5.4 The University of Texas El Paso (USA)

A significant amount of work in the field of *AM/M* mainly in *PBF-EB/M* has taken place at the university of Texas El Paso, mostly overseen by Ryan Wicker(UTEP, El Paso, TX, USA), the editor of the Elsevier journal '*Additive Manufacturing*' [88-91].

Rodriguez et al(2015)[88] use a 7-15  $\mu\text{m}$  microbolometer array instrument, with an *IFOV* of 175  $\mu\text{m}$ . They make a concerted effort to characterise the thermographic instrument and radiative properties of the part in situ. They use a printed blackbody cavity inside the build chamber and compare the 'known' radiance of the cavity to the radiance of a thermally linked, printed target surface. This arrangement allows for emissivity measurement of the surface up to the maximum

temperature that the artefact can be heated (by cartridge heaters). This method also provides an in-situ calibration or check of radiance for the thermographic instrument. This does not include the phase transition temperature or liquid phase.

Fisher (2017)[89] Use the same thermographic instrument as Rodriguez (2015)[88], to probe the effect of large scale temperature variations in Ti-6-4 *PBF-EB/M* prints. The work found that thermocouples embedded in the build plate gave a poor measure of the part temperature. The paper is primarily concerned with the bulk temperature of the part, they work to ignore local transients caused by the heat source.

Cordero et al(2017)[90] compare thermography to a single spot multiwavelength *IRT*, using the same thermographic system as Rodriguez (2015)[88] and Fisher (2017)[89]. The work found that the multiwavelength system was insensitive to the radiometric problems encountered with the thermographic system but limited by the fact that it can only measure the temperature at a single spatial point. As an aside, the multiwavelength system by Felice [92, 93], used in Cordero(2017)[90], is a controversial technology, which claims to be an emissivity independent measurement of surface temperature. The device expands on the justification of two colour radiation thermometry [72], to assume a minimally varying spectral model for the emissivity at many wavelengths. This approach has been largely discounted in the thermal metrology community, due to work by Coates [74, 94] ‘, who argues that the more wavelengths and free emissivity model parameters are added to a radiance measurement of temperature, the the less likely it is that the inferred temperature will be accurate. Multiwavelength systems also have the drawback of an uncertainty which is very difficult to quantify without careful characterisation of the true emissivity, which would render the technique obsolete.’

Fisher et al(2018)[91] used a coaxially mounted system, described in Lane et al (2017)[85] to monitor the size of a titanium alloy (containing 6% aluminium and 4% vanadium (Ti-6-4)) melt pools at a variety of power and speeds in *PBF-LB/M*.

### 1.5.5 Other work pertinent to this thesis

Boone et al (2018)[95], used a Si based instrument in the with a sensitive range of 0.85-1.1  $\mu\text{m}$  and an *IFOV* of 66-79  $\mu\text{m}$ . Machine learning was used to segment the images acquired from a *PBF-EB/M* process. This allowed dynamic application of emissivity correction to the melt pool. This kind of image processing using machine learning has the capability to improve thermographic measurements a great deal. By identifying different components of the scene (spatter, melt pool, un-melted powder etc.), and applying different processing to them, the overall accuracy, and the amount of useful information acquired from the thermography can be improved.

Lia (2018)[96] used embedded tungsten-rhenium (type C), thermocouples in Ti-6-4, to monitor the spatially localised thermal history of the print as multiple layers were built on top of the sensor. The work has the advantages of using contact thermometry, but it is not clear how the presence of the thermocouple in the melt pool affected the thermal fields or the behaviours of the metallurgy on solidification. The work clearly identifies phase transitions in the build including solid state phase transitions which are inaccessible for the temperature ranges measured by Si base thermographic systems.

### 1.5.6 *IR* imaging for process control / defect detection

There appear to be more examples in the literature of work oriented towards using *IR* imaging systems as process control tools, than there are examples of quantitative thermography. This approach is a more accessible tool for researchers engaged *AM/M* process research, because a lot of the theory and uncertainties involved with quantitative thermography are irrelevant. A good example of such an application is by Bartlett et al (2018)[97], who used an 8-14  $\mu\text{m}$  *IR* system to monitor the full bed in the *PBF-LB/M* process. The work found correlations between the appearance of *lack of*

*fusion* defects and a signature in the *IR* data. The group reported 100% detection rate for defects over 0.5 mm diameter (which is very large for a regular print) dropping to 50 % detection efficiency for 50  $\mu$ m diameter defects. However, the validity of the technique is not supported by an analysis of the false positive detection rate, which is necessary for the technique to be widely applicable for process monitoring. The low pixel count of long wavelength cameras limits the spatial resolution that full bed monitoring system (large *TFOV*) can achieve.

## 1.6 CONCLUSIONS

Thermography is a broad field of study. Different applications of thermography have their own distinct challenges. *IR* thermography has not been put on such a metrologically rigorous footing as infrared radiation thermometry. The main reason for this is likely to be the lack of optical image quality for extended area imaging. There is a need for easy to apply characterisation methods to assess the image quality and validated techniques to account for the errors that this causes.

Currently one of the most challenging and highly desirable applications of thermography is in the monitoring of, and research into, the *AM/M* processes. The high speeds and spatially localised heat sources, associated with *AM/M*, make the ability of the thermographic instrument to reproduce the scene a significant factor in the accuracy of the measurement of the thermal fields. The two main challenges to quantitative thermography in *AM/M* throughout literature are: the unknown radiative properties of the surface, and the ability of the thermographic instrument to reproduce the scene. Measurement of the radiative properties of the surface during the *AM/M* process requires a significant amount of specialist equipment which was unavailable to the author, and so is left for others to pursue. The ability of the thermographic instrument to accurately capture the scene forms the main body of work of this thesis. The majority of attempts at quantitative thermography in the *AM/M* field have concentrated on the large-scale monitoring of the whole part there exists a need for high detail imaging of the dynamic of the thermal fields localised to the heat source.

## 1.7 REFERENCES

1. Bentley, R.E., *Handbook Of Temperature Measurement*. Vol. 1. 1998: Springer Science & Business Media.
2. Hollandt, J., et al., *Chapter 1 - Industrial Applications of Radiation Thermometry*, in *Experimental Methods in the Physical Sciences*, Z.M. Zhang, B.K. Tsai, and G. Machin, Editors. 2010, Academic Press. p. 1-56.
3. FLIR, *Thermal imaging guidebook for industrial applications*, I.T. Centre, Editor. 2011, FLIR.
4. Seebeck, T.J., *Ueber den Magnetismus der galvanischen Kette (About the magnetism of the galvanic chain)*. 1822, Berlin, Germany: Deutsche Akademie der Wissenschaften zu.
5. Bisbee, T.L. and D.A. Pritchard. *Today's thermal imaging systems: background and applications for civilian law enforcement and military force protection*. in *Proceedings IEEE 31st Annual 1997 International Carnahan Conference on Security Technology*. 1997.
6. Crawford, F.J., *Electro-optical sensors overview*. IEEE Aerospace and Electronic Systems Magazine, 1998. **13**(10): p. 17-24.
7. Krapels, K., et al., *Minimum resolvable temperature difference (MRT): procedure improvements and dynamic MRT*. *Infrared Physics & Technology*, 2002. **43**(1): p. 17-31.
8. Singh, R., et al., *High Temperature Calibration of Thermal Imagers for Infrared Measurements on Military Platforms*. *Defence Science Journal*, 2017. **67**(2): p. 188-192.
9. Ring, E.F.J. and K. Ammer, *Infrared thermal imaging in medicine*. *Physiological Measurement*, 2012. **33**(3): p. R33.

10. Hildebrandt, C., C. Raschner, and K. Ammer, *An Overview of Recent Application of Medical Infrared Thermography in Sports Medicine in Austria*. *Sensors* (Basel, Switzerland), 2010. **10**(5): p. 4700-4715.
11. Saunders, P., *Radiation thermometry: Fundamentals and applications in the petrochemical industry*. 2007. 1-161.
12. Viale, M., et al. *Application of on-line infrared thermography in steel making industry*. in *Defense and Security Symposium*. 2007. SPIE.
13. Usamentiaga, R., et al., *Monitoring Sintering Burn-Through Point Using Infrared Thermography*. *Sensors*, 2013. **13**(8): p. 10287.
14. Shepard, S.M. and M.F. Beemer. *Advances in thermographic signal reconstruction*. in *Sensing Technology + Applications*. 2015. Baltimore, Maryland, USA: SPIE.
15. Ciampa, F., et al., *Recent Advances in Active Infrared Thermography for Non-Destructive Testing of Aerospace Components*. *Sensors*, 2018. **18**(2): p. 609.
16. Panwisawas, C., Y.T. Tang, and R.C. Reed, *Metal 3D printing as a disruptive technology for superalloys*. *Nature Communications*, 2020. **11**(1): p. 2327.
17. British Standards Institution, BS EN ISO/ASTM 52911-1:2019, Part 1: Laser-based powder bed fusion of metals, in *Additive manufacturing — Design*, 2019
18. British Standards Institution, BS EN ISO/ASTM 52900:2017, Additive manufacturing — General principles — Terminology, 2017
19. Gisario, A., et al., *Metal additive manufacturing in the commercial aviation industry: A review*. *Journal of Manufacturing Systems*, 2019. **53**: p. 124-149.
20. Yadroitsev, I., *Selective Laser Melting - Direct manufacturing of 3D-objects by selective laser melting of metal powders*. 2009, Germany: LAP LAMBERT Academic Publishing AG & Co. KG.
21. BIPM, *The International System of Units (SI)*, Bureau International des Poids et Mesures, Editor. 2019, STEDI Media Paris: BIPM.
22. Machin, G., *The kelvin redefined*. *Measurement Science and Technology*, 2018. **29**(2): p. 022001.
23. Newell, D.B., *A more fundamental International System of Units*. *Physics Today*, 2014. **67**(7): p. 35-41.
24. Preston-Thomas, H., *The International Temperature Scale of 1990 (ITS-90)*. *Metrologia*, 1989. **27**(1): p. 3-10.
25. Yoon, H.W., et al., *Guide to the Realization of the ITS-90: Radiation Thermometry*. 2017, International Committee for Weights and Measures: BIPM.
26. British Standards Institution, BS 1041-5: 1989, Part 5: Guide to selection and use of radiation pyrometers, in *Temperature measurement*, 1989
27. British Standards Institution, DD IEC/TS 62492-1:2008, Part 1: Technical data for radiation thermometers, in *Industrial process control devices — Radiation thermometers*, 2008
28. British Standards Institution, PD IEC/TS 62492-2:2013, Part 2: Determination of the technical data for radiation thermometers, in *Industrial process control devices — Radiation thermometers*, 2013
29. ASTM International, E1256-17, Standard Test Methods for Radiation Thermometers (Single Waveband Type), 2017
30. British Standards Institution, BS ISO 10878:2013, Non-destructive testing — Infrared thermography — Vocabulary, 2013
31. British Standards Institution, BS ISO 10880:2017, Non-destructive testing — Infrared thermographic testing — General principles, 2017
32. British Standards Institution, BS ISO 18251-1:2017, Part 1: Characteristics of system and equipment, in *Non-destructive testing — Infrared thermography*, 2017
33. British Standards Institution, BS ISO 18434-1-2008, Part 1: General procedures, in *Condition monitoring and diagnostics of machines — Thermography*, 2008

34. British Standards Institution, BS ISO 12233:2017, Resolution and spatial frequency responses, in *Photography — Electronic still picture imaging*, 2017
35. ASTM International, F3187-16, Standard Guide for Directed Energy Deposition of Metals, 2016
36. DeWitt, D.P. and G.D. Nutter, *Theory and Practice of Radiation Thermometry*. 1988: John Wiley & Sons.
37. DeWitt, D.P., *Advances and Challenges in Radiation Thermometry*. Heat Transfer 1994 - Proceedings of the Tenth International Heat Transfer Conference, Vol 1, 1994(135): p. 205-221.
38. DeWitt, D.P. and H. Kunz. *Theory and technique for surface temperature determinations by measuring the radiance temperatures and the absorptance ratio for two wavelengths*. in *Symposium on Temperature: Its Measurement and Control in science and Industry: The Fifth Symposium on Temperature*. 1971. Washinton, D.C.
39. Touloukian, Y.S. and D.P. DeWitt, *Thermal Radiative Properties: Metallic Elements and Alloys*. Thermophysical Properties of Matter. Vol. 7. 1970.
40. Peter, S. and E. Hamish, *On the characterization and correction of the size-of-source effect in radiation thermometers*. Metrologia, 2009. **46**(1): p. 62.
41. Saunders, P., *Correcting Radiation Thermometry Measurements for the Size-of-Source Effect*. International Journal of Thermophysics, 2011. **32**(7): p. 1633.
42. Saunders, P. and H. Edgar, *Size-of-source effect correction for a thermal imaging radiation thermometer*. High Temperatures - High Pressures, 1999. **31**(3): p. 283-292.
43. Saunders, P. and D.R. White, *A focus effect in some thermal imaging systems*. AIP Conference Proceedings, 2013. **1552**(1): p. 625-630.
44. Saunders, P., *Uncertainties in the Realization of Thermodynamic Temperature Above the Silver Point*. International Journal of Thermophysics, 2011. **32**(1): p. 26-44.
45. Saunders, P. and D.R. White, *Physical basis of interpolation equations for radiation thermometry*. Metrologia, 2003. **40**(4): p. 195-203.
46. Saunders, P., *General interpolation equations for the calibration of radiation thermometers*. Metrologia, 1997. **34**(3): p. 201-210.
47. Ricolfi, T. and L. Wang. *Experiments and remarks on the size-of-source effect in precision radiation thermometry*. in *TEMPMEKO '93, 5th Int. Symp. on Temperature and Thermal Measurements in Industry and Science 1993*. Pague.
48. Fischer, J., et al., *Uncertainty budgets for realisation of scales by radiation thermometry*. CCT document CCT/03-03, 2003.
49. Saunders, P., et al., *Uncertainty Budgets for Calibration of Radiation Thermometers below the Silver Point*. International Journal of Thermophysics, 2008. **29**: p. 1066-1083.
50. Coates, P. and D. Lowe, *The Fundamentals of Radiation Thermometers*. 2017: CRC Press, Taylor and Francis Group LLC, 6000 Broken Sound Parkway NW, Suite 300, Boca Raton, FL 33487-2742.
51. Whittam, A., R. Simpson, and H. McEvoy. *Performance tests of thermal imaging systems to assess their suitability for quantitative temperature measurements*. in *The 12th International Conference on Quantitative InfraRed Thermography*. 2014. Bordeaux - France.
52. McMillan, J.L., et al., *Towards quantitative small-scale thermal imaging*. Measurement, 2018. **117**: p. 429-434.
53. Machin, G., R. Simpson, and M. Broussely, *Calibration and validation of thermal imagers*. Quantitative InfraRed Thermography Journal, 2009. **6**(2): p. 133-147.
54. Robinson, D.W., et al., *3D thermography for improving temperature measurements in thermal vacuum testing*. CEAS Space Journal, 2017. **9**(3): p. 333-350.
55. McEvoy, H., R. Simpson, and G. Machin. *Review of current thermal imaging temperature calibration and evaluation facilities, practices and procedures, across EURAMET (European Association of National Metrology Institutes)*. in *11th International Conference on Quantitative InfraRed Thermography*. 2012. Naples, Italy.

56. Müller, I., et al., *Non-contact temperature measurement at the Physikalisch-Technische Bundesanstalt (PTB)*. Quantitative InfraRed Thermography Journal, 2020: p. 1-26.
57. Lane, B., et al., *Uncertainty of temperature measurements by infrared thermography for metal cutting applications*. Metrologia, 2013. **50**(6): p. 637.
58. Lane, B. and E.P. Whinton, *Calibration and measurement procedures for a high magnification thermal camera*. 2015, National Institute of Standards and Technology.
59. Heigel, J.C. and E.P. Whinton, *The Effects of Emissivity and Camera Point Spread Function on the Temperature Measurement of Segmented Chip Formation Using Infrared Thermography*. 2010(49460): p. 443-452.
60. Whinton, E.P., *High-Speed Dual-Spectrum Imaging for the Measurement of Metal Cutting Temperatures*, in *NIST Interagency/Internal Report (NISTIR)*. 2010, NIST.
61. Whinton, E.P., *An introduction for machining researchers to measurement uncertainty sources in thermal images of metal cutting*. Int. J. of Machining and Machinability of Materials, 2012. **12**(3): p. 195-214.
62. Heigel, J.C. and E.P. Whinton. *The effects of integration time and size-of-source on the temperature measurement of segmented chip formation using infrared thermography*. in *Proceedings of the ASME*. 2009.
63. Envall, J., et al., *Spatial Scatter Effects in the Calibration of IR Pyrometers and Imagers*. International Journal of Thermophysics, 2009. **30**(1): p. 167-178.
64. Zong, Y., et al., *Characterization and correction of stray light in optical instruments*. SPIE Remote Sensing. Vol. 6744. 2007: SPIE.
65. Zong, Y., et al., *Simple matrix method for stray-light correction in imaging instruments*. 2008.
66. Lai, F., et al., *Thermal image enhancement through the deconvolution methods for low-cost infrared cameras*. Quantitative InfraRed Thermography Journal, 2018. **15**(2): p. 223-239.
67. Rozanski, L. *Assessment of the possibility of comparing the infrared thermographs geometric resolution defined by various methods*. in *2014 IEEE Metrology for Aerospace (MetroAeroSpace)*. 2014.
68. Masaoka, K., et al., *Modified slanted-edge method and multidirectional modulation transfer function estimation*. Optics Express, 2014. **22**(5): p. 6040-6046.
69. Pospíšil, J., P. Jakubík, and L. Machala, *Light-reflection random-target method for measurement of the modulation transfer function of a digital video-camera*. Optik - International Journal for Light and Electron Optics, 2005. **116**(12): p. 573-585.
70. Etribeau, M. and P. Magnan. *Fast MTF measurement of CMOS imagers using ISO 12333 slanted-edge methodology*. in *Optical Systems Design*. 2004. SPIE.
71. Du, H. and K.J. Voss, *Effects of point-spread function on calibration and radiometric accuracy of CCD camera*. Applied Optics, 2004. **43**(3): p. 665-670.
72. Hooper, P.A., *Melt pool temperature and cooling rates in laser powder bed fusion*. Additive Manufacturing, 2018. **22**: p. 548-559.
73. Williams, R.J., et al., *In situ thermography for laser powder bed fusion: Effects of layer temperature on porosity, microstructure and mechanical properties*. Additive Manufacturing, 2019. **30**: p. 100880.
74. Coates, P., *Multi-Wavelength Pyrometry*. Metrologia, 1981. **17**(3): p. 103.
75. Yamada, Y. and J. Ishii, *Toward Reliable Industrial Radiation Thermometry*. International Journal of Thermophysics, 2015. **36**(8): p. 1699-1712.
76. Krauss, H., C. Eschey, and M.F. Zaeh. *Thermography for monitoring the selective laser melting process*. in *Proceedings of the Solid Freeform Fabrication Symposium*. 2012.
77. Krauss, H., T. Zeugner, and M.F. Zaeh, *Layerwise Monitoring of the Selective Laser Melting Process by Thermography*. Physics Procedia, 2014. **56**(C): p. 64-71.
78. Krauss, H., T. Zeugner, and M.F. Zaeh, *Thermographic process monitoring in powderbed based additive manufacturing*. AIP Conference Proceedings, 2015. **1650**(1): p. 177-183.

79. Mani, M., et al., *A review on measurement science needs for real-time control of additive manufacturing metal powder bed fusion processes*. International Journal of Production Research, 2017. **55**(5): p. 1400-1418.
80. Levine, L., et al., *Outcomes and Conclusions from the 2018 AM-Bench Measurements, Challenge Problems, Modeling Submissions, and Conference*. Integrating Materials and Manufacturing Innovation, 2020. **9**(1): p. 1-15.
81. Moylan, S., et al. *Infrared thermography for laser-based powder bed fusion additive manufacturing processes*. in *40TH ANNUAL REVIEW OF PROGRESS IN QUANTITATIVE NONDESTRUCTIVE EVALUATION*. 2014. AIP Conference Proceedings.
82. Heigel, J.C., B. Lane, and S. Moylan. *Variation of Emittivity with Powder Bed Fusion Build Parameters*. in *Proceedings of the 2016 Annual International SFF Symposium*. 2016.
83. Lane, B.M., et al., *Thermographic measurements of the commercial laser powder bed fusion process at NIST*. Rapid Prototyping Journal, 2016. **22**(5): p. 778-787.
84. Heigel, J.C. and B. Lane. *The effect of powder on cooling rate and melt pool length measurements using in situ thermographic techniques*. in *2017 Annual International Solid Freeform Fabrication Symposium*. 2017. Austin Texas.
85. Lane, B.M., et al. *Performance Characterization of Process Monitoring Sensors on the NIST Additive Manufacturing Metrology Testbed*. in *Solid Freeform Fabrication Symposium*. 2017. Austin, TX.
86. Heigel, J.C., B.M. Lane, and L.E. Levine, *In Situ Measurements of Melt-Pool Length and Cooling Rate During 3D Builds of the Metal AM-Bench Artifacts*. Integrating Materials and Manufacturing Innovation, 2020. **9**(1): p. 31-53.
87. Lane, B.M., et al., *Uncertainty of temperature measurements by infrared thermography for metal cutting applications*. Metrologia, 2013. **50**(6): p. 637-653.
88. Rodriguez, E., et al., *Approximation of absolute surface temperature measurements of powder bed fusion additive manufacturing technology using in situ infrared thermography*. Additive Manufacturing, 2015. **5**: p. 31-39.
89. Fisher, B.A., et al., *Consequences of Part Temperature Variability in Electron Beam Melting of Ti-6Al-4V*. JOM, 2017. **69**(12): p. 2745-2750.
90. Cordero, P.M., et al., *Evaluation of monitoring methods for electron beam melting powder bed fusion additive manufacturing technology*. Progress in Additive Manufacturing, 2017. **2**(1): p. 1-10.
91. Fisher, B.A., et al., *Toward determining melt pool quality metrics via coaxial monitoring in laser powder bed fusion*. Manufacturing Letters, 2018. **15**: p. 119-121.
92. Felice, R.A. *Multispectral expert system spectropyrrometer and its uses in industry and research*. in *Proceedings of the SPIE - Thermosense XXVI*. 2004. SPIE.
93. Felice, R.A. and D.A. Nash, *Pyrometry of Materials with Changing, Spectrally-Dependent Emissivity - Solid and Liquid Metals*. Temperature: Its Measurement and Control in Science and Industry, Vol 8, 2013. **1552**: p. 734-739.
94. Coates, P., *The least-squares approach to multi-wavelength pyrometry*. High Temperatures-High Pressures, 1988. **20**(4).
95. Boone, N., et al., *Thermal near infrared monitoring system for electron beam melting with emissivity tracking*. Additive Manufacturing, 2018. **22**(C): p. 601-605.
96. Lia, F., et al., *Thermal and microstructural analysis of laser-based directed energy deposition for Ti-6Al-4V and Inconel 625 deposits*. Materials Science and Engineering: A, 2018. **717**: p. 1-10.
97. Bartlett, J.L., et al., *In situ defect detection in selective laser melting via full-field infrared thermography*. Additive Manufacturing, 2018. **24**: p. 595-605.

## 2. THEORY

In this chapter the pertinent theoretical framework for radiometric determination of temperature will be outlined. The general concept is that radiation leaving the surface of a body, travelling through some media and impinging on a second surface is utilised to infer information about the first surface. The aim is to accurately measure the temperature of the first surface, the second surface being our detector. The detector has some property which varies with the quantity of light impinging upon it. The detector is a photon transducer. The properties of the emitting surface, the properties of the intervening media, the distribution of other emitting objects in front of the first surface and other confounding phenomena, affect the amount of radiation impinging on the detector.

Most radiation thermometry books deal in depth with parts of the theory laid out in this chapter, including a recent work; *'The Fundamentals of Radiation Thermometers'* by Coates and Lowe (2017)[1], which deals with radiation thermometry in a metrologically rigorous framework. Another treatise on radiation thermometry is *'Theory and Practice of Radiation Thermometry'* by Dewitt and Nutter (1988)[2], which is an excellent if somewhat dated work on the theory and implementation of radiation thermometry. In the field of thermography (also called thermal imaging), *'Infrared Thermal Imaging'* by Vollmer and Möllmann (2010)[3], and *'Infrared Thermography'* by Gaussorgues (1994)[4] provide good introductions. In this work elements from these books (and others) essential to the understanding of each topic will be condensed and presented. Where possible, the vocabulary conventions laid out in the standard ISO 10878:2013 [5], concerned with infrared thermography for non-destructive testing, are used.

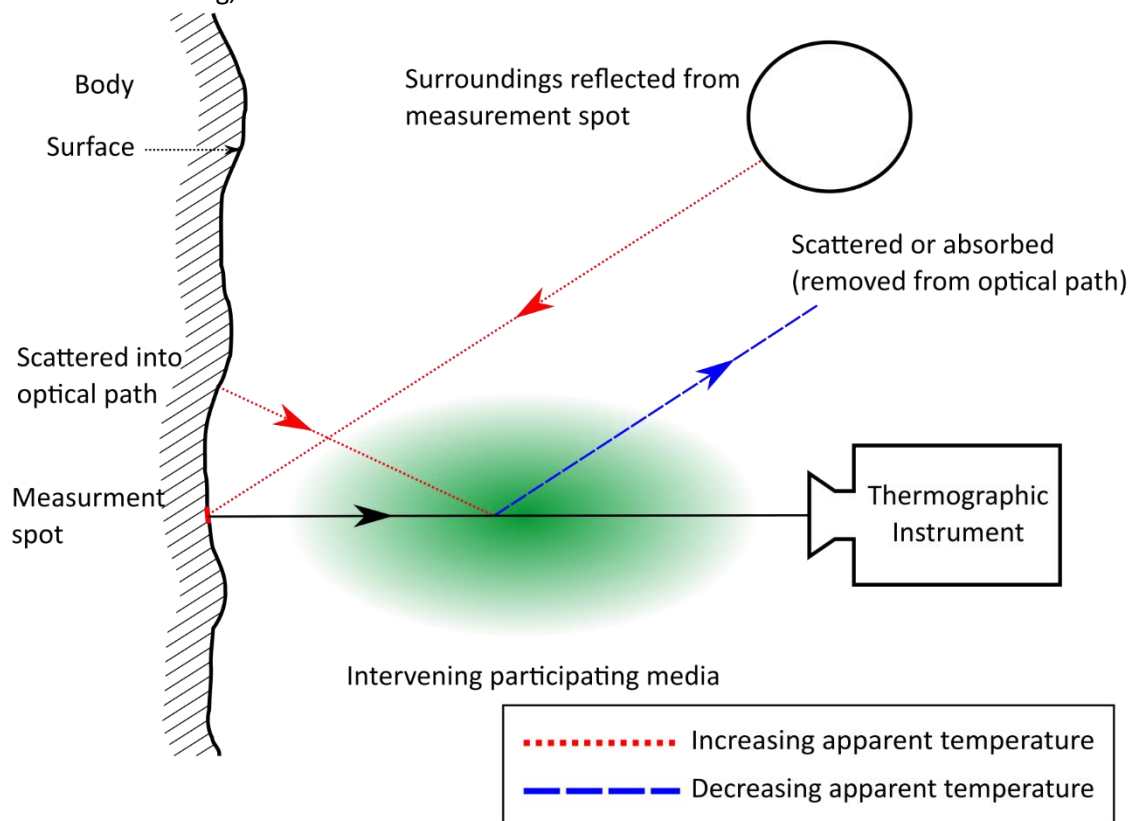


Figure 2-1. A typical radiation thermometry situation. Sources and drains of radiation for a typical radiation thermometry environment affect the measurement of the surface temperature.

Figure 2-1 depicts the typical radiation thermometry measurement environment. The *measurement spot* is the area of the target where the measurement of surface temperature is to be made and will be defined more precisely in section 2.1.3. This figure represents a typical situation and does not constrain the usages of thermography to this setup. It is assumed that the reader can accept the concept of light as energy, and that a certain quantity of light passing through or impinging upon a surface can be considered as a power or equivalently a flux of photons. The amount of power, or number of photons per second, contained within a light beam will be expanded upon in section 2.2. In section 2.1 the formalism of how light is emitted from a surface and collected by some idealised optical system will be presented. Section 2.4 will provide some of the framework for processing the images acquired from thermographic instruments, into measurements of real-world phenomena. The section titled Nomenclature at the beginning of this work is a list of all the abbreviations and symbols used throughout this work and should be referred to where necessary.

## 2.1 SURFACE TO SURFACE RADIATION TRANSFER

For reference '*Thermal Radiation Heat Transfer*', originally by Siegel and Howell (2011)[6] is an excellent reference book, with a comprehensive treatment of all aspects of surface to surface heat transfer by electromagnetic radiation. Radiometric measurements of surface temperature are made by capturing a fraction of the thermal radiation emitted by a surface. To relate this quantity of captured light to the surface temperature it must first be understood how the light propagates between the surface of interest and the detector. In section 2.1.2 the quantity *Radiance will be arrived at*, which is the technical description of what would be colloquially termed the 'brightness' of an emitting surface. To define this quantity, the power emitted from a surface is considered, and the geometry of how that power propagates into the volume above the surface is described.

### 2.1.1 Geometric considerations

Initially a coordinate system based on a small part of a locally flat surface  $dA'$  is constructed (see Figure 2.1-1). The solid angle ( $\Omega$ ) in Figure 2.1-1 describes the area ( $A_\Omega$ ) projected onto a unit radius sphere by the subtended angles  $d\theta$  and  $d\phi$ .

$$\Omega = \int \int \sin \theta \, d\theta \, d\phi \quad \text{Eq 2.1-1}$$

From evaluation of *Eq 2.1-1* it can be observed that there are  $2\pi$  sr in a hemisphere and  $4\pi$  sr in a sphere. Steradian abbreviated to sr is the dimensionless *SI* [7] unit of solid angle. The relation between  $\Omega$ , the radius ( $r$ ) and  $A_\Omega$  is:

$$\Omega = \frac{A_\Omega}{r^2} \quad \text{Eq 2.1-2}$$

If we assume that  $r \gg dx, dy$  then we can approximate  $A_\Omega$  as a plane rather than a curved surface, without the need to modify *Eq 2.1-2*. An important concept in the definition of radiance is the projected area  $dA$ , this is related to the area of the surface ( $dA'$ ) and the zenith angle of observation ( $\theta$ ).

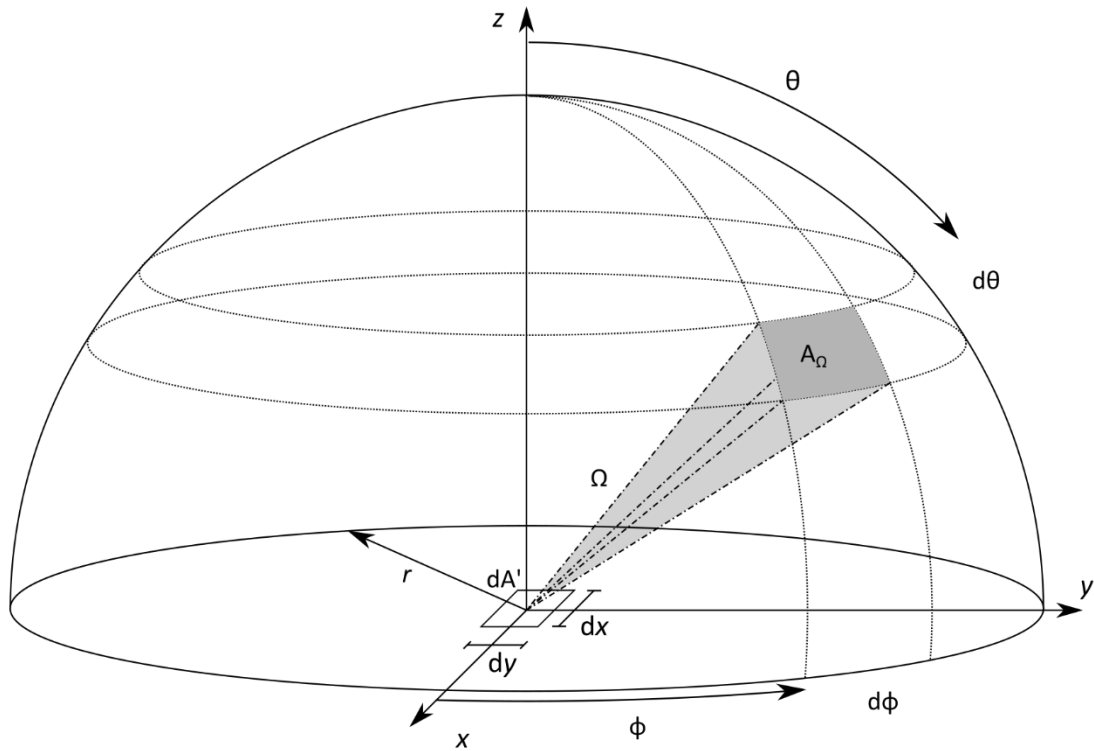


Figure 2.1-1 Spherical polar co-ordinate system for describing radiometric quantities related to a surface. The zenith (viewing angle) ( $\theta$ ) and azimuth ( $\phi$ ) angles describe a direction in space and  $r$  describes the distance.

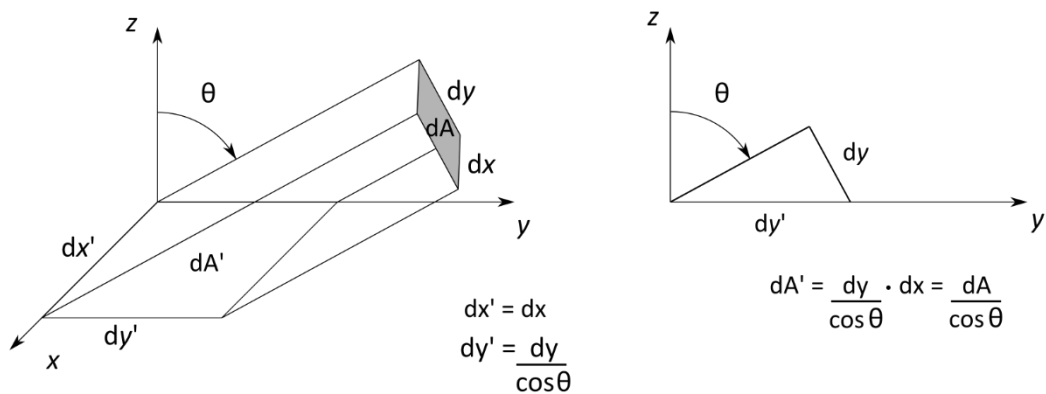


Figure 2.1-2 The projected area  $dA$  is invariant when observing a surface from any zenith (viewing) angle,  $\theta$ . The actual area of the surface  $dA'$  increases as the zenith angle increases proportionally to  $1/\cos\theta$ .

$dA$  is the quantity which remains invariant when using an optical system at any angle relative to the surface, this will be looked at again in section 2.1.4.

### 2.1.2 Radiation terms

The amount of energy transferred by radiation is, in general, wavelength ( $\lambda$ ) dependent. In this section only the  $\lambda$  independent quantities will be considered. The same relations for radiation transfer hold whether  $\lambda$  integrated quantities or their *spectral* equivalent are considered (assuming elastic scattering), where the term spectral means 'at one single  $\lambda$  ( $d/d\lambda$ )'. The definition of the radiation terms will be made in terms of transmitted power integrated over all  $\lambda$ , the spectral equivalents would be measured in  $W\ m^{-1}$  (or  $W\ \mu m^{-1}$ ).

An alternative to considering the transmitted power, is to consider the individual photons as quantised packets of energy. The power in Watts of a quantity of photons is the number of photons multiplied by the energy of each photon per second. Each photon of a given  $\lambda$  carries an amount of energy ( $E$ ) given by:

$$E = hf_{\gamma} = \frac{hc}{\lambda} \quad \text{Eq 2.1-3}$$

Where:  $h$  is Plancks constant ( $6.62607015 \times 10^{-34}$  J Hz<sup>-1</sup> CODATA 2018),  $f_{\gamma}$  is the frequency of the photon and  $c$  is the speed of light in the given medium.

The number of photons is important in the field of thermography, because the sensitivity of most sensors is quantified by its spectral Quantum Efficiency ( $QE$ ), which is expanded upon in section 2.3.1.

A summary of the radiation terms is given in Table 2.1-i. Listed below is a brief description of the main radiation terms used in the field of radiation thermometry:

- The total amount of power passing through a surface area  $dA$  is the *radiant flux* ( $\Phi$ ), measured in Watts. The radiant flux can be considered at an emitting surface, a receiving surface or any arbitrarily defined surface in free space, such as the entrance pupil of an optical system.
- The radiant flux per unit area ( $dA'$ ) is the *exitance* ( $M$ ) of the surface. The exitance from a surface propagates in all directions ( $\theta, \phi$ ) within the hemisphere above the surface. Exitance has no angular dependence. The complementary term for power arriving at a surface, per area, is the *irradiance* ( $E$ ).
- The radiant flux propagating from a surface into a given solid angle ( $\Omega$ ) is the *radiant intensity* ( $I$ ). The radiant intensity is an angle ( $\theta, \phi$ ) dependent quantity.
- The combination of exitance and radiant intensity is the *radiance* ( $L$ ). Radiance is defined in terms of the projected area ( $dA$ ) at the angle  $\theta$ , rather than the surface area of the emitting surface ( $dA'$ ) as is the case for exitance.

Radiance is the quantity which we usually consider to be measured by radiometric instruments. It is shown in Section 2.1.3 how an optical system converts the radiance of a surface into a radiant flux. The radiant flux is the quantity which a detector material is responsive to. The measured signal is related in some way to the incident radiant flux on the detector.

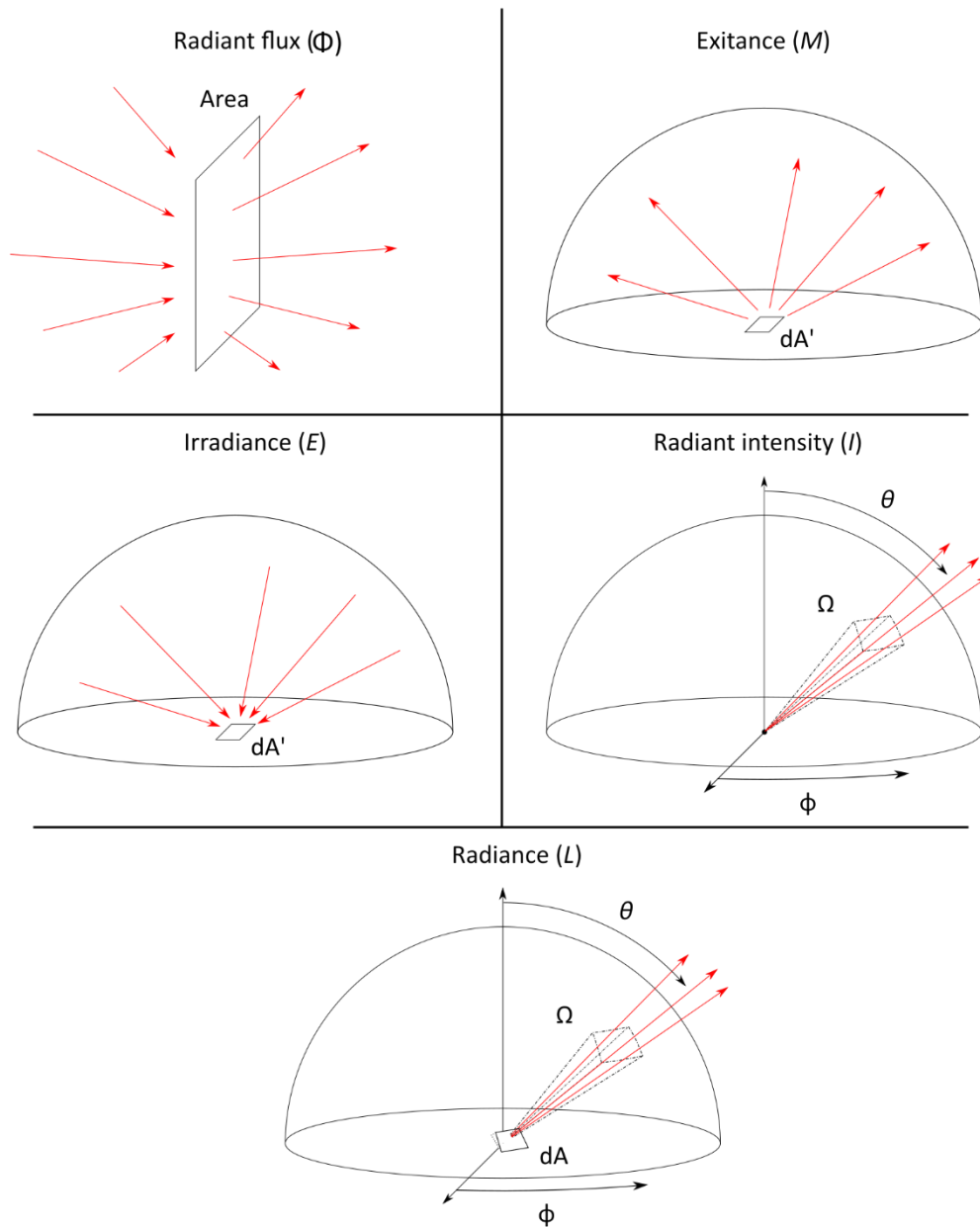


Figure 2.1-3 The most commonly used terms to describe radiation transfer, in the field of radiation thermometry.

Table 2.1-i Summary of radiation terms

term	symbol	SI unit	Relation to $\Phi$	description
Radiant flux	$\Phi$	W	-	Power passing through a surface of area $dA$
Exitance	$M$	$\text{W m}^{-2}$	$\frac{d\Phi}{dA'}$	Radiant flux per unit area leaving a surface
Irradiance	$E$	$\text{W m}^{-2}$	$\frac{d\Phi}{dA'}$	Radiant flux per unit area impingent upon a surface
Radiant intensity	$I$	$\text{W sr}^{-1}$	$\frac{d\Phi}{d\Omega}$	Radiant flux propagating into a solid angle $\Omega$
Radiance	$L$	$\text{W m}^{-2} \text{sr}^{-1}$	$\frac{d^2\Phi}{dA \cdot d\Omega}$	Radiant flux per solid angle per unit projected area.
The radiometric quantities can all be considered spectrally, denoted by a subscripted $\lambda$ (e.g. $\Phi_\lambda$ ) They may also be considered in terms of photon flux, denoted by a subscripted $\gamma$ (e.g. $\Phi_\gamma$ )				

### 2.1.3 Collection of radiation onto a detector

In this section geometric approximations of the propagation of light are used to model the measurement of the quantity of light emitted by a surface. The geometric model considers light as beams travelling in straight lines and being absorbed or deflected by passing through different media (see section 2.1.3.1). For more sophisticated models of how light propagates through an optical system, the system can be modelled with a software package such as Zemax [8]. A good undergraduate reference for the propagation of light through optical systems is ‘*Optics*’ by Hecht (2002)[9].

To make a measure of the radiance of a finite extended area (not infinitesimally small), two apertures between the emitting surface and the detector must be used. The two apertures define the radiant flux passing through (or impinging on), a given area. As can be seen from Figure 2.1-4, two apertures are required to define the measurement of radiance from a surface. The *aperture stop* (Stop 1) determines the solid angle ( $\Omega = \Omega_{AS}$ ) over which light from the surface is collected, and the *field stop* (Stop 2) determines from what projected area ( $dA$ ) that light is collected from.

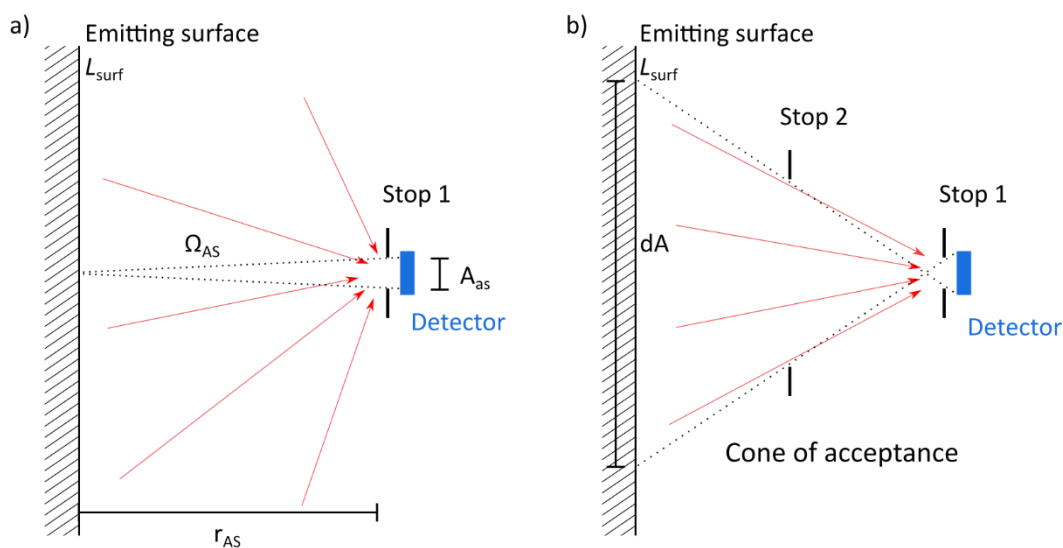


Figure 2.1-4 a) The aperture stop, of diameter  $D_{as}$  determines the solid angle ( $\Omega_{AS}$ ) over which radiation is collected from the surface, but the area of the emitting surface is ill defined. b) Only light emitted from inside the area  $dA$  is incident upon the detector. This kind of simple two stop system is not usually implemented without further light steering optics (lenses).

Using the system of apertures shown in Figure 2.1-4, it can be seen that the solid angle ( $\Omega_{AS}$ ) is related to the area of the aperture stop ( $A_{AS}$ ) and the distance from the aperture stop to the target surface ( $r_{AS}$ ). The projected area ( $dA$ ) of the emitting target surface is proportional to the area of the field stop ( $A_{FS}$ ). It can now be asserted that the radiance of a limited area of the target surface is converted into radiant flux by the application of a pair of defining apertures, the field stop and the aperture stop.

$$\Phi = L_{surf} \cdot \Omega_{AS} \cdot dA \quad \text{Eq 2.1-4}$$

The output of a detector is usually a voltage, current or resistance, which is proportional to the radiant flux incident upon it. This relation is not always linear, but careful characterisation of the detector will allow any non-linearity to be corrected. A radiant flux can be measured, and hence a radiance can be inferred, from the signal measured by the detector.

The simple dual aperture system outlined in Figure 2.1-4 has some significant drawbacks.

- Not all the power passing through the field stop passes through the aperture stop as the edges of  $dA$  are not sharply defined.
- The upper limit to the area of the aperture stop is limited by the size of the detector.
- $dA$  is large compared to the detector, which is not usually useful for radiometric thermometry purposes.

For these reasons, and others, nearly all radiometric temperature measurement systems use a focussing optical system in conjunction with the aperture pair, such as that outlined in Figure 2.1-5.

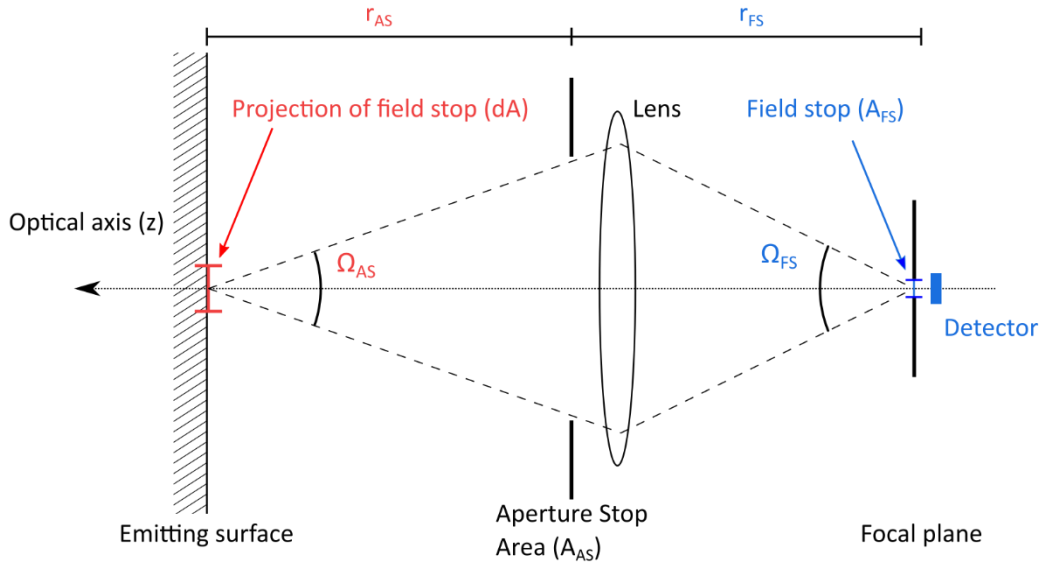


Figure 2.1-5 A typical optical system. All light passing through the field stop is incident upon / captured by the detector.

The quantity  $\Omega_{AS} \cdot dA$ , in the field of radiation thermometry, is termed the *Etendue* ( $E_{te}$ ) or *throughput* of the optical system. The  $E_{te}$  is a property of a lens system, in a given configuration, which will determine how much radiant flux is incident upon the detector, and therefore the magnitude of the signal. All light passing through the field stop in this arrangement can be considered as incident upon the detector. One important note is that the  $E_{te}$  can be measured from the perspective of the field stop (detector) or from the perspective of the measurement spot:

$$E_{te} = \Omega_{AS} \cdot A_{AS} = \Omega_{FS} \cdot A_{FS} \quad \text{Eq 2.1-5}$$

If it assumed that  $A_{AS}$  is small compared to  $r_{AS}$  (equivalent to Eq 2.1-2), then the radiant flux incident upon a detector can be approximated as:

$$\Phi = L_{\text{surf}} \cdot E_{te} \approx L_{\text{surf}} \cdot \frac{A_{AS} \cdot dA}{r_{AS}^2} \quad \text{Eq 2.1-6}$$

Care should be taken when calculating the  $E_{te}$  if the aperture stop is on the opposite side of a lens, in this case the area of the field stop and distance to the *image* of the aperture stop should be used. The area of the field stop and therefore the measurement area can be characterised by lengths. The characteristic length of the field stop  $D_{FS}$  combined with the shape determines the area. The projection of  $D_{FS}$  onto the scene is termed the Instantaneous Field of View (*IFOV*) for imaging systems, or just Field Of View (*FOV*) for single sensing element systems.

Table 2.1-ii relation between linear and area terms

Field stop Shape	Area of field stop ( $A_{FS}$ )	Area of measurement ( $dA$ )
Circle	$\pi \cdot D_{FS}^2/4$	$\pi \cdot IFOV^2/4$
Square	$D_{FS}^2$	$IFOV^2$

### 2.1.3.1 Geometric optics

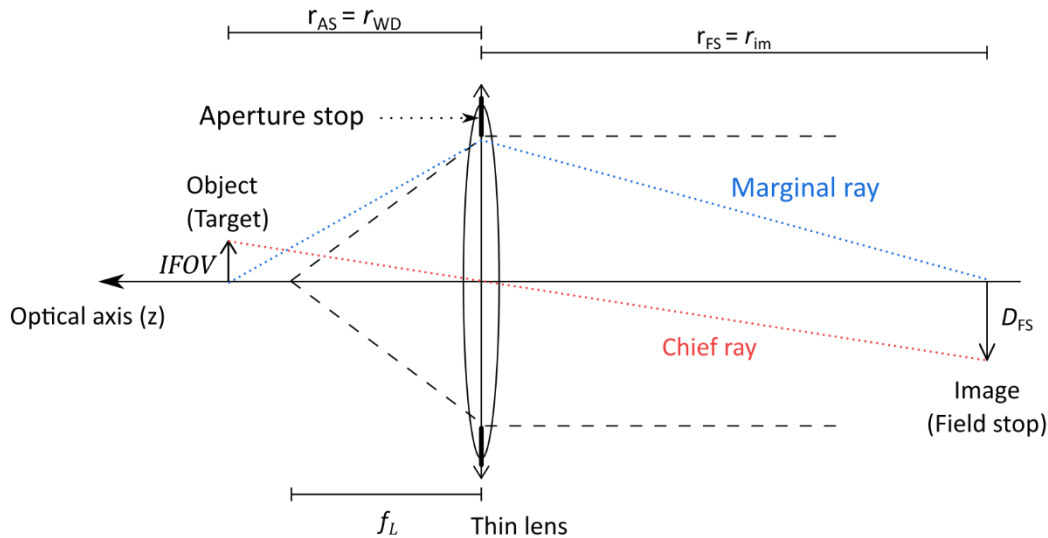


Figure 2.1-6 The focal length ( $f_L$ ) of a lens is the distance from the lens where parallel rays of light, incident on the lens, converge. The focal length is only well-defined for specific wavelengths of light, even then the focus is never perfect and can be measured or modelled for any lens system. The best possible focus of a lens system with a fixed aperture stop, is bounded by the diffraction limit.

Geometric optics [10] provide some useful tools, which can be used to estimate important parameters of a thermographic instrument. A central property of any lens or collection of lenses is its focal length ( $f_L$ ). The approximation of a lens depicted in Figure 2.1-6 can be expressed by the *thin lens equation*:

$$\frac{1}{f_L} = \frac{1}{r_{WD}} + \frac{1}{r_{im}} \quad \text{Eq 2.1-7}$$

Where  $r_{WD}$  is the distance from the emitting scene to the lens (working distance) and  $r_{im}$  is the distance from the field stop to the lens (see Figure 2.1-6). It is often assumed that the aperture stop is positioned at the same place as the lens ( $r_{AS} \approx r_{WD}$  &  $r_{FS} \approx r_{im}$ ), this is accurate if the projection of the aperture stop through the lens is used, rather than its physical dimensions, the lens and the aperture stop are usually very close, meaning the distinction is often ignored.

The *chief ray* (Figure 2.1-6) forms a pair of triangles, from which an equality can be made:

$$\frac{D_{FS}}{r_{im}} = \frac{IFOV}{r_{WD}} \quad \text{Eq 2.1-8}$$

The magnification  $M_{ag}$  is the ratio of image height to object height, which can be expressed as:

$$M_{ag} = \frac{D_{FS}}{IFOV} = \frac{f_L}{r_{WD} - f_L} \quad \text{Eq 2.1-9}$$

By considering the measurement area (dA) to be the projection of the field stop ( $A_{FS}$ ) onto the object plane, these simple equations can be used to estimate dA, at a given  $r_{WD}$ .

A common question that might be asked is ‘what is an estimate of the *IFOV* for a given optical system at a given working distance?’. Using Eq 2.1-9 we get:

$$(I)IFOV = \frac{D_{FS}}{M_{ag}} = \frac{D_{FS}(r_{WD} - f_L)}{f_L} \quad \text{Eq 2.1-10}$$

The term Total field of View (*TFOV*) is used to describe geometric extents of the object plane in imaging systems, which is distinct from the *IFOV*. The *IFOV* does not necessarily indicate the area from which light incident on the detector originated, this will be expanded upon in section 2.4. The area of the scene defined by the *IFOV* can be termed a *scenel*, being a subsection of the entire scene.

The *IFOV* defines the projected measurement area dA (used previously) as it is the image of the field stop on the surface. The *IFOV* is a property of the instrument, and is only affected by the distance from the instrument to the surface under inspection, or the magnification. Meaning that the *IFOV* (dA) is independent of the zenith angle  $\theta$  of observation. The *IFOV* can be projected onto the tilted surface to calculate the true area of the surface from which light is being collected. This is one of the reasons why the definition of radiance is in terms of projected area not emitting area.

The amount of light passing through a commercial lens is most commonly described by its ‘speed’, quantified by its *F#* (pronounced F number), which is the ratio of the  $f_L$  of the lens to the aperture stop diameter ( $D_{AS}$ ). The area of the field stop ( $A_{FS}$ ) and *F#* can be related to the *Etendue* at infinity focus ( $E_{te\infty}$ ). Infinity focus is when the field stop is at the  $f_L$  of the lens, and parallel light entering the optics is focussed on the field stop.

$$E_{te\infty} = \Omega_{FS} \cdot A_{FS} = \frac{\pi}{4(F\#)^2} \cdot A_{FS} \quad \text{Eq 2.1-11}$$

This gives a tool to estimate the maximum radiant flux which can be made to be incident upon the detector from a given radiance surface, using a given lens system. For non-infinity focused systems, the  $E_{te}$  decreases. The closer the object is moved towards the lens the smaller the  $E_{te}$ . If the aperture stop is assumed to be at the same position as the lens ( $r_{AS} = r_{WD}$ ), then the  $E_{te}$  for an object in focus at a given  $r_{WD}$  can be estimated as:

$$E_{te} = \frac{\pi A_{FS} D_{AS}^2}{4r_{im}^2} = \frac{\pi (r_{WD} - f_L)^2}{4F\#^2 r_{WD}^2} \cdot A_{FS}$$

The fractional change in  $E_{te}$  with working distance is illustrated in Figure 2.1-7 for some common  $f_L$  lenses, where the defining aperture is assumed to be at the same position as the lens.

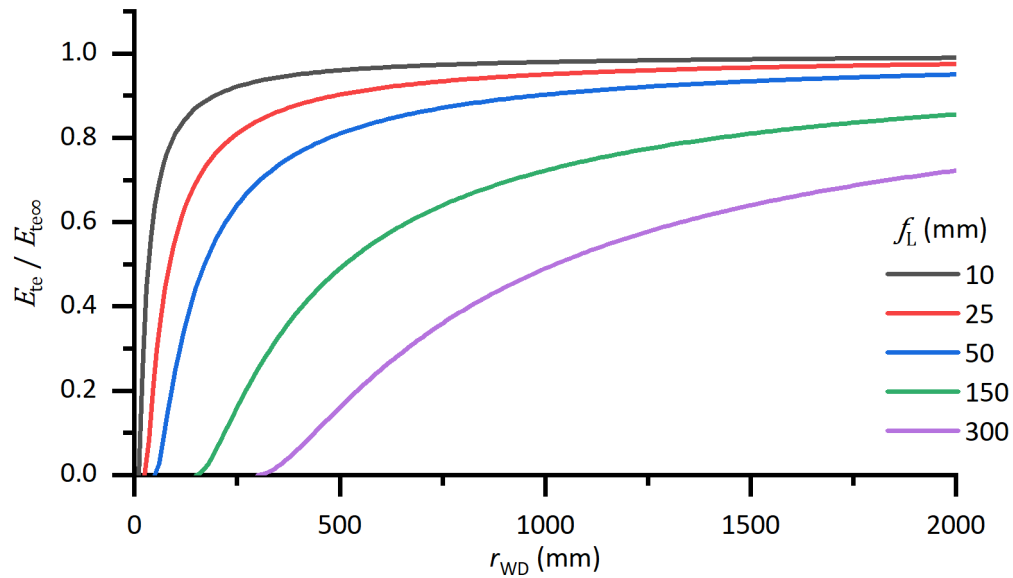
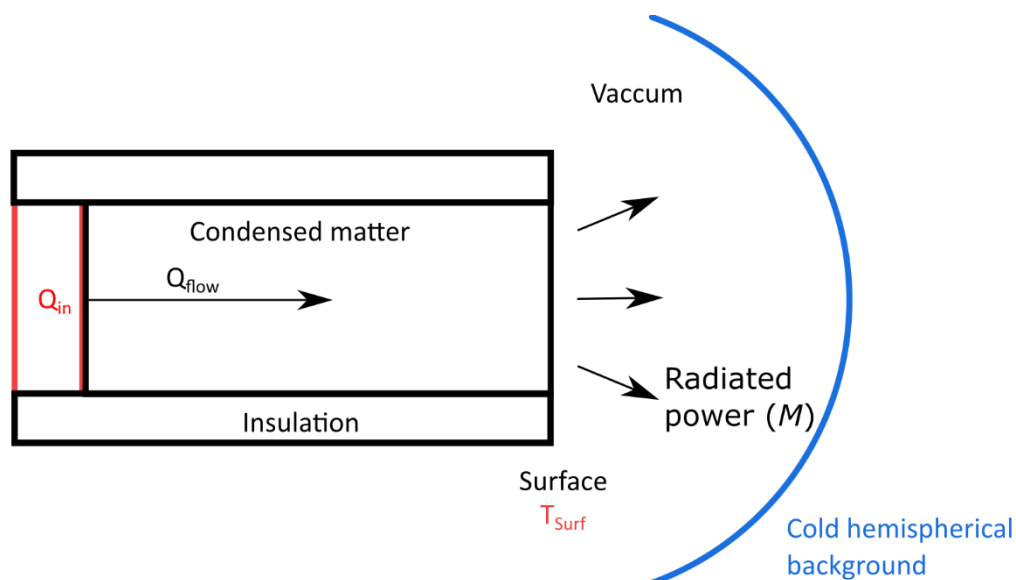


Figure 2.1-7 The Etendue of the optics, and therefore the signal measured from a fixed radiance source, is dependent upon the working distance ( $r_{WD}$ ) and focal length ( $f_L$ ) of the lens. This is most prevalent for long  $f_L$  lens systems.

Saunders & White (2013)[11], point out the problem of changing  $E_{te}$  for some commercial thermographic instruments. A thermographic system should either be designed with fixed focus or the aperture stop should be fixed relative to the detector fixing the solid angle.

#### 2.1.4 Emissivity, emission and reflection

At the interface between a condensed matter body and the surrounding medium, usually a rarefied gas (air) or a vacuum, there is a discontinuity in the refractive index. At this 'surface' we consider the radiation to be emitted in the way described in Section 2.1.2. The spectral component of this emitted radiation is the plank distribution (see Section 2.2), modified by a property specific to the surface known as the emissivity ( $\epsilon$ ), sometimes called the emittivity. The emittivity is strictly the intrinsic property of a given material, independent of its surface finish, and is rarely applicable to a real measurement situation. Occasionally effective emissivity is used to specify that the quantity is specific to a given measurement situation. There are many ways of defining  $\epsilon$ , depending upon the radiometric quantity of interest. Care must be employed when using a literature value of  $\epsilon$  to calculate surface temperature from radiometric measurements. Chapter 2 of *Thermal Radiation Heat Transfer* [12] and chapter 2 of *Theory and Practice of Radiation Thermometry* [13] describe the different measures of surface characteristics. In its most general sense,  $\epsilon$  is the ratio between the power emitted by a blackbody at the temperature of the surface and the actual power emitted by the surface.



*Figure 2.1-8 The amount of energy emitted by the surface is related to the surface temperature and the emissivity of the surface. The surface of the condensed matter can be thought to be freely radiating if the power impinging upon it from the cold hemispherical background is negligible compared to the radiated power. For the above situation the exitance ( $M$ ) is equal to the heat flow through the bulk of the material ( $Q_{flow}$ ), assuming perfect insulation. The front surface will heat up until it is hot enough to emit the energy input into the system.*

Emissivity is a property dependent upon the material, for which literature values can be found. It is also heavily dependent upon the condition of the surface. Thin surface layers of dissimilar materials, and the roughness of the surface will both significantly affect  $\epsilon$ . The rougher the surface in general the higher the  $\epsilon$ , with the  $\epsilon$  at longer wavelengths ( $\lambda$ ) being enhanced more than shorter  $\lambda$ . Thin surface layers, such as oxides, can act as etalons, making the spectral dependence of  $\epsilon$  behave in a non-smooth (oscillatory) fashion. Etalons are formed by two surfaces creating a resonant cavity for the spectral components of light which have wavelengths that are a multiple of the separation between the two surfaces. Emissivity is, in general, both  $\theta$  and  $\phi$  dependent, the  $\phi$  dependence is often small and ignored. The fact that surface conditions and oxidisation state have such a strong effect on  $\epsilon$ , means that it is very difficult, in a radiation thermometry measurement situation, to know the true  $\epsilon$  of the surface. Laboratory tests in well controlled or characterised conditions rarely reflect the conditions

during measurements in the field, making in situ measurements of  $\epsilon$  desirable. Unfortunately, this means that a non-radiometric measure of surface temperature must be employed, which is not always possible or desirable.

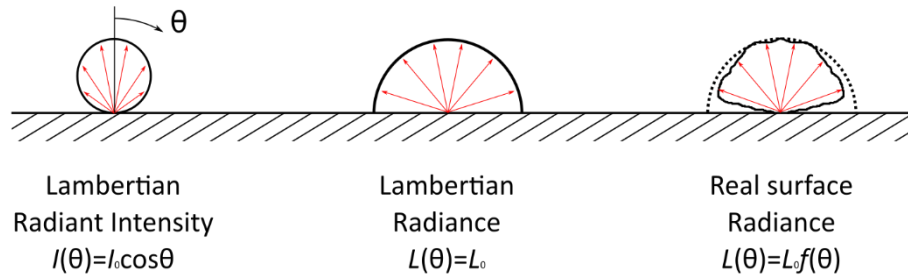


Figure 2.1-9 The Lambertian model of surface emission is a convenient model but rarely reflects behaviour of a real surface, especially at  $\theta$  approaching  $\pi$ . The angle independence of the radiance of a Lambertian surface can be understood by referring to Figure 2.1-2 and noting the  $1/\cos \theta$  dependence of the emitting surface area.

For a Lambertian emitting surface,  $M$  can be directly related to  $L$  by:

$$M = \pi L \qquad \text{Eq 2.1-12}$$

A standard model for the  $\theta$  dependence of  $\epsilon$  is known as the Lambertian approximation (Figure 2.1-9). Radiation passing through a surface in a blackbody radiation field behaves like a Lambertian surface. At large  $\theta$  the polarization of radiation emitted from a real surface becomes significant. Light polarised with the electric field component perpendicular to the plane of incidence (S-polarized) dominates, with the parallel (P-polarized) component decaying more rapidly with increasing  $\theta$ .

Reflections from surfaces under inspection usually present a problem for radiation thermometry, as they add to the apparent radiance of the surface, making radiometric measure of temperature an overestimate of the real surface temperature. The Ideal situation for making a measurement is to have a *freely radiating* surface, which means that no significant radiation is incident on the surface. An alternative is to ascertain the angular distribution of radiation sources and have a good model for the *nature* of the reflecting surface (see Figure 2.1-10). The nature of the reflecting surface is fully described by the Bi-Directional Reflectance Distribution Function (*BRDF*) [14].

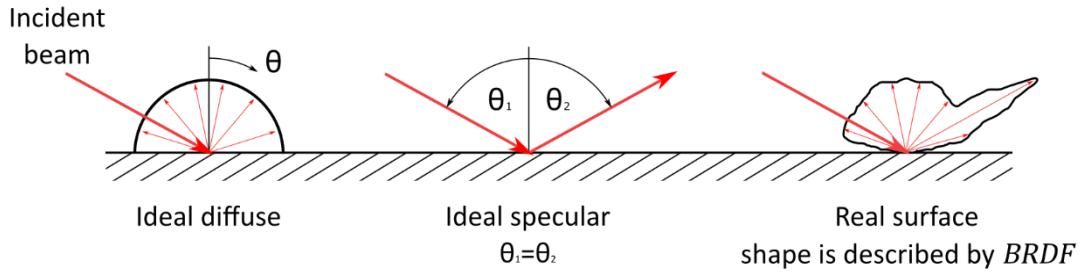


Figure 2.1-10 The apparent radiance of some reflective surfaces. A real reflective surface is usually some mixture of diffuse, specular and specular-like components. The Bi-Directional Reflectance Distribution Function (*BRDF*) describes how incident light is reflected.

For a non-transmissive material, a beam of incident light arriving from a direction described by the angles  $\theta'$  &  $\phi'$ , will have a fraction of the incident power reflected into the hemisphere above the surface. The fraction reflected is the reflectivity ( $\rho$ ) of the surface. Also, a fraction of the incident power will enter the surface and be absorbed, this fraction is the absorptivity ( $\alpha$ ) of the surface. When using literature values of the magnitudes of  $\rho$  and  $\alpha$ , the exact definition of which representation (angular, specular etc.) is being referred to is important. The direction of the reflected radiation  $\theta$  &  $\phi$  for a given  $\theta'$  &  $\phi'$  is described by the *BRDF* ( $\rho(\theta', \phi', \theta, \phi)$ ). The simplest approximations of the *BRDF* of a surface are diffuse and specular. For a diffuse reflector, for any  $\theta'$  &  $\phi'$ , the reflected radiance distribution is uniform, in the same way as a Lambertian emitter. For a specular reflector, it is assumed  $\theta = \theta'$  and that  $\phi$  &  $\phi'$  are coplanar. This is the behaviour which might be expected from a polished flat (or liquid) surface.

Information about the *BRDF* of a surface is essential if corrections to our radiometric measure of temperature for radiance sources reflected from the surface are to be made. Full knowledge of the *BRDF* for an opaque surface also tells us the  $\epsilon$  of the surface by use of Kirchhoff's law [15]. The directional-hemispherical reflectivity is:

$$\rho(\theta', \phi') = \int_0^{2\pi} \int_0^{\pi} \rho(\theta', \phi', \theta, \phi) d\theta d\phi \quad \text{Eq 2.1-13}$$

This quantity can be used to measure  $\epsilon$  at the angle  $\theta'$  &  $\phi'$ :

$$\epsilon(\theta', \phi') = 1 - \rho(\theta', \phi') \quad \text{Eq 2.1-14}$$

The thermal emissions of a photon from a surface is a fundamentally random process. The emission obeys Poisson statistics [16]. The variance in the number of photons emitted in a given time period is equal to the mean number of photons emitted, therefore the standard deviation in the number of emitted photons  $\sigma_{N_\gamma}$  is:

$$\sigma_{N_\gamma} = \sqrt{N_\gamma} \quad \text{Eq 2.1-15}$$

## 2.2 BLACKBODY RADIATION

The concept of a blackbody, and blackbody radiation, is central to the pursuit of temperature measurement by radiometric sampling of thermal radiation. In this section a simplified version of the theory of blackbody radiation, and how it is used in field of radiation thermometry, will be described. For more in depth reading, chapter 1 of *'Thermal Radiation heat Transfer'* by Siegel & Howell (2011)[17], and chapter 1 of *'Theory and Practice of Radiation Thermometry'* compiled by DeWitt & Nutter (1988)[18], are excellent texts on the subject.

### 2.2.1 Blackbody cavities

Figure 2.2-1 shows a typical blackbody cavity. The energy distribution of photons inside the cavity is purely a function of the temperature of the walls, assuming isothermal conditions. The term blackbody derives from the concept of making a small opening, or *keyhole*, into the cavity, and allowing light to fall upon it. Assuming the keyhole is infinitesimally small compared to the cavity, the fraction of incident light leaving the cavity through the keyhole will be zero. The incident light enters the cavity and is reflected from surface to surface until it is absorbed. This lack of reflection causes the surface forming the keyhole to be referred to as black. The only light exiting the keyhole is the intrinsic thermal radiation originating from the walls of the cavity (assuming a non-participating medium). For any cavity temperature above absolute zero (0 K, -273.15 °C), the cavity will contain a radiation field with an energy distribution defined by Planck's Law (Ignoring zero-point energy which is beyond the remit of this thesis).

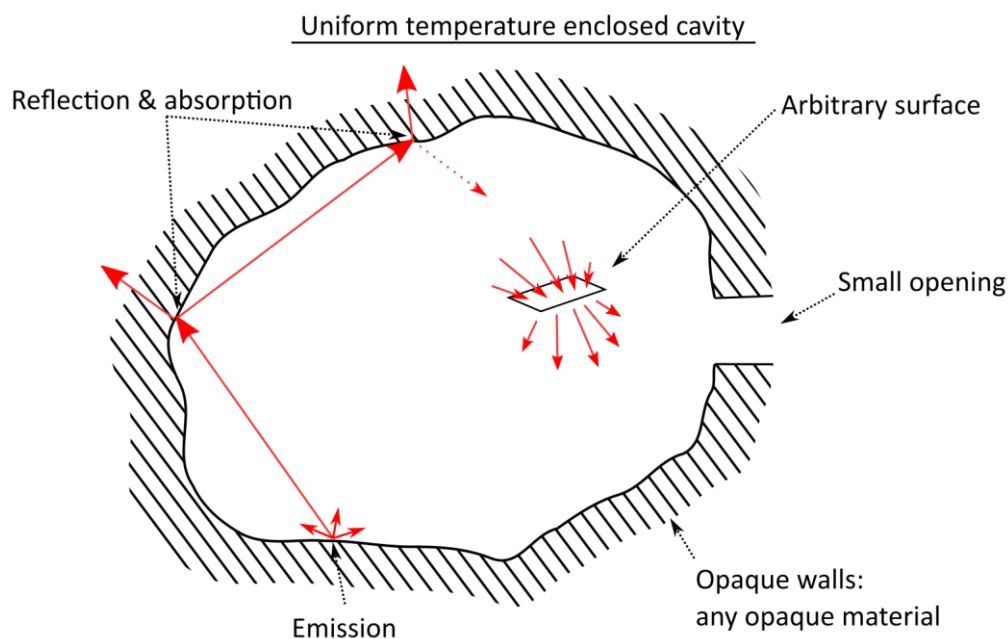


*Figure 2.2-1 The term blackbody cavity describes a space inside an opaque material, which is large compared to the relevant wavelengths of light. The radiant flux ( $\Phi$ ) passing through any arbitrary surface, over sufficient time, is independent of the position or orientation of the surface. A small opening in the walls of the cavity allows sampling of this radiation field, without significantly perturbing the radiative heat balance inside the cavity.*

Considering the arbitrary surface in Figure 2.2-1 as a thin disk with arbitrary absorbance ( $\rho$ ), the laws of thermodynamics state that heat will flow between the disk and the walls until the disk comes into thermal equilibrium with the cavity. If the disk is moved to some other arbitrary location and orientation, then it is evident that it will still be in thermal equilibrium. This implies that the radiation field inside the cavity must be isotropic, as no heat will flow. The keyhole allows sampling of the

radiation field inside the cavity. The arbitrary surface in Figure 2.2-1 can be moved to be coincident with the keyhole. The radiance of the opening will be isotropic. The keyhole surface will behave identically to a Lambertian emitter of unitary emissivity (see section 2.1.4).

### 2.2.2 Planck's law

For a full derivation of the Planck blackbody formula see books on radiation thermometry such as chapter 2 of *'the Fundamentals of Radiation Thermometers'* by Coates and Lowe (2017)[19], or one of many statistical mechanics books, such as chapter 10 of *'Statistical Physics'* by Mandl (1988)[20]. Planck's law of radiation for spectral radiance, in terms of photon frequency ( $\nu$ ), is:

$$L_{BB}(\nu, T) = \frac{2h\nu^3}{c^2} \cdot \frac{1}{e^{\frac{h\nu}{k_B T}} - 1} \quad \text{Eq 2.2-1}$$

In simple terms, this law outlines the most likely number of photons of each energy ( $h\nu$ ) present inside an enclosed isothermal cavity of infinite size, at a given thermodynamic temperature ( $T$ ). In the field of radiometric temperature measurement, the fundamental physical constants are usually condensed into the first two radiation constants,  $c_1$  and  $c_2$ , (see section: *Nomenclature-Physical constants* for values) and expressed in terms of  $\lambda$ .

$$L_{BB}(\lambda, T) = \frac{c_1}{\pi\lambda^5} \cdot \frac{1}{e^{\frac{c_2}{\lambda T}} - 1} \quad \text{Eq 2.2-2}$$

The factor of  $\pi$  in the denominator is due to the value chosen for the CODATA[21] definition of  $c_1$  being in terms of exitance, rather than the metric chosen for this thesis, which is radiance. Figure 2.2-2 shows some illustrative curves of spectral radiance for temperatures relevant to this thesis.

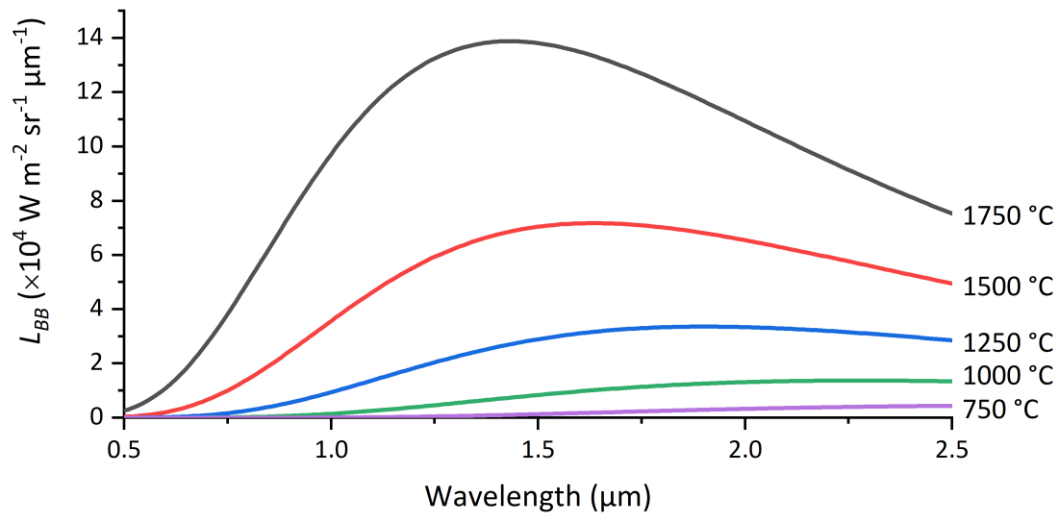


Figure 2.2-2 Spectral radiance of a blackbody surface at some temperatures relevant to this thesis. The choice of temperature scales between Kelvin and °C is somewhat arbitrary, although the distinction is important. Degrees Celcius (°C) is the primary expression of temperature in this thesis, because that is the scale most commonly used in the engineering applications of this work.

The energy of a photon is given by [22]:

$$E_{\gamma} = \frac{hc}{\lambda} \quad \text{Eq 2.2-3}$$

The number of photons ( $N_{\gamma}$ ) of energy  $E_{\gamma}$  passing through a surface in a given time ( $dt$ ) is a photon flux, sometimes called quantum flux:

$$\Phi_{\gamma} = \frac{dN_{\gamma}}{dt} \quad \text{Eq 2.2-4}$$

The spectral radiant flux ( $\Phi_{\lambda}$ ) passing through a surface, can be given in terms of quantised photons of energy  $E_{\gamma}$ , as:

$$\Phi_{\lambda} = \Phi_{\gamma} \cdot E_{\gamma} \quad \text{Eq 2.2-5}$$

The non-spectral equivalent is calculated by integration over all wavelengths. All the other spectral power radiant quantities in Table 2.1-i can be converted into spectral photon radiant quantities by division of the power quantity by the energy of a photon at that wavelength. The spectral radiance can be written in terms of number of photons as:

$$L_{\gamma BB} = \frac{L_{BB}}{E_{\gamma}} = \frac{c_1}{\pi hc \lambda^4} \cdot \frac{1}{e^{\frac{c_2}{\lambda T}} - 1} \quad \text{Eq 2.2-6}$$

This is important in the field of thermography, because the sensitivity of many detectors is given in terms of Quantum Efficiency ( $QE$ ), see section 2.3.1, rather than the power-equivalent, responsivity. Responsivity is used in the field of single detector based infrared radiation thermometry where the area of the detector, and therefore photon fluxes, are much higher. Figure 2.2-3 illustrates the photon radiances at the same temperatures as the power radiances depicted in Figure 2.2-2. It can be observed that the peak is somewhat less pronounced and slightly shifted to the longer wavelengths.

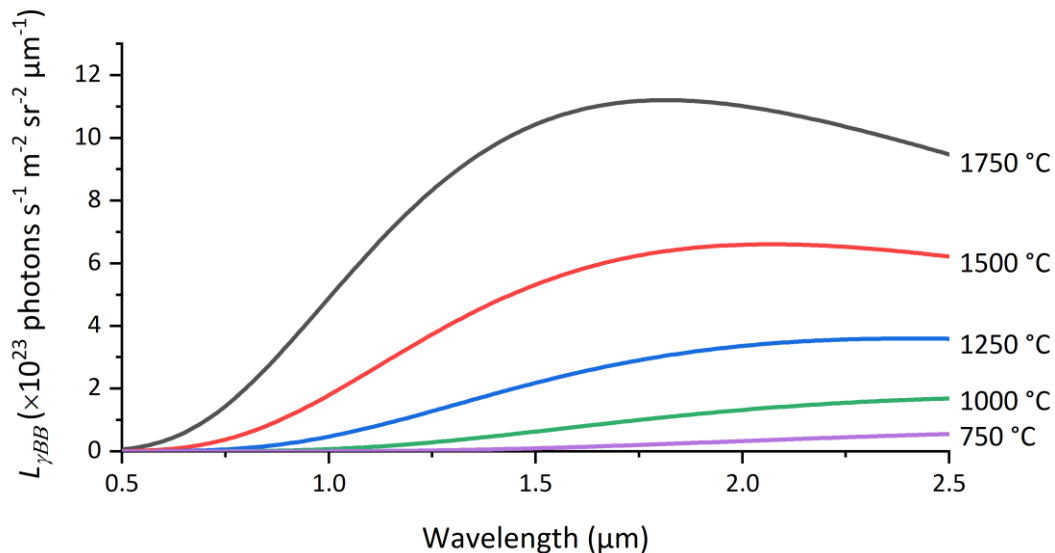


Figure 2.2-3 Spectral radiance in terms of photon flux. Relevant to the specification of sensitivity known as Quantum Efficiency ( $QE$ ), used for many focal plane array sensors.

A radiometric thermometer has a signal which varies with radiance. Therefore, the rate of change of radiance, with respect to temperature, gives an indication of the sensitivity of the instrument

operating in a given wavelength band (or at a given *effective* wavelength see section 2.2.4.3). This sensitivity must be balanced by the requirement for sufficient radiance to be detectable by the instrument above the *noise floor* (see section 2.3.3).

### 2.2.3 The spectral integral measurement equation

The tools developed preceding this section can now be employed to model a radiometric signal, sufficiently well for radiometric thermometry purposes. The expected signal for a *QE*-specified detector can be given as:

$$S(T) = G \cdot \Delta t \cdot \varepsilon \cdot E_{te} \cdot \beta \cdot \int_0^{\infty} QE(\lambda) \cdot \xi(\lambda) \cdot L_{\gamma BB}(\lambda, T) d\lambda \quad Eq\ 2.2-7$$

Where:  $\xi$  is the optical filter function of the instrument defined by the optical filters in place.  $G$  is the *gain*, which converts the number of electrons released in the sensor ( $N_e$ ) to a measured signal value. In the case of modern digital cameras  $G$  is in units of Digital Levels (DL) per electron,  $\Delta t$  is the instrument exposure time and  $\beta$  is the spectrally independent transmission of the system.

There are a series of assumptions required for Eq 2.2-7 to be valid:

- Spectrally invariant optical path.
- Optics for which geometric approximations are valid.
- Temporal invariance of the photon radiance over the exposure time.
- Spectral independence of the emissivity.
- Invariance of sensitivity of the instrument with increasing photon flux.
- Invariance of radiance with viewing angle, i.e. the surface is a Lambertian emitter.
- Freely radiating, no reflected sources of radiance.

The photon radiance of the emitting surface, ignoring reflections, can be modelled by:

$$L_{\gamma}(\lambda, T) = \varepsilon \cdot L_{\gamma BB}(\lambda, T) \quad Eq\ 2.2-8$$

Where  $\varepsilon$  is usually treated as spectrally invariant, but the spectral dependence can be included within the calculations if it is sufficiently well known (this is rarely the case). The spectral Photon flux ( $\Phi_{\gamma}(\lambda)$ ) which would be incident on an unfiltered detector is given by:

$$\Phi_{\gamma\lambda}(\lambda, T) = \varepsilon \cdot E_{te} \cdot L_{\gamma BB}(\lambda, T) \quad Eq\ 2.2-9$$

This step is explained in more detail in section 2.1.3. The combined *QE* of the sensor with the filter ( $\xi$ ) is given by:

$$QE^*(\lambda) = QE(\lambda) \cdot \xi(\lambda) \quad Eq\ 2.2-10$$

The number of electrons liberated per exposure in the detector material due to the filtered incident flux (assuming temporal invariance, see section 2.3.4) can be given as:

$$N_e(T) = \Delta t \cdot \int_0^{\infty} QE^*(\lambda) \cdot \Phi_{\gamma}(\lambda, T) d\lambda \quad \text{Eq 2.2-11}$$

A brief outline of what is meant by electron liberation can be found in section 2.3.1. For practical purposes the exact scaling quantities are not always precisely known and are often combined into a single constant ( $A$ ), which can be determined by calibration. This simplifies Eq 2.2-7 to:

$$S(T) = A \int_0^{\infty} QE(\lambda) \cdot \xi(\lambda) \cdot \varepsilon \cdot L_{\gamma BB}(\lambda, T) d\lambda \quad \text{Eq 2.2-12}$$

An alternative is to include all the instrument factors into one spectrally dependent instrument responsivity quantity  $R^*(\lambda)$  where:

$$R^*(\lambda) = G \cdot \Delta t \cdot E_{te} \cdot QE(\lambda) \cdot \xi(\lambda) \quad \text{Eq 2.2-13}$$

Then Eq 2.2-7 becomes:

$$S(T) = \int_0^{\infty} R^*(\lambda) \cdot \varepsilon \cdot L_{\gamma BB}(\lambda, T) d\lambda \quad \text{Eq 2.2-14}$$

In real situations a lot of the parameters characterising the response of the instrument are encapsulated into a blackbody calibration function ( $f_{BB,i}(T)$ ). where the  $i$  is the form of the function chosen. Some of the popular forms of these functions are discussed in more detail in the section 2.2.4. It is not always the case that a functional form is used, sometimes the instrument manufacturers calibrate the instrument at a large number of calibration points covering the range, and then use a smoothing interpolation function to 'join the dots'. This approach means that extrapolation of the calibration to temperatures outside the calibration range is usually meaningless. The signal reported by the instrument is then simply the calibration scaled by the emissivity of the surface:

$$S(T) = \varepsilon \cdot f_{BB,i}(T) \quad \text{Eq 2.2-15}$$

## 2.2.4 Alternative forms and approximations of Planck's law

The formation of the law governing the spectral distribution of energy has a long and interesting history. Some of precursors to Planck's law provide useful approximations, namely work by Wien in the late 19<sup>th</sup> and early 20<sup>th</sup> century [23]. We can also use modern approximations to help us manipulate Planck's law without the need to consider the integral in Eq 2.2-7.

### 2.2.4.1 Total radiation

The integral of Planck's law over all wavelengths provides a surprisingly simple functional form of total exitance of a blackbody, which is:

$$M_{BB}(T) = \frac{2\pi^5 k^4}{15c_0^2 h^3} \cdot T^4 = \sigma T^4 \quad \text{Eq 2.2-16}$$

Where  $\sigma$  is termed the Stephan-Boltzmann constant, which is a function of fundamental physical constants only, its value can be found in section: Nomenclature-Physical constants. This equation does not contribute to our understanding in terms of radiometric measurement of temperature, but does give an indication of how much energy in total is transferred between a surface and its surroundings. This is a useful tool in modelling the cooling of a surface by radiative heat transfer [6].

#### 2.2.4.2 Wien's displacement law

This law provides the position of the maxima of Planck's spectral radiance law and is usually expressed as:

$$T\lambda_{max} = b \quad \text{Eq 2.2-17}$$

Where  $b$  is the Wien wavelength displacement law constant, also known as the third radiation constant ( $c_3$ ). This relation can be found by numerical differentiation of Planck's law with respect to wavelength, the derivative is set equal to zero and solved for wavelength. One use of this relation is to indicate the nature of the increase in  $L(\lambda, T)$  with respect to temperature. For the spectral region where the product  $\lambda T \gg b$ , then  $L(\lambda, T)$  increases linearly proportional to  $T$  &  $\lambda$ . In the spectral region where the product  $\lambda T < b$ , then  $L(\lambda, T)$  increases exponentially with  $T$  &  $\lambda$ . This case ( $\lambda T < b$ ) is where the Wien approximation is valid.

#### 2.2.4.3 Wien approximation

A useful, and accurate (in the right circumstances), approximation of Plank's law in terms of radiance is [23]:

$$L_{vBB}(\lambda, T) = \frac{c_1}{\pi\lambda^5} \cdot e^{-\frac{c_2}{\lambda T}} \quad \text{Eq 2.2-18}$$

From this approximation, good estimates of the spectral radiance of a blackbody, which fulfil the inequality  $\lambda T < b$ , can be made. The Wien approximation is mathematically simple and allows quick estimation of some important factors. One important use of the Wien approximation is to abstract the spectral distribution of sensitivity ( $\xi \cdot QE$ ) to a single effective wavelength ( $\lambda_{Wien}$ ) over a given temperature range. This is only strictly valid over a limited temperature range and for narrow band systems. The signal measured by a narrow band radiometric thermometer by can be approximated using:

$$S(T) \approx G \cdot \Delta t \cdot E_{te} \cdot \Delta\lambda \cdot QE(\lambda_{Wien}) \cdot \varepsilon \cdot \frac{c_1}{\pi\lambda^5} e^{-\frac{c_2}{\lambda_{Wien} T}} \quad \text{Eq 2.2-19}$$

Where  $\Delta\lambda$  is the spectral band width of the system, which is often approximated by the Full Width at Half Maximum ( $FWHM$ ) of the sensitivity band for a narrow band system.  $QE(\lambda_{Wien})$  is the quantum efficiency of the instrument, evaluated at the Wien effective wavelength ( $\lambda_{Wien}$ ). It is convenient to compile all the factors in front of the exponential into a single calibration constant ( $A_{Wien}$ ) giving:

$$f_{BB,wien}(T) \approx A_{Wien} e^{-\frac{c_2}{\lambda_{Wien} T}} \quad \text{Eq 2.2-20}$$

Manipulation of this equation provides a way to measure  $\lambda_{Wien}$  &  $A_{Wien}$  from a series of  $S$  against  $T$ , for a given instrument, from a blackbody source ( $\varepsilon = 1, S(T) = f_{BB,Wien}(T)$ ).

$$\ln S(T^{-1}) \approx -\frac{c_2}{\lambda_{Wien}} \cdot \frac{1}{T} + \ln A_{Wien}$$

Eq 2.2-21

$$\lambda_{Wien} = -c_2 / \frac{d \ln S(T)}{dT^{-1}} \quad A_{Wien} = \exp(\ln S(T^{-1} = 0))$$

The approximation of the Wien effective wavelength for the simulated instrument from section 2.2.5 in the temperature range 1000 °C to 2000 °C, can be seen in Figure 2.2-4.

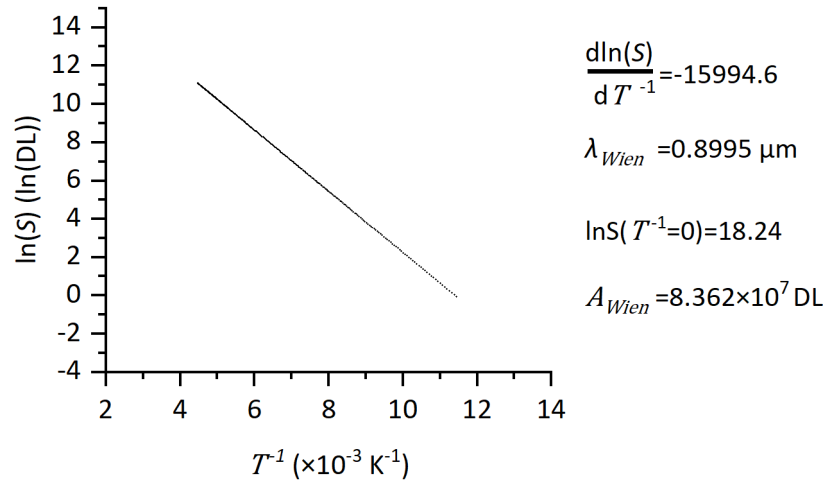


Figure 2.2-4 The Wien effective wavelength for the simulated instrument elucidated in section 2.2.5, a linear fit of the data provides both coefficients for the Wien approximation.

The most widespread utilisation of  $\lambda_{Wien}$ , is as an estimate for the sensitivity factor of the instrument. The sensitivity of a radiometric thermometer can be approximated using the 1<sup>st</sup> order Taylor expansion (see section 8.1 for details on Taylor expansion):

$$\Delta L_{yBB} = \frac{df_{BB,Wien}}{dT} \cdot \Delta T + \dots$$

Eq 2.2-22

Substituting Eq 2.2-18 as a model for the radiance and assuming all other factors are constant. The sensitivity (how much the signal changes for a given change in temperature) of a signal generated by a radiometric thermometer, as a function of wavelength and temperature, can be estimated as:

$$\frac{\Delta S}{S} \cdot \frac{1}{\Delta T} = \frac{\Delta f_{BB,Wien}}{f_{BB,Wien}} \cdot \frac{1}{\Delta T} \approx \frac{c_2}{T^2 \lambda_{Wien}}$$

Eq 2.2-23

Where  $T$  must be in K. This approximation allows visualisation of how the wavelength (characterised by  $\lambda_{Wien}$ ) of a system effects its sensitivity, see Figure 2.2-5.

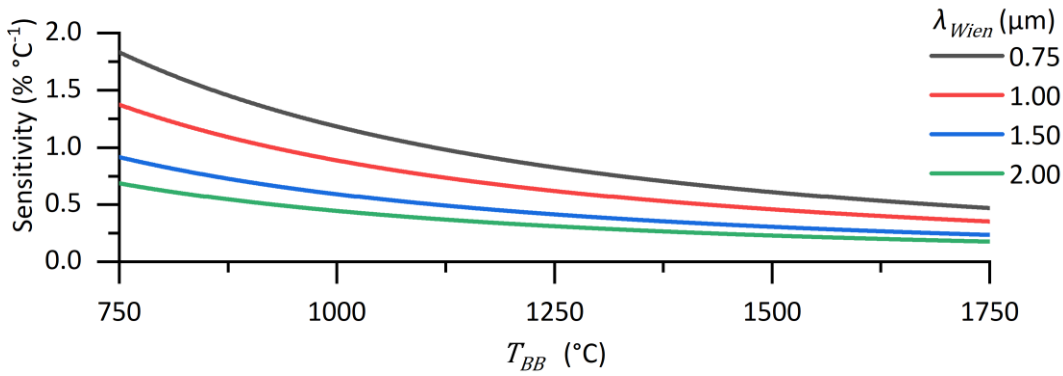


Figure 2.2-5 The sensitivity of a narrow band radiometric thermometer operating in the Wien regime, can be modelled by the Wien effective wavelength ( $\lambda_{Wien}$ ).

With a slight rearrangement, the uncertainty in inferred temperature ( $UT$ ) for any factor which linearly scales the signal can be estimated. This is valid for any non-spectral factor (does not affect  $\lambda_{Wien}$ ), such as emissivity or path transmission (common assumption). For any linear scaling factor ( $B_{Scale}$ ), the effect of an uncertainty in  $B_{Scale}$  ( $UB_{Scale}$ ) has the following effect on uncertainty in measured temperature:

$$\frac{UB}{B} = \frac{US}{S} \tag{Eq 2.2-24}$$

$$UT = \frac{T^2 \lambda_{Wien}}{c_2} \cdot \frac{UB}{B}$$

A common application of Eq 2.2-24 is to calculate the effect of uncertainty in emissivity on the uncertainty in measured temperature. Emissivity is often the biggest single source of uncertainty in radiometric temperature measurement of real-world surfaces. Some illustrative examples are depicted in Figure 2.2-6.

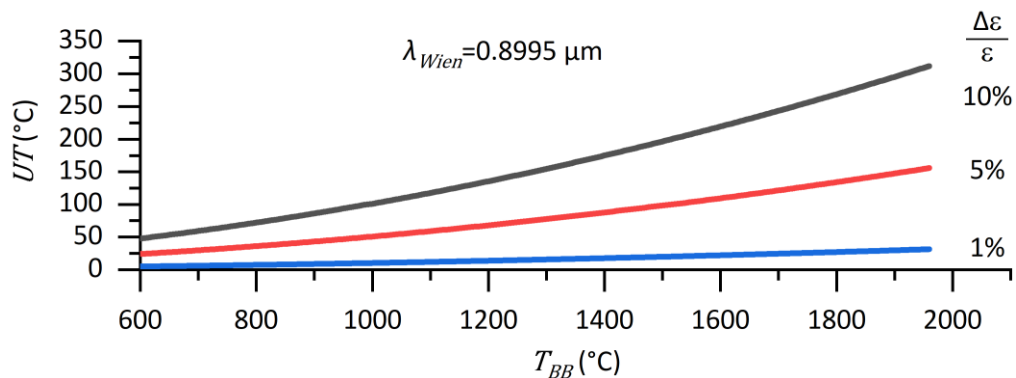


Figure 2.2-6 Uncertainty in measured temperature ( $UT$ ) for a given fractional uncertainty in emissivity for the simulated instrument exemplified in section 2.2.5.

#### 2.2.4.4 Sakuma-Hattori approximation

An approximation for the integral in Eq 2.2-7, which is used in primary radiation thermometry metrology applications [24], is the Planck form of the Sakuma-Hattori equation [25]. The most commonly used form, which shall be referred to as *the SH equation*, is:

$$f_{BB,SH}(T) = \frac{A_0}{\exp \frac{c_2}{A_1 T + A_2} - 1} \quad \text{Eq 2.2-25}$$

Where the  $A_i$  are coefficients which can be directly related to the spectral characteristics of the instrument or used as fitting coefficients to create an interpolation and extrapolation function from discrete calibration data. For a full description of the correspondence between the coefficients and the spectral characteristics of the instrument, see work by Saunders & White (2003)[26]. Here the coefficients for a reasonably narrow band system are calculated and their use is explained. The combined spectral sensitivity ( $QE^*(\lambda)$ ) distribution can be characterised by taking its statistical moments. The  $n^{\text{th}}$  central moment about the mean ( $\mu_n$ ) can be calculated by:

$$\mu_1 = \frac{\int_0^\infty (\lambda - \lambda_0)^i \cdot QE^*(\lambda) \cdot d\lambda}{\int_0^\infty QE^*(\lambda) \cdot d\lambda} \quad \text{Eq 2.2-26}$$

Where  $\lambda_0$  is the mean wavelength of the distribution  $QE^*(\lambda)$ , calculated by:

$$\lambda_0 = \frac{\int_0^\infty \lambda \cdot QE^*(\lambda) \cdot d\lambda}{\int_0^\infty QE^*(\lambda) \cdot d\lambda} \quad \text{Eq 2.2-27}$$

The SH equation is a truncation of a series expansion in powers of  $1/T$  (in K) starting at -1:

$$f_{BB,SH} = \frac{A_0}{\exp \frac{c_2}{A_1 T + A_2 + A_3/T + A_4/T^2 + \dots} - 1} \quad \text{Eq 2.2-28}$$

Assuming the spectral bandwidth of the system is relatively narrow, the radiance is sufficiently well modelled by truncating Eq 2.2-28 to two terms ( $A_1$  &  $A_2$ ). If the spectral band width is large then a third term ( $A_3$ ) should be included, the fourth term ( $A_4$ ) and above should not be needed. Using the total instrument response ( $R^*(\lambda)$ ) from Eq 2.2-13, and the characterisation metrics of the distribution of  $QE^*(\lambda)$  from Eq 2.2-26, the signal response of an instrument can be modelled by the coefficients:

$$A_0 = \frac{c_1}{\pi h c} \int_0^\infty \frac{R^*(\lambda)}{\lambda^4} \cdot d\lambda \quad \text{Eq 2.2-29}$$

$$A_1 = \lambda_0 \left( 1 - 6 \frac{\mu_1}{\lambda_0^2} + 21 \frac{\mu_3}{\lambda_0^3} - \frac{(4\mu_4 - 9\mu_2^2)}{\lambda_0^4} + \dots \right) \quad \text{Eq 2.2-30}$$

$$A_2 = \frac{c_2}{2} \left( \frac{\mu_2}{\lambda_0^2} - 7 \frac{\mu_3}{\lambda_0^2} + \frac{(4\mu_4 - 9\mu_2^2)}{\lambda_0^4} + \dots \right) \quad \text{Eq 2.2-31}$$

$$A_3 = \frac{c_2^2}{6\lambda_0} \left( \frac{\mu_3}{\lambda_0^3} - \frac{(16\mu_4 - 39\mu_2^2)}{2\lambda_0^4} + \dots \right) \quad \text{Eq 2.2-32}$$

For relatively narrow spectral bandwidths these series expansions can be truncated at terms in  $\mu_2$ . Noting that  $\mu_2$  is the variance of the distribution which is equal to the square of the standard deviation ( $\sigma_\lambda^2$ ). The signal from a radiometric thermometer can be modelled using the coefficients:

$$A_1 \approx \lambda_0 \left( 1 - 6 \left( \frac{\sigma_\lambda}{\lambda_0} \right)^2 \right) \quad \text{Eq 2.2-33}$$

$$A_2 \approx \frac{c_2}{2} \left( \frac{\sigma_\lambda}{\lambda_0} \right)^2 \quad \text{Eq 2.2-34}$$

The sensitivity factor for the SH equation (Eq 2.2-25) is:

$$\frac{\Delta f_{BB,SH}}{f_{BB,SH}} \cdot \frac{1}{\Delta T} = \frac{A_1 c_2}{(A_1 T + A_2)^2 \cdot (1 - \exp(-c_2/(A_1 T + A_2)))} \quad \text{Eq 2.2-35}$$

One useful feature of the SH equation is that it can be algebraically inverted to give the temperature (in K) as a function of signal and known scaling factors such as emissivity:

$$T = \frac{c_2}{A_1 \ln \left( \frac{\varepsilon A_0}{f_{BB,SH}} + 1 \right)} - \left( \frac{A_2}{A_1} \right) \quad \text{Eq 2.2-36}$$

This removes the need for numerical methods to invert the integral in Eq 2.2-7. The functional form is a useful concise way to record and transmit the calibration of an instrument. The integral method is usually implemented in a calibration by a numerical look up table of blackbody temperature against signal which can be scaled by the emissivity. A look up table requires significantly more information to be reported and stored than a simple mathematical equation with three or four coefficients.

#### 2.2.4.5 Radiance temperature

Sometimes it is informative to present radiometric measurements in terms of radiance temperature ( $T_{Rad}$ ) [27], sometimes called colour temperature [28].  $T_{rad}$  is used to quantify the radiance of a surface in a given measurement spectral band. The spectral characteristics of the instrument are not always well characterised, but the response of the instrument to a blackbody source is usually well known.  $T_{Rad}$  is the temperature of a blackbody radiator which would have the same spectrally integrated radiance as that measured by the thermographic instrument. Using the Wien approximation this would give:

$$T_{Rad} = \frac{-c_2}{\lambda_{Wien} \ln \frac{S}{A_{wien}}} \quad \text{Eq 2.2-37}$$

The radiance temperature can be calculated using any  $L_{BB}(T)$  model. The  $T_{Rad}$  is only strictly a valid measure of radiance for the same spectral band as the thermographic instrument and becomes an invalid metric for wider band or alternative band radiometers, where the spectral ( $T$ ) dependence of the radiance becomes increasingly changes.

#### 2.2.5 Illustrative example

It is informative to go through the process of modelling a radiometric thermometer signal from a set of simple simulated parameters. From this exercise the interaction between the Planck blackbody distribution of photon energies, and an instrument whose parameters are typical of the type of instruments used throughout this thesis, can be illustrated.

Table 2.2-i Simulated thermographic instrument parameters

Instrument parameter	
$G$	0.5 DL electron <sup>-1</sup>
$d\Omega$	$1.26 \times 10^{-3}$ sr ( $A_{AS} = \pi(10 \text{ mm})^2$ , $r_{ap} = 0.5 \text{ m}$ )
$dA$	$2.5 \times 10^{-11}$ m <sup>2</sup> ( $5 \mu\text{m}$ ) <sup>2</sup>
$QE$	Orca Flash 4.0 Si CMOS Datasheet [29]
$\xi$	Gaussian ( $\lambda_0 = 0.9 \mu\text{m}$ , $\sigma_\lambda = 0.02 \mu\text{m}$ , amplitude=1)
$\Delta t$	1 ms
Surface parameter	
$\epsilon$	0.5

Assuming the parameters laid out in Table 2.2-i, the expected signal for a given temperature can be modelled. The simulated instrument is spectrally a moderately narrow band system (having a 46 nm *FWHM*), operating with a silicon quantum detector, see Section 2.3.1.

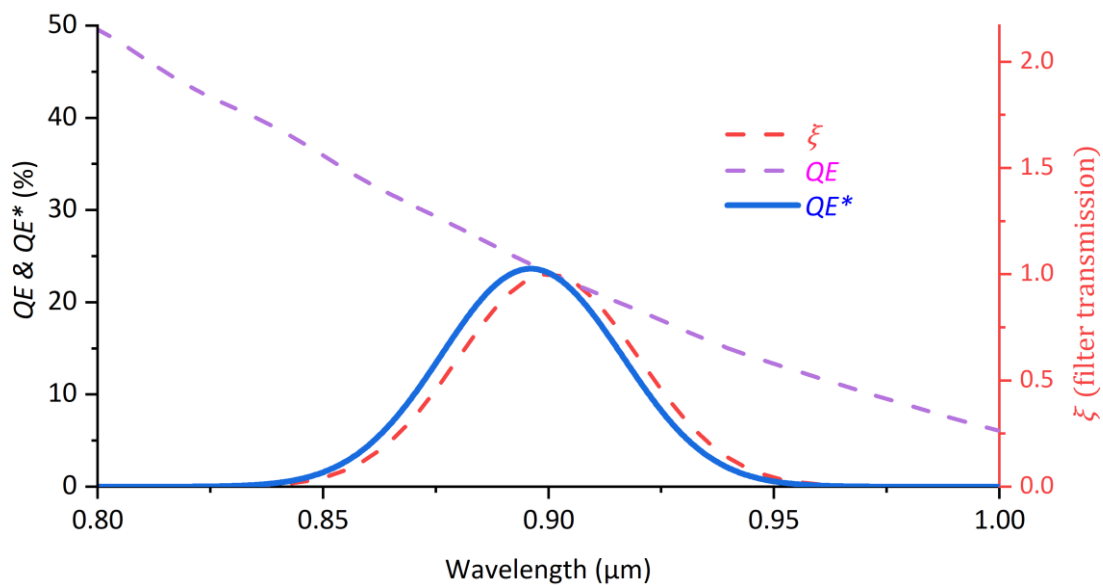


Figure 2.2-7 Illustration of the spectral response of a simulated radiometric thermometer. The shift in the central wavelength of the sensitive region away from the central wavelength of the band pass filter (see Table 2.2-i), is due to the spectral dependence of the QE.

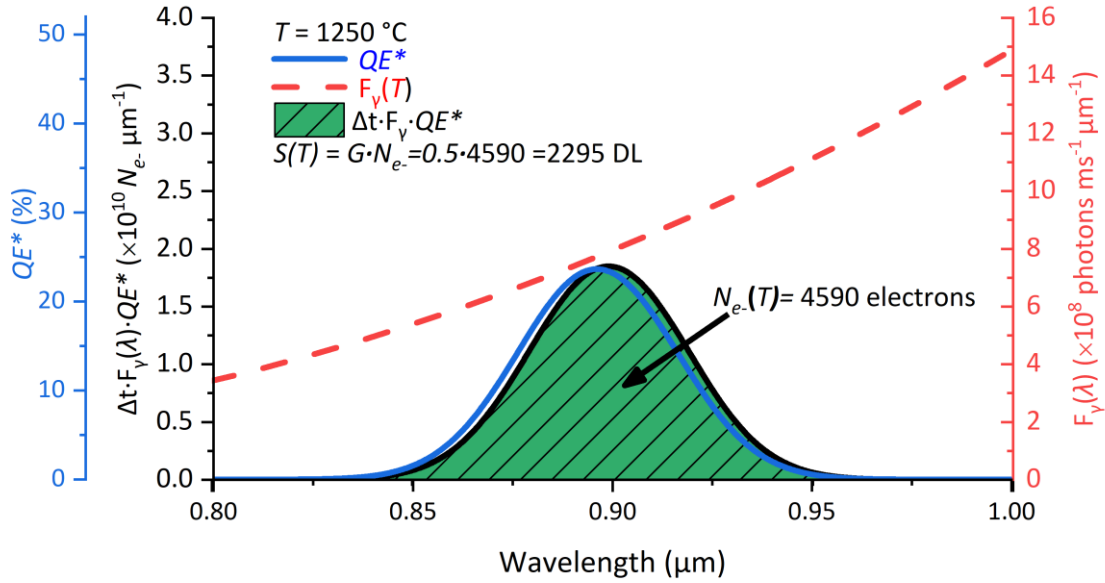


Figure 2.2-8 The area under the black curve is the number of electrons liberated in the detector (see section 2.3.1), the signal reported by the instrument is proportional to this.

The spectrally responsive region of the simulated instrument is the area under the  $QE(\lambda) \cdot \xi(\lambda)$  curve in Figure 2.2-7. Using Eq 2.2-9 we can estimate the spectral photon flux incident on the detector, if a filter was not in place. This is for illustrative purposes. The area under the black curve in Figure 2.2-8 is the number of electrons excited by the incident filtered photon flux in the detector material, assuming temporal invariance. The signal reported by this simulated instrument is the number of electrons excited in a single exposure multiplied by the Gain factor ( $G$ ).

Table 2.2-ii Spectral characteristics of  $QE^*$  for simulated instrument

Quantity	Equation	Value	Unit
$\lambda_0$	Eq 2.2-27	0.8961	$\mu\text{m}$
$\mu_2$	Eq 2.2-26	$3.924 \times 10^{-16}$	$\text{m}^2$
$\sigma_\lambda$	$\sqrt{\mu_2}$	0.01981	$\mu\text{m}$
$\Delta\lambda$ (FWHM)	$2\sqrt{2\ln 2} \cdot \sigma_\lambda$	0.04665	$\mu\text{m}$
$A_0$	Eq 2.2-29	$1.733 \times 10^8$	DL
$A_1$	Eq 2.2-33	0.8935	$\mu\text{m}$
$A_2$	Eq 2.2-34	3.515	$\mu\text{m} \cdot \text{K}$

## 2.2.6 Comparison of models

The three methods (integral, Wien, SH) of modelling the response of an instrument pertinent to this work are exemplified here. Using the illustrative parameters laid out in the previous section, the spectral characteristics from Table 2.2-ii and the relevant parameters from Table 2.2-i, the expected signals for a series of temperatures can be modelled.

Table 2.2-iii Three models for the signal expected from a simulated radiometric thermometer

Model	Equation	Notes
Integral	Eq 2.2-7	1000 evaluation point numerical integral (Simpson)
Wien-Raw	Eq 2.2-19	$\lambda_{Wien} = \lambda_0$ , & $A_{Wien}$ from Table 2.2-i & Table 2.2-ii
SH-Raw	Eq 2.2-25	$A_0, A_1, A_2$ from Table 2.2-ii

The results of modelling the signals with the three methods can be seen in Figure 2.2-9. All three models produce signals which appear nominally identical. It is difficult to visually compare the models when plotted on this scale as the signal itself varies by many orders of magnitude over the  $T$  range.

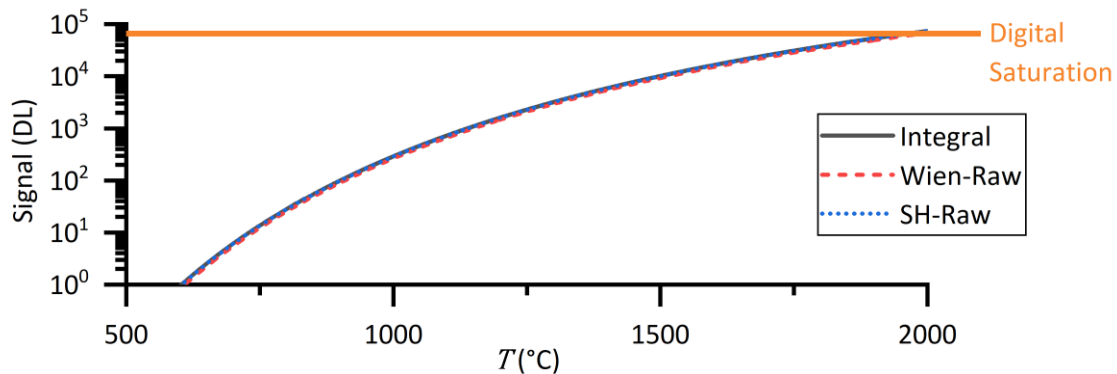


Figure 2.2-9 Simulated signal using the raw assumed parameters in Table 2.2-iii.

Assuming that the integral method has produced a true signal, the other two approximations can be compared to the integral method. The Wien and SH approximations can also be used in their more relevant form, as functions with free parameters, which can be fit to measured calibration data.

Table 2.2-iv Approximation equation fitted parameters

Model	Fit Equation	Fit Parameters	Best Fit Value	Unit
Wien-Fit	Eq 2.2-21	$\lambda_{Wien}$	0.8995	$\mu\text{m}$
		$A_{Wien}$	$8.362 \times 10^7$	DL
SH-Fit	Eq 2.2-36	$A_0$	$1.733 \times 10^8$	DL
		$A_1$	0.8940	$\mu\text{m}$
		$A_2$	$3.479 \times 10^{-6}$	$\mu\text{m} \cdot \text{K}$

The error in temperature terms,  $\Delta T$  in Figure 2.2-10, is generated by taking the difference in generated signal between the approximation model and the integral method signal ( $\Delta S$ ). This is then combined with the SH sensitivity factor (Eq 2.2-35) to give  $\Delta T$ . The SH-Fit sensitivity is used because it does not require numerical evaluation and closely matches the integral method.

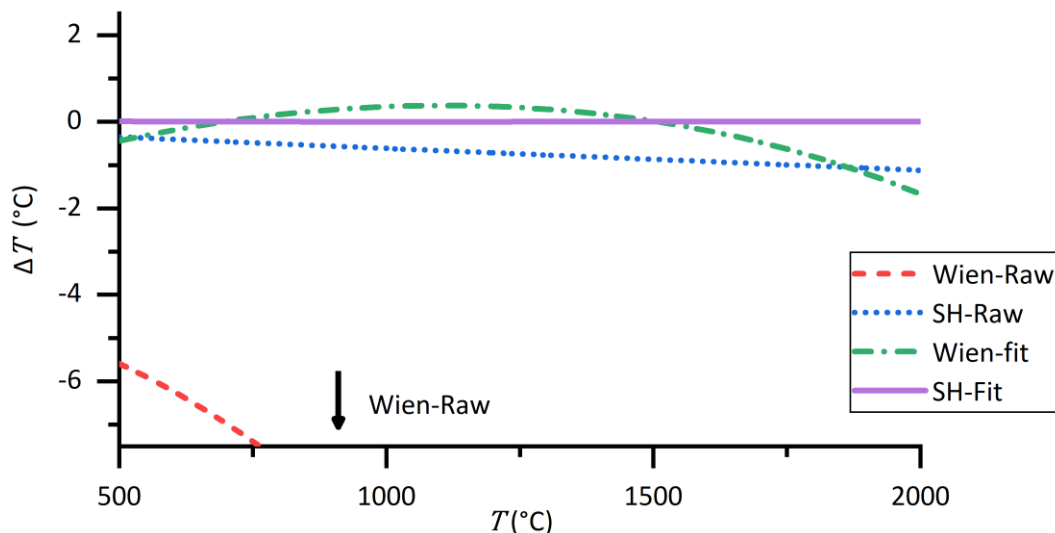


Figure 2.2-10 The difference between the approximations and the integral method shows that the fitted Sakuma-Hattori equation gives the least error for the instrument simulated in section 2.2.5. The curve in the error ( $\Delta T$ ) for the Wien approximation cannot be fully corrected by adjustment of the two fit parameters.

## 2.3 THERMOGRAPHIC INSTRUMENTS

The main components of a thermographic system are:

- Imaging system (the optics),
- Sensor (photon transducer),
- Electronics required to convert the output of the sensor into a usable digital format (image).

In this section I will concentrate on the sensor and the electronics components. These are usually packaged into one commercially available device, which will be referred to as the *camera*, as distinct from the *optics*.

The application chosen as the focus of this work is additive manufacturing of metals. The processing of feedstock into a part usually requires the application of a localised heat source which heats the feedstock to temperatures above the melting point of the metal. The melting temperature of most metals is over 900 K [30]. The high transient temperatures during the melting and re-solidification cause the surface of the part to emit a significant fraction of its energy as Near Infrared Radiation (NIR), thus allowing utilisation of NIR wavelengths for imaging purposes.

The most widely used sensor material for imaging systems is silicon (Si). Si is mainly sensitive in the visible light range ( $\sim 0.4 - 0.75 \mu\text{m}$ ), with some reduced sensitivity in the *NIR* (typically  $<15\%$  QE for  $\lambda > 0.85 \mu\text{m}$  [29]). Due to the commercial appeal of Si as a visible light camera, significant investment has been made in optimising the wafer processing and electronics integration to work with this detector material. It is therefore possible to get high specification cameras at a lower price than some dedicated infrared sensors such as Indium-Gallium-Arsenide.

The dominant wafer technology in Si radiometric sensors at the turn of the millennium was charge coupled devices (*CCD*). Since then Complementary Metal Oxide Semiconductor (*CMOS*) sensors have come to dominate the market. Chapter 5 of the *Hamamatsu Opto-Semiconductor handbook* [31] describes the operation of some of the focal plane array sensors produced by Hamamatsu.

### 2.3.1 Photon transducers

Thermographic instruments can be split into two categories, *scanning* and *staring array*. The transduction mechanism in both kinds of imagers can be either *thermal* or *quantum*. In this thesis I have utilised staring instruments with quantum detectors. The most common thermographic instruments utilised in the field of additive manufacturing are staring instruments, the sensing component of a staring thermographic instrument is termed a Focal Plane Array (*FPA*) see Figure 2.3-1.

Scanning instruments [32] usually use a single detector element and a beam steering mechanism to scan the image of the field stop / detector around the scene (see Section 2.1.3 for more detail). Scanning instruments have some advantages over staring instruments in that the optical performance can be more tightly constrained, increasing the imaging aspects of the radiometric accuracy. The main drawback with scanning instruments is that the time required to scan the single pixel around the scene usually leads to an instrument with a low *frame rate* (temporal sampling rate). The frame rate is the number of images of the whole scene or *TFOV*, which can be captured per unit time, usually quoted in frames per second (fps).

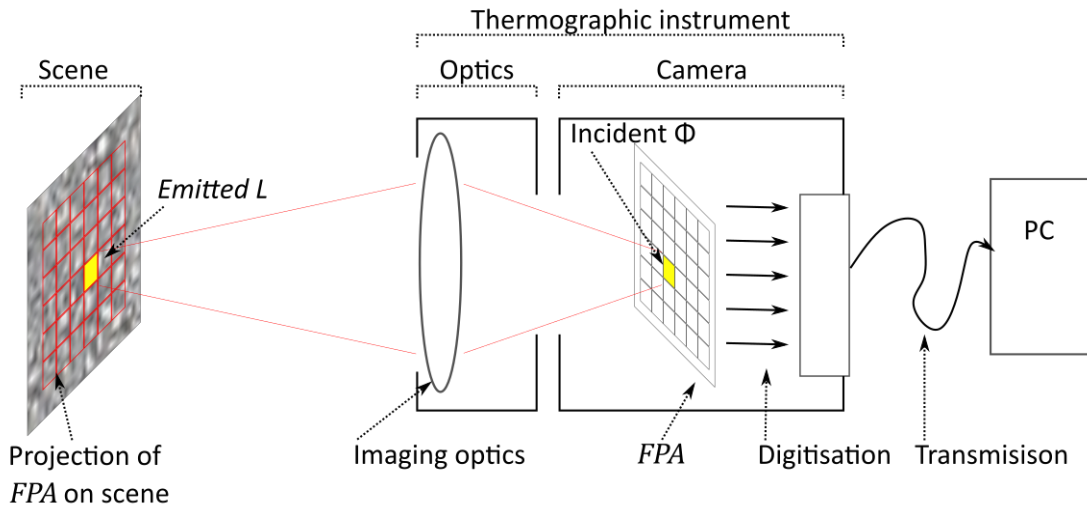


Figure 2.3-1 Schematic of the function of a focal plane array within a staring-array thermographic instrument.

Thermal detectors, such as microbolometer arrays, work by absorbing the incident radiant flux, which heats the sensing element. The change in temperature of the element affects the electrical conduction properties of the material which is monitored and digitised within the camera. Thermal detectors are usually optimised for long wavelength infrared but can nominally be operated at any wavelength where the sensing element can be made sufficiently absorptive.

Quantum detectors work by direct translation of an absorbed photon to a free charge carrier, see Figure 2.3-2. Chapter 2 of the 'Hamamatsu Opto-Semiconductor handbook' (2014)[33] is a good introduction to the theory of operation of Si photodiodes. The electronics in or adjacent to the sensor then sample the number of excited charge carriers (usually just referred to as electrons) and converts this to a digital signal via an Analogue to Digital Converter (ADC).

The main difference between quantum and thermal sensors in terms of performance is that quantum detectors have a significantly narrower spectral range of sensitivity. The low energy (long wavelength) bound is determined by the band gap of the detector material. Excitation of charge carriers requires direct state to state excitement. If there are no allowed states for the excitation to occupy, then the photon cannot be absorbed to create a charge carrier.

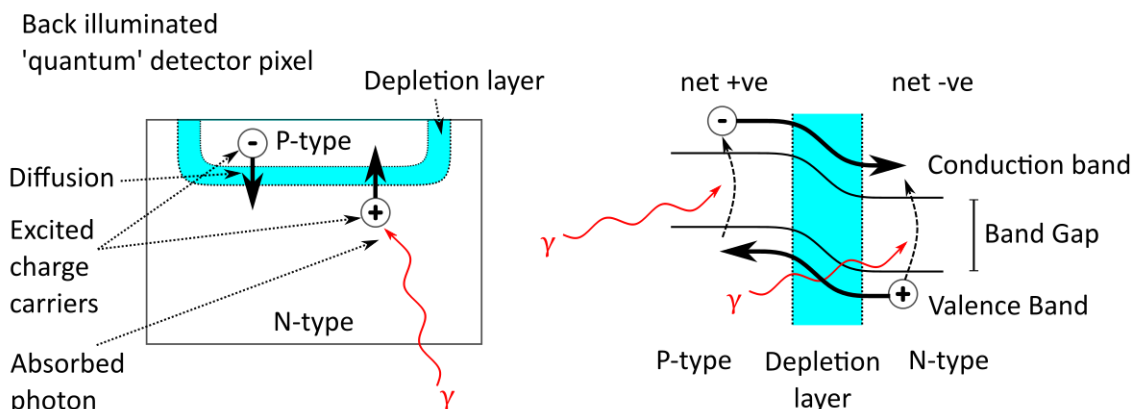


Figure 2.3-2 Schematic of a single pixel of a PIN photo diode on the left and the energy diagram across the depletion layer on the right.

For quantum FPAs, the detector is usually fabricated as a single wafer, etched into separate electrically isolated sensing elements, or pixels [31]. The excited charges can diffuse into adjacent

pixels, if the electrical isolation is insufficient. This is a mechanism by which the image degrades (blurs), especially in sensors with small pixels [34].

The exact architecture of each commercially available sensor is not well advertised, and properties about a specific variant can be difficult to find. It is instructive to illustrate the operating principles of a typical FPA sensor, as some of the features of the acquired data are affected by the details of operation. The operation of the Hamamatsu Orca Flash 4.0 V3 [29] Si CMOS is used as an example of a CMOS based FPA.

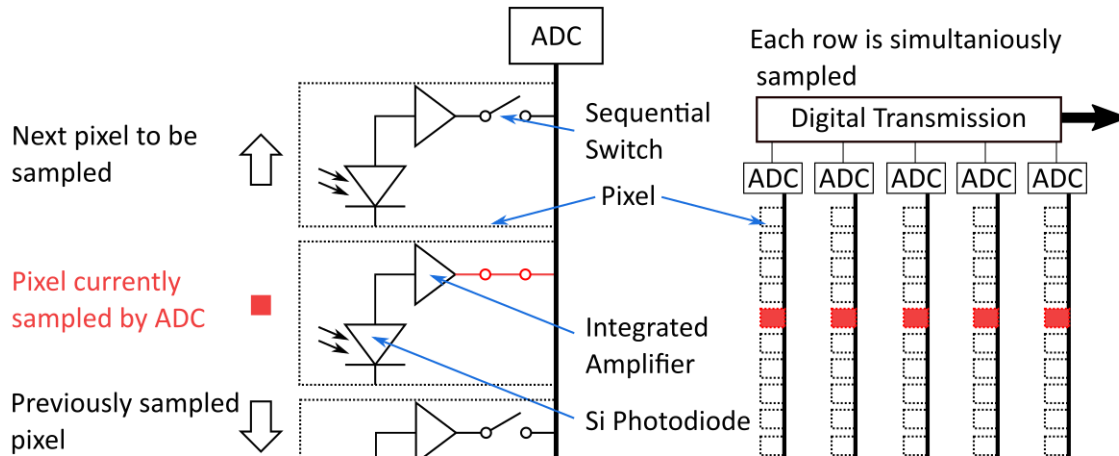


Figure 2.3-3 Representative schematic of the operating principles of a Si CMOS FPA sensor. The photocurrent generated in the Si photodiode is converted into a voltage by the integrated amplifier. The voltage is then sampled by the Analogue to Digital Converter (ADC) and transmitted to the PC for conversion into a digital image.

### 2.3.2 Dark and flat-field corrections

The signal reported by a camera system requires some pre-processing before the signal can be considered globally proportional to incident radiant flux ( $\Phi$ ) (section 2.1.1). It is a feature of most quantum detectors that they produce a small *dark current* even when no absorbable photons are incident upon the detector. Dark current is driven by the thermal energy inherent in the sensor itself, so can be mitigated by cooling. The dark current is indistinguishable from a photon induced current and will be digitised in the same way by the *ADC*. The dark current produces a signal which is proportional to the exposure time of the camera. The dark current in Si *CMOS* sensors is relatively small ( $<1$  DL pixel<sup>-1</sup> s<sup>-1</sup> [29]), but is significant for some longer wavelength detectors. In addition to the dark current, the *ADC* is usually set to give a finite reading at zero  $\Phi$ . This offset allows detection of the noise at zero signal, and allows confidence in the zero  $\Phi$  signal, should it fluctuate for any reason. Long wavelength cameras will also have the problem that the entire housing of the camera is emitting detectable photons. For these reasons it is always good practice to isolate the camera from the target (such as by placing a lens cap, or turning off the source), and taking some images at the same exposure time as the measurement. These *dark images* ( $S_{dark}$ ) are then removed from the acquired images to remove any offsets.

It is often assumed that the signal produced by the detector, and therefore the digital value produced by the *ADC*, has a linear response to  $\Phi$ . This assumption is usually valid for Si but invalid for some detectors such as Mercury Cadmium Telluride. The constant of proportionality between the reported signal and  $\Phi$  is heavily dependent on the amplifier and the electronics of the *ADC*. The constant of proportionality may not be uniform across the *FPA*, and may also drift with ambient temperature. For these reasons it may be necessary to apply a *Non-Uniformity Correction (NUC)* to normalise the response of the detector. The NUC is characterised by showing the camera a uniform radiance *flat-field* target, the individual pixels can then be corrected to make the image reported by

the instrument uniform. This is a tricky correction to perform, because a sufficiently uniform target, which fills the entire field of view of the instrument, is difficult to realise [35]. An alternative is to characterise the non-uniformity and include it in an assessment of the uncertainty of the measurement. The degree of non-uniformity across the sensor can then be thought of as spatial noise.

The image at pixel index  $(i, j)$  is then given by:

$$S(i, j) = S_{raw}(i, j) \cdot NUC(i, j) - S_{dark}(i, j) \quad Eq\ 2.3-1$$

### 2.3.3 Noise

References [34, 36] explain the details of sources of noise in radiometric systems. Both number of emitted photons in a given time interval (Eq 2.1-14), and the probability of excitation of electrons by these photons, obey Poisson statistics. The variance in the number of excited charge carriers ( $\sigma_{N_{e^-}}$ ) is a Poisson distribution. This combination of these two variations in the signal with time is termed *shot noise*.

$$\sigma_{N_{e^-}} = \sqrt{N_{e^-}} \quad Eq\ 2.3-2$$

The measurement also has components of noise which are not related to the signal level. These originate from such processes as:

- Instrument background noise
- Variation in dark current
- Amplifier noise
- Electrical noise

These components of the total noise often vary with the temperature of the instrument. Shot noise often dominates modern small-pixel Si cameras, where the number of electrons excited in each exposure is relatively small. Noise limits the minimum detectable radiance, and therefore temperature. Noise also forms a significant component of the uncertainty in measured temperature for transient systems, where temporal averaging cannot be implemented.

### 2.3.4 Exposure and rolling shutter

Each pixel in the *FPA* is exposed for a finite time determined by the exposure time ( $\Delta t$ ). It is usually considered that the exposure constitutes a ‘top hat’ function in time, see Figure 2.3-4. This assumption requires that the response time of the detector-amplifier circuit is small compared with the exposure time. If this assumption is not valid then the signal recorded in an exposure may be affected by the history of  $\Phi(t)$  incident on the pixel, this is a more significant problem when working with microbolometer arrays [37, 38]. With careful design of the electronics the response time of small area Si photodiodes can be as low as nanoseconds [39]. The mobility of the charge carriers, and the size of the sensitive area, limit the response time of a photodiode. The amount of amplification required for transmission of the signal also affects the response time. The small pixel sizes required for FPAs, the good mobility of charge carriers in Si, and the chip integrated amplification of CMOS, all contribute to the rapid response time of Si CMOS FPAs, making response time unlikely to be an issue in anything but the most rapid imaging systems.

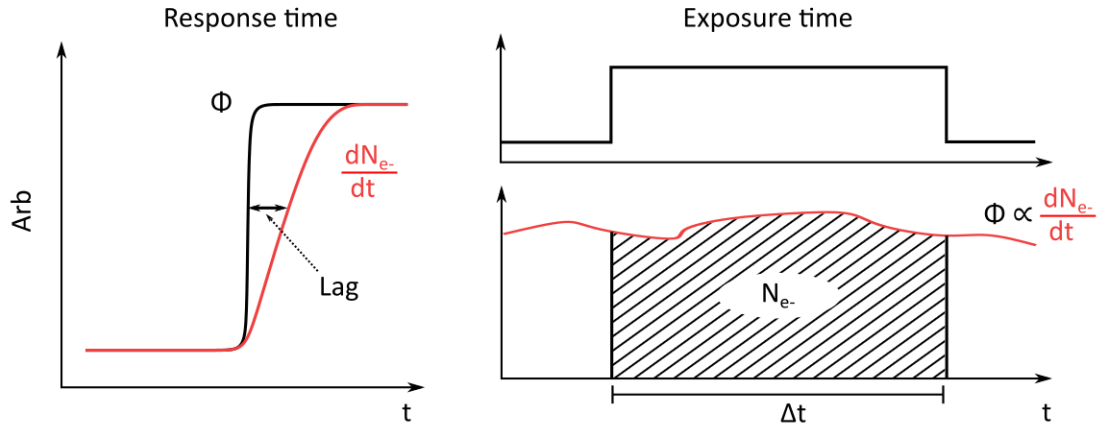


Figure 2.3-4 The Response time of the detector determines how well the detector signal ( $dN_{e^-}/dt$ ) keeps up with changes in the incident flux ( $\Phi$ ). The response time of a Si FPA is expected to be short compared with the lowest possible exposure time. The signal recorded in the digital image is proportional to the integral of the detector signal over the exposure time ( $\Delta t$ ).

If the scene is changing considerably during the exposure, then the image will be subject to motion blur. A fast-moving hot spot will appear as a path in the image. The intensity of the path will be reduced from the stationary case, because the photons emitted over the exposure time are distributed across the pixels in the path. A region which is heating or cooling rapidly compared to  $\Delta t$ , will produce an image which is the radiance (not  $T$ ) weighted average of the scene.

The signal ( $S$ ) reported by a camera is proportional to the incident radiant flux. From Eq 2.2-3 the rate of incident photons of a given energy is equivalent to the spectral radiant flux. If it is assumed that the radiant flux varies within a single exposure, then the signal given by the camera is:

$$S \propto N_{e^-} \propto \int_0^{\infty} \int_0^{\Delta t} \Phi_{\lambda}(t) \cdot dt \cdot d\lambda = \int_0^{\infty} E_{\gamma} \cdot \int_0^{\Delta t} \left. \frac{\partial N_{\gamma}}{\partial t} \right|_t \cdot dt \cdot d\lambda \quad \text{Eq 2.3-3}$$

If the scene is changing significantly within one exposure time of the sensor, then the image cannot be considered temporally resolved. A model for the variation must be employed.

The inherent architecture of *CMOS* sensors results in the digitisation of the signal usually being implemented sequentially in one dimension of the *FPA*. This leads to an image distortion effect known as the *rolling shutter*. For an image captured with a rolling shutter, the exposure for the pixels is not simultaneous across the sensor, see Figure 2.3-5.

Motion blur and the effect of the rolling shutter become important for rapidly changing scenes. The definition of rapid in terms of movement is a small number of pixels per exposure time. Ideally objects in the scene would move by less than one scnel (see section 2.1.3.1) within one exposure. The speed of the rolling shutter is characterised by the *line readout time* which can be of the order of  $10 \mu\text{s}$ . The rolling shutter will create a geometric distortion for moving objects but should not affect the radiance levels measured.

For the Orca-flash 4.0, the minimum exposure time is limited by the time it takes to digitise all the rows of the image. This allows higher frame rate acquisition when the vertical size of the image is restricted.

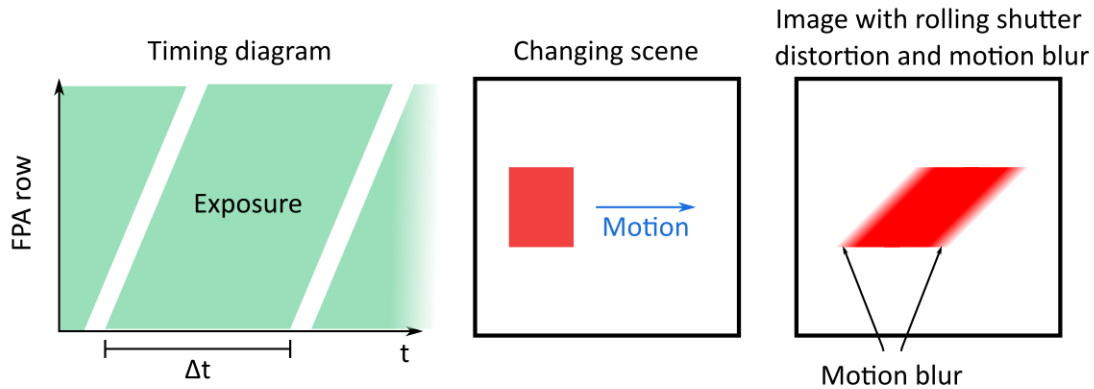


**Figure 2.3-5** Illustration of how the image of a moving scene will be affected by a rolling shutter and finite exposure time. The red square is moving to the right. At the leading and trailing edge, the effect of motion blur can be observed. The skewing of the image is a consequence of the rolling shutter. The exposure for the top of the square happens later than at the bottom, as per the timing diagram.

For Infrared Radiation Thermometers (*IRT*s) which use a single pixel detector, the device from the sensor to the readout can be conceptually considered as a radiant flux sensor. The signal reported is related to the incident power on the detector, with some averaging inherent in the electronics of the system. Due to the discrete exposure times of *FPA* cameras with quantum sensors, it can be more convenient to conceptualise the camera as an energy measuring device, rather than an average power measuring device.

### 2.3.5 Sampling and Fourier analysis

The data in modern measurement science is nearly always discretised in some way. Reality is usually considered to be a continuum, which is sampled by instruments at some defined rate or interval. The topic of sampling theory is laid out in most electronics text books on signals or digital signal processing, such as *'Applied Digital Signal Processing'* by Manolakis (2002)[40]. The main driving force for the development of sampling theory is time based communications systems [41], where the best possible fidelity of signal reproduction is key to the rate of information transfer achievable. Sampling theory can be applied to any situation where a continuum is sampled by a discrete operation.

In thermography, the framework of sampling theory can be used to help understanding of both the spatial, and temporal aspects of data acquisition. The temporal sampling is determined by the exposure time of the camera and its frame rate. Spatial sampling is defined by the optics and the spatial dimensions of the *FPA*.

#### 2.3.5.1 Fourier transforms

An important concept in sampling is to consider the scene in terms of its frequency components. A continuous function ( $f(x)$ ) can be represented in reciprocal space ( $\omega_x$ ) by its Fourier transform ( $\mathcal{F}$ ).

*Fourier Transform:*

$$1d \quad \hat{f}(\omega_x) = \mathcal{F}(f(x)) = \int_{-\infty}^{\infty} f(x)e^{-ix\omega_x} dx \quad Eq\ 2.3-4$$

$$2d \quad \hat{f}(\omega_x, \omega_y) = \mathcal{F}(f(x, y)) = \int_{-\infty}^{\infty} \int_{-\infty}^{\infty} f(x, y)e^{-ix\omega_x} \cdot e^{-iy\omega_y} dx \cdot dy \quad Eq\ 2.3-5$$

Where  $x$  and  $y$  can be any dimensions. For thermographic applications, only up to 2d space and 1d time are usually considered. There are a series of constraints on the validity of Fourier analysis [42], but we can usually consider that anything we can measure with an instrument will conform to these constraints. The inverse Fourier transform  $\mathcal{F}^{-1}$  is used to transform from reciprocal space back into real space.

*Inverse Fourier Transform:*

$$1d \quad f(x) = \mathcal{F}^{-1}(\hat{f}(\omega_x)) = \frac{1}{2\pi} \int_{-\infty}^{\infty} \hat{f}(\omega_x) e^{ix\omega_x} d\omega_x \quad Eq 2.3-6$$

$$2d \quad f(x, y) = \mathcal{F}^{-1}(\hat{f}(\omega_x, \omega_y)) \\ = \frac{1}{(2\pi)^2} \int_{-\infty}^{\infty} \int_{-\infty}^{\infty} \hat{f}(\omega_x, \omega_y) e^{ix\omega_x} \cdot e^{iy\omega_y} \cdot d\omega_x \quad Eq 2.3-7$$

The functions in Eq 2.3-4 to Eq 2.3-7 are of continuous variables. The same kind of operations can be applied to discrete data. The discrete Fourier transform is a digital operation, which can be applied to discretely sampled data to convert it into reciprocal space. The Fast Fourier Transform (*FFT*) is the most widely used digital operation of this class.

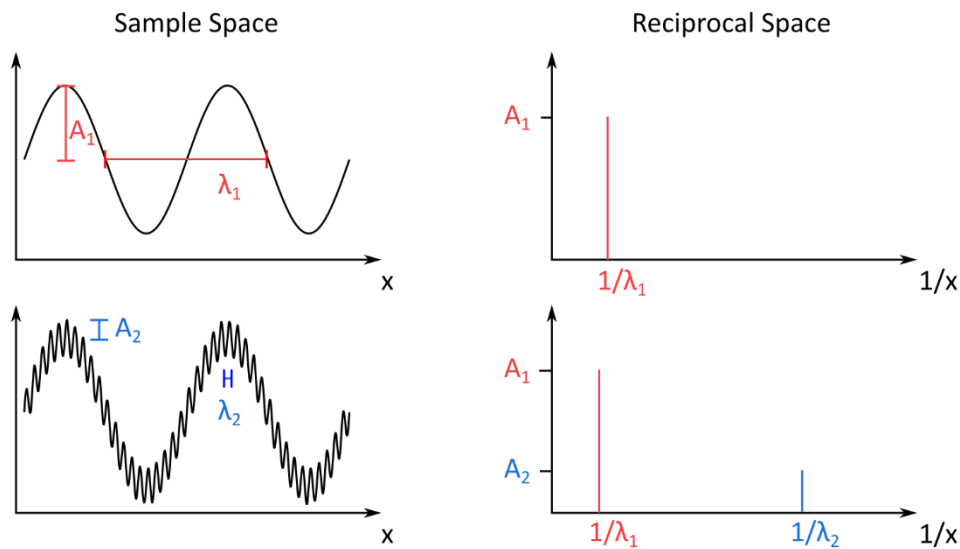


Figure 2.3-6. The magnitude of the Fourier transform of a true sine wave is a Dirac delta  $\delta$  at the frequency of the sine wave.

The FFT is an efficient programmatic implementation of the equations:

*FFT:*

$$1d \quad \hat{S}(p) = \sum_{m=0}^{m=M-1} S(m) e^{-i2\pi m/M} \quad Eq 2.3-8$$

$$2d \quad \hat{S}(p, q) = \sum_{m=0}^{M-1} \sum_{n=0}^{N-1} S(m, n) e^{-i2\pi m/M} \cdot e^{-i2\pi n/N} \quad Eq 2.3-9$$

Where:  $m$  &  $n$  are the coordinates of the discretely sampled data in the sampling domain (pixels or frames);  $p$  &  $q$  are the coordinates in reciprocal space (pixels<sup>-1</sup> or frames<sup>-1</sup>); and  $M$  &  $N$  are the total number of discrete data points in the original sample. The inverse *FFT* (*iFFT*) is used to convert from reciprocal coordinates back into the original sampling domain.

iFFT:

$$1d \quad S(m) = \frac{1}{M} \sum_{p=0}^{M-1} \hat{S}(p) e^{i2\pi p/M} \quad \text{Eq 2.3-10}$$

$$2d \quad S(m, n) = \frac{1}{MN} \sum_{p=0}^{M-1} \sum_{q=0}^{N-1} \hat{S}(p, q) e^{i2\pi p/M} \cdot e^{-i2\pi q/N} \quad \text{Eq 2.3-11}$$

The  $p$  &  $q$  coordinates in reciprocal space depend on the exact form of the *FFT* used. The most common form is when zero frequency is the first data point ( $\hat{S}(0)$ ). The  $m$  &  $n$  coordinates of a data set are mirrored around its central value. Assuming that the sample frequency is  $F_s$ , then the central value of the FFT will be at  $F_s/2$  (the Nyquist frequency). The spacing between frequency points on the  $m$  axis is  $F_s/M$ , and similarly on the  $n$  axis it is  $F_s/N$ . The *FFT* of a function is normally the same length as the original function, unless zero padding is applied. If zero padding is applied, then  $M$  &  $N$  must be adjusted to include the number of padding values.

### 2.3.5.2 Nyquist frequency

The Nyquist frequency is strictly 'The maximum frequency component present in a bandwidth limited signal'. The Nyquist frequency is often also used to describe the maximum frequency which can be measured by a system. It is half the sampling frequency ( $F_s$ ) of the system.

$$\text{Nyquist frequency} = F_s/2 \quad \text{Eq 2.3-12}$$

In real world measurement situations in thermography, it is not possible to restrict the frequencies present in the scene, either temporally or spatially. Some frequency components of the scene are always likely to exist above the Nyquist frequency of the system. The frequency components above the Nyquist frequency will be folded back below the limit. Some features such as sharp edges have multiple frequency components stretching to high frequencies, which may be truncated by the Nyquist frequency causing *ringing*.

Noise, either from the scene (see section 2.3.3), or inherent to the instrument [43], will be present in any measured data. Different sources of noise have different frequency dependencies. White noise (equal power at all frequencies) is unavoidable, clever instrument design often means it is small compared to the signal to be measured. There is a prevalence of noise in most measurement (and natural) systems which usually decays in power proportional to  $1/\text{frequency}$  [43]. It is normally referred to as  $1/f$  noise. Noise can be reduced at high, or specific frequencies by filtering [44].

It is not usually the case that the instrument will reproduce the scene with perfect fidelity all the way up to the Nyquist frequency. The characterisation of this fidelity is known as the *transfer function* ( $T_F$ ) of the instrument.

### 2.3.5.3 Transfer functions

Instruments, such as thermographic instruments, are used to take measurements of properties of the real world. The ideal measurement is a perfect representation of the true situation. A real measurement is an interpretation of this situation passed through the prism of the instrument. In addition to the problems of under sampling discussed in section 2.3.5.2, the instrument will also modify the true scene (spatial and temporal) and report this modified version. Using the vocabulary of signal processing, 'the modifications that the system (instrument) makes to the input (scene) are specified by the *transfer function* ( $T_F$ ) of the system'.

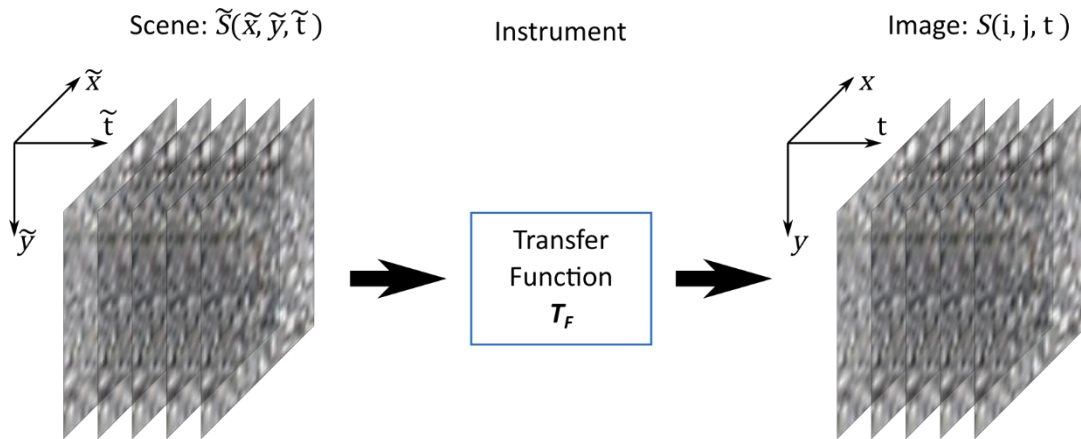


Figure 2.3-7 The thermographic instrument can be considered a single system which operates on the scene to produce the image.

The transfer function is, in its most general sense, an *operator* ( $T_F$ ), which acts upon the input to produce an output. Based on the assumption that the transfer function contains only linear invariant operations, and using well documented digital signal processing tools [45], the 1d temporal tools provided in [45] can be expanded to incorporate the 2d spatial components of the transfer function.

Linearity means that the effect of all parts of the  $T_F$  operation superimpose rather than having interdependence. Linearity implies that doubling the magnitude of one part of the scene will double its total contribution to the image. Invariance requires that a signal originating at one space and time is modified in an identical way to any other. Invariance is trickier to assume in the spatial aspect, as it imposes the condition that the optics reproduce the scene with identical fidelity over the whole FPA sensor. Strictly, this is rarely true in real optical systems.

The assumption of linear invariance allows some mathematical statements about the actions of the transfer function on the scene. In sample space  $(x, y, t)$  the image is a convolution (symbolised by  $*$ ) of the impulse response function ( $T_F$ ) with the scene. In frequency space  $(F_x, F_y, F_t)$ , this is a multiplication of the Fourier transform of the impulse response function ( $\hat{T}_F$ ) with the Fourier transform of the scene ( $\hat{S}$ ). This operation is looked at in more detail in section 2.4.1.

General case: 
$$S = T_F(\hat{S}) \quad \text{Eq 2.3-13}$$

Linear invariant, sample space: 
$$S = T_F * \hat{S} \quad \text{Eq 2.3-14}$$

Linear invariant, frequency space: 
$$S = \mathcal{F}^{-1}(\hat{T}_F \cdot \hat{S}) \quad \text{Eq 2.3-15}$$

### 2.3.6 Data handling

Due to the highly nonlinear response of radiance (and therefore signal) to temperature (see section 2.2), a large *bit depth* is required for thermography over any significant range of temperatures in the NIR. Bit depth is the total number of discrete Digital Levels (DL) that the *ADC* in the camera can measure. A 16 bit *ADC* can measure  $2^{16}$  distinct incident radiant flux magnitudes. Figure 2.3-8 illustrates the expected range of temperatures for an 8, 12 & 16 bit camera operating with the surface and spectral characteristics of the instrument simulated in section 2.2.5.

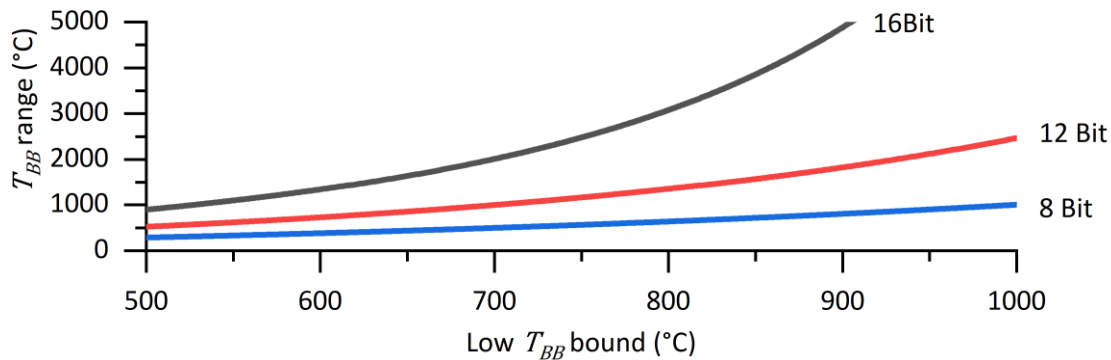


Figure 2.3-8 The range of measurable temperatures for some common bit depths. The lowest temperature (*x*-Axis) is assumed to be one count (1 DL). This measure of the range of temperatures does not take into account noise considerations which affect minimum detectable temperature. A well-designed system will have a noise which is on the same order as 1 DL, so as not to waste range on the noise.

A single 2048 by 2048 pixel, 16-bit image occupies a minimum of 8 Mb of digital space.

$$\text{Image size(Mb)} = \frac{\text{number of pixels}(2048 \times 2048) \times \text{number of bits}(16)}{\text{bits / byte}(8) \times \text{bytes / Kb}(1024) \times \text{Kb/Mb}(1024)} = 8 \text{ Mb} \quad \text{Eq 2.3-16}$$

The maximum frame rate of the Orca-flash 4.0 is 100 fps at full frame size (2048 by 2048 pixels). This will generate data at a rate of  $800 \text{ Mb s}^{-1}$ . A high rate of data generation causes problems in both transmission and storage of acquired data. A typical modern Solid State Drive (SSD) sustained write speed is around  $500 \text{ Mb s}^{-1}$  [46], therefore continuous streaming at this rate requires a special arrangement. The highest speed digital Si CMOS cameras save the data locally to the camera, on a specially designed high speed solid state storage system [47]. The locally stored data is then streamed to a PC or other system for analysis and permanent storage. This methodology means that only finite bursts of data can be gathered.

The Orca-Flash 4.0 camera has two distinct parts of the sensor, each of which digitise and stream data independently. The data is transmitted via a pair of high speed *camera link* cables to a two port PCIe *frame grabber* [48] card in a PC. The Data at the PCIe port can be either buffered in the RAM of the PC or streamed directly to a hard drive. If the RAM option is used, then only finite bursts are possible. Large amounts of RAM in the PC allow for extended bursts. To allow continuous streaming to a hard drive the frame rate or frame size must be reduced below the maximum of the camera. Or alternatively a specialised distributed writing system must be employed.

## 2.4 IMAGING AND IMAGE PROCESSING

In this section the basic concept of image quality and the language of image quality metrics will be described. The basis for some image processing techniques which will be used in this thesis will also be provided. For a solid introduction to all aspects of imaging with light, 'Optics' by Hecht (2002)[9] is a good reference. For the fundamentals of digital image processing there are several editions of a work by Gonzalez which provide a solid foundation. 'Digital Image Processing using Matlab' 2<sup>nd</sup> Edition by Gonzalez (2009)[49] was used in this work.

The geometric optics models presented in section 2.1.3 provide useful approximations. However, when making quantitative radiometric measurements, deviations from these idealised conditions are important. The optics of the thermographic instrument usually provide the main source of perturbation (blurring) in the spatial components of the transfer function ( $T_F$ ). The camera itself will further transform to the image projected by the optics. Assuming the optical ( $\hat{T}_{F_{optics}}$ ) and the camera ( $\hat{T}_{F_{camera}}$ ) spatial transfer functions have linear invariance, the transforms can be treated as a single system or be characterised individually and multiplied together (in reciprocal space).

$$\hat{T}_F = \hat{T}_{F_{optics}} \cdot \hat{T}_{F_{camera}} \quad \text{Eq 2.4-1}$$

The theory of optical transfer functions is well developed, and the fidelity of thermal imaging systems is often described in these terms. The spatial component of the transfer function of the instrument will therefore be described in terms of their optical transfer equivalents. The arguments made for the fidelity of the optical system can be readily expanded to include the camera transfer function. Without specialised optical characterisation tools, the individual transfer function of the optics cannot be accessed, only the entire transfer function of the system can be readily measured.

### 2.4.1 Optical transfer functions

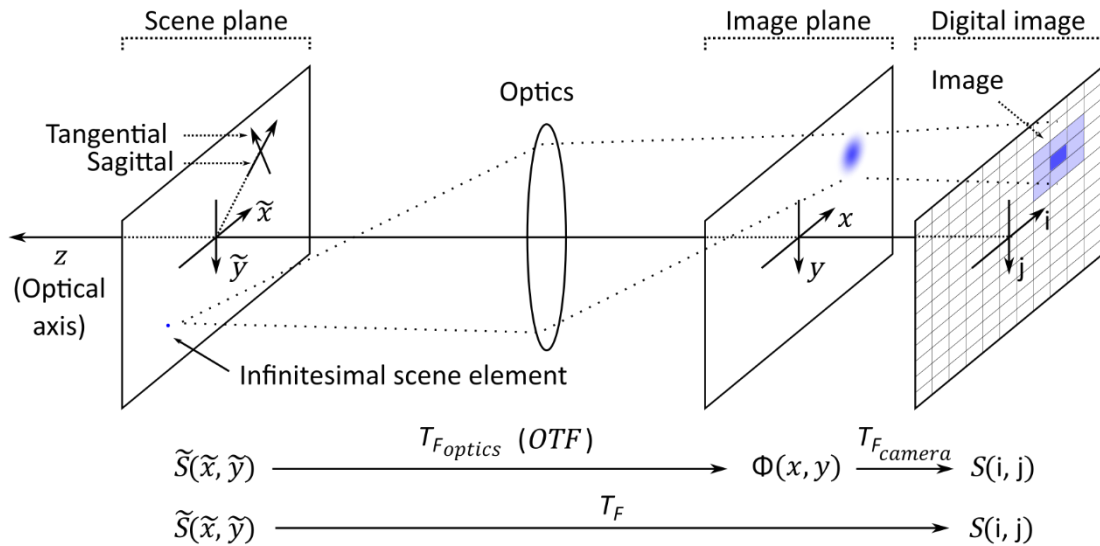


Figure 2.4-1 The Transfer Function ( $T_F$ ) operates on the scene to convert it into the image. The Optical Transfer Function (OTF) is the main component of  $T_F$ . The vocabulary of optical transfer is often used in literature to describe the whole instrument spatial transfer function.

The Optical Transfer Function ( $OTF \equiv \hat{T}_{F_{optics}}$ ) is the mathematical transform which can be applied to a scene to provide the spatial coordinates of the components of the scene in the image [50]. It is worth noting that the relation between the two coordinate systems is not unitary. A single infinitesimal element of the scene ( $\tilde{S}(\tilde{x}, \tilde{y})$ ) can be spread across multiple coordinates in the image.

The total energy from the point source will be conserved, unless it is transformed out of the image bounds (*FPA*). Standard diffraction-based lens systems are rotationally symmetric, the axis of rotation is termed the optical axis. In this thesis the convention that the optical axis points from the sensor toward the scene will be used.

In spatial coordinates, the Point Spread Function ( $PSF \equiv T_{F_{optics}}$ ) transforms an infinitesimal element of the scene ( $\tilde{S}(\tilde{x}, \tilde{y})$ ) into its image in the image plane [50]. The *PSF* is, in general, dependent upon the position of the originating element ( $\tilde{x}$  &  $\tilde{y}$ ).

$$\Phi(x, y) = \iint PSF(x, y; \tilde{x}, \tilde{y}) \cdot \tilde{S}(\tilde{x}, \tilde{y}) \cdot d\tilde{x} \cdot d\tilde{y} \quad Eq\ 2.4-2$$

Over a limited range of  $\tilde{x}$  &  $\tilde{y}$  values, the *PSF* can be considered spatially invariant. The integral then becomes:

$$\Phi(x, y) = \iint PSF(x - \tilde{x}, y - \tilde{y}) \cdot \tilde{S}(\tilde{x}, \tilde{y}) \cdot d\tilde{x} \cdot d\tilde{y} \quad Eq\ 2.4-3$$

The integral in this form, can be expressed as a convolution (\*) of the *PSF* with the scene [51]:

$$\Phi(x, y) = PSF * \tilde{S} \quad Eq\ 2.4-4$$

Convolution will be explored in a little more detail in section 2.4.4.2. The Fourier transform of the *PSF* is the *OTF*:

$$OTF(F_x, F_y; \tilde{x}, \tilde{y}) = \mathcal{F}(PSF(x, y; \tilde{x}, \tilde{y})) \quad Eq\ 2.4-5$$

The complex function  $OTF(F_x, F_y; \tilde{x}, \tilde{y})$ , can be expressed as either real and imaginary components, or as a magnitude and phase. In magnitude and phase representation the  $OTF(F_x, F_y; \tilde{x}, \tilde{y})$  is:

$$OTF(F_x, F_y; \tilde{x}, \tilde{y}) = MTF(F_x, F_y; \tilde{x}, \tilde{y}) e^{iPTF(F_x, F_y; \tilde{x}, \tilde{y})} \quad Eq\ 2.4-6$$

Where *MTF* is the Modulation Transfer Function, and *PTF* is the Phase Transfer Function. Alternatively, the *MTF* is the magnitude of the Fourier Transform of the one-dimensional projection of the *PSF*, thus:

$$MTF(F_x; \tilde{x}) = |OTF(F_x; \tilde{x})| = \left| \mathcal{F} \left( \int PSF(x, y; \tilde{x}, \tilde{y}) \cdot dy \right) \right| \quad Eq\ 2.4-7$$

The *MTF* is a metric commonly used to specify the performance of optical systems. *MTF* is usually quoted in tangential and sagittal frequency components as opposed to  $x$  &  $y$  (see Figure 2.4-1). *MTF* is sometimes used to describe the magnitude of the transfer function of any harmonic scene, such as a bar target. The *magnitude* or *contrast* of a modulation is measured [50] as:

$$Modulation = \frac{S_{max} - S_{min}}{S_{max} + S_{min}} \quad Eq\ 2.4-8$$

Where  $S_{max}$  is the maximum measured signal and  $S_{min}$  is the minimum measured signal, assuming dark corrections have been made (see section 2.3.2).

#### 2.4.2 Measurement field of view

The measurement field of view (*MFOV*) is the area of uniform radiance required for a single pixel to make an accurate measure of radiance. The *MFOV* is, in general, larger than the *IFOV* (unless the sensitive area of the pixel is only a small fraction of the distance between pixels). The *MFOV* of a pixel can be calculated by starting with the convolution of the area of the pixel with the *PSF*.

$$f_{weight}(x, y) = A_{FS} * PSF \quad \text{Eq 2.4-9}$$

$f_{weight}(x, y)$  is the weighting function for radiance around the projection of the centre point of the pixel. If the *IFOV* is small compared to the *MFOV* and the *PSF* is rotationally symmetric then  $S_{weight}$  can be assumed to be a rotationally symmetric function centred on the pixel centre. The radius of the *MFOV* ( $r_{MFOV}$ ) is then given by:

$$EE = \frac{\int_0^{r_{MFOV}} f_{weight}(r) \cdot dr}{\int_0^{\infty} f_{weight}(r) \cdot dr} \quad \text{Eq 2.4-10}$$

Where: *EE* is the fractional enclosed energy. This is a constraint on the performance of the instrument. The higher the fraction, the less the signal can be affected by radiance from outside the *MFOV*, for industrial *IRT*s this is usually fixed at 0.95 or 0.99. This method of calculating the *MFOV* will be termed the *pixel convolution* method.

An alternative way to calculate the *MFOV* is to convolve the *PSF* with a uniform radiance circle and average the convolved image over the area of a pixel. This is the equivalent of simulating the aperture measurements described in section 2.4.3.4, without the inclusion of the scatter effects present in a real system. This method is termed the *aperture simulation* method. These two methods of *MFOV* determination are implemented in chapter 6.

#### 2.4.3 Targets

Characterisation of the spatial aspects of the instrument transfer function requires showing the instrument a known scene, then observing how the instrument reports that scene as an image. It is difficult to manufacture scenes with a continuum of transmission characteristics in a broad spectral band, therefore binary targets are much more common. Figure 2.4-2 shows some commonly used binary targets. The targets can either be transmission or reflection, for the purposes of thermography transmission targets are more useful. Transmission targets can be placed in front of a blackbody radiator, meaning the *high radiance* sections of the target will emit a well characterised spectral distribution. Ideally the *low radiance* sections would have a finite transmission (or be at a different temperature), but this is not usually the case, thus targets with regions of zero and high transmission are used.

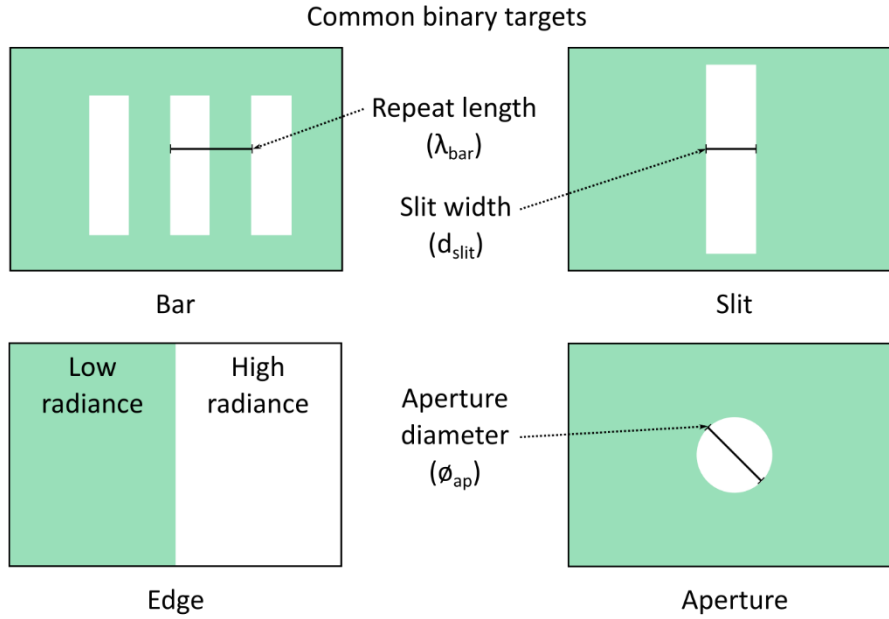


Figure 2.4-2 Binary targets used for spatial response function characterisation.

Assuming the transfer function produces the scene with perfect fidelity, the exact image ( $S_{ideal}(x, y)$ ) is known. The spatial transfer function can then be ascertained from the deviations of the measured image ( $S(x, y)$ ) from the ideal image by:

$$OTF = \frac{\hat{S}(F_x, F_y)}{\hat{S}_{ideal}(F_x, F_y)} \quad Eq\ 2.4-11$$

This is only a valid measure of the *OTF* for spatial frequencies which are present in the scene, i.e. a scene with a single sine wave component will only provide the *OTF* at that single spatial frequency.

### 2.4.3.1 Bar Target

Bar targets are commonly used in spatial characterisation of thermal imagers. The *primary* spatial frequency of a bar target is:

$$F_{bar} = \frac{1}{\lambda_{bar}} \quad Eq\ 2.4-12$$

Because of the binary nature of a bar target (and all binary targets) with sharp transitions, the scene contains frequency components above the primary frequency ( $F_{bar}$ ), see Figure 2.4-3. The frequency spectrum of a bar target contains components at odd multiples of the primary frequency. The transfer function of a bar target is often referred to as the Contrast Transfer Function *CTF* [52, 53], to distinguish it from the sinusoidal (Fourier) version of *MTF*. The *CTF* and *MTF* can easily be confused or not defined sufficiently. In this work the *MTF* will always refer to the sinusoidal amplitudes and the *CTF* will be used to refer to the transfer function of a bar target.

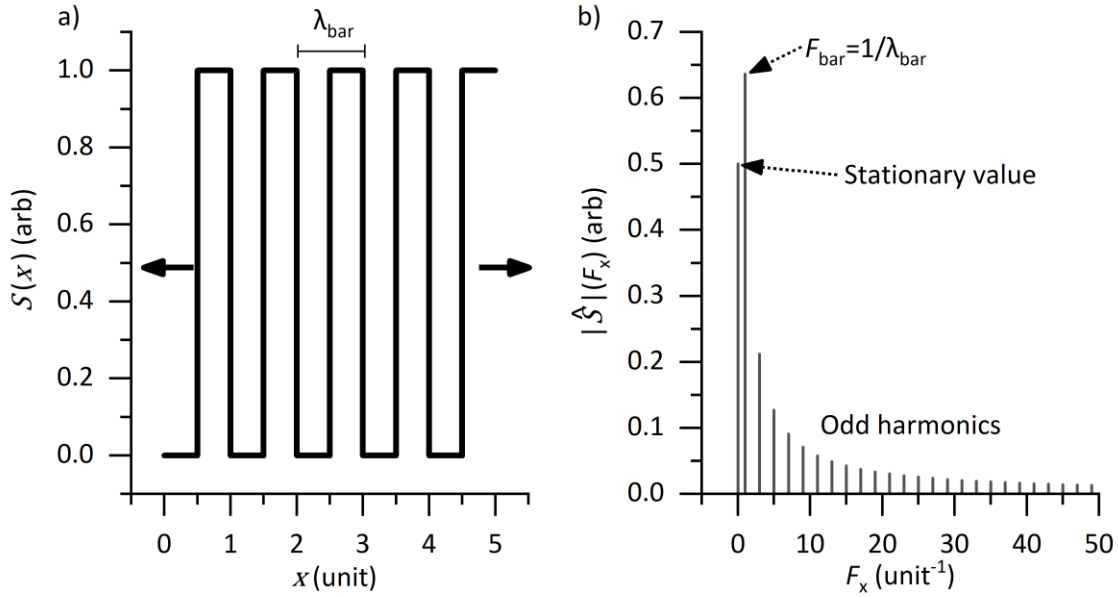


Figure 2.4-3 a) Line profile ( $S(x)$ ) of a bar target and b) Its Fourier components. The primary frequency component ( $F_{\text{bar}}$ ) has a larger amplitude than might be expected from the amplitude of the square wave, which is 0.5 (arbitrary units). The stationary (sometimes called DC (Direct Current)) value is the mean magnitude of  $S(x)$ .

#### 2.4.3.2 Slit Target

A slit target can take the form of a set of slit apertures with varying *slit widths* ( $d_{\text{slit}}$ ), or a pair of parallel adjustable knife edges. Taking a line profile ( $S(x)$ ) across the bar produces a ‘top hat’ function modified by the transfer function. As  $d_{\text{slit}}$  is reduced toward zero,  $S(x)$  becomes the Line Spread Function ( $LSF$ ).

$$\begin{aligned} \lim_{d_{\text{slit}} \rightarrow 0} S_{\text{ideal}}(x) &= \delta(x) \\ \lim_{d_{\text{slit}} \rightarrow 0} S(x) &= LSF(x) \end{aligned} \quad \text{Eq 2.4-13}$$

In the limit of  $d_{\text{slit}} \rightarrow 0$  the idealised scene becomes a Dirac delta in  $x$  ( $\delta(x)$ ). Unfortunately, as  $d_{\text{slit}} \rightarrow 0$  the amplitude of the signal measured by the detector also tends towards zero ( $S(x) \rightarrow 0$ ). The image of a  $\delta(x)$  function is the transfer function itself [42]. The  $LSF$  is the one-dimensional projection of the  $PSF$ :

$$LSF(x) = \int_{-\infty}^{\infty} PSF(x, y) \cdot dy \quad \text{Eq 2.4-14}$$

The profile across a slit is sometimes referred to as the slit response function  $SRF$  [54].

#### 2.4.3.3 Edge target

A profile perpendicular to an idealised edge is mathematically known as a Heavyside step function. The spatial derivative of the Heavyside step function is the  $\delta(x)$  function. The spatial derivative of the line profile ( $S(x)$ ) of an edge is the  $LSF$ .

$$\begin{aligned} \frac{dS_{\text{ideal}}(x)}{dx} &= \delta(x) \\ \frac{dS(x)}{dx} &= LSF(x) \end{aligned} \quad \text{Eq 2.4-15}$$

The Profile across an edge function is termed the Edge Spread Function ( $ESF$ ) [55].

### 2.4.3.4 Aperture target

Aperture targets are used extensively in *IRT* characterisation to determine the spatial performance of the instrument. As the diameter of the aperture ( $\phi_{ap}$ ) tends towards zero, the target becomes a point source in two dimensions ( $\delta(x, y)$ ). The image of the 2d point source is the *PSF*.

$$\begin{aligned} \lim_{\phi_{ap} \rightarrow 0} S_{ideal}(x, y) &= \delta(x, y) \\ \lim_{d_{slit} \rightarrow 0} S(x, y) &= PSF(x, y) \end{aligned} \quad Eq\ 2.4-16$$

The area of the aperture ( $\pi \cdot (\phi_{ap}/2)^2$ ) can be used to measure the area from which the signal arriving at a pixel originated (see section 2.4.2). Ideally 100% of the signal at a pixel would be from the *IFOV* of that pixel. This is not the case in real systems, some light is scattered into the pixel from surrounding scenes and some light which originated from inside the *IFOV* is scattered out to the surrounding pixels. Figure 2.4-4 shows how the peak radiant flux ( $\Phi_{max}$ ) and corresponding signal ( $S_{max}$ ) can vary with  $\phi_{ap}$  for a hypothetical system. The signal reported by a pixel is the average of  $\Phi(x, y)$  over the area of the pixel, therefore the pixel value is not directly proportional to  $\Phi_{max}$  for small  $\phi_{ap}$ .

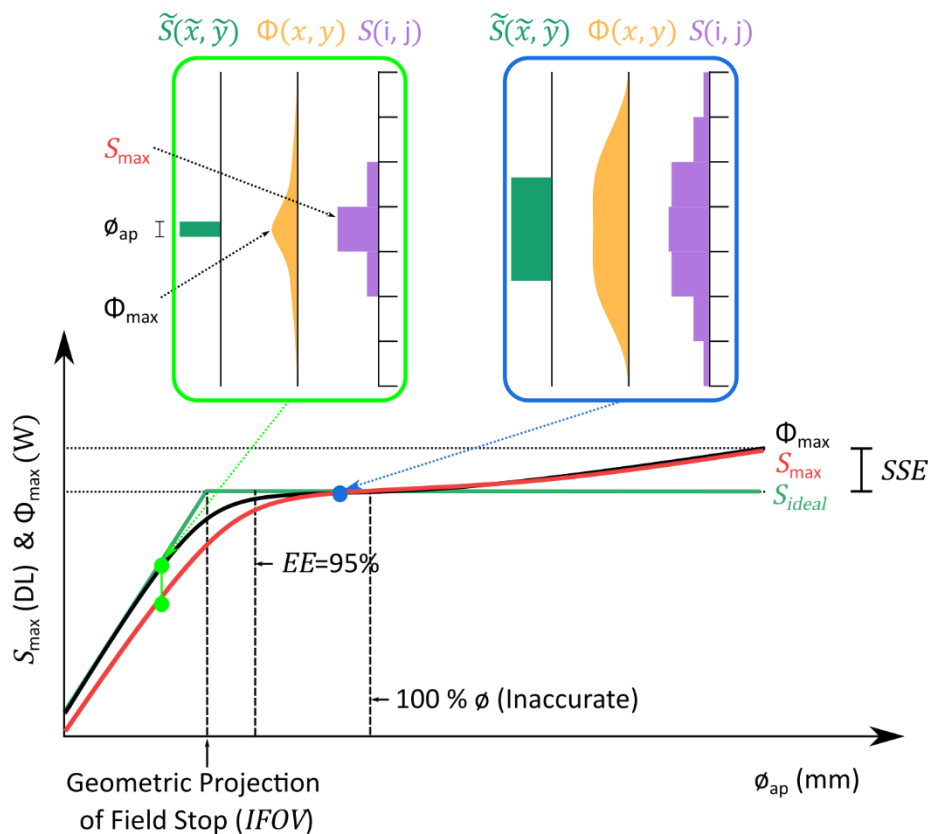


Figure 2.4-4 These arbitrary representative curves are used to illustrate the behaviour of the measured signal as a function of emitting target size. Size of Source Effect (*SSE*) is used to describe the large-area deviations from the '100 %  $\phi$ ' signal.

Looking at the '100 %  $\phi$ ' plateau in signal, the assertion can be made that only energy emitted from inside the area of the aperture is incident on the detector in other words the enclosed energy is unity (ignoring Size of Source Effects (*SSE*)). Below the 100 %  $\phi$  ( $EE = 1$ ) level, the pixel is collecting light (or lack of) from outside the area of the aperture. Varying apertures are used to characterise single pixel *IRT*'s [56, 57]. The 95% enclosed energy ( $EE = 0.95$ ) or the '95 %  $\phi$ ' is commonly used as the *MFOV*. The distinction between *IFOV* & *MFOV* along with *SSE* are the major, instrument related, confounding factors in thermography. The *SSE* is usually quoted as a range in terms of temperature.

### 2.4.4 Image processing

From the previous section it can now be asserted that the measurement resolution is a combination of the sampling rate of the system (Nyquist limit) and the spatial transfer function of the instrument (*OTF*). These two factors combine to limit the highest frequency components that can be resolved by the system. Ideally thermographic images would be a direct map of the scene at higher resolution than any feature sizes present, this is not often possible. Therefore, in such cases an attempt must be made to reconstruct the best estimate of the scene from the imperfect images, by applying image manipulation techniques.

#### 2.4.4.1 Geometric transforms

The ideal scene ( $\tilde{S}(\tilde{x}, \tilde{y})$ ) is a plane perpendicular to the optical axis. The image recorded by the instrument is a *projection* of the scene. The book 'Multiple View Geometry' by Hartley & Zisserman (2000)[58], provides a comprehensive mathematical basis for dealing with the various projections encountered in imaging for engineering purposes, where the true dimensions of the scene, as measured by the image, are important. The simplest image geometry to process is an *orthographic* projection perpendicular to a planar scene (see Figure 2.4-5). Normal lens systems do not project the scene onto the *FPA* in this way. A *telecentric* lens is required to create a direct orthographic image on the *FPA*. Taking the assumption of a standard lens, the image on the image plane can be modelled as the projection emanating from a point  $\mathbf{P}_{sc}$ , which is the centre of the lens.

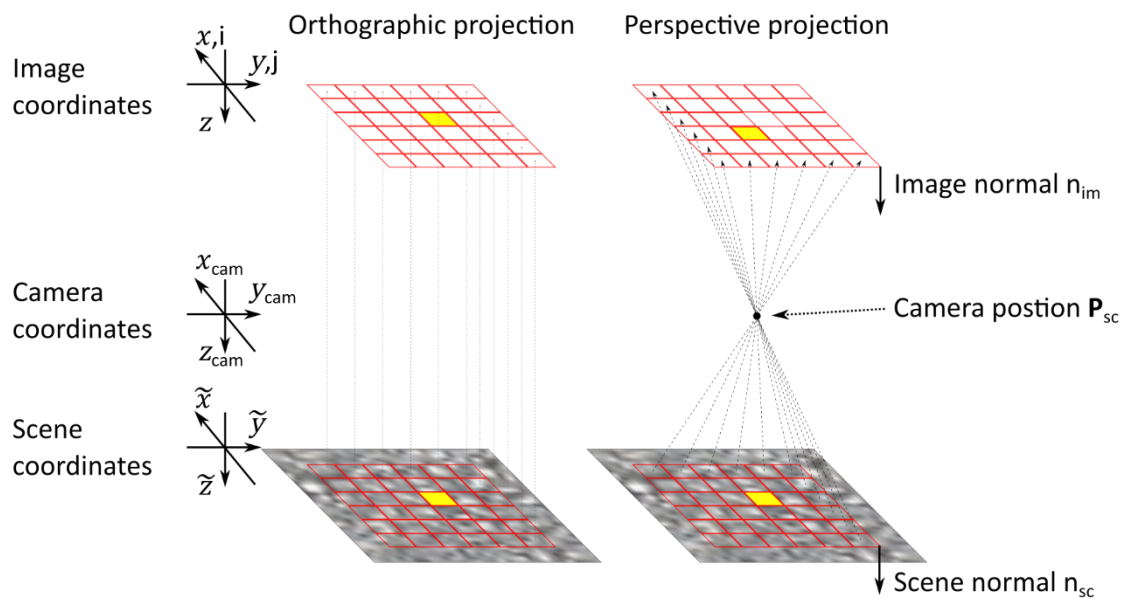


Figure 2.4-5 The image acquired by a regular imaging system is a perspective projection of the scene onto the image plane. Camera position  $\mathbf{P}_{sc}$  (relative to the scene) can be conceptualised as the position of the pinhole in a pinhole camera, or the centre of the lens in geometric optics. The continuous image coordinates are  $x$  &  $y$ , which are discretised by the pixels into  $i$  &  $j$ .

The Image projected onto the *FPA* is usually mirrored in the horizontal and vertical axis by the lens. It is common for the image to be inverted inside the camera before it is transmitted. The image can then be considered as a plane between the camera position and the scene as per Figure 2.4-6. The mathematical treatment of these 3d geometries is usually implemented in matrix notation. The  $x$  &  $y$  axes are determined by the pixel row and column orientation of the camera, and the  $z$  axis is the optical axis of the thermographic instrument.

The effect of viewing angle ( $\theta$ ) and the working distance ( $r_{WD}$ ) on the image of a scene

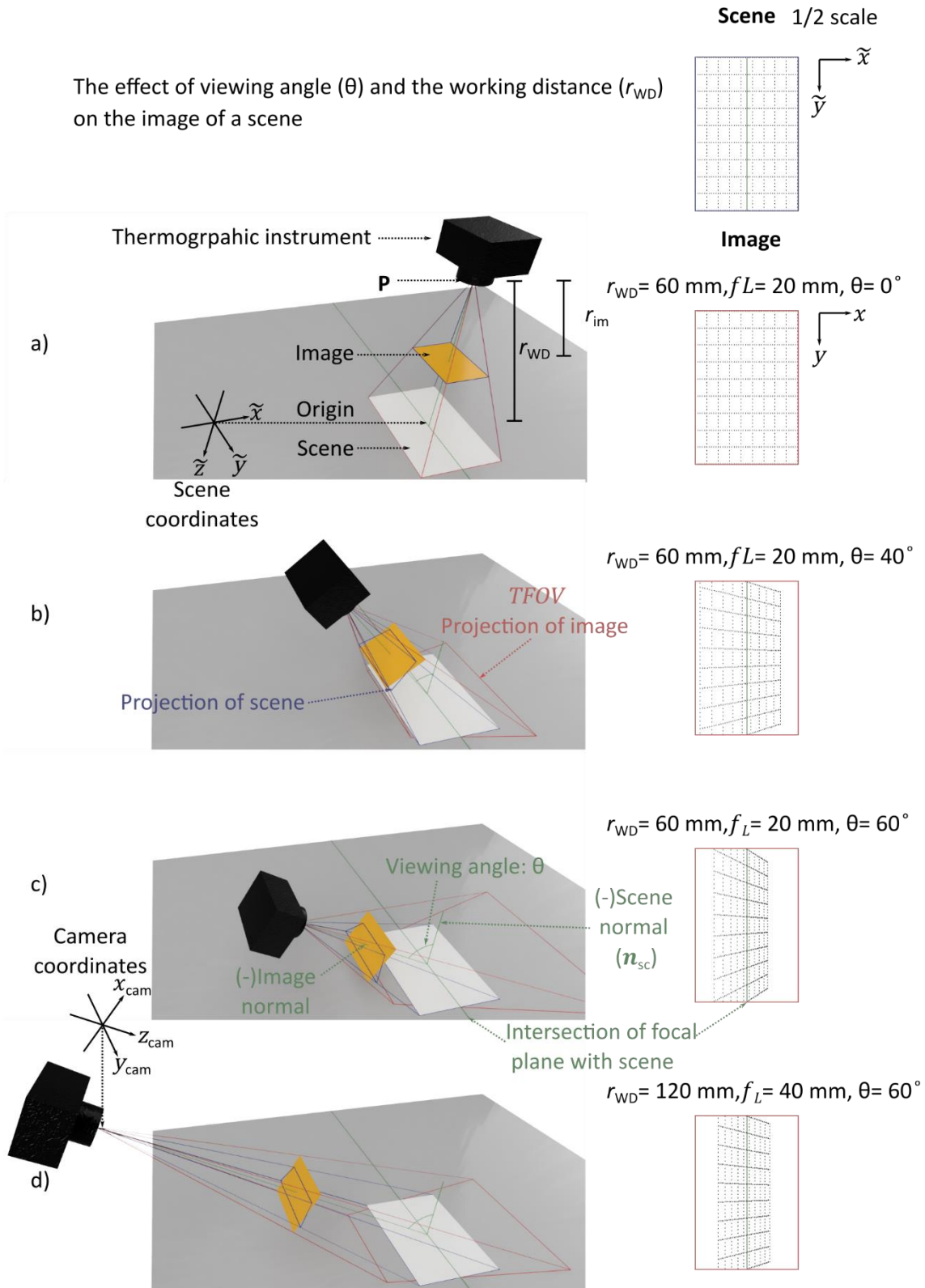


Figure 2.4-6 The image of a planar scene changes depending upon the viewing angle and separation between the camera position ( $P$ ) and the intersection of the focal plane with the scene. The scene and image normals show their negatives for visual clarity.

For an imaging system tilted to a plane, the size of the *IFOV* projected onto the plane changes across the *TFOV*, as can be observed in Figure 2.4-5. The effect of this change in projected *IFOV* is minimised by maximising the working distance ( $r_{WD}$ ) or equivalently maximising the  $f_L$ .

Geometric arguments in Cartesian space will be used to solve the problem of a single axis tilt.

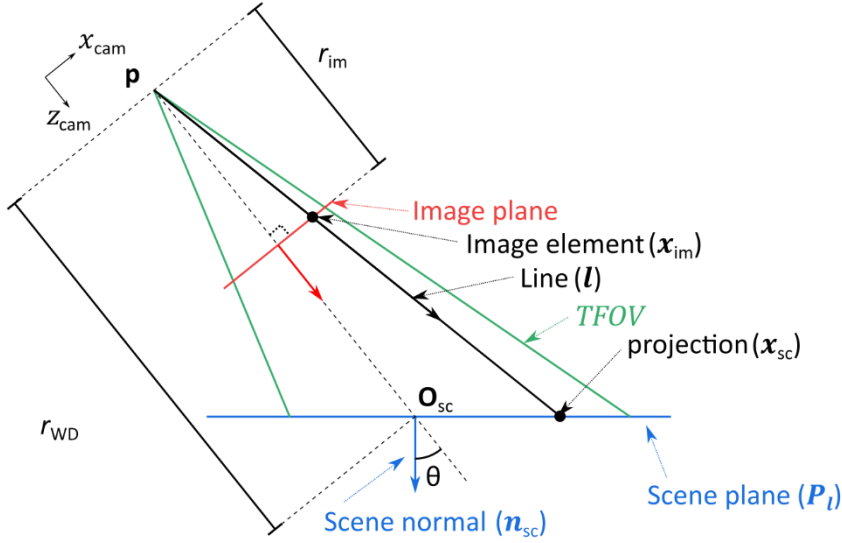


Figure 2.4-7 Projection of an image element (position in image space) onto a tilted plane.

Working in the Cartesian coordinate system of the camera ( $x_{cam}, y_{cam}, z_{cam}$ ). Any point on a line ( $l$ ) passing from the origin ( $\mathbf{P} = (0,0,0)$ ) to a position in the image plane ( $\mathbf{x}_{im} = (x, y, r_{im})$ ), can be defined by a direction vector ( $\mathbf{x}_{im}$ ), a starting position ( $\mathbf{P}$ ), and a fractional length along the vector ( $r$ ).

$$\mathbf{l} = r\mathbf{x}_{im} + \mathbf{P} = r\mathbf{x}_{im} \quad \text{Eq 2.4-17}$$

The line passing through the point in the image can be extended until it intersects with the scene plane. Any point on a plane ( $\mathbf{P}_l$ ) is described by its normal ( $\mathbf{n}_{sc} = \mathbf{R}(\theta)(0,0,1)$ ) and a point lying on the plane, the most obvious of which is the intersection of the focal plane and the scene plane ( $\mathbf{O}_{sc} = (0,0,r_{WD})$ ).

$$(\mathbf{P}_l - \mathbf{O}_{sc}) \cdot \mathbf{n}_{sc} = 0 \quad \text{Eq 2.4-18}$$

Equating the point in the line with the point in the plane, Eq 2.4-17 can be inserted into Eq 2.4-18, and rearranged for  $r$  to get:

$$\begin{aligned} (r\mathbf{x}_{im} - \mathbf{O}_{sc}) \cdot \mathbf{n}_{sc} &= 0 \\ r &= \frac{\mathbf{O}_{sc} \cdot \mathbf{n}_{sc}}{\mathbf{x}_{im} \cdot \mathbf{n}_{sc}} \end{aligned} \quad \text{Eq 2.4-19}$$

Substituting Eq 2.4-19 into Eq 2.4-17, the projection of the image point onto the scene plane ( $\mathbf{x}_{cam}$ ) (still in camera coordinates) is:

$$\begin{aligned} (r\mathbf{x}_{im} - \mathbf{O}_{sc}) \cdot \mathbf{n}_{sc} &= 0 \\ \mathbf{x}_{cam} &= \mathbf{x}_{im} \left( \frac{\mathbf{O}_{sc} \cdot \mathbf{n}_{sc}}{\mathbf{x}_{im} \cdot \mathbf{n}_{sc}} \right) \end{aligned} \quad \text{Eq 2.4-20}$$

Assuming a rotation around the  $\tilde{y}$  axis only this equation can be expanded to:

$$\mathbf{x}_{\text{cam}} = \left( \begin{array}{c} \begin{bmatrix} 0 \\ 0 \\ r_{\text{WD}} \end{bmatrix} \cdot \begin{bmatrix} \cos(\theta) & 0 & \sin(\theta) \\ 0 & 1 & 0 \\ -\sin(\theta) & 0 & \cos(\theta) \end{bmatrix} \begin{bmatrix} 0 \\ 0 \\ 1 \end{bmatrix} \\ \begin{bmatrix} x \\ y \\ r_{\text{im}} \end{bmatrix} \cdot \begin{bmatrix} \cos(\theta) & 0 & \sin(\theta) \\ 0 & 1 & 0 \\ -\sin(\theta) & 0 & \cos(\theta) \end{bmatrix} \begin{bmatrix} 0 \\ 0 \\ 1 \end{bmatrix} \end{array} \right) \begin{bmatrix} x \\ y \\ r_{\text{im}} \end{bmatrix} \quad \text{Eq 2.4-21}$$

The last step is to convert the point in the scene plane from camera coordinates to scene coordinates.

$$\mathbf{x}_{\text{sc}} = \mathbf{R}(-\theta)(\mathbf{x}_{\text{cam}} - \mathbf{O}_{\text{sc}})$$

$$\begin{bmatrix} \tilde{x} \\ \tilde{y} \\ \tilde{z} \end{bmatrix} = \begin{bmatrix} \cos(\theta) & 0 & -\sin(\theta) \\ 0 & 1 & 0 \\ \sin(\theta) & 0 & \cos(\theta) \end{bmatrix} \left( \begin{bmatrix} x_{\text{cam}} \\ y_{\text{cam}} \\ z_{\text{cam}} \end{bmatrix} - \begin{bmatrix} 0 \\ 0 \\ r_{\text{WD}} \end{bmatrix} \right) \quad \text{Eq 2.4-22}$$

Figure 2.4-7, illustrates the process. This methodology allows the image of a tilted plane to be transformed into the orthographic perpendicular projection of the plane by a 3-parameter model ( $\theta$ ,  $r_{\text{WD}}$  &  $r_{\text{im}}$ ). The parameters  $r_{\text{im}}$  &  $r_{\text{WD}}$  can be determined from the focal length ( $f_L$ ) and magnification ( $M_{\text{ag}}$ ) using Eq 2.1-7 & Eq 2.1-9.

Looking at the difference in the images in Figure 2.4-6 c and Figure 2.4-6 d. The longer focal length (and therefore  $r_{\text{WD}}$ ) in Figure 2.4-6 d can be seen to reduce the change in magnification across the image in the x direction. The ratio of  $TFOV$  to working distance determines the magnitude of this distortion. In the case where the working distance is very large compared with the  $TFOV$  in the non-tilt axis ( $x$ ), the change in magnification is small. In the case of  $r_{\text{WD}} \gg TFOV$  then the geometric correction between the image and the scene is simplified to a stretch in the  $x$  dimension. The transform between a length in the image ( $\Delta x$ ) and a length in the scene ( $\Delta \tilde{x}$ ) is given by:

$$\Delta \tilde{x} = \frac{1}{M_{\text{ag}}} \cdot \frac{\Delta x}{\cos \theta} \quad \text{Eq 2.4-23}$$

Or expressing a length in the image, in units of pixels ( $\Delta i$ ), the length in spatial coordinates of the scene is approximated in the orthographic projection as:

$$\Delta \tilde{x} = IFOV \cdot \frac{\Delta i}{\cos \theta} \quad \text{Eq 2.4-24}$$

#### 2.4.4.2 Convolution and deconvolution

The convolution ( $*$ ) of two one dimensional functions,  $f(x)$  &  $g(x)$ , produces a third one-dimensional function  $\Phi(x)$ .

$$\Phi(x) = f(x) * g(x)$$

$$\Phi(x) = \int_{-\infty}^{\infty} f(x') \cdot g(x' - \xi) d\xi \quad \text{Eq 2.4-25}$$

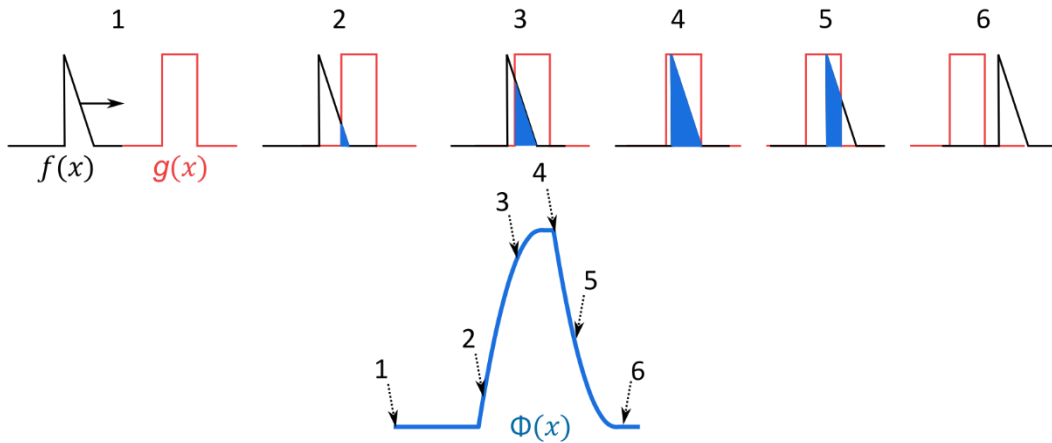


Figure 2.4-8 Convolution of  $f(x)$  with  $g(x)$  can be visualised by sliding one function past the other, and plotting the integral of the overlapping region.

The Dirac delta function  $\delta(x')$  is a mathematical construct, which has the properties of infinitesimal (zero) width in  $x$ , at a position  $x'$ , and a total integral equal to unity. The convolution of any function with  $\delta(x')$  reproduces the function itself:

$$f(x) * \delta(x - x') = f(x) \quad \text{Eq 2.4-26}$$

Conventionally when one of the functions is a (large) measurement (such as an image) and the other is the (small) impulse response of the measurement device ( $PSF$ ), the smaller function is often termed a kernel. The result of the convolution is usually cropped to be the same size as the original measurement. The same procedure can be achieved using  $FFTs$ , which requires many less calculations and therefore takes less time (or computational resources), the Fourier representation of a convolution is simply a multiplication:

$$\Phi(x) = \mathcal{F}^{-1}(\mathcal{F}(f(x)) \cdot \mathcal{F}(g(x))) \quad \text{Eq 2.4-27}$$

And the individual component  $g(x)$  can be extracted by:

$$g(x) = \mathcal{F}^{-1}\left(\frac{\mathcal{F}(f(x))}{\mathcal{F}(\Phi(x))}\right) \quad \text{Eq 2.4-28}$$

This procedure is known as deconvolution. Deconvolution is mathematically an ill posed problem, for which there is not necessarily a unique solution. This non uniqueness is exacerbated by the presence of noise in the image. Deconvolution is a field of study in itself, and there are many methods available for reconstructing the original scene from the convolved image [59, 60]. The OTF may well be zero at certain spatial frequencies. A zero in the denominator makes direct evaluation of Eq 2.4-28 impossible.

The measured image is the convolution of the scene with the transfer function of the instrument, plus a random noise element ( $\eta$ ). Including the noise term in Eq 2.4-4, the measured image becomes:

$$\Phi = PSF * \tilde{S} + \eta \quad \text{Eq 2.4-29}$$

A well-documented and utilised way to deal with the non-uniqueness problem is to introduce a *regularisation* figure of merit for the determination of  $\Phi$  from  $\tilde{S}$ . This regularisation can take many forms but is commonly a figure of smoothness, such as minimisation of the second spatial derivative.

## 2.5 REFERENCES

1. Coates, P. and D. Lowe, *The Fundamentals of Radiation Thermometers*. 2017: CRC Press, Taylor and Francis Group LLC, 6000 Broken Sound Parkway NW, Suite 300, Boca Raton, FL 33487-2742.
2. DeWitt, D.P. and G.D. Nutter, *Theory and Practice of Radiation Thermometry*. 1988: John Wiley & Sons.
3. Vollmer, M. and K.P. Mollmann, *Infrared Thermal Imaging*. 2010, Wiley-VCH Verlag GmbH & Co. KGa, Boschstr. 12, 69469 Weinheim, Germany: Wiley-VCH.
4. Gaussorgues, G., *Infrared Thermography*. Microwave Technology Series 5. 1994: Chapman & Hall, 2-6 Boundary Row, London SE1 8HN.
5. British Standards Institution, BS ISO 10878:2013, Non-destructive testing — Infrared thermography — Vocabulary, 2013
6. Siegel, R., J.R. Howell, and M.P. Mengüç, *Thermal Radiation Heat Transfer*. 5th ed. 2011: CRC Press, Taylor and Francis Group LLC, 6000 Broken Sound Parkway NW, Suite 300, Boca Raton, FL 33487-2742.
7. BIPM, *The International System of Units (SI)*, Bureau International des Poids et Mesures, Editor. 2019, STEDI Media Paris: BIPM.
8. Zemax, *Optic Studio*. 2020, Zemax LLC, NE Points Drive, Suite 500, Kirkland, Washington 98033, USA.
9. Hecht, E., *Optics*. 4th International ed. 2002: Addison Wesley, 1301 Sansome St., San Francisco, CA9411.
10. Hecht, E., *Geometrical Optics*, in *Optics*. 2002, Addison Wesley, 1301 Sansome St., San Francisco, CA9411. p. 149-242.
11. Saunders, P. and D.R. White, *A focus effect in some thermal imaging systems*. AIP Conference Proceedings, 2013. **1552**(1): p. 625-630.
12. Siegel, R., J.R. Howell, and M.P. Mengüç, *Definitions of Properties at Interfaces*, in *Thermal Radiation Heat Transfer*. 2011, CRC Press, Taylor and Francis Group LLC, 6000 Broken Sound Parkway NW, Suite 300, Boca Raton, FL 33487-2742. p. 47-85.
13. DeWitt, D.P. and J.C. Richmond, *Thermal Radiative Properties of Materials*, in *Theory and Practice of Radiation Thermometry*, D.P. Dewitt and G.D. Nutter, Editors. 1988, John Wiley & Sons. p. 91-188.
14. Wang, H., W. Zhang, and A. Dong, *Measurement and modeling of Bidirectional Reflectance Distribution Function (BRDF) on material surface*. Measurement, 2013. **46**(9): p. 3654-3661.
15. Kirchoff, C., *Ueber den Einfluss der Wärmeleitung in einem Gase auf die Schallbewegung*. Annalen der Physik, 1868. **134**(6): p. 17.
16. Hobbs, P.C.D., *Basic Optical Calculations*, in *Building Electro-Optical Systems : Making It All Work*. 2009, John Wiley & Sons, Incorporated: Hoboken, UNITED STATES. p. 1-51.
17. Siegel, R., J.R. Howell, and M.P. Mengüç, *Introduction to Radiative Transfer*, in *Thermal Radiation Heat Transfer*. 2011, CRC Press, Taylor and Francis Group LLC, 6000 Broken Sound Parkway NW, Suite 300, Boca Raton, FL 33487-2742. p. 1-46.
18. DeWitt, D.P. and F.P. Incropera, *Physics of Thermal Radiation*, in *Theory and Practice of Radiation Thermometry*, D.P. Dewitt and G.D. Nutter, Editors. 1988, John Wiley & Sons. p. 21-90.
19. Coates, P. and D. Lowe, *Fundamental Laws*, in *The Fundamentals of Radiation Thermometers*. 2017, CRC Press, Taylor and Francis Group LLC, 6000 Broken Sound Parkway NW, Suite 300, Boca Raton, FL 33487-2742: Florida. p. 19-49.

20. Mandl, F., *Black-Body Radiation*, in *Statistical Physics*. 1988, John Wiley & Sons. p. 246-259.
21. Tiesinga, E., et al., *2018 CODATA recommended values*. 2019, National Institute of Standards and Technology,: National Institute of Standards and Technology,.
22. Tipler, P.A. and G. Mosca, *Wave-Particle Duality and Quantum Physics*, in *Physics for Scientists and Engineers*. 2003, W. H. Freeman and Company: USA. p. 1117-1148.
23. Wien, W.C.W.O.F.F., *On the division of energy in the emission-spectrum of a black body*. The London, Edinburgh, and Dublin Philosophical Magazine and Journal of Science, 1897. **43**(262): p. 214-220.
24. Yoon, H.W., et al., *Guide to the Realization of the ITS-90: Radiation Thermometry*. 2017, International Committee for Weights and Measures: BIPM.
25. Sakuma, F. and S. Hattori, *Establishing a practical temperature standard by using a narrow-band radiation thermometer with a silicon detector*. Bulletin of NPL, 1983. **32**(2): p. p91-97.
26. Saunders, P. and D.R. White, *Physical basis of interpolation equations for radiation thermometry*. Metrologia, 2003. **40**(4): p. 195-203.
27. DeWitt, D.P., *Advances and Challenges in Radiation Thermometry*. Heat Transfer 1994 - Proceedings of the Tenth International Heat Transfer Conference, Vol 1, 1994(135): p. 205-221.
28. Kostkowski, H.J. and R.D. Lee, *Theory and Methods of Optical Pyrometry*, N.B.o. Standards, Editor. 1962, Government Printing Office: Washington D.C.
29. Hamamatsu Photonics K.K., *ORCA-Flash4.0 V3 Digital CMOS Camera C13440-20CU / C13440-20CU01 Instruction Manual*. 2016.
30. Wright, R.N., *Chapter 19 - Physical Properties*, in *Wire Technology (Second Edition)*, R.N. Wright, Editor. 2016, Butterworth-Heinemann: Oxford. p. 285-288.
31. Hamamatsu Photonics K.K. *Image Sensors*. Hamamatsu Semiconductor Handbook [Online Handbook] 2014 Accessed on: 02/01/2020. p. 93-164. Available from: [https://www.hamamatsu.com/resources/pdf/ssd/e05\\_handbook\\_image\\_sensors.pdf](https://www.hamamatsu.com/resources/pdf/ssd/e05_handbook_image_sensors.pdf).
32. Gaussorgues, G., *Scanning and Imaging*, in *Infrared Thermography*. 1994, Chapman & Hall, 2-6 Boundary Row, London SE1 8HN. p. 213-243.
33. Hamamatsu Photonics K.K. *Si Photodiodes*. Hamamatsu Semiconductor Handbook [Online Handbook] 2014 Accessed on: 02/01/2020. p. 14-28. Available from: [https://www.hamamatsu.com/resources/pdf/ssd/e02\\_handbook\\_si\\_photodiode.pdf](https://www.hamamatsu.com/resources/pdf/ssd/e02_handbook_si_photodiode.pdf).
34. Hobbs, P.C.D., *Optical Detection*, in *Building Electro-Optical Systems : Making It All Work*. 2009, John Wiley & Sons, Incorporated: Hoboken, UNITED STATES. p. 91-144.
35. Gutschwager, B., D. Taubert, and J. Hollandt, *Analysis of Reference Sources for the Characterization and Calibration of Infrared Cameras*. International Journal of Thermophysics, 2015. **36**(2): p. 303-314.
36. Coates, P. and D. Lowe, *Radiation thermometer design considerations*, in *The Fundamentals of Radiation Thermometers*. 2017, CRC Press, Taylor and Francis Group LLC, 6000 Broken Sound Parkway NW, Suite 300, Boca Raton, FL 33487-2742: Florida. p. 75-101.
37. Oswald-Tranta, B., *Temperature reconstruction of infrared images with motion deblurring*. Journal of Sensors and Sensor Systems, 2018. **7**(1): p. 13-20.
38. Oswald-Tranta, B., M. Sorger, and P. O'Leary, *Motion deblurring of infrared images from a microbolometer camera*. Infrared Physics and Technology, 2010. **53**(4): p. 274-279.
39. Briggman, K.A., L.J. Richter, and J.C. Stephenson, *Imaging and autocorrelation of ultrafast infrared laser pulses in the 3–11- $\mu$ m range with silicon CCD cameras and photodiodes*. Optics Letters, 2001. **26**(4): p. 238-240.
40. Manolakis, D.G., *Applied digital signal processing : theory and practice*, ed. V.K. Ingle. 2011, Cambridge: Cambridge : Cambridge University Press, 2011.
41. Nyquist, H., *Certain topics in telegraph transmission theory*. Proceedings of the IEEE, 2002. **90**(2): p. 280-305.

42. Manolakis, D.G., *Fourier representaiton of signals*, in *Applied digital signal processing : theory and practice*, V.K. Ingle, Editor. 2011, Cambridge : Cambridge University Press, 2011: Cambridge. p. 134-200.
43. Horowitz, P., *Low-Noise Techniques*, in *The art of electronics*, W. Hill, Editor. 2015, New York, NY, USA : Cambridge University Press, 2015: New York, NY, USA. p. 473-593.
44. Manolakis, D.G., *Design of FIR filters*, in *Applied digital signal processing : theory and practice*, V.K. Ingle, Editor. 2011, Cambridge : Cambridge University Press, 2011: Cambridge. p. 624-704.
45. Manolakis, D.G., *Discrete-time signals and systems*, in *Applied digital signal processing : theory and practice*, V.K. Ingle, Editor. 2011, Cambridge : Cambridge University Press, 2011: Cambridge. p. 23-88.
46. Intel®USA. *Solid-State Drive 530 Series (2.5-inch)*. [Product Specification] 2015 Version: 329212-004US, Accessed on: 07/01/2020 Available from: <https://www.intel.com/content/dam/www/public/us/en/documents/product-specifications/ssd-530-sata-specification.pdf>.
47. Photron USA. *Fastcam SA-Z*. [Datasheet] 2017 Version: REV# 19.12.17, Accessed on: 07/01/2020 Available from: [https://photron.com/wp-content/uploads/2019/12/SA-Z\\_19.12.17\\_compressed.pdf](https://photron.com/wp-content/uploads/2019/12/SA-Z_19.12.17_compressed.pdf).
48. Active Silicon Ltd. *Firebird camera link, 80 bit Frame Grabber*. [Datasheet] 2018 Version: November 2018, Accessed on: 07/01/2020 Available from: <https://www.activesilicon.com/wp-content/uploads/DATASHEET-Frame-grabber-Camera-Link-AS-FBD-1XCLD-2PE8.pdf>.
49. Gonzalez, R.C., *Digital image processing using MATLAB*. Second edition. ed, ed. R.E. Woods and S.L. Eddins. 2009, U.S.]: U.S. : Gatesmark, 2009.
50. Hecht, E., *Fourier Optics*, in *Optics*. 2002, Addison Wesley, 1301 Sansome St., san Fransisco, CA9411. p. 519-559.
51. Saunders, P. and H. Edgar, *Size-of-source effect correction for a thermal imaging radiation thermometer*. *High Temperatures - High Pressures*, 1999. **31**(3): p. 283-292.
52. Krapels, K., et al., *Minimum resolvable temperature difference (MRT): procedure improvements and dynamic MRT*. *Infrared Physics & Technology*, 2002. **43**(1): p. 17-31.
53. Michail, C.M., et al., *Figure of Image Quality and Information Capacity in Digital Mammography*. *BioMed Research International*, 2014. **2014**: p. 11.
54. Envall, J., et al., *Spatial Scatter Effects in the Calibration of IR Pyrometers and Imagers*. *International Journal of Thermophysics*, 2009. **30**(1): p. 167-178.
55. Lane, B.M., et al. *Performance Characterization of Process Monitoring Sensors on the NIST Additive Manufacturing Metrology Testbed*. in *Solid Freeform Fabrication Symposium*. 2017. Austin, TX.
56. British Standards Institution, BS 1041-5: 1989, Part 5: Guide to selection and use of radiation pyrometers, in *Temperature measurement*, 1989
57. ASTM International, E1256-17, Standard Test Methods for Radiation Thermometers (Single Waveband Type), 2017
58. Hartley, R. and A. Zisserman, *Multiple View Geometry in computer viison*. 2000, UK: Cambridge University Press, Cambridge, CB2 2RU.
59. Jansson, P.A., *Deconvolution of Images and Spectra*. 2009: Dover Publications Inc.
60. Gonzalez, R.C., *Image Restoration and Reconstruction*, in *Digital image processing using MATLAB*, R.E. Woods and S.L. Eddins, Editors. 2009, U.S. : Gatesmark, 2009: U.S. p. 209-277.

### 3. EXPERIMENTAL METHODS

This chapter details the practical aspects of the experimental methods used in this thesis. Practical considerations, which may not be immediately obvious to non-specialists in thermography or radiometry, are described. A basic level of laboratory experience is assumed. The non-trivial task utilisation of optomechanics to implement alignment and vibration isolation is beyond the scope of detailed explanation in this thesis.

The original contribution to the field in this chapter is:

- A deconvolution method which utilises a thermal field model as the basis for the reconstruction.

#### 3.1 BLACKBODY REFERENCE

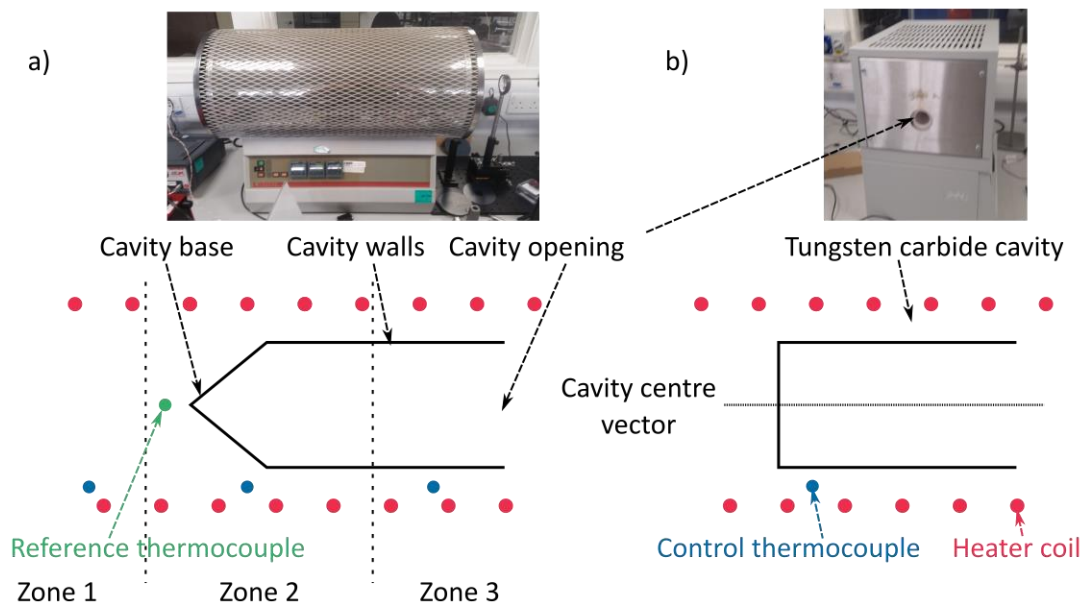


Figure 3.1-1 a) LAND P1200B (AMETEK Land, Sheffield, UK) 3 zone blackbody reference with simplified schematic. b) LAND RT1500T blackbody reference with schematic. Both reference sources consist of a solid tungsten carbide cylinder forming a cavity which is open at one end. The cylinder is suspended centrally to spiral heating coils. The power to the heating coils is controlled by control thermocouples mounted close to the cylinder.

Two high temperature furnaces, with installed blackbody calibration targets (blackbody references [1]), were utilised for calibration and characterisation of the thermographic instruments in this thesis. The cavities were made from a high emissivity material. The furnace and cavity combinations are commercially available, and were designed to make as much of the cavity walls and cavity base as isothermal as possible. There is a significant heat flux through the cavity opening, due to the high temperature, meaning that some thermal gradients along the cavity are difficult to avoid. Thermal gradients can be partially corrected in the P1200B, by adjusting the three independent heating zones. The effective emissivity of both the calibration furnaces is quoted as above 0.99.

The apparent emissivity of a blackbody cavity with known geometry can be modelled [2, 3], but the difference from unity can usually be considered small compared to other sources of uncertainty for the application in this thesis. A thermal gradient along the cavity walls makes the effective emissivity of the cavity temperature and wavelength dependent [4, 5], this is most relevant for short

wavelength radiation. Depending on what the thermal profile along the cavity walls is, compared to the temperature at the reference point, the apparent emissivity of a cavity can be greater than unity.

Due to the heat flux through the cavity opening, the blackbody target never truly reaches thermal equilibrium. Instead, the cavity is considered ready to use as a known radiance source (calibration source), when the temperature has stabilised, and the heating coils are inputting the same amount of energy lost through the cavity opening. This is a thermal steady state. Figure 3.1-2 shows the timescales required for the cavities to reach this steady state. It can clearly be seen that the RT1500T furnace has a much shorter response time than the P1200B. The minimum time to leave the furnaces at a setpoint before radiometric measurements can be made is presented in Table 3.1-1. The maximum heater power to thermal mass ratio is significantly larger for the RT1500T, meaning it reaches temperature faster. The large thermal mass of the P1200B makes the temperature of the cavity very stable once the steady state has been reached.

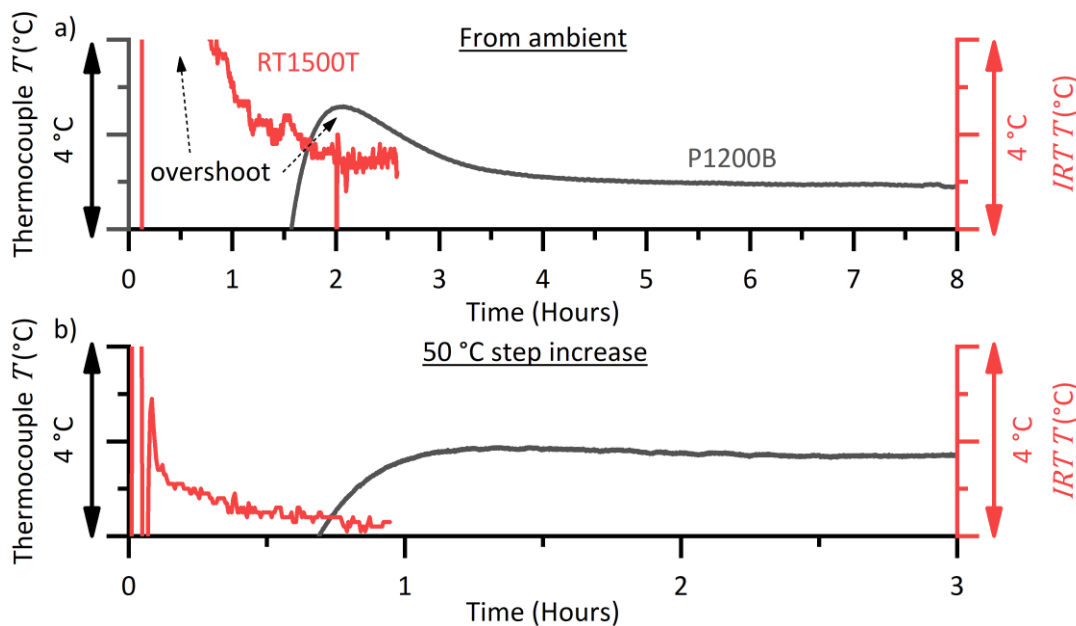


Figure 3.1-2 Measured temperature of industrial blackbody cavities over time from when the furnace is first switched on at time = 0, until it reaches a new thermal steady state at the setpoint. b) Measured temperature of the two blackbody calibration furnaces, from when the setpoint is changed by +50 °C at time = 0.

Table 3.1-1 Minimum time to thermal steady state, for laboratory blackbody calibration furnaces.

	From ambient	50 °C step increase
RT1500T	2.5 Hours	1 hour
P1200B	6 Hours	2.5 Hours

When using the blackbody calibration furnace as a known-radiance source, the ideal situation is that only light from the cavity base enters the collection optics of the instrument under test. The base is the most isothermal part of the cavity, some thermal gradient will be present in the walls. A problem with flat base cavities, such as the one in the RT1500T, is that any specular reflections from the base will be of the cold cavity opening (more specifically what is outside it). This problem is minimised by using a material with diffuse reflection characteristics.

Any target or aperture placed in front of the cavity opening which reflects a significant amount of radiant energy, will affect the energy balance inside the furnace, making the blackbody cavity temperature change. Time must be allowed after placing any target in front of the cavity opening for

the system to reach a new equilibrium (i.e. new steady state). This causes problems when using an aperture smaller than the measurement field of view of the Infrared Radiation Thermometer (*IRT*). This can be mitigated by using plates with high emissivity (low reflectivity) coatings or putting the target at a significant distance from the cavity opening, which will reduce the fraction of radiation reflected into the cavity. Increasing the distance makes the angle of light passing through the aperture which originates from the walls smaller (from the cavity centre vector), meaning it is more likely to enter the instrument collection cone (see section 2.1.3).

### 3.1.1 Radiometric calibration

The thermographic instruments used in this work were calibrated by comparison with other traceably calibrated instruments. These instruments were calibrated at United Kingdom Accreditation Services (*UKAS*) accredited calibration laboratories, ensuring traceability to international standards. In the case of the P1200B furnace, an Isotech Platinum-Rhodium model 1600 type R reference thermocouple (isothermal technology limited, Merseyside, UK) sensor [6], with an Isotech MilliK precision thermometer [7] (measurement electronics), was used as the transfer standard. For the work involving the RT1500T, an Amatek-land Cyclops L100 *IRT* [8] was used. *NMIs* and some primary calibration laboratories use phase transitions at known temperatures to ensure that the blackbody references are at fixed temperatures. Such fixed points are not usually available in university laboratories. Calibration here relies on the chain of traceability ensured by *UKAS* accreditation, to ensure that the temperature of the blackbody reference, measured by the calibrated instruments in the laboratory, matches the *ITS-90* temperature scale within the uncertainty of the accredited calibration.

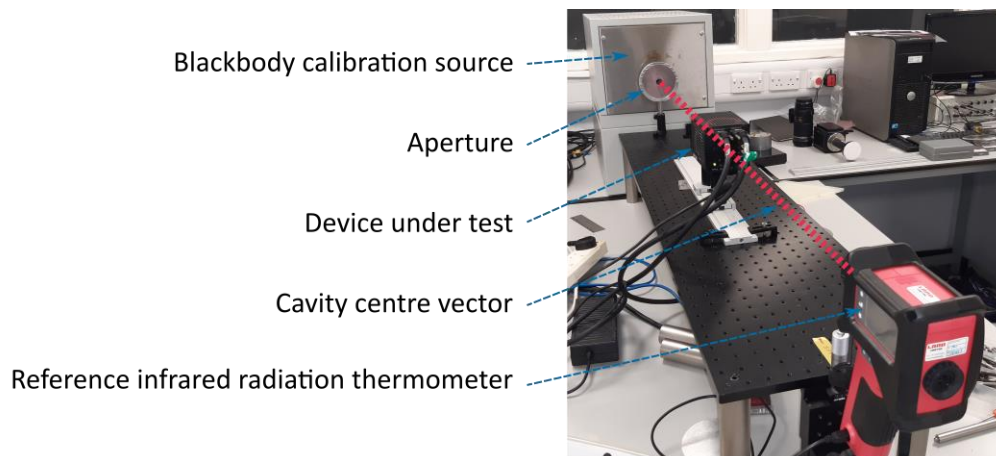


Figure 3.1-3 Typical radiometric calibration of a camera, the reference *IRT* and the camera are placed on the cavity centre vector and aligned on the centre of the aperture.

Depending on the method of interpolation used (see section 2.2), a small number of calibration temperatures can be used if desired. One more calibration point than the number of parameters to be calibrated is required. Zero signal at 0 K is usually assumed as a fixed point. Parameterised interpolation models (section 2.2.4) can be over specified by using many calibration points. In this case the model parameters were fit to the calibration points by *least squares* or other optimisation method. Fitting allows the behaviour across the entire accessible range to be included in the interpolation function. The interpolation curve will not pass directly through each of the calibration points, the spread of the calibration points around the fitted interpolation function is characterised by the Standard Error of Estimate (*SEE*)[9].

The blackbody response model ( $f_{BB,i}$ ) consisting of coefficients to be fit  $A_i$  (all coefficients =  $\{A_i\}$ ), is fit to the temperatures ( $T_{90}$ ) and measured signals ( $S_{cal}$ ).

$$S_{cal} = f_{BB,i}(\{A_i\}, T_{90}) \quad \text{Eq 3.1-1}$$

in practice the inverse model,

$$T_{cal} = f_{BB,i}^{-1}(\{A_i\}, S_{cal}) \quad \text{Eq 3.1-2}$$

is often used for fitting the  $\{A_i\}$ . This is because the  $T_{cal}$  are all similar in magnitude whereas the signals change by more than four orders of magnitude over the digital range ( $1 - 2^{16}$ ). Which means the higher temperatures are given significantly more weight in the fit, which is not the behaviour required.

Once the parameters  $\{A_i\}$  are fit, the fit residuals error ( $\Delta T_{cal}$ ) in terms of temperature is calculated by:

$$\Delta T_{cal} = f_{BB,i}^{-1}(\{A_i\}, S_{cal}) - T_{90} \quad \text{Eq 3.1-3}$$

The *SEE* is calculated as the root mean square of the fit residuals,  $\Delta T_{cal}$ . The aperture size chosen to perform the calibration is important for instruments which have a poor Size of Source Effect (*SSE*) (see section 2.4.3.4). The aperture is chosen so that the diameter is as close to the nominal 100 % signal level as possible. The average of the central pixel signals was used. Ideally this radiometric calibration would be performed after a non-uniformity correction, but it is not always practicable to measure for instruments with poor size-of-source effect performance. The Si based instruments used in this work usually have very good uniformity in quantum efficiency and onboard amplification, due to the level of investment in Si wafer processing technologies, compared to other longer wavelength detector materials such as InGaAs.

### 3.1.2 Thermal field mapping methods

It is sometimes necessary to apply a deconvolution method to the images acquired from a thermographic instrument. This is necessary when the spatial response function of the instrument affects the measured radiance of the scene, i.e: the scene contains spatial frequencies above the measurement resolution limit of the instrument. Two methods of deconvolution are used in this work. In the case where this is not necessary, the direct method of conversion can be used.

#### 3.1.2.1 Direct

Each of the pixel values is converted directly into temperature via the calibration function, after being scaled to account for the emissivity of the surface. This is the standard method of thermal imaging and how most thermographic instruments report their results.

#### 3.1.2.2 Regularised deconvolution

The method of deconvolution used by Lane & Whinton (2015)[10], is a method of regularised deconvolution which comes as a built in function (`deconvreg`) with MATLAB (Mathworks, Natick, MA, USA). This method was trialled and found to poorly reproduce the validation scenes used in this thesis. The `deconvreg` function utilises minimisation of the second spatial derivative to generate the deconvolved scene [11]. The algorithm does not require any information about the original scene, other than an optional inclusion of the magnitude of the noise in the image.

### 3.1.2.3 Model deconvolution

Initial investigations indicated that regularised deconvolution produced ringing in the deconvolved images and gave inaccurate results in the validation tests. The validation tests are described in section 5.3. Because of this performance an alternative methodology was devised. The alternative method uses a parametrised model for the thermal field, this is passed through the calibration curve to convert it into radiance, and then convolved with the *PSF* of the instrument and compared to the measured image. The process is laid out in schematic form in Figure 3.1-4.

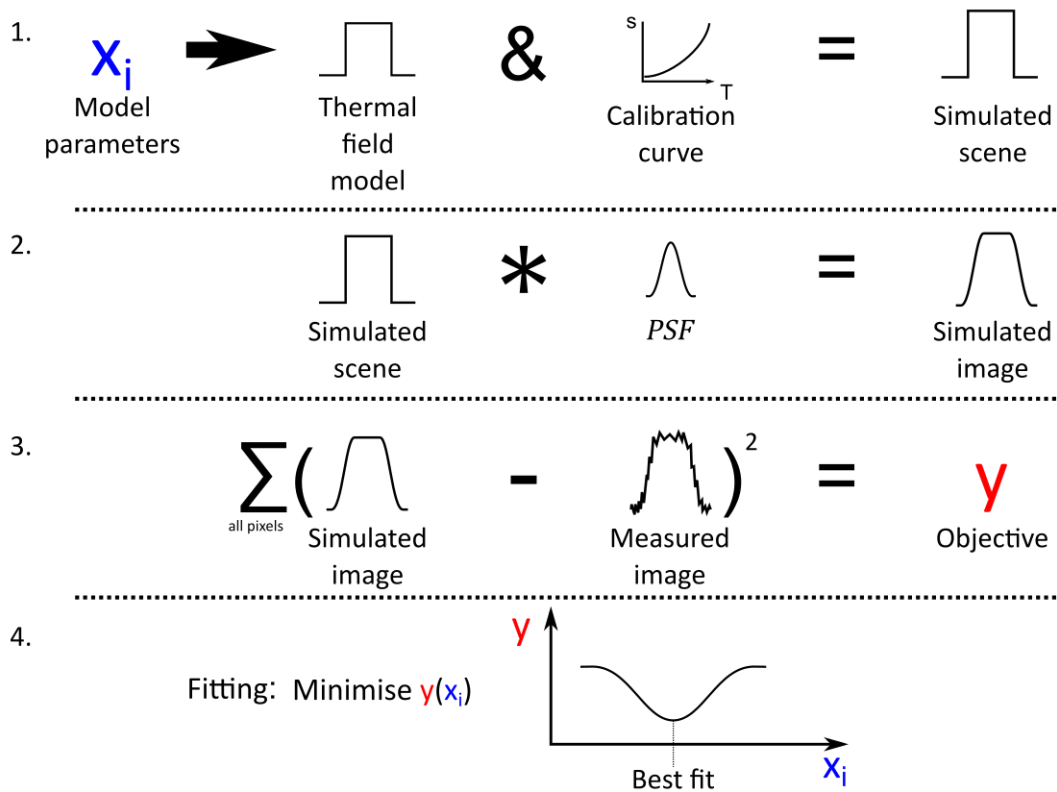


Figure 3.1-4 Workflow for implementation of model fitting deconvolution method. An optimisation algorithm automatically varies the model parameters ( $x_i$ ) until a (ideally global) minima in the objective function is found.

Model deconvolution has the advantage that it only requires the convolution operation, which is a well-defined operation with none of the problems of multiple solutions inherent in deconvolution. The main drawback with model deconvolution is that initially a suitable model for the thermal field must be devised, then a large amount of computational energy must be expended in evaluating the convolution of the model with the Point Spread Function (*PSF*) of the instrument.

## 3.2 CHARACTERISATION TARGETS

### 3.3

The blackbody references also act as a good source of spectrally characterised radiance for spatial transfer function measurements. A typical use is shown in *Figure 3.3-1*. The transmissive components of binary transmission targets (see section 2.4.3) have the same radiance as a surface at the temperature of the blackbody cavity, with an emissivity close to unity. Assuming that care was taken in the setup of the optical system.

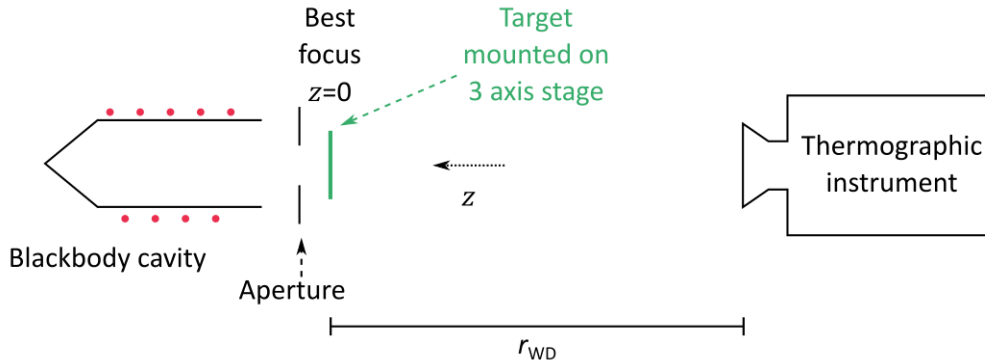


*Figure 3.3-1* General setup for characterisation target imaging.

It is important that any optical systems are aligned parallel to the cavity centre vector. This minimises the amount of signal originating from the walls of the cavity, which will have a different radiance than the base. This can be difficult to achieve with extended Total Field Of View (*TFOV*) systems, such as focal-plane-array-based thermographic instruments. The system should be rotated to maintain the same radiance from the target at the extremes of the *TFOV*, see *Figure 3.3-2*. This is not always practical with the large systems used in this work.

Alignment with the cavity centre vector can be maintained during movement of the device under test by using a pair of apertures. When the device under test is rotated (see *Figure 3.3-2*), then the device must be translated to see the blackbody cavity through the pair of apertures. This ensures that coaxial alignment between the chief (central) ray of the given pixel and the cavity centre vector (fixed by the aperture pair vector) is maintained. The optical axis is not always concentric with the sensor array.

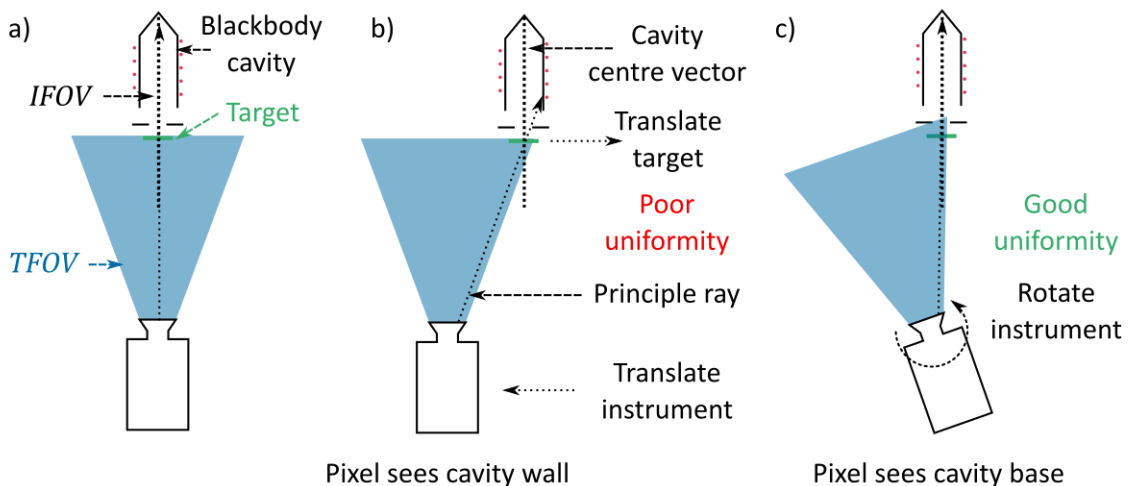


*Figure 3.3-2* a) The target is central to the *TFOV* of the thermographic instrument, the majority of the light incident on the pixel originated from the cavity base. b) The instrument or the target is translated to make the target occupy the extreme pixels in the *TFOV*. The section of the cavity from which the light originates will change. c) When the instrument is rotated, the optical path of the pixel maintains alignment with the cavity centre vector.

### 3.3.1 Five-bar transmission target

The NBS 1963A microscopy resolution test target is a commercially available industry standard imaging resolution target. The pattern for the target was originally developed by the US National Bureau of Standards in 1963 [12] and has been widely used since. The target consists of sets of 5 bars arranged horizontally and vertically. The spatial frequency ( $F_{\text{bar}}$ , see section 2.4.3) of these bars are measured in line pairs per mm (lppmm), the values of which are printed adjacent to each set of lines. The NBS 1963A target (seen in Figure 3.3-3 a) has spatial frequencies from 1 lppmm to 18 lppmm. It was found that 1 lppmm was not a sufficiently low spatial resolution to be confident that the behaviour of the transfer function, as it approached unity, had been characterised. Therefore, a custom resolution target was manufactured. The design for which can be seen in Figure 3.3-3 b. The number of dots adjacent to the targets represent the reciprocal of the spatial frequency of the target. The spatial frequencies of the custom target vary from 1/14 lppmm to 1 lppmm.

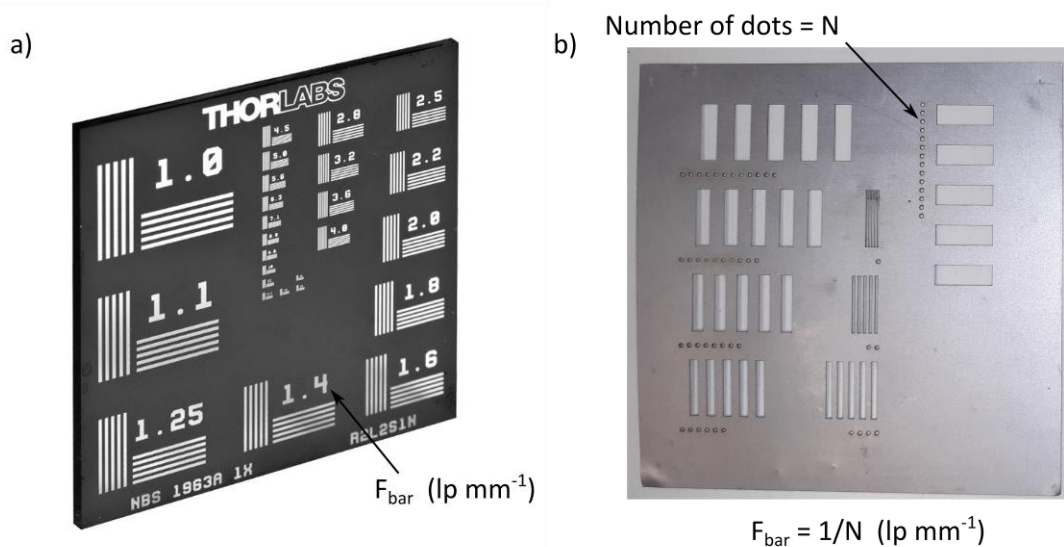


Figure 3.3-3 a) Is a commercially available standard resolution test target, consisting of a laser cut film sandwiched between two soda lime glass slides. Image reproduced with permission from Thorlabs GMBH. b) A test target, laser-cut from a roughened 0.35 mm thick steel plate.

### 3.3.2 Knife edge target

Ideally the radiance would be a blackbody scene at the same temperature as the scene in the intended application. This would provide the identical spectral content, but the temperatures found in *AM* of metals are too high to be readily reproducible in commercial blackbody targets, therefore a lower temperature must be used. For this work a commercial blackbody cavity was used, set at a fixed temperature. Temperature stability was checked with an *IRT*.

A sharp knife edge mounted on a rigid 3-axis translation stage was used. The knife edge was deemed to be straight and uniform (smooth), by inspection with a microscope, compared with the *IFOV* of the instrument. A carefully cleaned scalpel blade was used in this work. Ink was used to minimise specular reflections from the blade surface. Care was taken to keep the whole knife edge in the focal plane of the instrument (perpendicular to the optical axis). Ideally the knife edge would have a finite optical density [13]. This is difficult to realise with transmission targets, because the low radiance part must have a uniform optical density, while maintaining the edge properties required for the test. Therefore an opaque edge was used as per Lane & Whitenton (2015)[10].

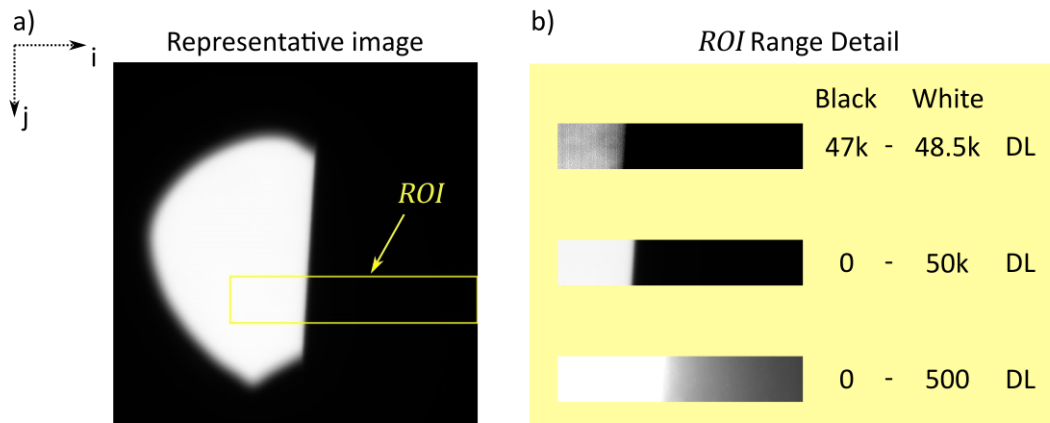


Figure 3.3-4 a) Representative SKE image. b) Details of the high and low ranges (contrast) of the image. Care is taken to avoid artefacts in the images such as large dust spots or reflections from the knife edge.

The extents of the scene were limited to minimise the effects of *SSE* (see section 2.4.3.4) in the thermographic instrument. The balance was made between reducing the effect of *SSE* and capturing as much of the extents of the Edge Spread Function (*ESF*) as possible. A  $\phi_{ap}=2$  mm aperture was used in this work, which is the out of focus component in Figure 3.3-4 b. The exposure time of the instrument was adjusted to make the high radiance signal level close to the saturation signal level of the instrument ( $\approx 4/5$  saturation), without the signal (including the noise) reaching saturation. This maximises the signal resolution of the slanted knife edge image and therefore the *ESF*, and ultimately the *PSF*.

200 images were taken and averaged, to minimise the effect of noise and provide statistics on the noise in the measurement. The temporal noise provides information about the stability of the scene. Vibration of the target can be seen in the result which acts to artificially broaden the measured *PSF*. Every effort was made to minimise vibration in the experiment by isolation of the instrument and target from the rest of the laboratory, but some level of vibration is unavoidable in this kind of experimental setup. The higher radiance part of the image has a higher temporal noise, consistent with theory (section 2.3.3).

Ideally a Non-Uniformity Correction (*NUC* see Section 2.3.2) would have been applied to remove inhomogeneities in the sensitivity of the sensor, and any other position-dependent artefact of the imaging system. Experimental difficulties in determining the *NUC* prevented this correction from being made in this work. Further exploration of this is done in Section 6.1.4. The uniformity in photon sensitivity of the camera used is quoted as  $<0.3\%$  *rms* across the whole sensor [14], making this component of the correction small.

The Region Of Interest (*ROI*) was chosen by examination of the upper and lower ranges of the image (Figure 3.3-4 c). Care was taken to avoid any large defects caused by dust in the optics or specular reflections from the scene. The *ROI* was chosen to avoid other transitions (aperture edge), as these affect the signal levels of the *ESF*.

### 3.3.3 Aperture targets

Three distinct sets of apertures were used throughout this work, each set covering a different size range. The main features of the three sets are laid out in Table 3.3-1. The production methodologies for the three different aperture sets define the precision with which their dimensions can be assumed. The small aperture set uses a very thin etched chromium blocking region which is encased in soda lime glass. Similar to the commercial five-bar target described in section 3.3.1.

Table 3.3-1 Description of aperture sets

Name	$\phi_{ap}$ Range (mm)	Description
Large	0.5 - 12	Drilled & chamfered in 4" diameter Al disks,
Medium	0.06 - 1	Laser cut 0.35 mm thick steel plate.
Small	0.025 - 2	Lithographically etched chrome in fused silica substrate.

### 3.3.4 Aerosol jet printed checkerboard targets

An *Optomec* (Optomec Inc, Albuquerque, NM, USA) aerosol jet printer was used to print sintered silver nanoparticles onto glass slides, allowing the printing of arbitrary shaped characterisation targets. The device provides the possibility of creating variable radiance targets, with tuneable (varying in small discrete steps) optical densities, using dyed polymers or similar. However, the print quality (roughness of print edges) was not sufficient for the work in this thesis, which has spatial resolution of the micron scale. Another problem to be solved in this methodology is the inhomogeneity in the optical density (layer thickness) of the printed target. Despite these drawbacks, checkerboards printed with this methodology were used in chapter 6 to validate the geometric image transform applied to the additive manufacturing data. With some more development the possibility of printing continuously varying arbitrary radiance scenes is promising for the purpose of thermographic instrument characterisation and image processing methodology validation.

The printed slides were mounted on a series of stages described in Figure 3.3-5. The aim of the experiment was to validate the geometric transform used to process the data in chapter 6. Careful alignment of: the centre of the checkerboard scene, the rotation axis of the stage, the focal plane of the instrument and the centre of the image was required. This was achieved by comparing the image of the tilted checkerboard with the perpendicular image, while adjusting the four degrees of freedom. Successful transformation changes an image of the tilted checkerboard to be identical to an image of the non-tilted checkerboard.

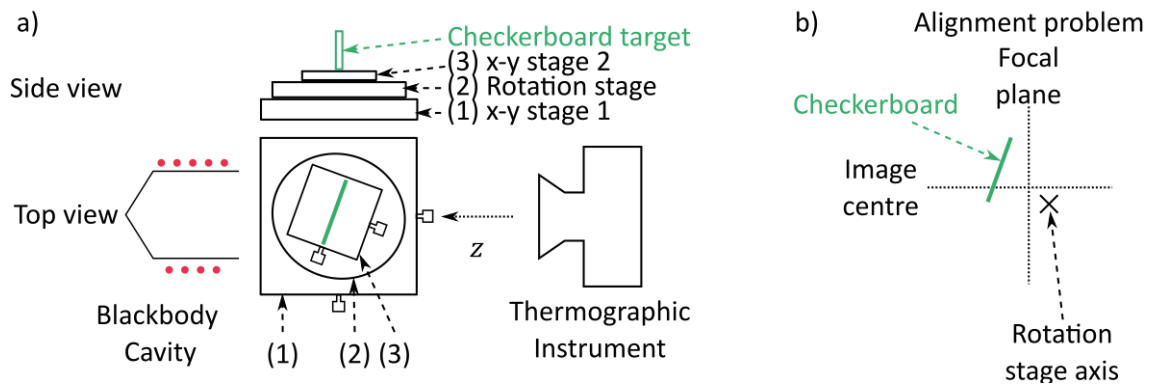


Figure 3.3-5 a) Schematic of alignment stage setup. Two x-y stages and one rotation stage were used to simulate the tilted view in the field experiment. b) Illustration of the alignment problem to be solved

### 3.4 IR IMAGE ACQUISITION IN AN AM PROCESS

The application chosen to implement the thermographic techniques is the challenging process of Additive Manufacturing (AM) of metals. Three distinct experimental setups are described in this section. Each one corresponds to an experimental chapter in the thesis.

#### 3.4.1 BeAM Magic 2.0, DED-LB/M – Chapter 4

The Beam Magic 2.0 (BeAM Machines, Strasbourg, France) Laser-based Direct Energy Deposition of metals (DED-LB/M) AM machine, has a large build chamber approximately 3×2×3 m volume. The entire chamber can be filled with Argon (Ar) for inert environment printing. The large build chamber allows simple, off-axis optical access of the process. The thermographic instrument (PiCam) was placed inside the build chamber (see Figure 3.4-2 c). Near Infrared Radiation (NIR) data was saved locally to a Raspberry pi (RasPi) (Raspberry pi Ltd, Cambridge, UK) then transmitted via ethernet through a feedthrough port between builds. The custom designed lens system used for this, and other work [15-17] utilising the PiCam system is shown in Figure 3.4-1.

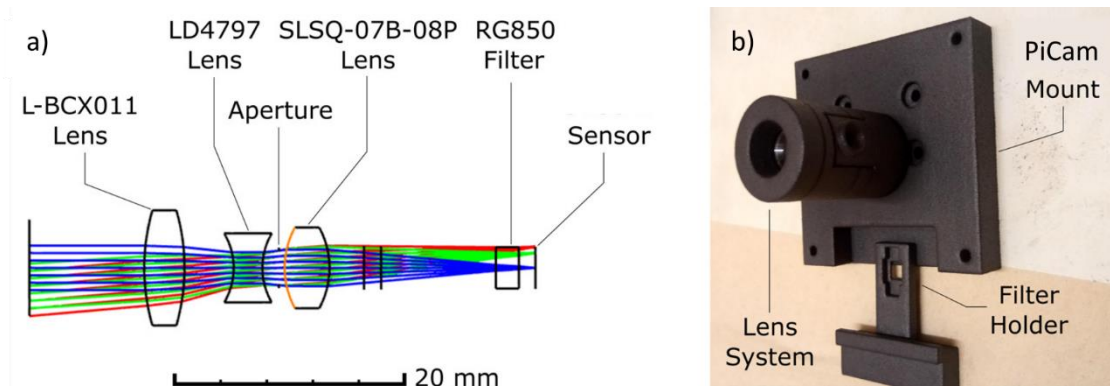


Figure 3.4-1 a) Optics software design schematic of the custom designed PiCam lens system, based on a cook triplet design. b) Custom designed 3d printed plastic housing for the lens system which allows insertion of a filter cube.

Table 3.4-1 Experimental setup of AM imaging in Chapter 4

AM Process	
Process	DED-LB/M
Machine	BeAM Magic 2.0
Build laser	2kW Ytterbium, continuous wave, 1030-1070 nm
Laser beam diameter	700 $\mu\text{m}$
Feedstock	316L stainless steel
Thermographic instrument	
Sensor type	PiCam Version 2, NoIR
Sensor details	Si CMOS, 10 bit
Collection optics	Custom cook triplet [15, 17] $f_L = 21.58 \text{ mm}$
Aperture diameter	3 mm
Spectral filtering, $\xi$	Thorlabs: FGL 850, 850 nm long pass. Thorlabs: FES1000, 1000 nm short pass
Exposure time, $\Delta t$	144 $\mu\text{s}$
Frame rate	3 fps

The build platform of the Beam Magic 2.0 sits on a 2-axis rotation stage which can be seen in Figure 3.4-2 c, this allows the deposition head to access different facets of the build geometry. For the

experiments carried out with the PiCam system, the aim was to capture the best images possible with the chosen, low-cost thermographic instrument. Therefore, the five possible axes of motion were restricted to two. The PiCam system has a low frame rate (2-5 fps) when used without any compression. The low frame rate of the PiCam means that a process where the hot zone moves rapidly around the *TFOV* would be difficult to interpret from the sparsely sampled data. A cylinder geometry was chosen to test the performance of the PiCam as a thermographic instrument in an *AM* application. The cylinder geometry depicted in Figure 3.4-2 a & b means that the hot zone is relatively stationary in the *TFOV* of the instrument. The only motion in the image is the random variation and the gradual raising of the deposition head as the cylinder builds.

Unfortunately, the outbreak of Covid-19 in early 2020 precluded the proper calibration of the PiCam system used in these tests. Where this directly effects the results is described in chapter 4.

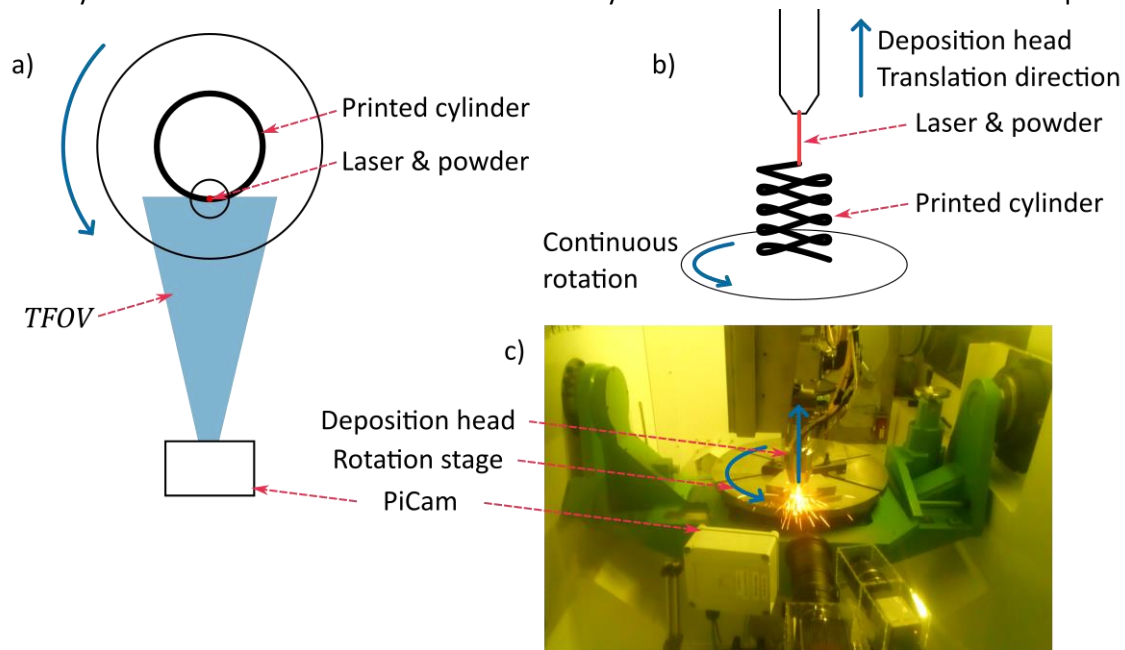


Figure 3.4-2 a) Top down view of the DED-LB/M thermographic monitoring setup. b) Isometric schematic showing continuous spiral build scheme. The rotation of the stage allows the heated zone to stay stationary in one axis of the *TFOV* of the thermographic instrument. c) Photo into the build chamber through the laser-safe glass during the print process.

### 3.4.1.1 Process for Bayer filter removal

The V1 PiCam comes with a smartphone-like lens and a Bayer filter for colour imaging. To take full advantage of the sensor the lens and filter must be removed [18]. This can be achieved using the procedure laid out here.

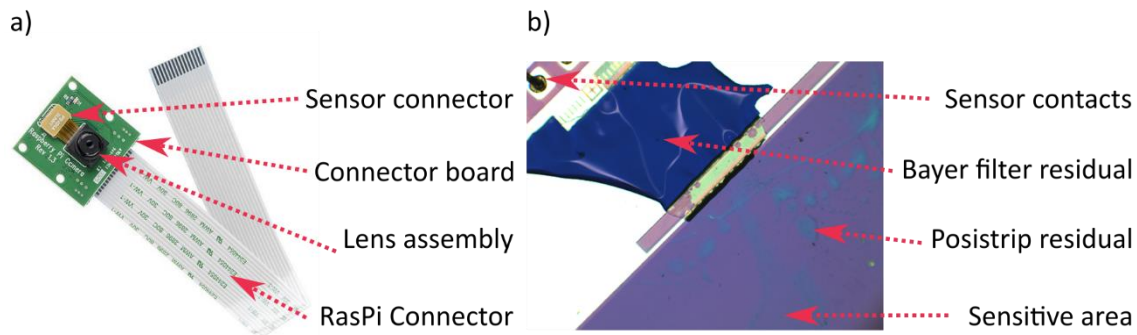


Figure 3.4-3 a) Is the PiCam as it comes with the lens system and sensor attached to a connector board which plug into the RasPi via the RasPi connector. b) Is a microscope image of the sensor area after it has been sat in Posistrip for ~30 minutes.

The Chemicals required are:

- Posistrip EKC830 (Posistrip)(DuPont, Wilmington, DE, USA)
- N-Butyl Acetate
- Acetone
- Isopropyl alcohol

The camera system comes mounted on a connector board, see Figure 3.4-3 a. initially the *lens assembly* should be removed from the *connector board* by disconnecting the *sensor connector*, this is done carefully with tweezers. The lens assembly can be removed from the sensor by using a scalpel and tweezers or in later versions can be unscrewed. The sensor connector and sensor are now placed in a petri dish of Posistrip ensuring that the sensitive side of the sensor is facing up and fully submerged in the liquid. The sensor is left in the liquid until the Bayer filter can be seen to have fully detached from the sensor, this usually takes about 30 minutes. Mechanical agitation can be used to expedite the process.

Once the Bayer filter has detached from the sensor, the sensor is moved to a second petri dish of clean Posistrip to clean off partially dissolved residue. The sensor is cleaned using a standard three stage cleaning process which is:

- Put the sensor in a beaker of N-butyl Acetate (heated to 70 °C) for five minutes
- Move the sensor to a beaker of Acetone for several minutes
- Move the sensor to a beaker of Isopropyl alcohol for several minutes

Once the sensor comes out of the alcohol a clean room nitrogen gun can be used to stop streaks forming on the surface. A clean room swab can be used to remove particularly resistant *Bayer filter residual* (see Figure 3.4-3 b). Care must be taken if using a swab not to touch the gold *sensor contacts*, because they will easily bend, destroying the sensor. once clean the sensor should have no *Posistrip residual* or any other contaminating material left on the surface of the sensor. This can be examined using a microscope, or taking dark images using the sensor. Residual contaminants will show up on the dark image as distinct features in the image. The three-stage process is repeated until the sensor is clean.

### 3.4.2 Renishaw SLM 125, *PBF-LB/M* – Chapter 5

Thermographic imaging of the laser-based Powder bed Fusion of metal (*PBF-LB/M*) *AM* process was implemented on a Renishaw SLM 125 (Renishaw PLC, Wotton-under-Edge, UK) machine. The experimental setup is shown in Figure 3.4-4. The setup is similar in execution to some other setups found in the literature [19-21]. Constraints in budget and access to the machine meant that the thermographic equipment was attached to the machine on a temporary basis. It was therefore decided to modify the inspection port of the SLM 125 machine to allow unrestricted optical access to the top surface of the powder bed, rather than integrate the monitoring system more permanently into the body of the machine as per Boone (2018)[22] or Hooper (2018)[23].

The camera used was a Hamamatsu Orca Flash 4.0 V3 Digital *CMOS* camera (Hamamatsu photonics K.K., Hamamatsu City, Japan). Which is a High specification Si *CMOS* camera originally designed for radiometric application in life sciences. The main advantages of this camera over others on the market are: it is 16 bit, has a high sensor pixel count (2048 by 2048), thermoelectric temperature stabilisation of the sensor and the system can operate at high speeds, mainly due to the dual Camera link® data transfer capability.

Table 3.4-2 Experimental setup of *AM* imaging in Chapter 5

AM Process	
Process	<i>PBF-LB/M</i>
Machine	Renishaw SLM 125
Thermographic instrument	
Sensor type	Hamamatsu Orca Flash 4.0
Sensor detail	Si <i>CMOS</i> , 16 bit
Collection optics	Commercial telephoto lens set at $f_L = 300$ mm
Aperture	F# = F/8
Spectral filtering, $\xi$	Thorlabs: FGL 850, 850 nm long pass Thorlabs: FESH1000, 1000 nm short pass filter Thorlabs: NF1064-44, 1064 nm Notch filter
Frame rate	1600 fps
Exposure time, $\Delta t$	653 $\mu$ s

The original view port was used for visible (0.35-0.7  $\mu$ m) monitoring of the build progress, it was laser-safe glass which was opaque to all *IR* wavelengths. The original window was removed, and a custom machined panel was put in its place. The custom panel had a smaller inspection port with laser-safe glass and a circular sapphire window. Sapphire is transmissive in the *NIR*, allowing the radiation to pass from the hot surface to the instrument unimpeded.

The sapphire window was necessary because the atmospheric seal must be maintained to allow the process to be undertaken in an inert atmosphere. The SLM 125 produces a vacuum inside the chamber and then backfills the chamber with argon, to a slight pressure slightly over atmospheric. This leads to a much lower usage of argon than some other machines. However, this also means all components must be vacuum and over-pressure safe. An aluminium cover was secured over the sapphire window when the instrument was not in place, to maintain the build chamber as a sealed laser-safe chamber. A light-tight collar was bolted onto the modified port which also attached to the lens.

The acquisition-start trigger of the camera was linked to the output of the laser. Alignment was achieved by imaging an artefact placed at a known location on the powder bed with a high temperature halogen light. The build file for the print was then modified to place the build coincident with this fixed *TFOV*. The build was constructed to ensure that the area imaged was the first location to be visited by the laser on each layer.

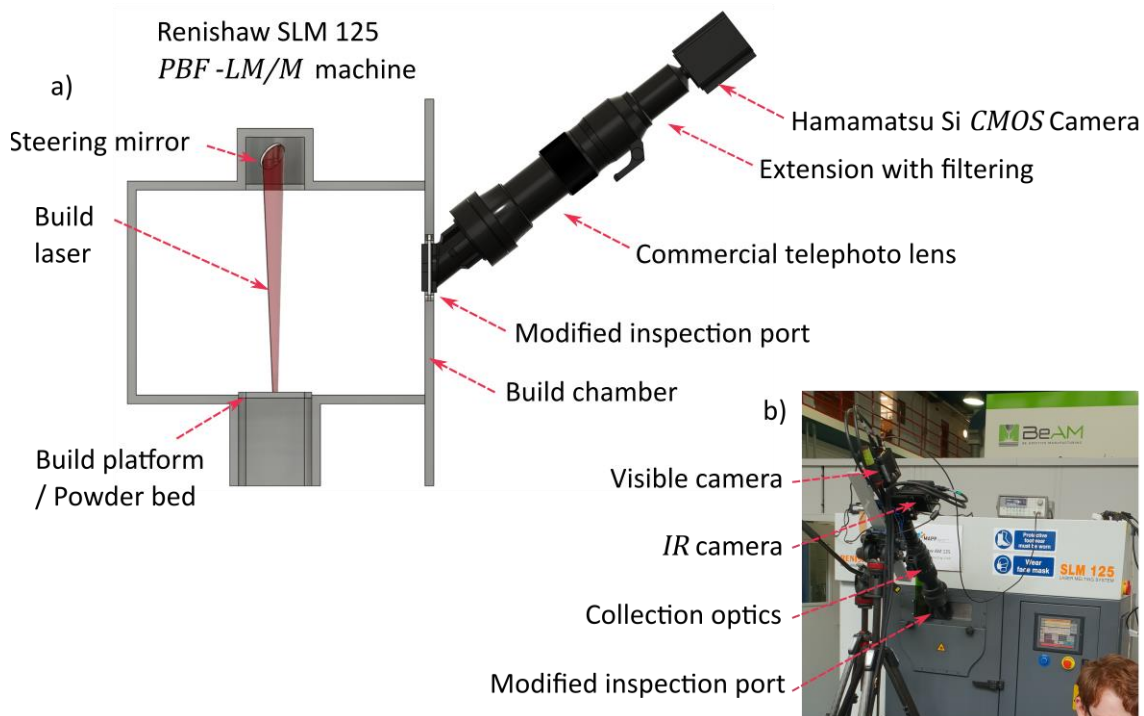


Figure 3.4-4 a) Schematic of the experimental setup for acquisition of infrared images from a commercial additive manufacturing machine. b) Photo of the thermographic instrument attached to the commercial PBF-LB/M machine. The setup shown had a split optical axis with synchronous visible and IR acquisition.

### 3.4.3 Laser Additive Manufacturing Process Replicator – Chapter 6

The limitations placed on thermography in commercially available *AM* machines, such as that described in section 3.4.2, provide motivation to create a customised test bed facility. A custom test bed can be instrumented to provide the maximum amount of information about the process, without the inherent limitations of a commercial machine. The Laser Additive Manufacturing Process Replicator mk2 (*LAMPRIi*) [24-26] system was conceived and constructed by a group based out of the Rutherford Appleton laboratories, UK. A schematic of the System can be seen in Figure 3.4-5.

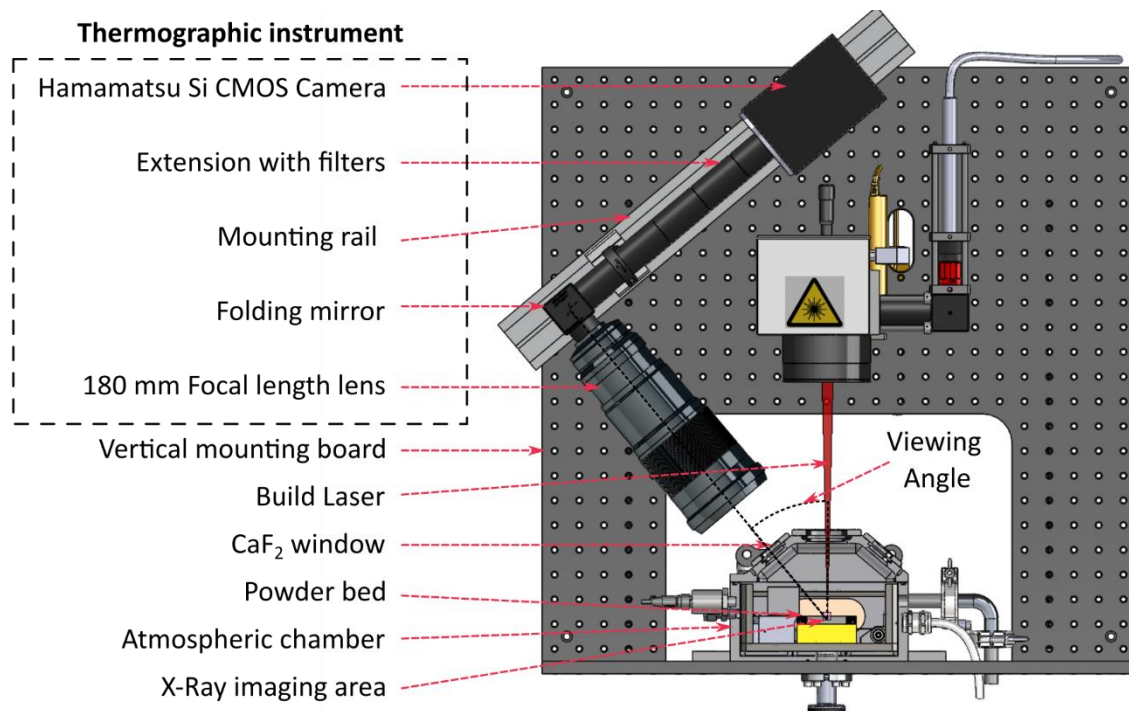


Figure 3.4-5 The laser additive manufacturing process replicator mark 2 schematic. Base image courtesy of Sebastian Marussi (Rutherford Appleton laboratories, Harwell, UK).

The *LAMPRIi* was designed to allow the *PBF-LB* process to be probed using multiple imaging modalities simultaneously. The imaging modalities implemented were: x-ray imaging (either diffraction, or direct radiographic), high speed optical, and *NIR* thermographic. This thesis is concerned with the thermographic instrument and the data acquired using it. The atmospheric chamber means the process can be done in an inert (argon) atmosphere. The inert gas is constantly flowed through the chamber creating a slight positive pressure and a constant, low velocity, gas flow across the powder bed. CaF<sub>2</sub> windows at the top sides of the chamber allow optical access to the top of the powder bed. CaF<sub>2</sub> is transparent in the *NIR* wavelength region.

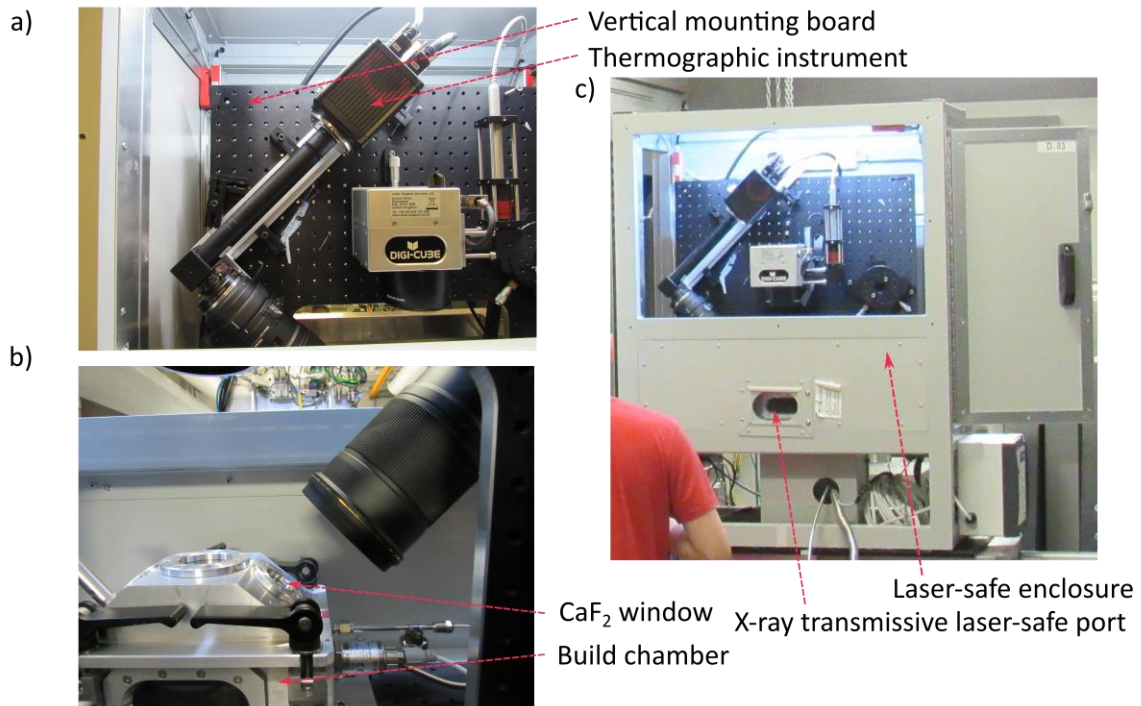


Figure 3.4-6 a) Shows how the thermographic instrument was mounted in the LAMPRII rig. b) Shows detail of the lens relative to the build chamber and viewing window. c) Shows the extents of the laser enclosure. During operation all panels were shut, an interlock system prevented activation of the build laser while the panels were open.

Figure 3.4-6 shows the thermographic instrument in situ at the European Synchrotron Research Facility (*ESRF*). A large synchrotron is required to provide the high flux of collimated x-rays required for this kind of x-ray imaging. The laser-safe enclosure was manufactured at the Rutherford Appleton laboratories and transported to the *ESRF* for the allocated beam time. Limited setup time meant that the thermographic instrument needed to be attached to the vertical mounting board with minimal scope for modification or adjustment once attached. Care was taken prior to the beam time to ensure that the instrument worked as expected when used.

Figure 3.4-7 shows the basic operation of the LAMPRII system during operation. In operando thermography can allow exposure of the formation of defects in the printed part below the surface layer [27]. Inclusions and cracks can be observed during their formation [24], and their evolution through subsequent layers. Diffraction imaging in operando during the *PBF-LB/M* process [28], probes the evolution of the crystal structure of the material as it goes through the phase transitions driven by the heat source (laser). From this information the different rates of precipitation and crystallisation of the various phases (liquation) of the alloy components can be probed.

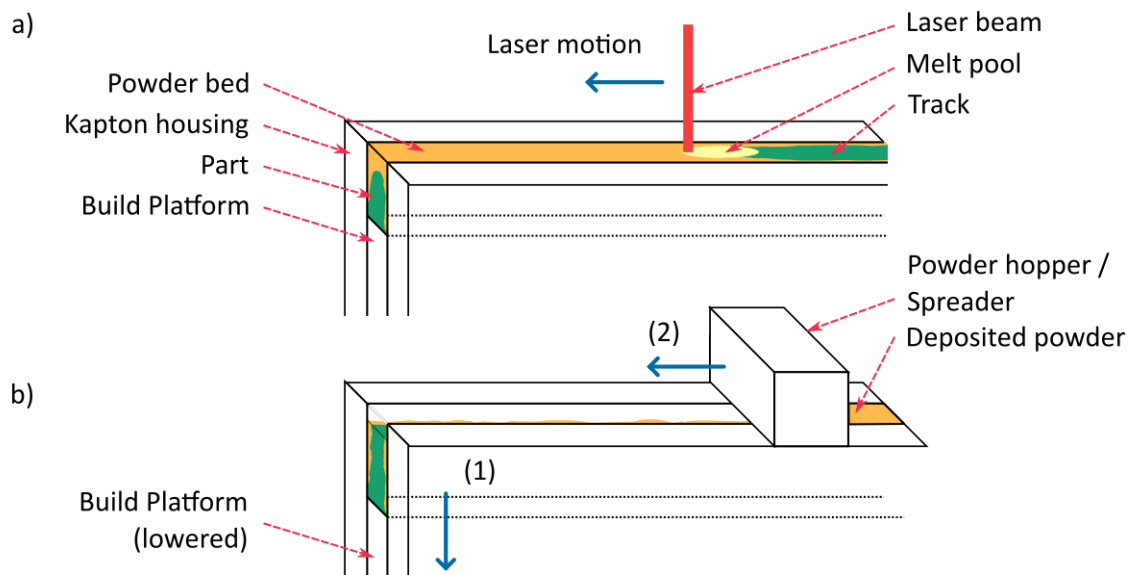


Figure 3.4-7 a) Is a schematic of the system in operation. The laser beam is steered across the powder bed. The thermographic instrument and x-ray imaging are triggered to acquire the print process as the laser passes across the powder bed. b) The build platform is lowered (1), then a new layer of powder is deposited as the powder hopper traverses across the bed (2). The Kapton housing is transparent to x-rays and allows the interaction between the heat source and the previous layers to be probed.

The setup allows numerous operating parameters to be varied during an experimental run. Throughout the course of this work, three beam times were implemented with the thermographic instrument in place. One at the Diamond light facility (Harwell, UK), 26-29 Jan 2018, and two more at the *ESRF* (Grenoble, France), 15-22 April 2018 (*ESRF1*) & 30 May – 3 June 2018 (*ESRF2*). The experimental session at the Diamond light source and *ESRF1* utilised radiographic x-ray measurements, and *ESRF2* concentrated on x-ray diffraction imaging of the process. The highest quality data was collected in the *ESRF* beam times, therefore the data presented in Chapter 6 comes from these experimental sessions.

It was considered more important in *ESRF1* that the *IR* data did not saturate, therefore an extra neutral density filter was used during that experimental session. The neutral density filter was placed between the lens and the  $\text{CaF}_2$  window. The window and the neutral density filters were replicated in the calibration setup.

The tilt in the optical axis is illustrated in Figure 3.4-8. The *TFOV* of the instrument was reduced digitally to maximise the speed of the acquisition. Only the build platform is lased, so the vertical *TFOV* could be restricted to 128 pixels ( $384\ \mu\text{m}$ ) while still acquiring all the build data from between the Kapton housings.

Table 3.4-3 Experimental setup of AM imaging in chapter 6

<i>AM Process</i>	
Process	<i>PBF-LB/M</i> – replicator
Machine	<i>LAMPRII</i> – custom designed process replicator
Build laser	200 W Ytterbium, continuous wave, 1070 nm
Feedstock material	Inconel 713C, Ti-6Al-4V, Ti-1Al-8V-5Fe, SS316L,
Total number of layers	1-25
Thermographic Instrument	
Sensor type	Hamamatsu, Orca Flash 4.0
Sensor detail	Si <i>CMOS</i> , 16 bit
Lens	Commercial $f_L = 180$ mm, macro lens (Sigma, APO MACRO F2.8 EX DG OS HSM)
Aperture	$F\# = F/10$
Spectral filtering, $\xi$	Thorlabs: FGL 850, 850 nm long pass 2 × Edmund optics: #47-590, 1000 nm short pass
Frame rate	1600 fps
Exposure time, $\Delta t$	$ESRF1 = 624 \mu s$ , $ESRF2 = 633 \mu s$

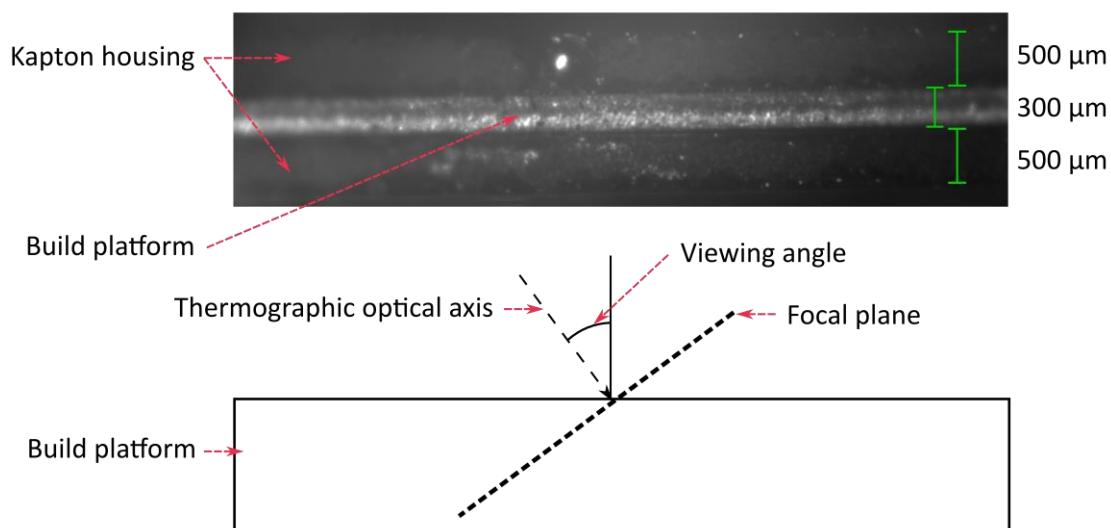


Figure 3.4-8 The *TFOV* of the thermographic instrument is shown at the top. The image was taken with the scene illuminated by a high temperature halogen lamp at a long exposure time.

A machine screw, inserted from the back side of the vertical mounting board, was used for precise vertical (in the image) alignment of the *TFOV* on the build platform. The mounting mechanism (clamps) allowed for many degrees of freedom when mounting the instrument to the vertical mounting board. The focus of the lens was fixed, and the camera was manually moved to make an artefact placed in the centre of the build platform in best focus and at the centre of the image (horizontally). The angle between the build platform normal and the optical axis could not be accurately measured due to the physical restrictions of the laser enclosure. The viewing angle was deemed to be  $40^\circ \pm 5^\circ$  by measurements taken at the time and analysis of photos of the setup, the relatively large uncertainty in the angle should account for the difficulties in mounting the setup at a fixed angle.

The mounting issues were exacerbated by not having access to the *LAMPRII* apparatus between experimental sessions. All mounting operations needed to be devised without access to the *LAMPRII* system, making the need for simplicity of mounting, robustness and versatility more significant than precise reproducible alignment, which would have been advantageous.

Each beam time produced ~ 100 Gb of *NIR* image data. The processing and analysis of this data to extract useful information pertaining to the *AM* process is primarily the domain of the materials scientists working with the multimodally imaged data. For this work some metrics have been extracted from sample datasets, rather than performing a full analysis of all the data which was deemed unnecessary for this thesis.

## REFERENCES

1. British Standards Institution, BS ISO 10878:2013, Non-destructive testing — Infrared thermography — Vocabulary, 2013
2. Saunders, P., *MSL Technical Guide 35 Emissivity of Blackbody Cavities*. 2016: Measurement Standards Laboratory of New Zealand.
3. Quinn, T.J., *The calculation of the emissivity of cylindrical cavities giving near black-body radiation*. British Journal of Applied Physics, 1967. **18**(8): p. 1105.
4. Bedford, R.E. and C.K. Ma, *Emissivities of diffuse cavities: Isothermal and nonisothermal cones and cylinders*. Journal of the Optical Society of America, 1974. **64**(3): p. 339-349.
5. Ohwada, Y., *Evaluation of effective emissivities of nonisothermal cavities*. Applied Optics, 1983. **22**(15): p. 2322-2325.
6. ISOTECH, *Solutions for Primary & Secondary Laboratories*. 2020. p. 42.
7. ISOTECH, *Calibraiton Solutions for; -Temperature Sensors; -Infrared Thermometers; - Thermocouple Referencing System*. 2020. p. 62-67.
8. Amatek and Land, *CYCLOPS L, A family of high precision non-contact pyrometers*. 2017.
9. Lane, B.M., et al., *Uncertainty of temperature measurements by infrared thermography for metal cutting applications*. Metrologia, 2013. **50**(6): p. 637-653.
10. Lane, B. and E.P. Whinton, *Calibration and measurement procedures for a high magnification thermal camera*. 2015, National Institute of Standards and Technology.
11. Gonzalez, R.C., *Image Restoration and Reconstruction*, in *Digital image processing using MATLAB*, R.E. Woods and S.L. Eddins, Editors. 2009, U.S. : Gatesmark, 2009: U.S. p. 209-277.
12. Washer, F.E. and I.C. Gardner, *Method of Determining the resolving power of Photographic Lenses*, N.B.o. Standards, Editor. 1973, Government Printing Office: Washington D.C.
13. British Standards Institution, BS ISO 12233:2017, Resolution and spatial frequency responses, in *Photography — Electronic still picture imaging*, 2017
14. Hamamatsu Photonics K.K., *ORCA-Flash4.0 V3 Digital CMOS Camera C13440-20CU / C13440-20CU01 Instruction Manual*. 2016.
15. Wilkes, T.C., et al., *The Development of a Low-Cost, Near Infrared, High-Temperature Thermal Imaging System and Its Application to the Retrieval of Accurate Lava Lake Temperatures at Masaya Volcano, Nicaragua*. Remote Sensing, 2018. **10**(3): p. 450.
16. Pering, T.D., et al., *A Rapidly Convecting Lava Lake at Masaya Volcano, Nicaragua*. Frontiers in Earth Science, 2019. **6**(241).
17. Stanger, L., et al., *Thermal Imaging Metrology with a Smartphone Sensor*. Sensors, 2018. **18**(7): p. 2169.
18. Wilkes, T., et al., *Ultraviolet Imaging with Low Cost Smartphone Sensors: Development and Application of a Raspberry Pi-Based UV Camera*. Sensors, 2016. **16**(10): p. 1649.
19. Krauss, H., C. Eschey, and M.F. Zaeh. *Thermography for monitoring the selective laser melting process*. in *Proceedings of the Solid Freeform Fabrication Symposium*. 2012.

20. Ansari, M.J., D.-S. Nguyen, and H.S. Park, *Investigation of SLM Process in Terms of Temperature Distribution and Melting Pool Size: Modeling and Experimental Approaches*. Materials (Basel, Switzerland), 2019. **12**(8).
21. Heigel, J.C., B.M. Lane, and L.E. Levine, *In Situ Measurements of Melt-Pool Length and Cooling Rate During 3D Builds of the Metal AM-Bench Artifacts*. Integrating Materials and Manufacturing Innovation, 2020. **9**(1): p. 31-53.
22. Boone, N., et al., *Thermal near infrared monitoring system for electron beam melting with emissivity tracking*. Additive Manufacturing, 2018. **22**(C): p. 601-605.
23. Hooper, P.A., *Melt pool temperature and cooling rates in laser powder bed fusion*. Additive Manufacturing, 2018. **22**: p. 548-559.
24. Leung, C.L.A., et al., *In situ X-ray imaging of defect and molten pool dynamics in laser additive manufacturing*. Nature Communications, 2018. **9**(1): p. 1355.
25. Leung, C.L.A., et al., *The effect of powder oxidation on defect formation in laser additive manufacturing*. Acta Materialia, 2019. **166**: p. 294-305.
26. Leung, C.L.A., et al., *Effect of preheating on the thermal, microstructural and mechanical properties of selective electron beam melted Ti-6Al-4V components*. Materials & Design, 2019. **174**: p. 107792.
27. Bartlett, J.L., et al., *In situ defect detection in selective laser melting via full-field infrared thermography*. Additive Manufacturing, 2018. **24**: p. 595-605.
28. Hocine, S., et al., *Operando X-ray diffraction during laser 3D printing*. Materials Today, 2019.

## 4. LOW COST THERMOGRAPHY METROLOGY IN COMMERCIAL DIRECTED ENERGY DEPOSITION ADDITIVE MANUFACTURING

---

In this chapter a low cost, widely accessible, imaging sensor system (PiCam) is converted into a high-temperature thermographic instrument. This thermographic instrument is trialled in a laser-based directed energy deposition of metals (*DED-LB/M*) Additive Manufacturing of Metals (*AM/M*) application. Common performance metrics are implemented on the system, to quantify its performance. A standard method of spatial transfer function measurement is expanded upon and applied. Melt pool metrics are extracted from the data captured in the additive manufacturing process. Finally, the viability of the instrument for this application is discussed.

The Raspberry Pi (RasPi) (Raspberry pi Ltd, Cambridge, UK) and associated peripherals, such as the raspberry pi camera (PiCam) are mass market, low cost electronics, which have their roots in the maker movement [1]. The main advantages of using such devices are their affordability, the community of peer support, and the accessibility of the hardware and software through repositories such as GitHub. This kind of accessible science is an important part of the development of young scientists and a general public engagement in science.

Using the PiCam system in an *AM* application has several advantages. Due to its low cost, the PiCam can be considered as disposable when exposed to the harsh environments inside AM chambers. Multiple systems can be used and linked to create 3D models[2] of the prints. The mature technology of the PiCam means that the relative performance is very high compared to other technologies. The PiCam cameras use the same sensors as modern smart phone cameras [3, 4], hence research applications found for these devices could be expanded to the smartphone market. Low cost accessible instruments increase the amount of data which can be acquired from these high value *AM* machines [5], improving the accessibility of the process to researchers.

Smart phone sensors are very high in pixel density, typically 2-10  $\mu\text{m}$  per pixel [6]. High pixel density gives a high spatial sample rate. Therefore, these imaging systems are usually limited in resolution by the optics (oversampled) and not the sample rate. The *resolution* of oversampled imaging systems is not a discrete figure like the sampling rate (usually expressed as a number of pixels e.g. 5 Mpixel). This chapter explores the different definitions of resolution and their applicability to thermographic applications.

Original contributions to the field, in this chapter are:

- Conversion of a PiCam system to a functioning thermographic instrument.
- Modification of a standard resolution test method to fit into the Fourier framework of transfer function measurement.
- Use of a PiCam system to measure melt pool characteristics in an *AM/M* application.

## 4.1 PREPARATION OF THE PiCAM SYSTEM

The PiCam system used for this characterisation work was a version 1 sensor using the OmniVision OV5647 (OmniVision Technologies, Santa Clara, CA, USA) Si CMOS sensor. The pixel size of the V1 PiCam sensor is  $1.4\ \mu\text{m}$ , the FPA consists of  $2592 \times 1944$  pixels. The V1 sensor comes coated with a Bayer filter, to allow creation of colour images. For the characterisation work carried out in this thesis, the Bayer filter was removed using the process described in section 3.3.1.1 [4]. The process of removing the Bayer filter must be done inside an extraction hood as it requires some toxic heated chemicals. A clean room was used to perform the final cleaning of the stripping chemical and any residuals of the filter.

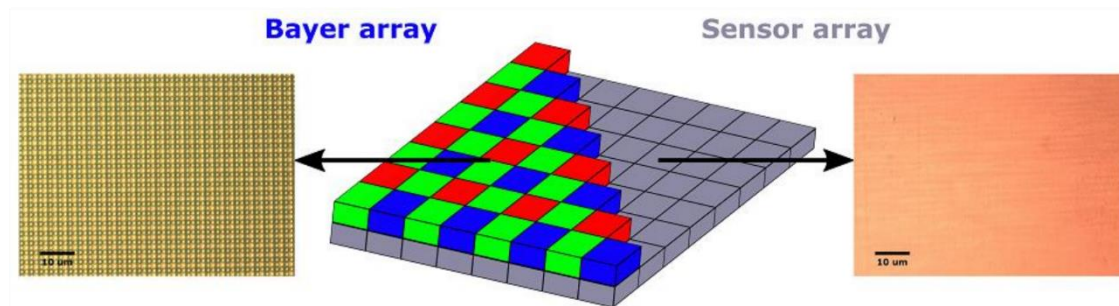


Figure 4.1-1 Removal of the Bayer filter improves spectral sensor uniformity and sensitivity outside the visible range. Image reproduced from Wilkes (2016) [4], with permission from Thomas Wilkes.

The process of removing the Bayer filter, described in section 3.3.1.1, was originally developed by Thomas Wilkes (University of Sheffield, Sheffield, UK) in collaboration with Jon Willmott (University of Sheffield, Sheffield, UK). Initially this process was developed to allow use of the ultraviolet sensitivity of the Si PiCam sensor [4]. The same sensors which were used to capture ultraviolet data in volcanology applications, were also used to capture Near Infrared Radiation (NIR) data of the high temperature lava pools. The characterisation work carried out in this chapter was aimed at validating the use of these instruments in that application. The PiCam systems were also used in AM/M to test their suitability to this application, with a view to building on this work with future projects.

The RasPi system is a small, cheap, open source computing system. The Picam is designed to operate smoothly with the RasPi system. The basic, freely available camera software does not allow sufficient control of the camera parameters to allow scientific radiometric applications. Therefore, custom software was developed, in collaboration with Nicholas Boone (University of Sheffield, Sheffield, UK), to allow the control required for the desired applications. The RasPi was programmed to act as a server to stream the raw 10-bit images to a PC via ethernet cable. Software was also used which could capture the data locally to the RasPi to be extracted later.

## 4.2 CALIBRATION & CHARACTERISATION

### 4.2.1 Radiometric calibration

The three-zone furnace, described in section 3.1, was used to calibrate the prepared PiCam system. The thermographic system was calibrated at 8 fixed temperatures as measured by a standard reference thermocouple.

The sensor has an analogue gain, which can be set, or allowed to auto adjust, based on the scene. The gain was fixed at the same value during calibration and field usage. We chose to fix the gain at the minimum value (one). The minimum was chosen because amplification decreases the signal to noise

ratio. A 25 mm diameter aperture from the large aperture set (see section 3.2.3) was used to define the limits of the scene inside the back cone of the blackbody cavity. The furnace was left to stabilise in temperature between each fixed calibration temperature.

Tests with a type k thermocouple showed a slight temperature gradient along the length of the cavity at 800 °C, this was corrected as well as possible by introducing a + 10°C offset into the front zone of the three-zone furnace.

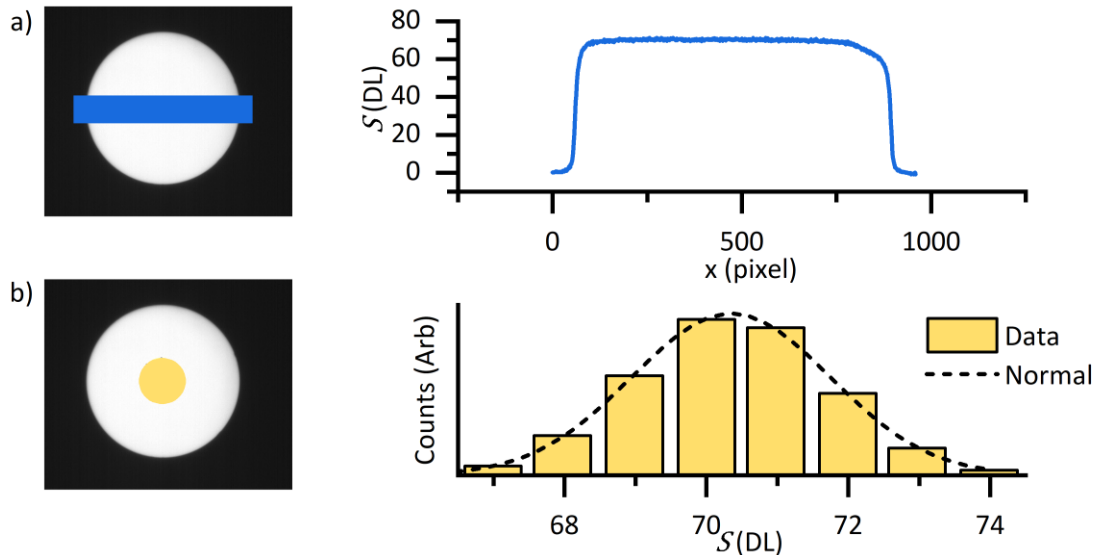


Figure 4.2-1 a) Is a line profile across a typical mean image of the calibration aperture. b) Shows that the measurement of radiance forms a normal distribution around the mean signal level for the central portion of the pixels in the image of the aperture.

Figure 4.2-1 shows that the image of the calibration aperture is close to uniform across the aperture. The calibration signal level is the mean of the central pixels of the image of the aperture. Figure 4.2-1 b shows that the signal levels of each of the pixels in the central region form a normal distribution around the mean. 30 images were taken for each calibration point, and the average image was used to ascertain the calibration signal level.

#### 4.2.2 Spectral responsivity

The spectral responsivity of the PiCam system was measured using a monochromator and a commercial InGaAs photodiode of known responsivity. Light from a spectrally broad source was split by a diffraction grating, and a small fraction of the dispersed spectrum was used to illuminate the PiCam system and the commercially characterised photodiode. The response of the PiCam system was scaled to account for the spectral nonuniformity of the dispersed light.

#### 4.2.3 Standard thermographic performance metrics

When choosing a thermographic system for a specific application some important performance parameters are often used to allow the user to acquire the right system for their application. The *minimum resolvable temperature difference* is a commonly used performance metric defined as the 'measure of the ability of an infrared imaging system and the human observer to recognise periodic bar targets on a display'[7]. This makes this metric a subjective measure of performance as it depends on the modality of the display and the standardisation of the human response. A more quantitative measure is the Noise Equivalent Temperature Difference (*NETD*). This is a definition of the noise in the system expressed in terms of a temperature. It is then simple for the user to decide whether the device can resolve the temperature differences required for the application, or if averaging may be required.

#### 4.2.4 Spatial transfer function characterisation

An important metric which is often quoted for an imaging system is the Modulation Transfer Function (*MTF*) (described in section 2.4.1). There is some ambiguity in literature over the precise definition of an *MTF*. In the book *optics* by Hecht (2002) [8] the *MTF* is used to describe the change in amplitude of any regular pattern of fixed amplitude, defined as: ‘*The ratio of the image modulation to the object modulation at all spatial frequencies*’[9]. There is no stipulation that the object must consist of only sinusoidal components at a single spatial frequency ( $F_x$ ). The transfer function of a bar target is sometimes confusingly referred to as the *MTF* and is often quoted in units of line pairs per mm for this reason. In most modern literature the distinction is made between the *MTF* and the transfer function of a bar target, which is sometimes referred to as a Contrast Transfer Function (*CTF*)[10,11].

The *MTF* is often referred to as the Fourier transform of the impulse response function [12-14] of an imaging system. It should be noted that the *MTF* is usually expressed as the Fourier transform of the Line Spread Function (*LSF*), which is the one dimensional impulse response function, and not the Fourier transform two dimensional impulse response function as might be expected.

As was shown in section 2.4.3.1, a binary, one dimensional bar target (square wave) function contains many  $F_x$  above the fundamental frequency ( $F_{bar} = 1/\lambda_{bar}$ ). It has been shown in literature [10, 10, 14] that the *CTF* can be numerically converted to the Fourier definition (sine components) of the *MTF* by use of the Coltman formula [16]. The *MTF* in terms of the *CTF* at each  $F_x$  is given by the series:

$$MTF(F_x) = \frac{\pi}{4} \left[ CTF(F_x) + \frac{CTF(3F_x)}{3} - \frac{CTF(5F_x)}{5} + \dots \right] \quad Eq\ 4.2-1$$

The *CTF* can be calculated from the measured modulation depth of a bar target using the maximum ( $S_{max}$ ) and minimum ( $S_{min}$ ) signal levels of a line profile across the lines [9, 12, 13] by:

$$CTF = \frac{S_{max} - S_{min}}{S_{max} + S_{min}} \quad Eq\ 4.2-2$$

This method of determining the depth of the modulation is highly sensitive to noise in the line profile. Therefore, averaging along the direction of the bars was used to reduce the noise in the measurement. This is in addition to the use of an average of 50 frames to reduce temporal noise. The mean (of 50) dark image was subtracted from each mean scene prior to manual selection of the Region Of Interest (*ROI*)

Both the commercial *CTF* plate and the custom plate were used to cover the range of measured *CTF* values (see section 3.2.1). The *CTF* at the lowest spatial frequency available on the custom plate was not at the maximum measurable modulation depth; therefore, a plate with lower spatial frequencies was made. The commercial plate is not fully transmissive in the high-transmission regions (soda-lime glass substrate); therefore, a correction was made to account for the change in radiance between the custom plate (which was fully transmissive) and the commercial plate. The correction was made by normalising the *CTF* at the crossover point of the two targets, 1 lp mm<sup>-1</sup>. Using this method, the transmission coefficient of the glass substrate was found to be 0.92. The correction for non-unity-transmission is not necessary if all the spatial frequencies are measured with the same transmission, because it is the relative modulation depth at the different spatial frequencies which is important. It is however important that the transmission is zero in the low-transmission regions.

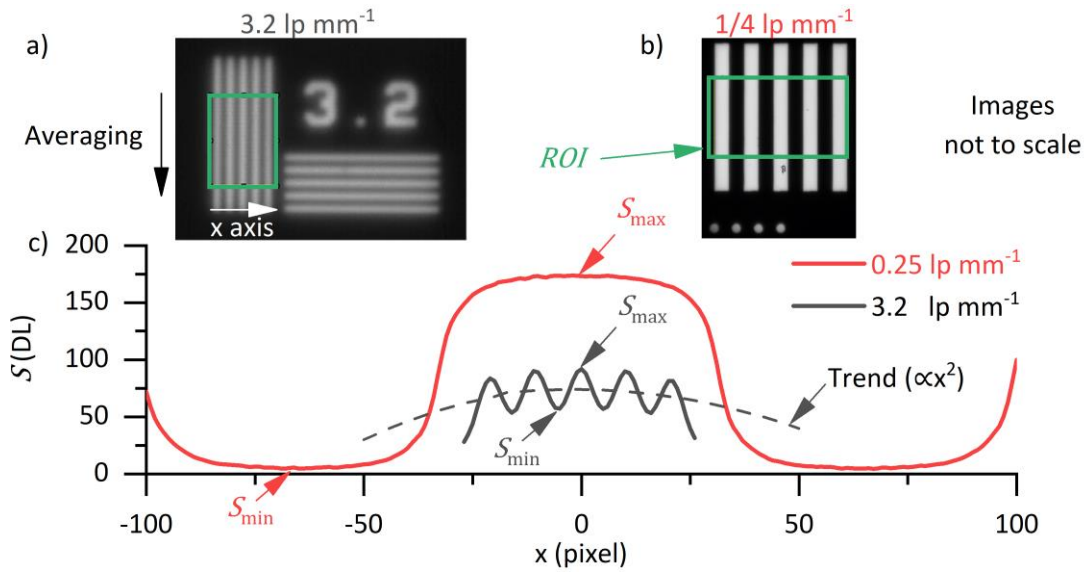


Figure 4.2-2 a) Image of the 3.2 line pair  $\text{mm}^{-1}$  ( $\text{lp mm}^{-1}$ ) commercial target. b) Image of the 0.25  $\text{lp mm}^{-1}$  custom made target. c) Signal profile across the Region Of Interest (ROI). The modulation depth (Eq 4.2-2) of a bar target remains constant in terms of radiance, but the measured modulation depth reduces with increased spatial frequency.

The trend which can be observed in Figure 4.2-2 c, illustrates a drawback with the 5 bar target method of measuring the *MTF*. The trend shows that the adjacent bars are still building up the radiance. A *steady state* of modulation depth has not been reached. For this reason, this kind of *CTF* measurement should ideally be undertaken with a large number of lines and only the regions of steady state should be used to measure the modulation depth. For these reasons the  $S_{\text{max}}$  and  $S_{\text{min}}$  of the central phase of the target were used to calculate the modulation depth. The 5-bar target (NBS 1963A[17]), despite its shortcoming, is a well-known standard for resolution measurements, and was therefore used here.

When the spatial frequency approaches the Nyquist frequency of the system, the phase angle between the scene (bars) and the pixels becomes important. Ideally the modulation depth would be measured at many phase angles. This was impractical to implement with the equipment available so only spatial frequencies up to 5  $\text{lp mm}^{-1}$  were measured directly. Above 5  $\text{lp mm}^{-1}$  an exponential approximation was used to estimate the higher order components needed to convert the *CTF* to the *MTF*. The exponential was fit to the 7 highest frequency measured points and extrapolated up to the Nyquist frequency. The measured *MTF* is relatively insensitive to these higher order components.

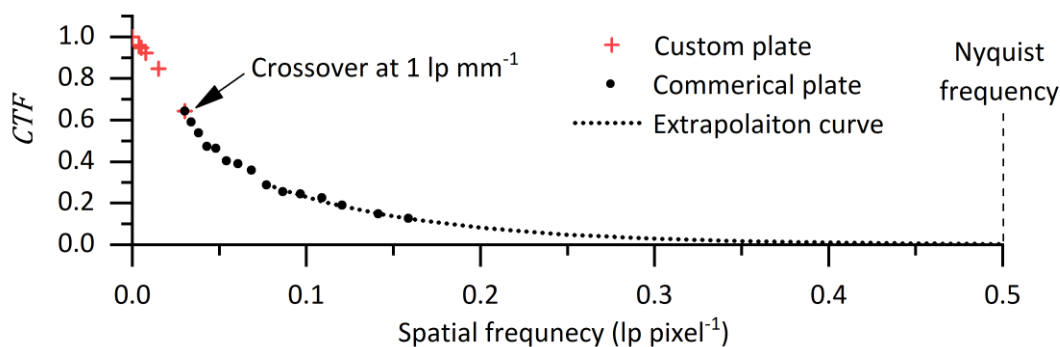


Figure 4.2-3 Extrapolated with an exponential decay.

### 4.3 CALIBRATION & CHARACTERISATION RESULTS

The results are split into two sections both of which are based on results measured using a PiCam system. The calibration and characterisation results were obtained using a deBayered V1 PiCam, and the *AM* results (steady state *DED-LB/M*) were acquired using a V2 sensor with the Bayer filter still in place. This discrepancy is mainly due to the V2 being released towards the end of the PhD project and presenting the most useful tool for future development in *AM* monitoring. Therefore, it was decided that the V2 camera should be trialed in the *AM/M* application.

#### 4.3.1 Blackbody calibration

The PiCam system was calibrated as per section 4.2.1. The response was found to be well modelled by the Sakuma Hattori model and the Wien model. This is evidenced by the small and random residuals of the fits shown in Figure 4.3-1 b.

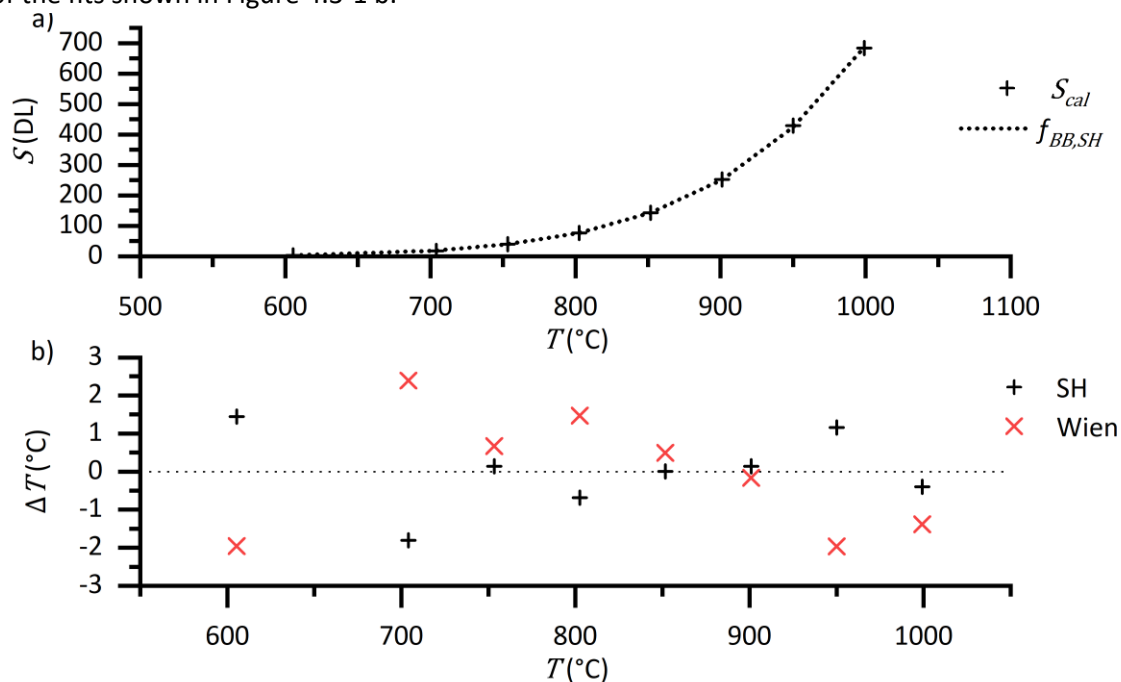


Figure 4.3-1 a) Calibration of the deBayered V1 PiCam system. b) The residuals of the SH fit in terms of temperature. The residuals are small and approximately random, thus the calibration curve is a good representation of the calibration data.

Table 4.3-1 Calibration coefficients for the thermographic instrument (see section 2.2.4).

Spectral fit coefficients		value	
	$A_1$	$8.606 \times 10^{-7}$	
	$A_2$	$4.859 \times 10^{-5}$	
	$\lambda_{Wien}$	$9.577 \times 10^{-7}$	
Scaling fit coefficients			SEE
SLM 125	$A_0$	$2.00 \times 10^8$	2.71 °C
	$A_{Wien}$	$9.074 \times 10^7$	4.27 °C

The mean noise floor for the dark image is located at  $\sigma_S = 0.60$  DL.

The PiCam system is limited to 10 bits of dynamic range. The exposure time can be adjusted to slide this range in temperature, but the limited dynamic range will always limit the range of temperatures which the PiCam system can measure.

#### 4.3.2 Spectral responsivity

The results of the spectral responsivity measurements shown in Figure 4.3-2 show unexpected undulations in the responsivity. This could be caused by etalons left behind from the deBayering process. The undulations have a period of  $\sim 600$  nm meaning that they could be caused by a  $\sim 1$   $\mu\text{m}$  thick etalon.

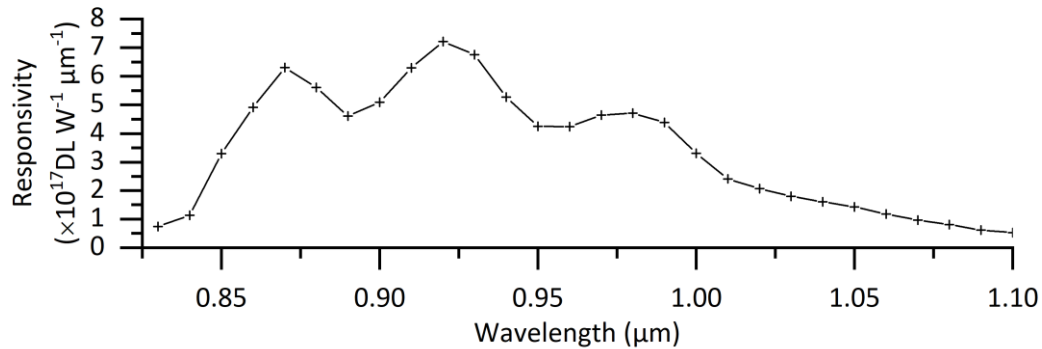


Figure 4.3-2 The spectral responsivity of the PiCam system shows some unexpected oscillatory behaviour

#### 4.3.3 Noise equivalent temperature difference

The *NETD* was found to increase rapidly at the bottom of the range as might be expected. The signal to noise ratio increases rapidly as the signal approaches the noise floor of the instrument. The *NETD* is dependent upon the exposure time chosen, so this measurement is intended as an exemplar calculation. The noise can be reduced by averaging of images, which is only possible in steady state systems.

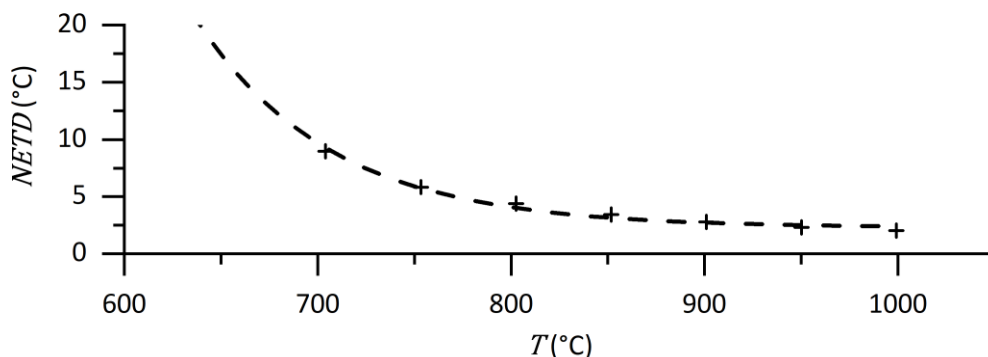


Figure 4.3-3 The Noise Equivalent Temperature Difference (*NETD*) is an important performance metric for a thermographic system.

#### 4.3.4 Modulation transfer function

The *MTF* in Figure 4.3-4 was measured by processing of images of binary *CTF* plates. The *MTF* curve shows that the amplitude of a sine wave would be attenuated, by the given amount, at the given spatial frequency. Imaging systems usually consider that spatial frequencies below an *MTF* of 0.1 can be resolved [18], but this would mean a reduction in signal amplitude of 90%, making accurate radiometric measurement of temperature impossible at these frequencies. A more useful measure of resolution would be to define a spatial frequency below which the amplitude has been reduced by less than some small percentage. This could be 0.9 for industrial measurements, or 0.99 for strict low uncertainty metrological applications [19].

It would be hoped that professionally designed radiometric thermography systems have a high  $MTF$  ( $> 0.9$ ) at the spatial sampling frequency (pixel spacing) of the instrument, but this is not always the case and should not be expected. Without careful characterisation of the instrument it is not obvious to a user that the higher spatial frequencies are being attenuated, because objects within the image are still clearly observable at much lower  $MTFs$  than those required for accurate radiometric measurements. Conversion of the  $CTF$  to  $MTF$  makes a  $\sim 50\%$  difference to the calculated measurement resolution.

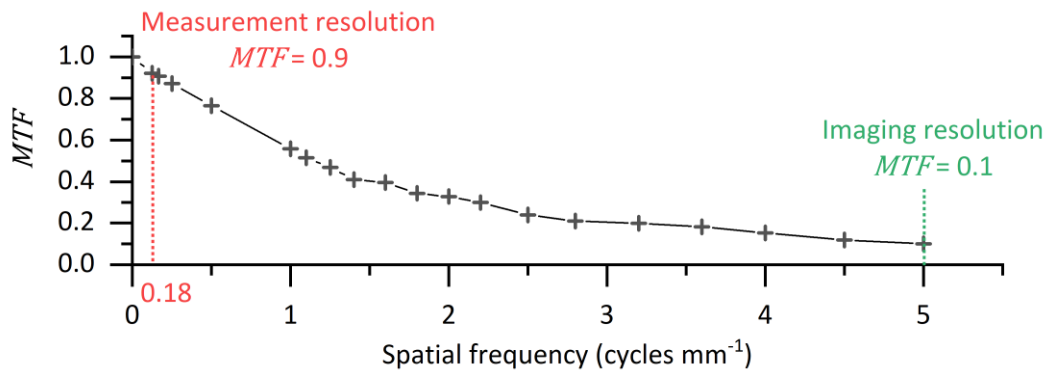


Figure 4.3-4 The  $MTF$  shows how well an imaging system can reproduce a scene containing the given spatial frequencies.

#### 4.4 THERMOGRAPHY OF STEADY STATE DED-LB/M RESULTS

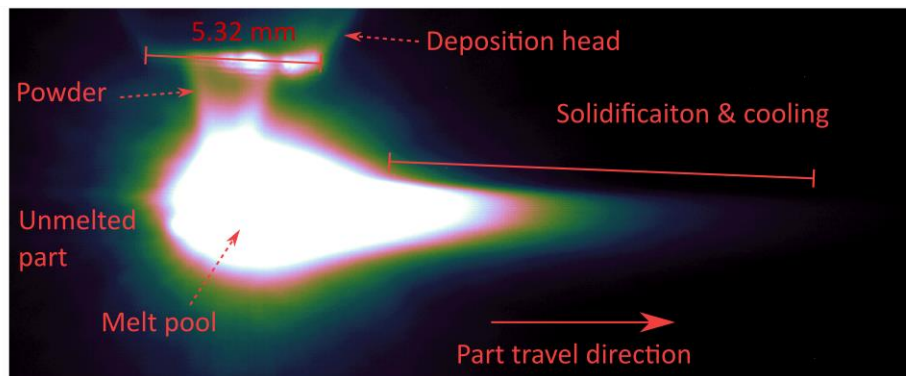


Figure 4.4-1 Low digital range  $NIR$  image of the  $DED-LB/M$  process showing reflected radiance from the deposition head. This was used to calculate the  $I\text{FOV}$  of the system.

Removal of the Bayer filter is a risky procedure, and a new method must be developed for each iteration of the PiCam device. Therefore, it would be advantageous to be able to use the PiCam sensor without the need to remove the Bayer filter. The exact spectral characteristics of the PiCam colour sensor are not known, but it is expected that Bayer filters are similar for all modern colour cameras. Figure 4.4-2 shows that the typical Bayer transmission profile for all three colour channels is similar in the wavelength range  $0.85\text{-}1.1\ \mu\text{m}$ . This is the range which we intend to use the PiCam as a thermographic system in  $AM/M$ . Usually the Near Infrared Radiation ( $NIR$ ) sensitivity of the sensor is blocked by an  $IR$  filter. Versions of the PiCam are readily available which come without this  $NIR$  filter present (PiCam-NoIR). The version 2 PiCam NoIR systems described in section 3.3.1 were used to capture data from a laser-based Direct Energy Deposition of metals ( $DED-LB/M$ )  $AM$  application.

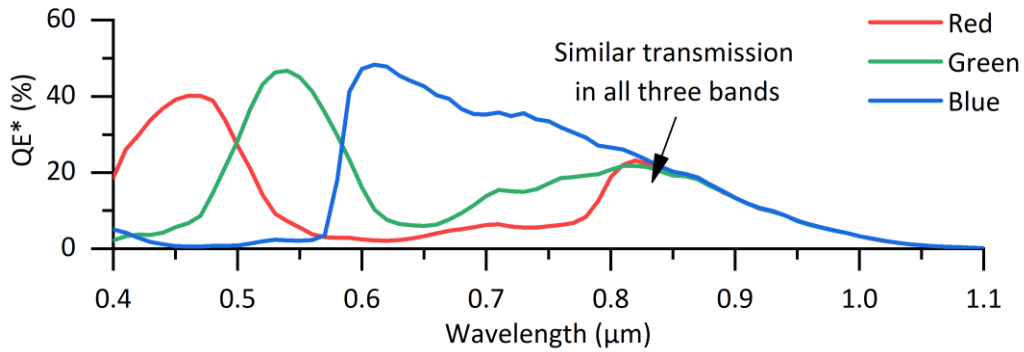


Figure 4.4-2 Typical Bayer filter  $QE^*$  curve for a colour Si camera. Reproduced, with permission, from the Thorlabs Kiralux 1.3 MP CMOS Compact Scientific Camera CS135CU datasheet, with permission.

#### 4.4.1 Instantaneous field of view

The Instantaneous Field Of View (*IFOV*) of the system used in this *AM/M* application was determined using an artefact of known dimension within the image (see Figure 4.4-1). The tip of the deposition head was measured to have a diameter of  $5.32 \pm 0.1$  mm ( $k=2$ ). The diameter was measured in the image to be  $199 \pm 6$  pixels ( $k=2$ ) using the reflection of the melt pool as illumination as per Figure 4.4-1. Giving a measured ***IFOV* =  $26.8 \pm 0.4$   $\mu\text{m}$**  ( $k=2$ ).

#### 4.4.2 Insufficient laser filtering & mosaic response

Some frames of data contain what appear to be specular reflections of the build laser, see Figure 4.4-3. For future *NIR* thermography with laser based *AM*, greater consideration to laser band blocking must be given when using Si detectors. There are frames where the specular laser reflections are not present in the image and these alone will be used for analysis. Rejecting the frames where specular reflections are present is possible because of the steady state nature of the experiment (see section 3.3.1). Frame to frame the thermal field does not significantly change in the *TFOV*.

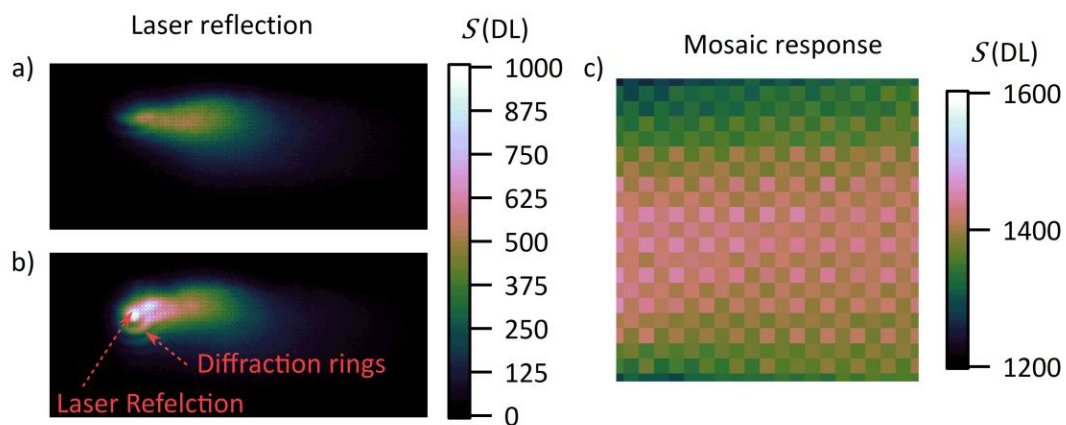


Figure 4.4-3 a) & b) Consecutive *NIR* images showing a specular reflection of the build laser. c) The Bayer filter causes a difference in responsivity despite the similarities in transmission profile above 850 nm.

#### 4.4.3 Freezing plateau as a radiometric fixed point

The outbreak of Covid-19 during 2020 meant that proper calibration of the system used to capture the *NIR* data from the *AM/M* process was impossible. Therefore the  $\lambda_{wien}$  from the V1 camera used in the characterisation work (with the same filtering) was used.  $A_{Wien}$  was adjusted to make the freezing plateau, shown in Figure 4.4-4, appear at the correct temperature. The freezing plateau was measured at  $118 \pm 1$  DL. The freezing temperature (solidus) of the stainless steel used is  $1675 \pm 15$  K [20]. The liquation (alloy content separation) inherent in the *DED-LB/M* process [21], and the sensitivity of the solidus temperature to alloy composition [20], indicates that that the uncertainty in this temperature is an underestimate. Using Eq 2.2-19 & Eq 2.2-20, the value of the emissivity multiplied by the Wien coefficient was calculated to be:  $\varepsilon \cdot A_{Wien} = 9.27 \times 10^5$ . Pichler(2020)[20] assumes that emissivity is independent of temperature. However, evidence is provided by Schöpp (2012)[22] that there may be a negative relation between emissivity and temperature in the liquid phase of steel.

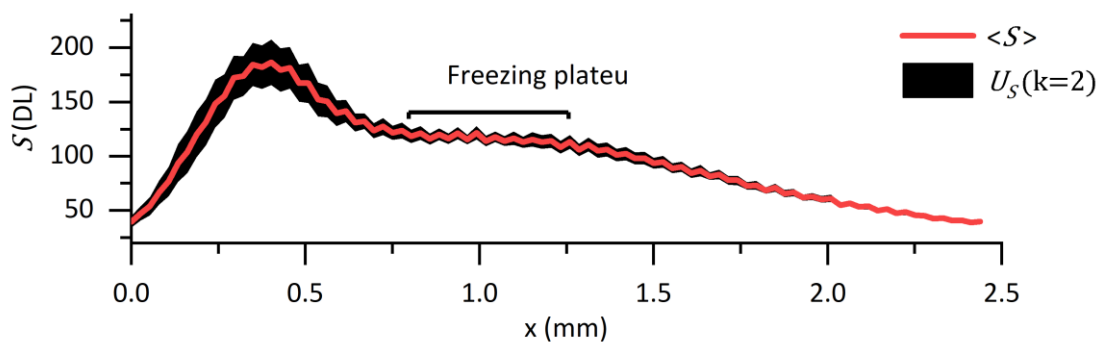


Figure 4.4-4 The average line profile through the melt pool clearly shows the freezing plateau where the temperature, and therefore radiance, is close to stationary.

#### 4.4.4 Melt pool as a function of linear energy density

The *AM/M* process parameter varied for this test was the speed of rotation of the cylinder (see section 3.3.1). The rotation speed affects the amount of energy put into each volume (or mass) of the part. The faster the part moves past the laser, the lower the energy density. This change in energy density should affect the melt pool size, which has a significant effect on part properties [23-27]. The energy density is expressed as the power of the laser divided by the speed of movement. Figure 4.4-5 shows qualitatively the difference in shape of the melt pool for the four different part velocities tested. Each image is the average of five frames of PiCam data.

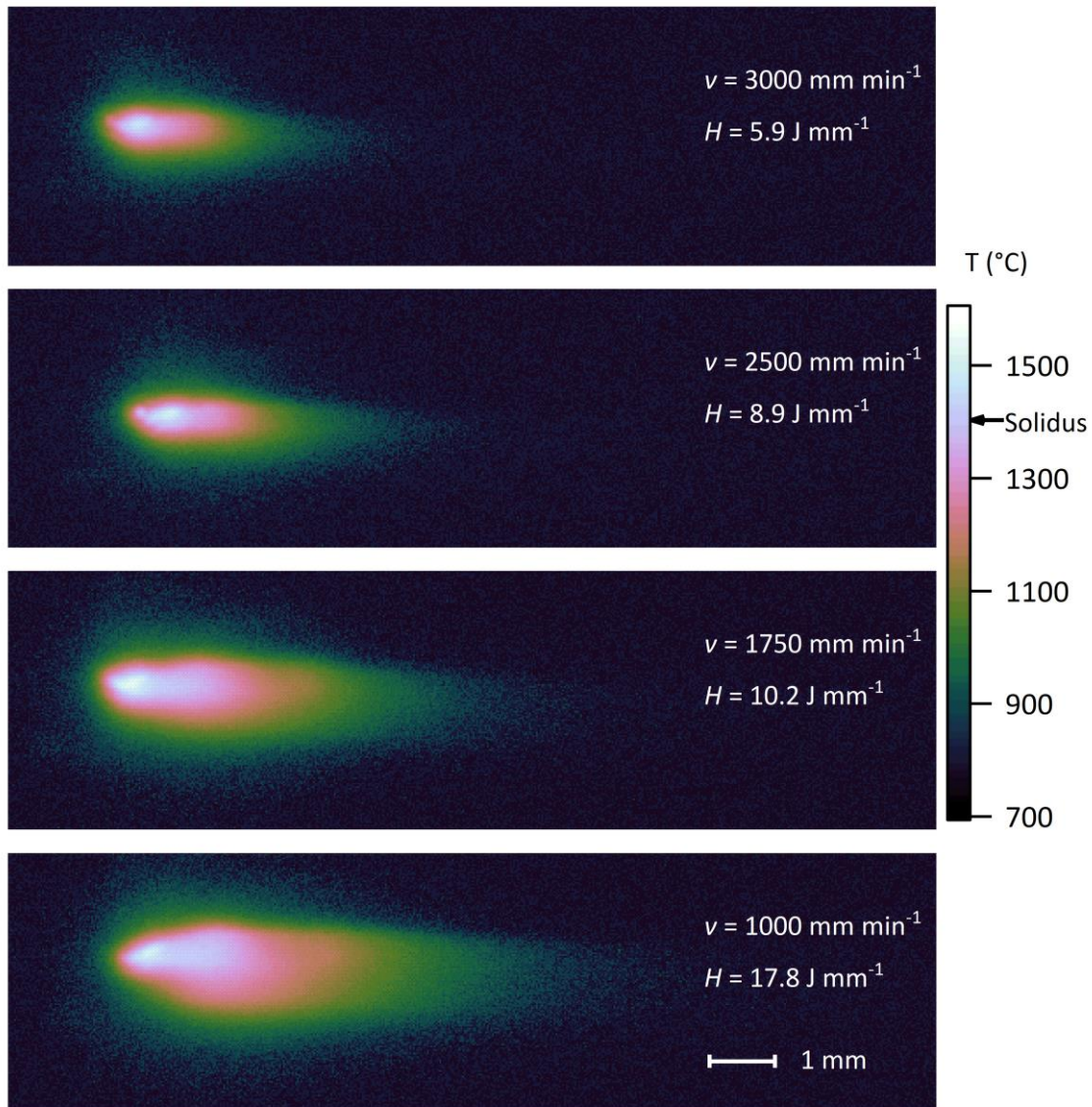


Figure 4.4-5 Average of 5 frames of PiCam data from 4 different laser (part) velocities ( $v$ ). Qualitatively the higher linear energy density ( $H$ ) the greater the extents of the high-temperature thermal field.

The data in Figure 4.4-6 shows how the size of the melt pool measured from the PiCam thermal images varies with linear power density. Ideally post build analysis of the different process parameters would be conducted to allow comparison of the crystal growth and hardness of the part. The data however, does allow us to show that the PiCam system is capable of making some of the measurements required for *AM/M* applications.

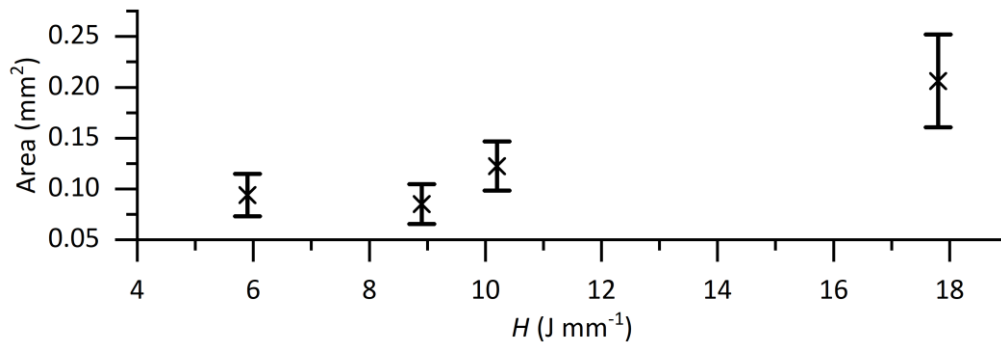


Figure 4.4-6 The measured melt pool shows the expected trend with linear power density ( $H$ ).

## 4.5 CONCLUSIONS

This chapter has shown that the PiCam system can operate as a high temperature thermographic system. The noise equivalent temperature difference shows that the instrument can resolve temperatures over a usable range. The software on the RasPi system can be modified to allow sufficient control of the camera parameters for quantitative thermographic measurements. The very small pixels of the sensor mean that the system is optically limited in measurement resolution, well below the spatial sample frequency of the system.

However, the low frame rate limits the use of the PiCam in *AM/M* applications, because the steady state can rarely be assumed. The PiCam will therefore miss the vast majority of the print, capturing only disparate snapshots of the build. Also, insufficient filtering of the laser wavelengths means that radiometric measurements of the melt pool are unreliable.

Due to the optically limited performance of the system, measurement of the *MTF* and the expected spatial frequency components of the scene are necessary to understand the expected levels of error in measurement of a thermal field. The most useful image quality metric for thermographic applications is the *measurement resolution* of the instrument. The non-smooth spectral response of the PiCam is a problem that should be solved before the deBayered system can be considered a serious thermographic instrument. Using the PiCam with the Bayer filter in place is an attractive prospect, but the mosaic response highlighted means that the three different colour pixels must be calibrated independently to account for three different spectral responses. This correction could be coded into the PiCam, but the spectral shape of the source will affect the relative responsivity of the colour pixels. A way to mitigate this problem would be to reduce the spectral band pass of the system, but this would raise the low temperature limit.

## 4.6 REFERENCES

1. Waller, M.A. and S.E. Fawcett, *Click Here to Print a Maker Movement Supply Chain: How Invention and Entrepreneurship Will Disrupt Supply Chain Design*. Journal of Business Logistics, 2014. **35**(2): p. 99-102.
2. Robinson, D.W., et al., *3D thermography for improving temperature measurements in thermal vacuum testing*. CEAS Space Journal, 2017. **9**(3): p. 333-350.
3. Stanger, L., et al., *Thermal Imaging Metrology with a Smartphone Sensor*. Sensors, 2018. **18**(7): p. 2169.
4. Wilkes, T., et al., *Ultraviolet Imaging with Low Cost Smartphone Sensors: Development and Application of a Raspberry Pi-Based UV Camera*. Sensors, 2016. **16**(10): p. 1649.
5. Li, J., B. Wu, and C. Myant, *The current landscape for additive manufacturing research*. 2016.

6. FLIR Integrated Imaging Solutions Inc, *Mono camera Sensor Review*, <https://www.flir.com/globalassets/iis/guidebooks/2019-machine-vision-emva1288-sensor-review.pdf>, Document Number: R: 19-0709-B&CS, 2019, accessed on 09/04/2021
7. British Standards Institution, BS ISO 10878:2013, Non-destructive testing — Infrared thermography — Vocabulary, 2013
8. Hecht, E., *Optics*. 4th International ed. 2002: Addison Wesley, 1301 Sansome St., san Francisco, CA9411.
9. Hecht, E., *Fourier Optics*, in *Optics*. 2002, Addison Wesley, 1301 Sansome St., san Francisco, CA9411. p. 519-559.
10. Michail, C.M., et al., *Figure of Image Quality and Information Capacity in Digital Mammography*. BioMed Research International, 2014. **2014**: p. 11.
11. Nill, N.B., *Conversion Between Sine Wave and Square Wave Spatial Frequency Response of an Imaging System*. 2001, Center for Integrated Intelligence Systems: MITRE corporation.
12. Vollmer, M. and K.P. Möllmann, *Characterization of IR cameras in student labs*. European Journal of Physics, 2013. **34**(6): p. S73.
13. Gunapala, S.D., et al. *Modulation transfer function of infrared focal plane arrays*. in *SPIE Optical Engineering + Applications*. 2015. San Diego, Ca, USA: SPIE.
14. Lane, B.M., et al. *Performance Characterization of Process Monitoring Sensors on the NIST Additive Manufacturing Metrology Testbed*. in *Solid Freeform Fabrication Symposium*. 2017. Austin, TX.
15. Bhushan, J. and A.K. Jaiswal, *Limitations in the determination of the sine-wave response from the square-wave response*. Optics Communications, 1974. **12**(2): p. 181-182.
16. Coltman, J.W., *The Specification of Imaging Properties by Response to a Sine Wave Input*. Journal of the Optical Society of America, 1954. **44**(6): p. 468-471.
17. Swyt, D.A., *The National Measurement System for Optics*, N.B.o. Standards, Editor. 1976, National Institute of Standards and Technology: USA.
18. British Standards Institution, BS ISO 12233:2017, Resolution and spatial frequency responses, in *Photography — Electronic still picture imaging*, 2017
19. Envall, J., et al., *Spatial Scatter Effects in the Calibration of IR Pyrometers and Imagers*. International Journal of Thermophysics, 2009. **30**(1): p. 167-178.
20. Pichler, P., et al., *Measurements of thermophysical properties of solid and liquid NIST SRM 316L stainless steel*. Journal of Materials Science, 2020. **55**(9): p. 4081-4093.
21. DebRoy, T., et al., *Additive manufacturing of metallic components – Process, structure and properties*. Progress in Materials Science, 2018. **92**: p. 112-224.
22. Schöpp, H., et al.. "Temperature and emissivity determination of liquid steel S235." Journal Of Physics D: applied Physics, 2012. **45**(23): 235203.
23. Ansari, M.J., D.-S. Nguyen, and H.S. Park, *Investigation of SLM Process in Terms of Temperature Distribution and Melting Pool Size: Modeling and Experimental Approaches*. Materials (Basel, Switzerland), 2019. **12**(8).
24. Clijsters, S., et al., *In situ quality control of the selective laser melting process using a high-speed, real-time melt pool monitoring system*. The International Journal of Advanced Manufacturing Technology, 2014. **75**(5): p. 1089-1101.
25. Fisher, B.A., et al., *Toward determining melt pool quality metrics via coaxial monitoring in laser powder bed fusion*. Manufacturing Letters, 2018. **15**: p. 119-121.
26. Ghosh, S., et al., *Single-Track Melt-Pool Measurements and Microstructures in Inconel 625*. JOM, 2018.
27. Hooper, P.A., *Melt pool temperature and cooling rates in laser powder bed fusion*. Additive Manufacturing, 2018. **22**: p. 548-559.

## 5. SPATIALLY RESOLVED HIGH DYNAMIC RANGE THERMOGRAPHY IN COMMERCIAL POWDER BED FUSION ADDITIVE MANUFACTURING

---

This chapter presents the characterisation and use of a high specification, custom designed thermographic instrument. A numerical method for measuring the spatial transfer function of the instrument is developed and implemented. A technique for quantitatively assessing the accuracy of the thermal field mapping is developed. The technique uses small, known radiance scenes similar to those found in the additive manufacture of metals (*AM/M*). This assessment technique is used to validate and compare the three mapping methods described in chapter 3. Finally, data acquired with the instrument from a modified commercial *AM/M* machine is presented, the effect of the reconstructions on the measured thermal fields and the quality of the data is discussed.

In this chapter, a commercial laser-based powder-bed-fusion of metals (*PBF-LB/M*) *AM* machine was retrofitted to allow acquisition of *IR* data from the top surface of the build during the metal printing (melting - solidification) process, as per section 3.3.2. The thermographic instrument was calibrated and characterised using the laboratory-based techniques described in chapter 3.

Commercial *AM/M* is a significant and expanding tool in the manufacturing sector [1, 2]. Infrared Radiation (*IR*) thermography can be used to make quantitative measurements of the thermal fields in commercial *AM* processes [3, 4]. Quantitative measurements of the thermal fields allow for validation of physical models [5]. Validation is necessary to give material scientists and product engineers confidence that the models can be relied upon to predict material and part properties. Specifically, the liquation and solidification dynamics around the melt pool are of particular concern as they heavily influence the grain structure and formation of defects, and hence material properties, of the final printed part [6].

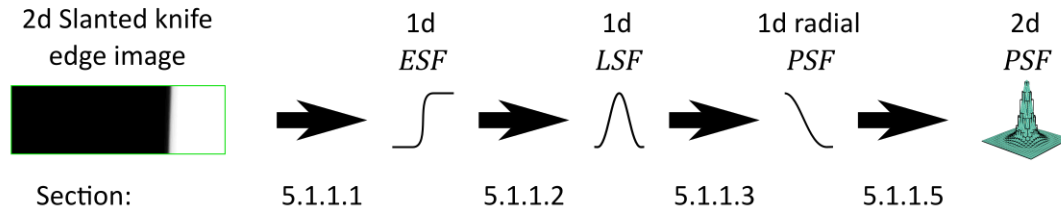
*IR* imaging is a key tool for process control of commercial *AM* machines [7, 8]. Process control does not inherently require quantitative measurement of temperature (thermography). It can sometimes be sufficient, for commercial purposes, to use the direct measurement of the radiance of the surface to act as a feedback process parameter, rather than expending the additional effort required to convert measurements of radiance into quantitative thermal measurements. Whether quantification of the thermal field is required or not, the spatial transfer function of the instrument plays an important role in the fidelity of the measured image.

Original contributions to the field in this chapter are:

- Use of numerical methods to convert the measured edge spread function to the point spread function.
- A thermal field mapping method which uses a thermal field model as the basis for the deconvolution rather than allowing the thermal field to take any shape.
- Quantitative assessment of the accuracy of thermal field mapping, by use of known thermal fields of similar size and distribution to the thermal fields found in *AM/M* processes.

Aim : Improve accuracy of thermal field measurements

Objective: Measure the *PSF*



Objective: Validate reconstruction methods

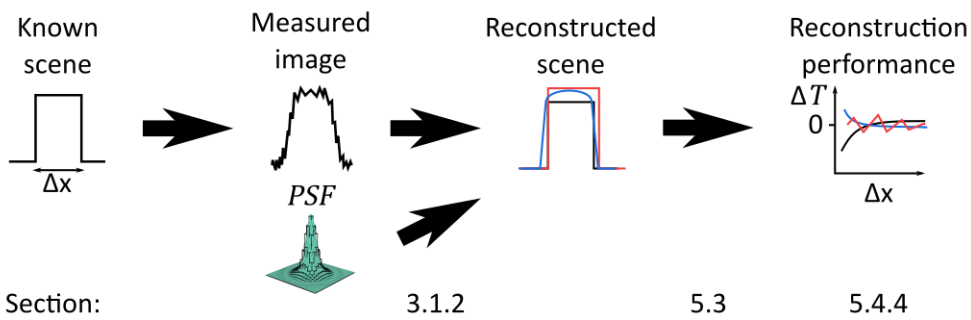


Figure 5-1 Summary of the main objectives of this chapter.

The summary in Figure 5-1 is intended as a reference for the relatively dense numerical methods explained in this chapter. The *sections* in Figure 5-1, show where details about the corresponding step can be found.

## 5.1 CHARACTERISATION ANALYSIS

### 5.1.1 *PSF* determination

A slanted knife edge was used to determine the Point Spread Function (*PSF*), which is a representation of the spatial transfer function of the thermographic instrument (see section 2.4 for theory & 3.2.2 for practical implementation). The Method for calculation of the Edge Spread Function (*ESF*) from an image of the slanted knife edge is similar to that of Lane & Whintont (2015)[9]. Lane & Whintont (2015)[9] fit a model (referred to here as: *3G Fit* (3 Gauss)) to the *ESF* data directly and then algebraically convert this fitted function into the *PSF*. Their method has the advantage that no smoothing of the data is required, and the model can be fit directly to the linearised data (linearised in this context means transformation from a 2d knife edge image to a 1d *ESF*). Also, once the model is deemed sufficiently well fit, manipulation is relatively simple. this work differs from the in that no model was used to approximate the *ESF* Instead numerical methods were utilised to convert the *ESF* to the *PSF*. This method has the advantage that details of the *PSF* are not obscured by the model. Comparisons between the methods are made throughout the description of the analysis.

Du & Voss (2004)[10] measured the *PSF* of an imaging system with a different method to that used here. Their assumption of an exponential decay of *PSF* with radius at large radii (referred to here as: *Exp Fit*) was implemented to remove noise in the low amplitude wings of the *PSF* distribution.

#### 5.1.1.1 *Knife edge image to ESF*

Once the *ROI* was determined manually, a Matlab script was used to convert the images into regularly super-sampled (more than every pixel) *ESF* data. This was done by the following procedure.

- Determination of the 'Mid value', as the midpoint between the 'High value' and 'Low value'. Which are taken from the mean pixel values at the two extremes of the *ROI*.
- Linear interpolation of the position of the Mid value (in the *i* dimension), for each row (*j*).
- Linear regression to find the gradient and position of 'Edge fit line' passing through these Mid value positions.
- Determination of the position ( $x_{ESF}$ ) of each pixel as their perpendicular distance from the Edge fit line. as per Eq 5.1 1.
- Manual determination of the best regular super-sampling frequency ( $F_{SS}$ ) to use, based on the distribution of  $x_{ESF}$ .
- Resampling of arbitrarily spaced data to a regular mesh by linear interpolation (Figure 5.1 2 b).

The exact position of the edge fit line ( $c_l$ ) is not important as it can be shifted later to centre the origin at the correct location. The Gradient ( $m_l$ ) is significant in determining the  $x_{ESF}$  values for each pixel. Some structure remains in the edge fit line residuals (Figure 5.1-1 b)), their magnitudes are small, meaning that the edge fit line is acceptable. The calculation for  $x_{ESF}$  is the magnitude of a line passing through the pixel centre position (*i,j*) and intersecting with the edge fit line, perpendicularly to it.

$$x_{ESF} = \frac{j - m_l i - c_l}{\sqrt{m_l^2 + 1}} \quad \text{Eq 5.1-1}$$

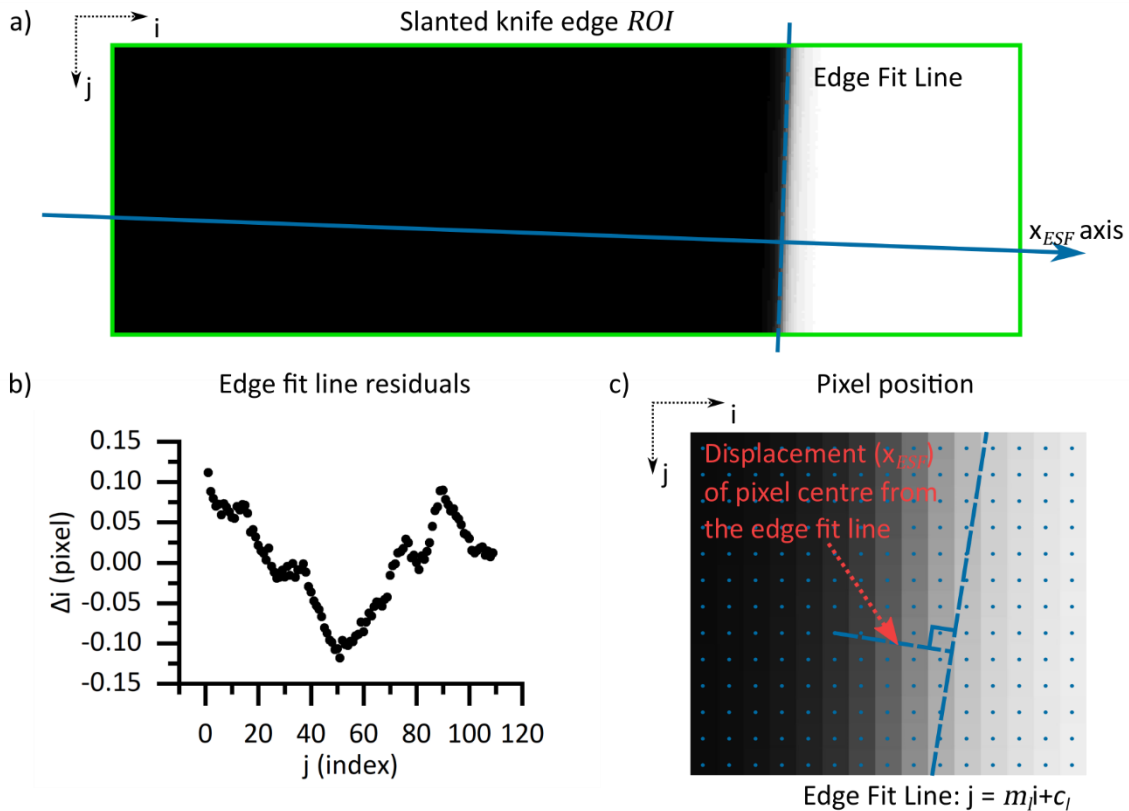


Figure 5.1-1 a) Typical ROI showing edge fit line. b) Difference between the position of the mid value in each row and the edge fit line. c) The  $x_{ESF}$  position of each pixel centre is determined by its perpendicular distance from the edge fit line.

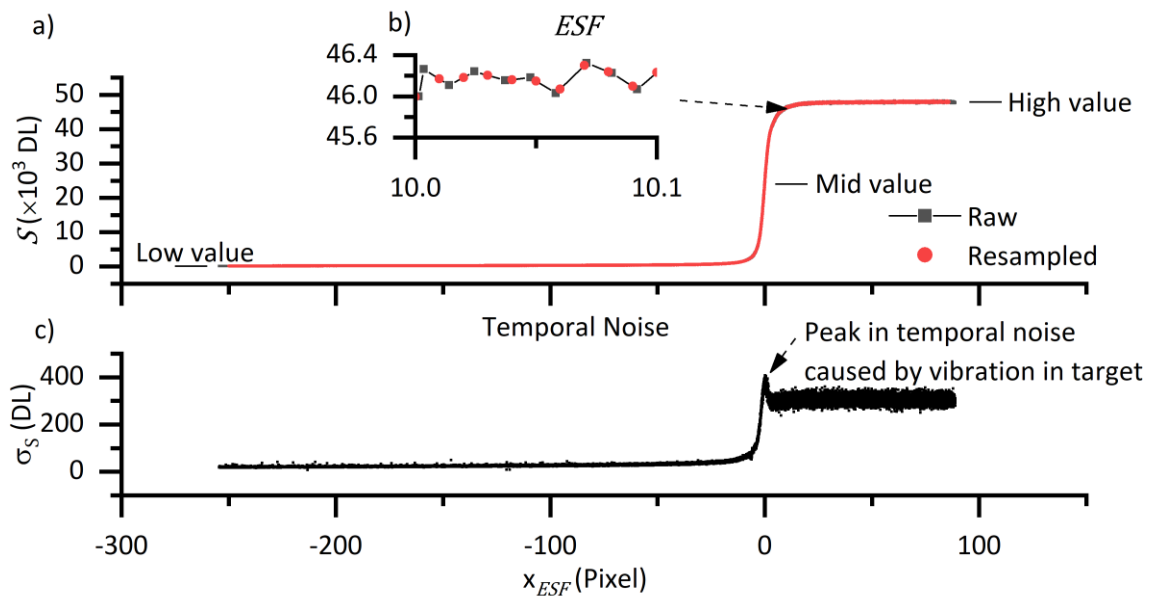


Figure 5.1-2 a) Representative ESF Data from a linearised slanted knife edge image. b) Detail of the resampling of arbitrarily spaced to regularly spaced data. c) Standard deviation of each pixel between frames (time).

### 5.1.1.2 *ESF to LSF*

The Line Spread Function (*LSF*) is the spatial derivative of the *ESF* (see section 2.4.3). Numerical differentiation of real data, containing noise, requires smoothing (filtering), for this work frequency space filtering was used. The steps to convert the *ESF* to the *LSF* are:

- Padding of the data to bring the edge values to zero, with only low frequency components.
- Application of a suitable low-pass smoothing filter, in frequency space as per Figure 5.1-3 c).
- Numerical differentiation of the smoothed data,  $\Delta S/\Delta x_{ESF}$ .

*ESF* data does not tend to zero at the edges, meaning that a Fast Fourier Transform (*FFT*) (see section 2.3.5) will treat the data as having a sharp transition to zero at the ends (edge effects). This will add high amplitude, high frequency components to the *FFT* which are not truly present in the data. To remove end effects, the data was padded with a slowly varying (compared with the *ESF*) gaussian roll off, see Figure 5.1-3 a). A Gaussian padding with a  $\sigma$  of 1000 pixels was used, the padding was extended to  $15\sigma$  (15000 pixels) beyond the original extents of the data.

The *FFT* of the padded *ESF* curve is shown in Figure 5.1-3 b). A low-pass filter was applied to the padded data to remove the high frequency noise component. The low frequency padding was not affected by the filtering, and was trimmed after filtering to regain the smoothed *ESF* (Figure 5.1-3 d)). The low-pass filter (*Filter*) is defined by two parameters,  $W_0$  &  $W_\sigma$ , which determine the shape of *Filter* in frequency space as:

$$\begin{aligned} 0 < F_x < W_0 & \quad \text{Filter}(F_x) = 1 \\ W_0 < F_x < F_s/2 & \quad \text{Filter}(F_x) = e^{-\frac{(F_x - W_0)^2}{2W_\sigma^2}} \end{aligned} \quad \text{Eq 5.1-2}$$

The *Filter* is applied to the data by point-by-point multiplication in the frequency domain:

$$ESF = iFFT(\text{filter} \times |\tilde{S}(F_x)|) \quad \text{Eq 5.1-3}$$

Once the data was filtered, numerical differentiation was applied. A representative result of this can be seen in Figure 5.1-4. The noise in the *LSF* was larger on the high-signal side of the knife edge. This can be explained by looking at the high range detail in the representative knife edge image in section 3.2.2. There is a patchiness in the high-range-part of the image, which is probably caused by imperfections in the lens system and possibly by local variation of the Quantum Efficiency (*QE*) of the Si detector material. This large-scale noise is not filtered out sufficiently by the low-pass filter. Therefore, the low side of the signal only is used to determine the *PSF*. There is still a small magnitude of noise left in the tails of the *ESF*, but this is addressed in section 5.1.1.4.

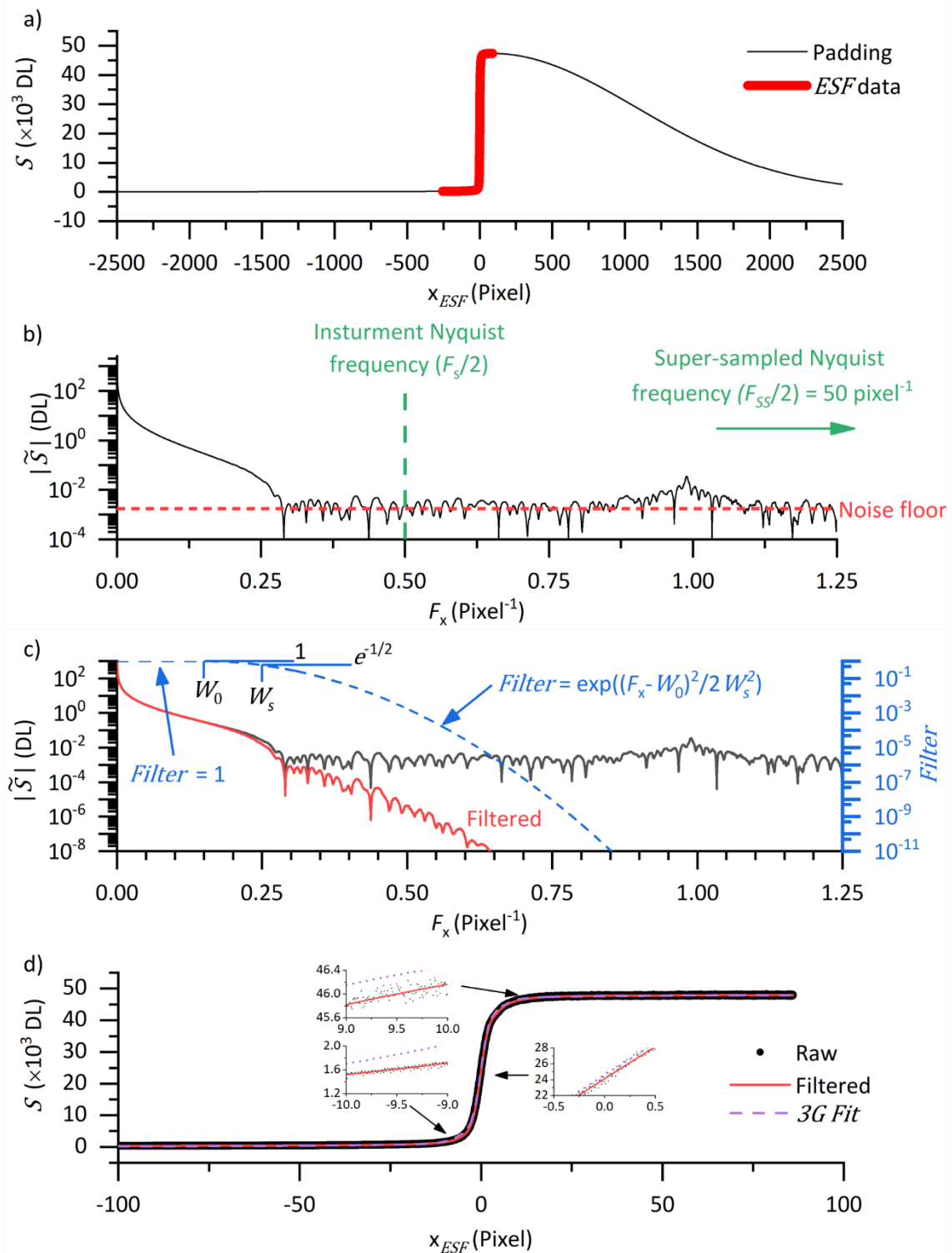


Figure 5.1-3 a) Gaussian padding is used to remove edge effects of the data. b) FFT of the padded data in a). c) A filter is used in the frequency domain as per Eq 5.1-3 to remove noise in the ESF to allow numerical differentiation. d) The  $iFFT$  of the data in c) with the padding removed. The 3G Fit model is shown for comparison. The 3G Fit method misses some of the detail of the ESF of this instrument, as can be seen for the insets of d).

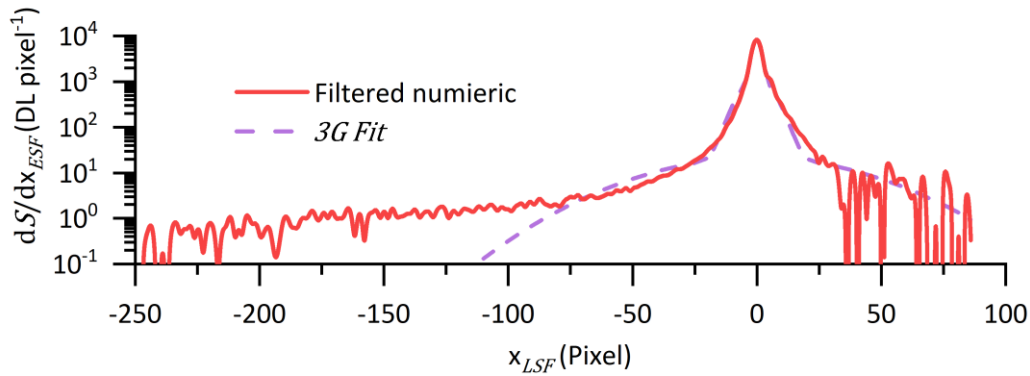


Figure 5.1-4 Measured line spread function. The noise on the high-signal side (right) of the peak is significantly larger than on the low signal side after the low pass filter has been applied.

The parameters  $W_0$  and  $W_\sigma$  affect the shape of the measured  $LSF$ . Their values were chosen to minimise the perturbations to the central peak of the  $LSF$ , while minimising noise in the low amplitude wings, the lower the noise which can be achieved in the wings the further out from the impulse (edge) the response function can be measured. From Figure 5.1-4 the noise on the high side (right) limits the measurement of the  $LSF$  to  $\sim 25$  pixels, whereas on the low signal (left) side the curve looks good (smooth) out to  $\sim 175$  pixels.

#### 5.1.1.2.1 Choosing The right filter parameters

The determination of the optimal filter is a deep problem. The purpose of the filter is to remove all artefacts from the data which are noise, while leaving all the underlying form. Filter design is a self-contained discipline, and more time than was available could have been devoted to optimising the filter process. In this work, the form of the output (the  $LSF$ ) is used to inform the choice of filter parameters. The balance must be found between minimising the flattening of the peak of the  $LSF$ , and maximising the reduction in noise in the wings. Some of the parameter sets around the optimal values are shown in Figure 5.1-5 and Figure 5.1-6. A judgment call was made, and the filter parameters for the  $LSF$  data generated from this experiment are shown in Table 5.1-1

Table 5.1-1 Frequency space filtering - parameters

$W_0$	0.2 Pixel <sup>-1</sup>
$W_\sigma$	0.1 Pixel <sup>-1</sup>

Variation of the filter parameters about those chosen in Table 5.1-1 reveals what might be considered to be the underlying form of the  $LSF$ . The peak shape and position tends towards a value with a low degree of filtering, and the wings tend towards a form with a high degree of filtering. Comparison with the  $3G Fit$  used in Lane & Whitenton (2015) [9], shows that no combination of filter parameters will bring the  $LSF$  measured by numerical methods in line with the model. Thus the model is inappropriate for this instrument. This kind of comparison of the form of the measured  $PSF$  may be more informative than comparing the  $ESF$  data with the  $3G Fit$ , or any model, directly.

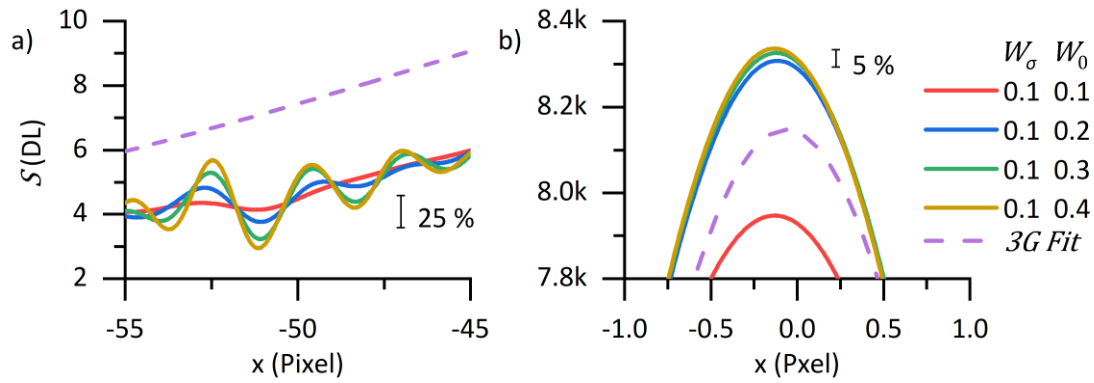


Figure 5.1-5 Using a  $W_0$  which is too high leaves too much noise in the low-amplitude wings of the distribution, shown by the yellow curve in a) ( $W_0 = 0.4, W_\sigma = 0.1$ ). Using a  $W_0$  which is too low, removes too many of the high frequency components, reducing the amplitude of the peak of the LSF. The effect of over filtering can be seen in the red line in b) ( $W_0 = 0.1, W_\sigma = 0.1$ ).

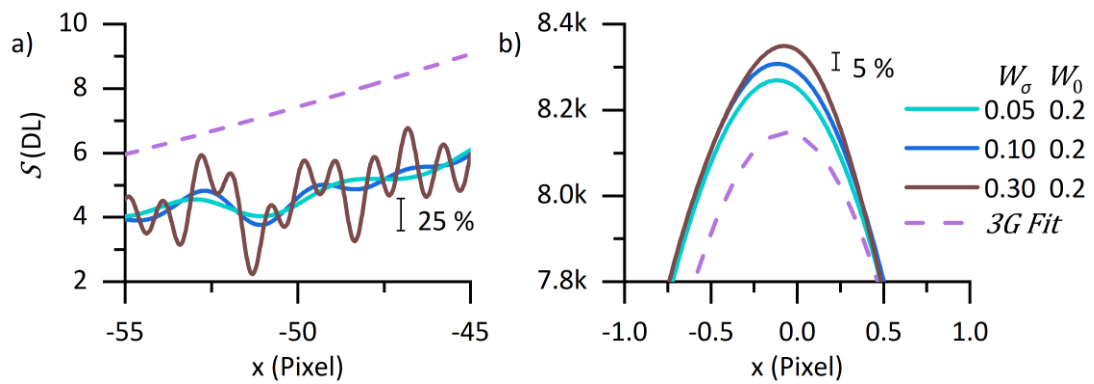


Figure 5.1-6 The rate of roll-off of the filter is specified the by the  $W_\sigma$  parameter. Making  $W_\sigma$  too large keeps too many of the very high frequency components in the data, shown by the brown line in a) ( $W_0 = 0.2, W_\sigma = 0.3$ ). a) & b) show the apparent failure of the 3G Fit method to replicate the form of the LSF calculated by numerical methods.

### 5.1.1.3 LSF to PSF

The *PSF* is the one-dimensional projection of the *LSF* (see Section 2.4.3). Inversion of the integral to calculate the *PSF* from the *LSF* is achieved by an inverse Abel transform [11]. Mathematically this is:

$$PSF(r) = -\frac{1}{\pi} \int_r^\infty \frac{1}{\sqrt{x^2 - r^2}} \left( \frac{dLSF(x)}{dx} \right) dx \quad Eq 5.1-4$$

If the functional form of the *LSF* is known (or assumed) then the transform can be solved algebraically. A numerical solution of the transform is not trivial. A popular solution is by Pretzier (1991)[12]. The method uses Fourier analysis to decompose the unknown *PSF*, and uses least squares optimisation to fit the forward Abel transform of these components to the known *LSF*. The method has been implemented in Matlab by Killer (2013)[13]. The algorithm was tested with simulated data of known inverse Abel transform and was found to reproduce the analytic solution accurately, in the presence of noise at the same scale as the data. A parameter in the algorithm is the number of Fourier components ( $N_{Abel}$ ) in the unknown *PSF* to be optimised.

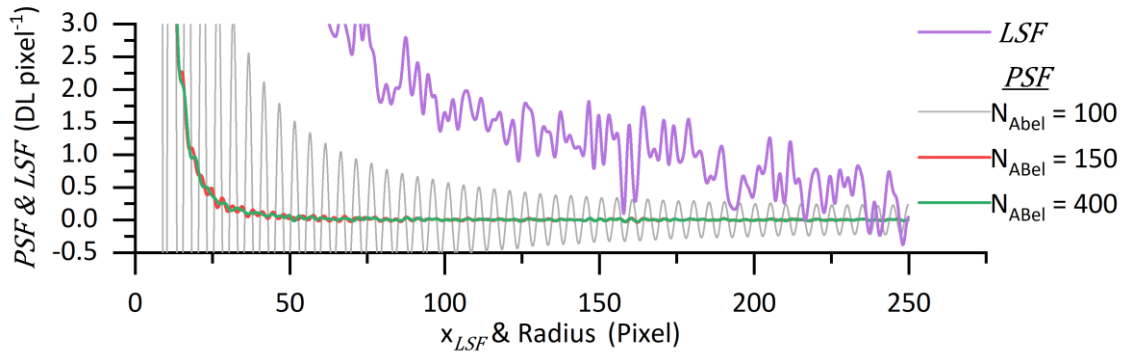


Figure 5.1-7 The inverse Abel Transform converts the *LSF* to the *PSF*. Above  $N_{Abel} \approx 150$ , the solution converges. The *LSF* has a Cartesian x-axis, whereas the x-axis of the *PSF* is radial.

The peak in the *LSF* is used to split the *LSF* into two sections. The section between the peak and the low-signal-side of the distribution is used. The signal to noise ratio of this part of the data was significantly better than the high-signal side, meaning that the *PSF* can be measured to a larger radius. When this split is made the *PSF* must be assumed to be rotationally symmetric, this assumption is implicit in the *3G Fit* method [9].

Numeric Abel transform - number of components used

$N_{Abel}$  200

#### 5.1.1.4 Large-radius exponential decay fit

There are features in the measure *PSF* which persist to the extents of the distribution. It was assumed that these features are related to the non-uniformity noise in the knife edge image.

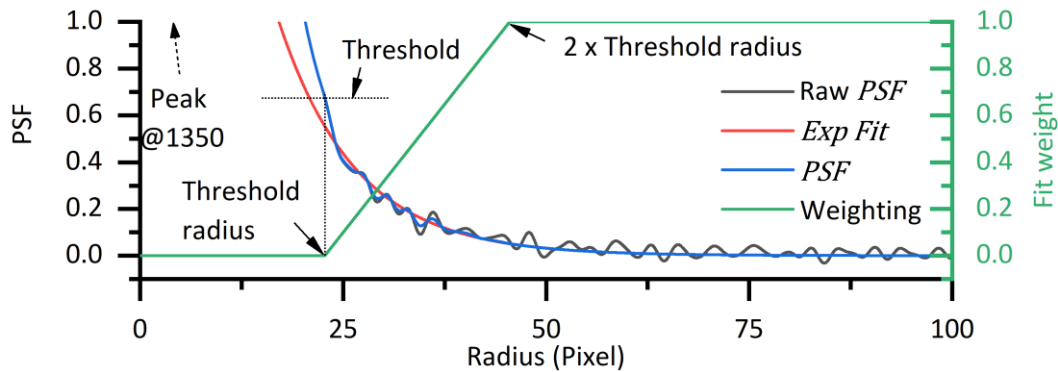


Figure 5.1-8 An exponential decay is fit to the large radius components of the *PSF* to remove noise in the signal.

Taking a similar approach to Hong & Voss[10], the tails of the *PSF* distribution was modelled as an exponential. This was implemented using an arbitrary amplitude threshold, 1/2000 of the amplitude of the peak. An exponential was then fit to the *PSF* from the point where the amplitude fell below this threshold (Threshold Radius) to the extreme of the measure distribution (250 pixels). The fit function used was:

$$Exp Fit = A_0 e^{A_1 \cdot Radius} \quad Eq 5.1-5$$

Where  $A_1$  is negative. linear weighting function (illustrated in Figure 5.1-8), between the threshold radius and twice the threshold radius, was used to remove any discontinuities in the transition between the raw measured  $PSF$  and the exponential model.

### 5.1.1.5 $PSF$ to 2d distribution

Convolution or deconvolution operations (see Section 2.4.3.2) require two arrays of data with the same number of dimensions and the same sampling frequency. To convolve or deconvolve images, the radial  $PSF$  calculated in the previous sections was converted into a 2d pixel-sampled array by:

- Manual selection of the number of Sub pixel evaluation points ( $N_{Sub}$ ), and total number of pixels in the generated  $PSF$  ( $N_{Pix}$ ).
- Create a square array of cartesian coordinates, with the origin at the centre, these are the 'evaluation points'. The sampling is determined by  $N_{Sub}$  (see Figure 5.1-9).
- Calculate the radial position of each of the evaluation points.
- Evaluate the  $PSF$  at each of these radial positions by linear interpolation of the  $PSF$  created in Section 5.1.1.3.
- Take geometric average of  $N_{Sub} \times N_{Sub}$  point, to resample to the same sample frequency as an image.

Some uses for the  $PSF$  allow sub pixel evaluation to be utilised, in which case the fifth step can be omitted. The  $PSF$  was normalised to have a total 2d integral value of unity, in order to maintain the total signal level of any image to which the  $PSF$  is applied (moves signal from one pixel to another).

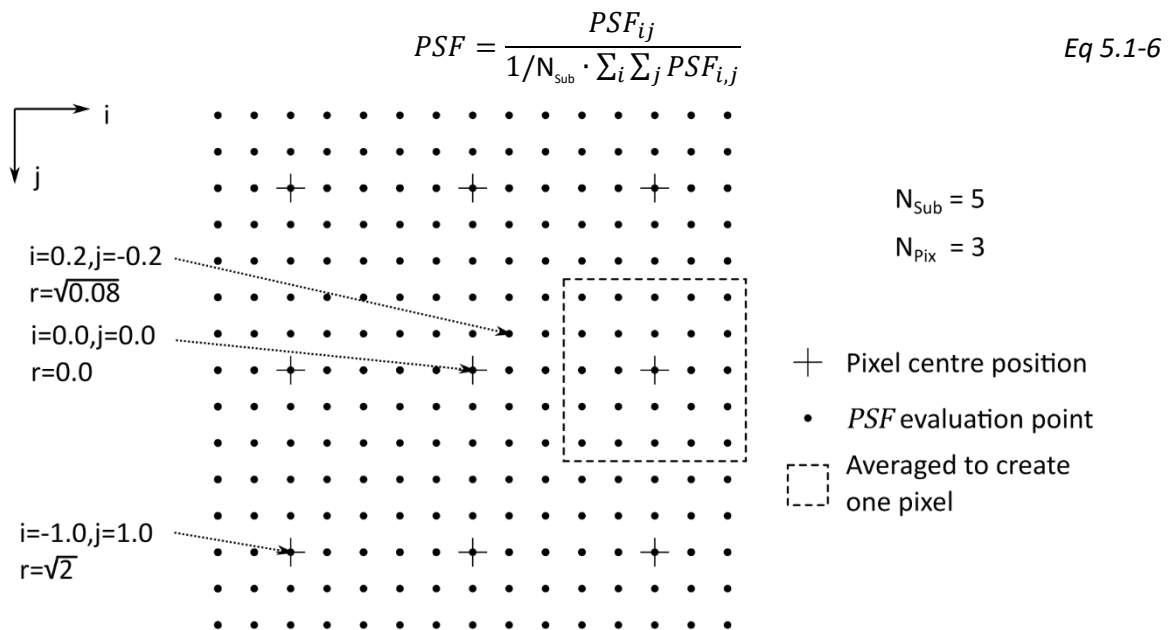


Figure 5.1-9 Exemplar  $PSF$  sampling grid. The radial  $PSF$  was sampled at multiple points and then averaged over each pixel to create the  $PSF$  convolution kernel.

Sub pixel evaluation of the  $PSF$  is advantageous because the  $PSF$  changes significantly within a single pixel, and a single evaluation of the function will poorly represent the true behaviour of the  $PSF$ .

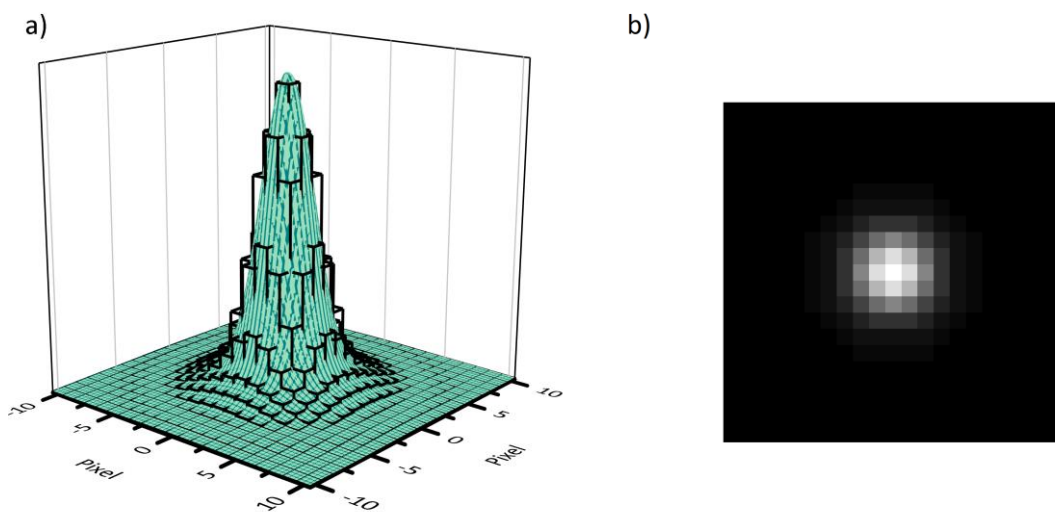


Figure 5.1-10 a) Shows the PSF taken from Figure 5.1-9 mapped to a rotationally symmetric distribution.  $N_{Sub} = 5$ ,  $N_{pix} = 21$ . b) Shows the pixelated PSF kernel, which can be used in conjunction with an image to either convolve a simulated scene or deconvolve a measured image.

#### 5.1.1.6 Z dependence of PSF

The PSF was measured at 0.5 mm increments along the z axis. The z position of *best focus* was not known before analysis. There are different ways of specifying best focus. The PSF is affected differently by the various aberrations present in the imaging system [14]. The position of best focus is somewhat subjective as the effect of the various aberrations can be minimal at different positions. Figure 5.1-11 a) shows that the magnitude of the peak of the PSF behaves similarly to a second order polynomial over the range of z values measured. The maximum ( $z_{Extrema}$ ) in Figure 5.1-11 b) shows that the extrema of the PSF, when assumed second order polynomial, does not stay in the same location. The second order polynomial approximation also becomes less valid at increasing radius. The position of best focus is chosen as the extrema of the polynomial approximation at zero radius. The extrema is calculated from the polynomial coefficients  $B_i$  (see Figure 5.1-11 a)) by:

$$Z_{Extrema} = -\frac{B_1}{2B_2} \quad \text{Eq 5.1-7}$$

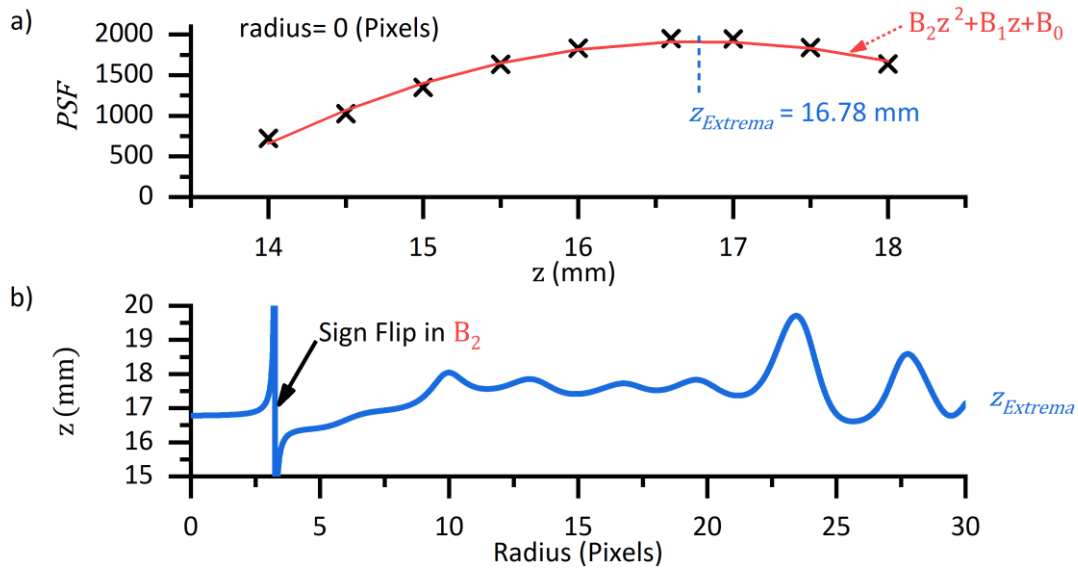


Figure 5.1-11 a)  $z$  dependence of the magnitude of the PSF at the central position. The  $z$  scale here has an arbitrary origin taken from the micrometer attached to the 3-axis stage. b) Ill-behaved nature of the second order polynomial approximation of the PSF as a function of radius. There is a rapid change, followed by an inversion of the sign of the second order term of the polynomial fit as a function of radius.

## 5.2 IR AM DATA ANALYSIS

This section describes the analysis and data preparation used to assess the *IR* data acquired from the experimental setup described in section 3.3.2.

### 5.2.1 Mean thermal field

A laser exposure detection algorithm was developed within the group by Thomas Rockett (University of Sheffield, Sheffield, UK), which processed the many frames of *IR* data to identify the mean thermal field. The build laser was a pulsed system. Each exposure of the laser created a distinct *heated zone* in the scene. Multiple heated zones were imaged within a single exposure of the camera, forming a straight line of hot spots on the laser travel vector. An automated heated zone detection algorithm was developed to identify the heated zones which met a set of detection criteria. The method involved a  $29 \times 195$  pixel *ROI* that was cropped within the image and added to a historical database of *ROIs* for each video frame. The algorithm searched for regions of high signal level within an image and used the measured laser travel vector (determined from multiple frames) to reject ejected particles and other anomalous readings.

The heated zones at the beginning and end of the exposure were less intense than the central Laser exposures. The physical explanation for this behaviour is that only a portion of the detectable heating and cooling cycle was acquired. We can infer from this behaviour that an entire cycle of heating and cooling occurred for the uniform central heated zones of each image. The detection algorithm required at least 3 detected heated zones for each *ROI* added to the database, the central heated zone of interest and one heated zone to each side. Any detected heated zone with a missing adjacent detected heated zone was rejected from the database. It can, therefore, be asserted that the entire thermal cycle was present for each central heated zone in the database.

### 5.2.2 Thermal field model

The heated zones were assumed to be rotationally symmetric gaussians in shape. The gaussian distribution is characterised by two parameters, the magnitude of the peak ( $T_{Peak}$ ) and the width ( $\sigma_T$ ).

This is justified by the standard assumption of a gaussian beam profile for the heat source [15]. The model was projected at 45° to the normal to account for the off-axis viewing angle of the thermographic instrument. The slope of the laser travel vector (see Figure 5.5-3) was calculated by fitting a straight line to the positions of the peaks in the mean image. The scene was assumed to be an orthographic projection at 45° to the normal of the powder bed. There were eight free fitting parameters in total for the thermal field model laid out in Table 5.2-1.

Table 5.2-1 fit parameters for 'Fit Deconvolution' of the thermal fields measured.

$T_{peak}$ of the central laser exposure
$\sigma_T$ width of the central laser exposure
$\sigma_T$ width of the adjacent laser exposures
Separation of the laser exposures
Radiance scaling factor of the adjacent heated zones
Radiance scaling factor of the adjacent +1 heated zones
Radiance scaling factor of the adjacent +2 heated zones
Radiance scaling factor of the adjacent +3 heated zones

The apparent radiance of the adjacent heated zones are reduced, compared to the central detected heated zone. The peak position relative to the central heated zone is affected by inhomogeneities in the powder bed topology. The detection algorithm (section 5.2.1) ensures that there was a laser exposure adjacent to every measured exposure, but the exposures outside this may be missing all together or reduced in amplitude due to the exposure capturing an incomplete thermal cycle. These factors reduce the amplitude of the adjacent exposures, which is accounted for in the model by the radiance scaling factors.

### 5.3 ASSESSMENT OF DECONVOLUTION METHODS

There is currently no literature on a quantitative assessment of the deconvolution process on real acquired data. Ideally, scenes which are similar to the radiance scenes found in *AM* would be used. Characterised validation scenes would require utilisation of variable-optical-density-printing (non-binary) to create a scene which had similar radiance characteristics to those found in *AM*. As a proxy for the varying thermal scenes found in *AM*, uniform circular binary targets (apertures) similar in size to the thermal fields found in *AM* were used to assess the performance of the deconvolution methods [16]. The small aperture targets, described in section 3.2.3, were used to assess the performance of the deconvolution algorithms. The temperature was at steady state of  $1188.8 \pm 0.2$  °C throughout the acquisition of all small aperture target images, as periodically checked by *IRT*.

Representative thermal images of the small-aperture validation targets can be seen in Figure 5.3-1 a). The radial profiles in Figure 5.3-1 b) were extracted using an algorithm which locates the geometric centre of the distribution (centroid). Circles of expanding radius were then traced around the centroid and the average pixel value along the circumference of that circle was used to calculate the value of the radial profile at that radius. There is some oscillation in the radial profiles caused by the discrete sampling (pixels). The measured signals were converted to temperature by application of the calibration, enumerated in Table 4.3-1.

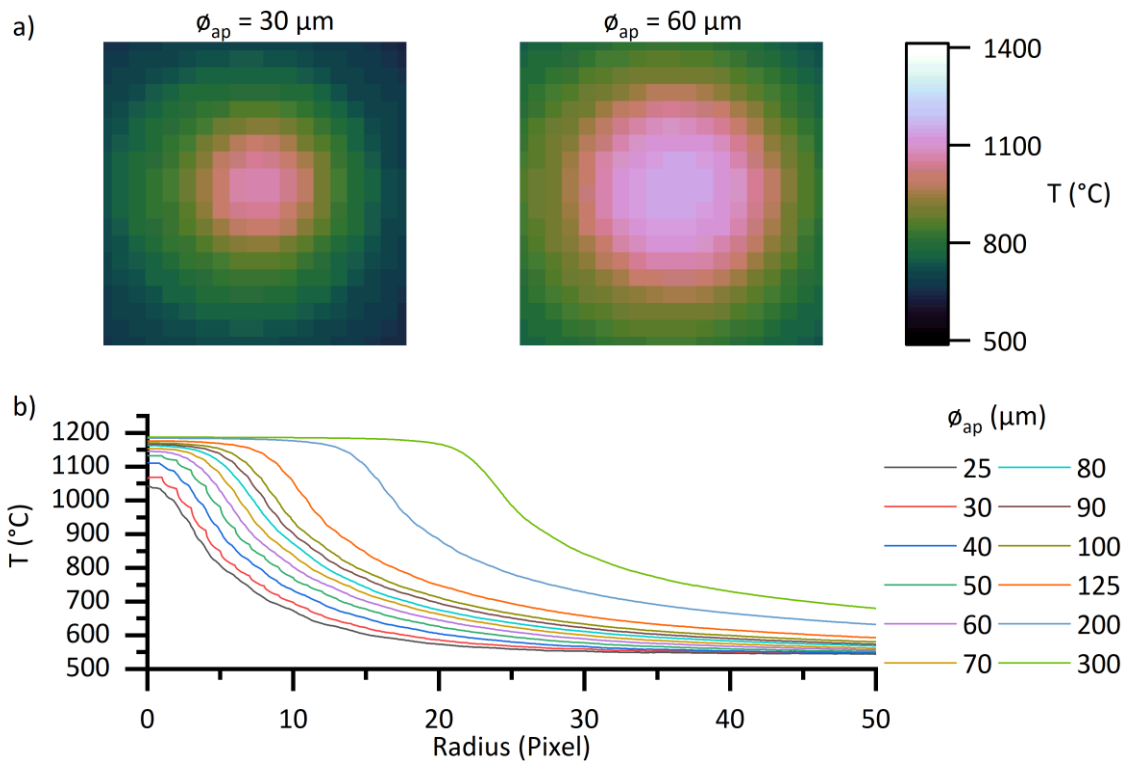


Figure 5.3-1 a) Representative images of validation targets. b) Radial profiles of validation targets. The temperatures were calculated by direct conversion of each of the pixel value (or radial average) to temperature.

The value of the radial profile at Radius = 0, is the value that an *IRT* (single pixel) would measure if it were aligned centrally on the aperture (see section 2.4.3.4).

In a similar way to section 5.1.1.6, the  $z$  position of best focus was determined to be the position of maximum signal in the  $\phi_{ap} = 40 \mu\text{m}$  aperture. The smaller apertures were not used for this due to pixel-centroid misalignment. The position of best focus was determined to be at  $z = 1.06 \text{ mm}$

### 5.3.1 Thermal field model

Radiance across the apertures was assumed to be uniform. The model used was a simple circle of uniform temperature. The radius of the circle and the temperature were allowed to vary in the fit as free parameters (see section 3.3.2). The measured centroid of the distribution was used to locate the centre of the model.

## 5.4 CHARACTERISATION RESULTS

### 5.4.1 IFOV measurement

The Instantaneous Field of View (*IFOV*) of the system was calculated to be  $6.58 \mu\text{m}$  from measurements of the five-bar transmission target described in section 3.2.1. A sine wave was fit to each of the known spatial frequencies ( $\lambda_{\text{bar}}$  ( $\mu\text{m}$ )) in Figure 5.4-1, the measured  $\lambda_{\text{bar}}$  (Pixel) is the inverse of the fitted frequency.

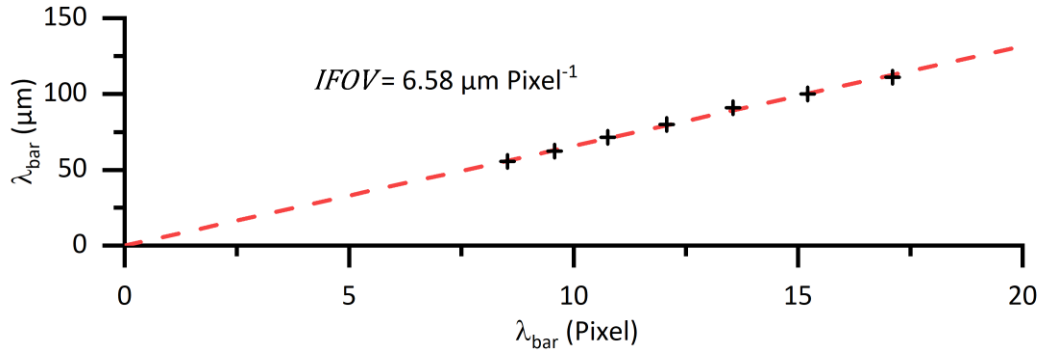


Figure 5.4-1 The IFOV as measured by the known spatial frequency Five-bar targets.

### 5.4.2 Blackbody calibration

A blackbody calibration was carried out, following the procedure detailed in section 3.1. The 3 Sakuma-Hattori coefficients and Wien approximation coefficients measured in these experiments are laid out in table Table 4.3-1. The instrument was calibrated with a  $\phi_{\text{op}} = 0.5 \text{ mm}$  clear aperture for the SLM 125 measurements. It is an experimental limitation that the temperature range of the blackbody target does not cover the possible range of temperatures measurable by the thermographic instrument.

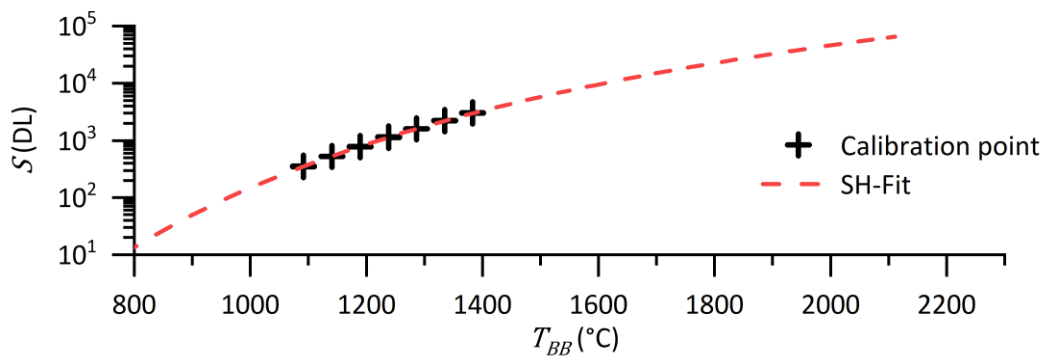


Figure 5.4-2 Calibration points and Sakuma Hattori (SH) interpolation curve shown on a log plot. The response of the instrument must be extrapolated because of the limitations of the blackbody temperatures available.

Table 5.4-1 Calibration coefficients for thermographic instrument (see section 2.2.4)

Spectral fit coefficients		value	
	$A_1$	$8.375 \times 10^{-7}$	
	$A_2$	$2.337 \times 10^{-5}$	
	$\lambda_{Wien}$	$8.670 \times 10^{-7}$	
Scaling Fit coefficients			SEE
SLM 125	$A_0$	$8.027 \times 10^7$	7.81 °C
	$A_{Wien}$	$6.721 \times 10^7$	7.70 °C
Pinhole Tests	$A_0$	$4.3082 \times 10^9$	3.02 °C
	$A_{Wien}$	$3.657 \times 10^9$	6.43 °C

It is a limitation of the experimental procedure that the whole range of temperatures expected in *PBF-LB/M*, cannot be replicated in the laboratory. Such high temperature furnaces are difficult to operate in a laboratory environment and expensive to buy and maintain and are therefore impractical for most university level research groups to operate. The uncertainty in interpolation of calibration points can be quantized more readily than the uncertainty of a measured temperature extrapolated significantly away from the calibration points.

#### 5.4.3 PSF measurement

The measured small-radius *PSF* is shown in Figure 5.4-3 for a range of measured *z* values about the best focus position ( $z = 0$ ). The *PSF* measurement allows for deconvolution of the measure image with the *PSF* to get a more accurate estimate of the radiance of the scene.

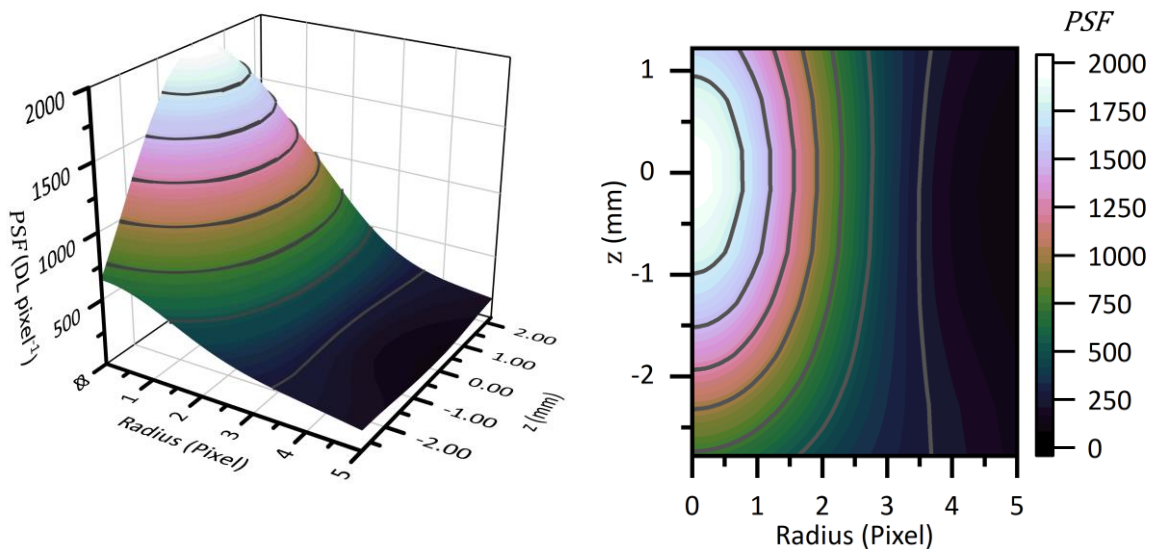


Figure 5.4-3 Measured radial *PSF* as a function of *z* (optical axis). The data has not been normalized in any way linking the magnitude of the *PSF* to the radiance & exposure of the original scene.

#### 5.4.4 Comparison of thermal field measurement methods

The apertures used to assess the performance of the reconstruction methods are of similar size to the thermal fields measured in the *AM* process and can therefore be considered as thermal field simulators [16]. The sharp edges of the apertures mean that the assessment targets contain higher spatial frequency components than might be expected in the non-binary thermal fields found in *AM*. Figure 5.4-4 shows a representative thermal field converted to temperature by the three methods laid out in section 3.1.2.

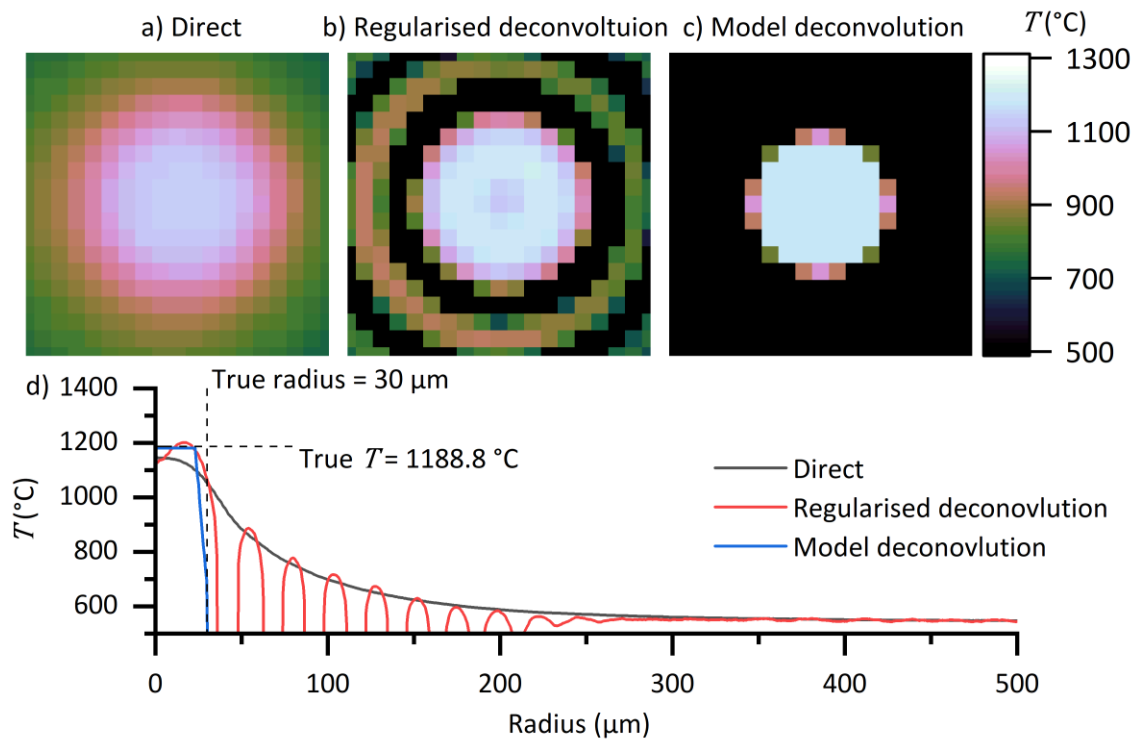


Figure 5.4-4 Representative thermal Field of the  $\phi_{\text{ap}} = 60$   $\mu\text{m}$  aperture target as measured by: a) Direct pixel conversion. b) Regularised deconvolution. c) Model deconvolution. d) Is a comparison of the radial profiles of the three methods.

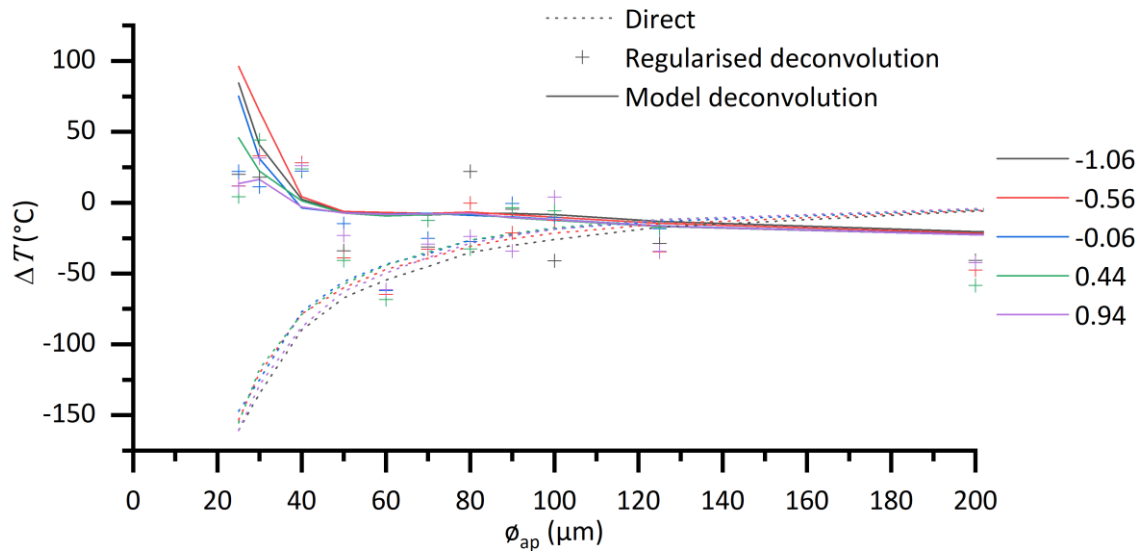


Figure 5.4-5 Improved temperature accuracy obtained with novel deconvolution method.

Regularized deconvolution introduces unphysical thermal distributions into the measured temperatures. A significant effect of the deconvolution is ringing [17], which can be seen in Figure 5.4-4 b) & d). Ringing is caused by truncation of the high frequencies required to describe a very rapid transition (edge). The reduction in error by utilisation of the model deconvolution method for small diameter targets is demonstrated in Figure 5.4-5. The accuracy (error,  $\Delta T$ ) of the central pixel is a measure of how small the uniform region of the thermal field can be, while maintaining an accurate measurement of the radiance, similar in concept to the *MFOV* of an *IRT*. the smaller the error the better the instrument is measuring the thermal fields at the centre of the distribution.

The temperature error at the centre of the aperture constitutes a quantitative measure of the accuracy of the reconstruction technique. There is a marked reduction in error for the model deconvolution processed images. The regularised deconvolution provides some improvement but there is significantly reduced precision in the results, caused by ringing and amplification of the noise. The model deconvolution method (see section 3.1.2) performed the best in the 40 – 80  $\mu\text{m}$  object size region with errors on the order of 1-8  $^{\circ}\text{C}$  compared with 30-80  $^{\circ}\text{C}$  error using the direct mapping of surface temperature, and 10-60  $^{\circ}\text{C}$  for regularized deconvolution.

The methodology of using apertures to represent the thermal fields found in *AM* to quantitatively test the efficacy of deconvolution methods, is believed to be a unique undertaking. Lane et al (2013)[9, 18] qualitatively showed regularised deconvolution improved the modulation depth of bar targets. The same work also utilises models of the scene to estimate the error in the thermographic images. The binary nature of the aperture targets makes them in some ways poor simulations of the continuous thermal fields found in *AM* but they do well represent the behaviors of such artefacts as the edge of the melt pool and other discontinuities in the thermal fields. ideally known-radiance validation scenes with continuously varying thermal fields would be developed for the purpose.

## 5.5 RESULTS OF THERMOGRAPHY OF AM IN A MODIFIED COMMERCIAL MACHINE

Using the setup described in section 3.3.2, 312 layers of a cube of CM247 were acquired. The AM of superalloy CM247 and other nickel-based superalloys is of current interest to the AM community [19-21].

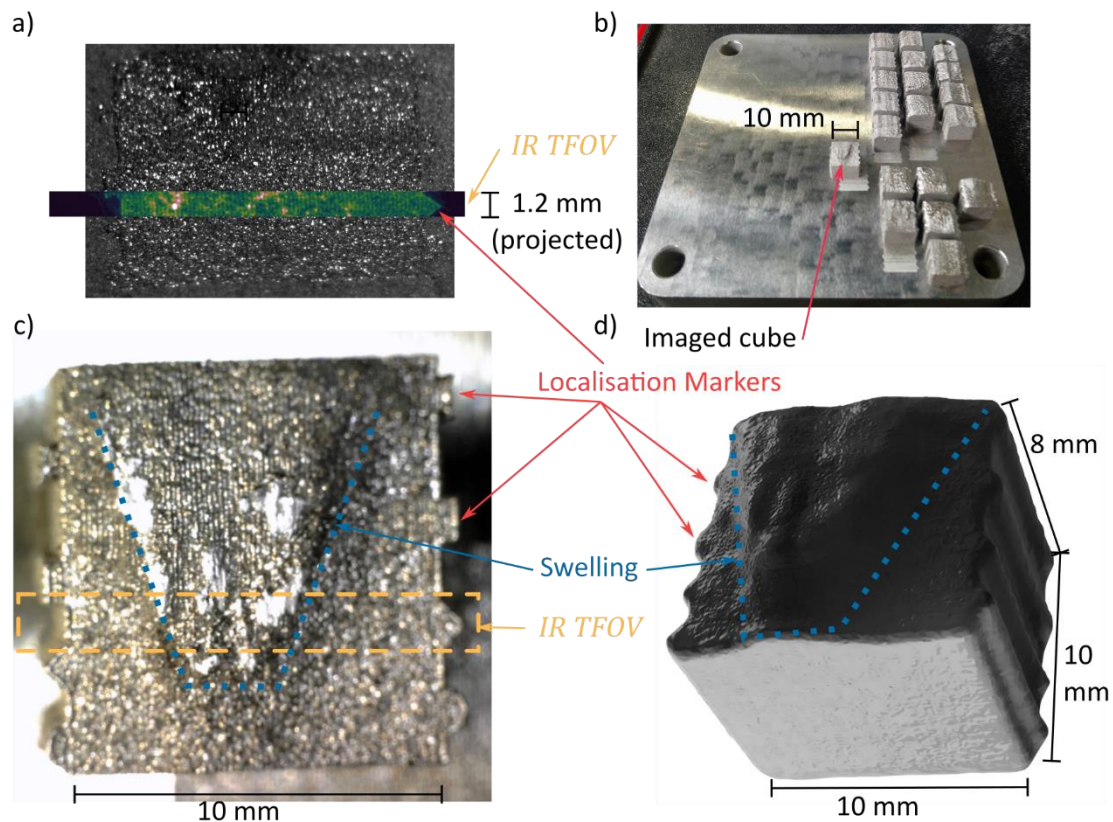


Figure 5.5-1 a) Composite of a visible light image (single long exposure), and the mean of one layer of IR data. The visible scene was illuminated using a broadened visible LED light source inside the build chamber. b) Photo of the build platform after removal from the machine and cleaning. c) Microscope image of the cube. d) 3D scan of the build cube after removal from the build platform.

The cube shown in Figure 5.5-1 was made using the machine parameters laid out in Table 5.5-1. The 3d scan of the cube in Figure 5.5-1 d was acquired using a Shining 3D, 2X plus, handheld 3d scanner (Shining 3D Technology GmbH, Stuttgart, Germany) . The build parameters are somewhat atypical for a ‘good’ build. The pulses are shorter than usual and the mark spacing (distance between pulses) is large. This parameter set was chosen to minimise the *return time* of the laser to a local spot on the build. Return time is the time between the laser passing an area then returning to an adjacent area on the next hatch. The hatches are smaller than the laser spot and so will re-melt the material from the previous hatch.

Table 5.5-1 Renishaw SLM 125 PBF-LB/M machine build parameters.

Laser Exposure time	56 $\mu$ s	Material	CM247
Mark Spacing	135 $\mu$ m	# layers Captured	312 contiguous from start out of 405 total
Laser Peak Power	150 W	Assumed $\epsilon$ [22]	0.2
Hatch Spacing	40 $\mu$ m		

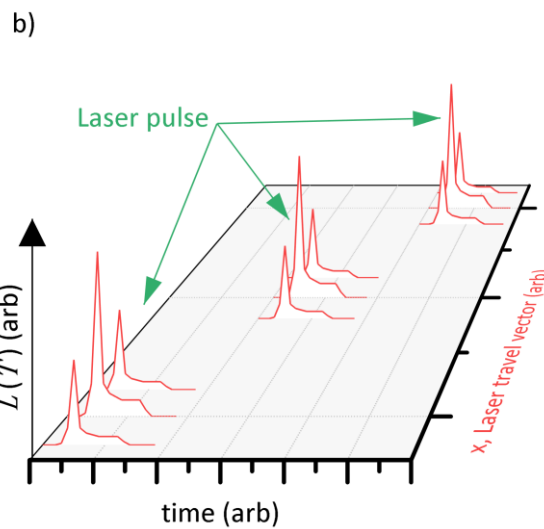
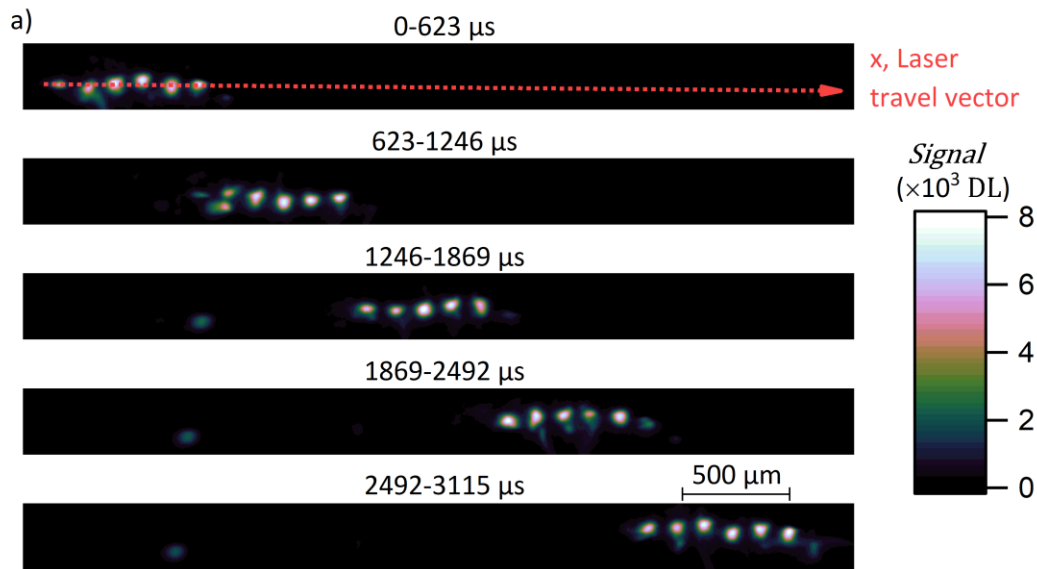


Figure 5.5-2 a) Representative cropped IR images of the cube build. The pulsed nature of the build laser can be seen clearly. Each exposure is  $\Delta t = 623 \mu\text{s}$ . The frame rate is 1600 fps. b) Graphical representation of the entire heating and cooling curve occurring within one exposure of the camera. The data shown here is for illustrative purposes and does not represent any modelling of the thermal fields.

A series of typical cropped frames captured throughout the build are shown in Figure 5.5-2. Several heating and cooling cycles occur during each exposure of the camera as can be seen from the representative data in Figure 5.5-2. This makes inference of thermal fields problematic. The IR data cannot be considered temporally resolved. The detail of the shape of the radiance curve (depicted in Figure 5.5-2 b) for illustration purposes) is not retrievable from this IR data, so it is not possible to make inferences about the temporal shape of the thermal field. It would be useful to be able to infer the total emitted power, but again this is problematic because of the need to know the shape of the spectral distribution of power. The spectral distribution is heavily temperature dependent and therefore, cannot be considered constant over the heating and cooling cycle. The only information which can be extracted from this data without resorting to a temporal model for the thermal field (the development of which is beyond the scope of this work), is the time integrated spectral radiance in the collection band of the system.

The focus of this thesis is on characterising and improving the spatial aspects of thermal field measurement. To this end, it is informative to consider how the spatial processing affects the measurements in terms of temperature. To implement this a simple temporal model is used, such that the thermal field is constant throughout some fraction of the exposure ( $\Delta t^*/\Delta t$ ) and below the detection limit outside this period. The effective Temperature ( $T^*$ ) is:

$$T^* = \frac{c_2}{A \cdot \ln\left(\frac{\Delta t^*}{\Delta t_{\text{cal}}} \cdot \frac{\epsilon C}{S_m} + 1\right)} - \frac{B}{A} \quad \text{Eq 5.5-1}$$

The assumed  $\Delta t^*/\Delta t$  is 0.2. This gives a comparable thermal field to that measured in literature. The presentation of the results as temperature is intended to show the effect of deconvolution in the measurement process.

### 5.5.1 Mean radiance field

The mean radiance field measured by the thermographic instrument described in section 3.4.2 is depicted in Figure 5.5-3. The thermal fields generated by the discrete exposures of the laser can be clearly seen. The system is a pulsed laser system. The laser was considered stationary on the powder bed throughout the exposure of the laser. The detection algorithm described in section 5.2.1 identified 2156 usable discrete heated zones. The surrounding signal was included in the cropped *ROI* because the spread of the radiance may influence the measured radiance of the central heated zone. There is a large variation in the position of the surrounding heated zones because of inhomogeneities in the surface of the print. There is also a slight tilt between the axis of the laser travel and the horizontal in the image.

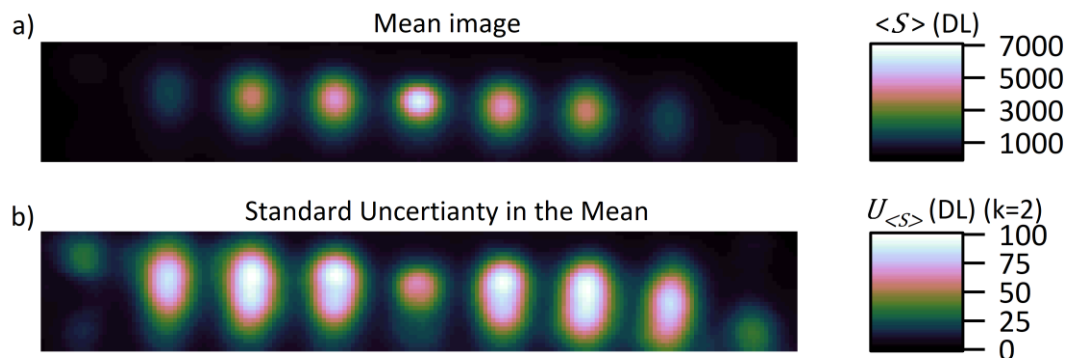


Figure 5.5-3 a) Mean of 2156 discrete heated zones (central spot). b) Standard uncertainty in the mean of the detected heated zones.

### 5.5.2 Measurement of the thermal field

The *PSF* of the instrument at  $z=0$  was used to deconvolve the mean measured radiance field. The mean measured image was converted to temperature by the three distinct conversion methods (see section 3.1.2) using Eq 5.5-1. The results in terms of effective temperature are shown in Figure 5.5-4. The images in Figure 5.5-4 have been stretched to account for the off-axis acquisition of the images (see section 2.4.3.1). The optical axis was estimated to be tilted by  $45^\circ$  to the normal of the powder bed surface. A simple orthographic projection was assumed.

Table 5.5-2 Peak Effective Temperature.

Method	Peak $T^*$ (°C)	Difference from 'direct' method	peak $\frac{dT^*}{dx}$ (°C $\mu\text{m}^{-1}$ )	Fractional Difference from direct method
Direct	2815	-	18.6	-
Regularised deconvolution	3114	+299 °C	31.7	+70%
Model deconvolution	3076	+261 °C	32.3	+73%

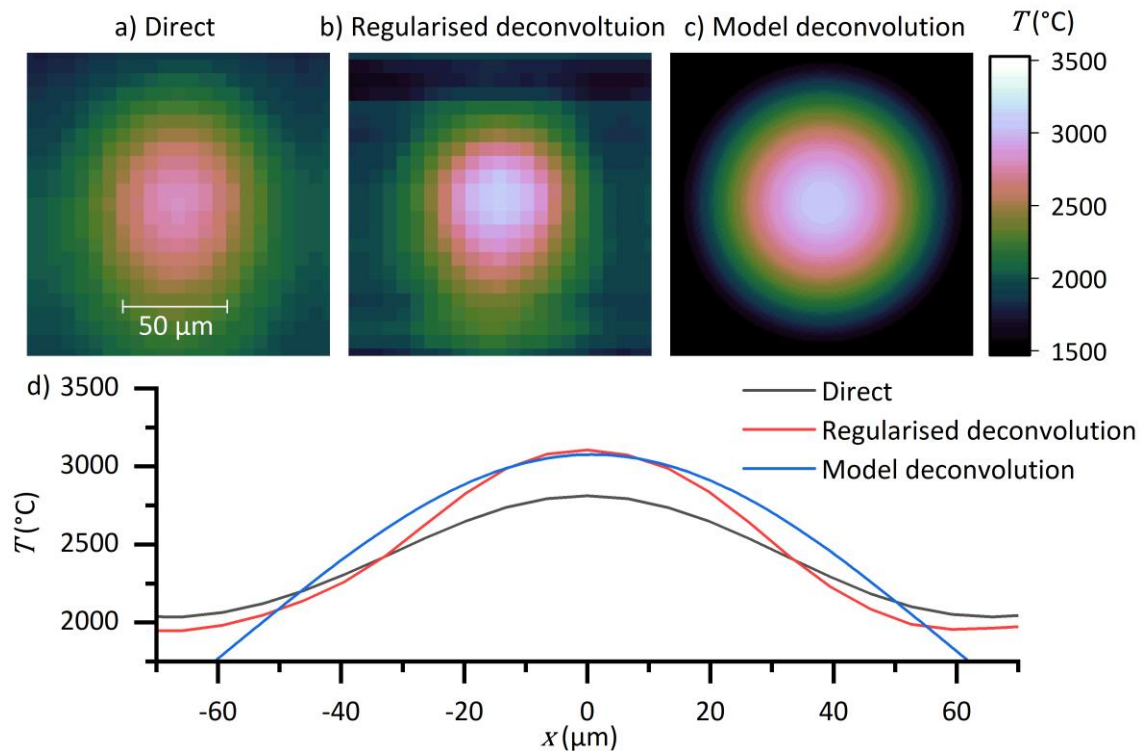


Figure 5.5-4 a) Is the direct conversion of the pixel values to effective temperature by Eq 5.5-1. b) Is a conversion of the deconvolved image with the measured PSF by regularised deconvolution. c) Is the fit deconvolution of the measured data using the model described in section 5.2.2. d) is a horizontal line profile across each of the three images.

The peak effective temperature and the peak spatial gradient of the mean heated zone, as measured by the 3 conversion methods are summarised in Table 5.5-2. It can be clearly seen that deconvolution makes a significant difference to the important metrics of  $PBF-LB/M$ . The peak temperatures are similar in magnitude to those measured by Hooper (2018)[3], although direct comparison of temperature is problematic due to the temporally unresolved nature of the data. The comparison shows that the effect of deconvolution on temperature for similarly spatially distributed scenes would be similar.

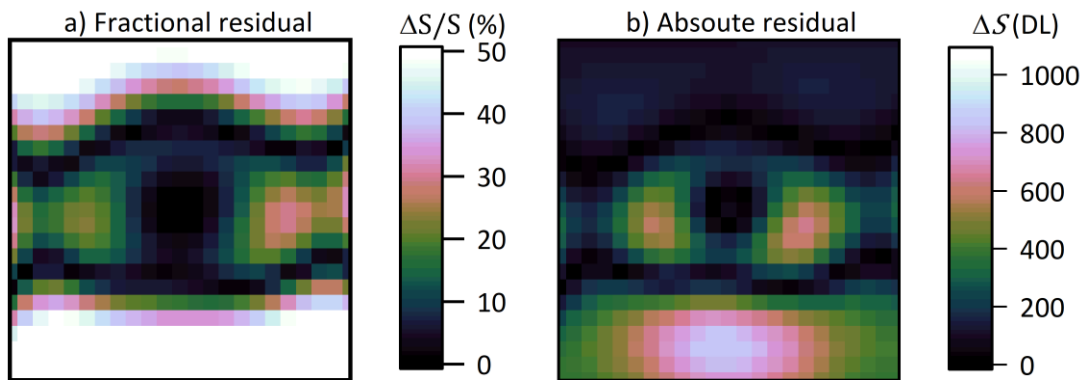


Figure 5.5-5 Fit residuals show that the model reproduces the measured thermal field well around the main peak. There is a rotational asymmetry in the data which is not accounted for in the model, probably caused by the non-planar nature of the heated zone.

## 5.6 CONCLUSIONS

This chapter has shown the characterisation and use of a high-performance thermographic system. A novel, numerical processing method for measurement of the point spread function has been explained and applied. The measured point spread function was used to reconstruct thermal fields in an additive manufacturing application and for known validation scenes in the laboratory. A method for quantitatively assessing the accuracy of reconstruction techniques (section 5.4) was proposed and used to compare the developed technique (model deconvolution) with a standard technique (regularised deconvolution) and the native performance (direct mapping) of the instrument. Finally, data acquired from an additive manufacturing application was presented and its merits and limitations were discussed.

The results of the deconvolution assessment show that the model deconvolution method significantly increased the accuracy of the measured temperature for small isolated thermal fields. The drop in measured temperature by the direct method for the small targets implies that the instrument cannot make an accurate measurement of the heated zones in the *PBF-LB/M* process. The failure of the regularised deconvolution method to accurately reproduce the assessment targets is probably due to the rapid transitions in the binary targets creating a ringing phenomenon in the result. More investigation would be required to find the maximum spatial frequency which could be recreated by the regularised deconvolution method.

The magnitude of the difference in measured peak temperature,  $\approx 300$  °C, shows that the peak temperature as measured directly by pixel signal conversion cannot be relied upon as an accurate measure of the peak temperature. The significant outperformance of the model deconvolution method over the regularised deconvolution method in the validation tests suggests that this methodology should be applied where possible.

Analysis of the slanted knife edge images to produce a  $z$  dependent *PSF*, which fully captures the measured data, is believed to be a novel approach. It is certainly novel in the field of thermography of *AM/M* and the author has not encountered a similar methodology in thermography literature in other fields. The advantage of this method of *PSF* determination over that used by Lane et al (2013)[18] (to which it is most similar) is that an arbitrary model is not required to capture the behaviour of the vast majority of the *PSF* function. The unique combination of the deconvolution method and *PSF* determination has been shown to produce a  $\sim 300$  °C improvement in the accuracy of the thermal field measurement in *PBF-LB/M* (see Figure 5.5-4 for validation).

## 5.7 REFERENCES

1. Frazier, W.E., *Metal Additive Manufacturing: A Review*. Journal of Materials Engineering and Performance, 2014. **23**(6): p. 1917-1928.
2. Bandyopadhyay, A., Y. Zhang, and S. Bose, *Recent developments in metal additive manufacturing*. Current Opinion in Chemical Engineering, 2020. **28**: p. 96-104.
3. Hooper, P.A., *Melt pool temperature and cooling rates in laser powder bed fusion*. Additive Manufacturing, 2018. **22**: p. 548-559.
4. Rodriguez, E., et al., *Approximation of absolute surface temperature measurements of powder bed fusion additive manufacturing technology using in situ infrared thermography*. Additive Manufacturing, 2015. **5**: p. 31-39.
5. Tan, J.H.K., S.L. Sing, and W.Y. Yeong, *Microstructure modelling for metallic additive manufacturing: a review*. Virtual and Physical Prototyping, 2020. **15**(1): p. 87-105.
6. Panwisawas, C., et al., *Mesoscale modelling of selective laser melting: Thermal fluid dynamics and microstructural evolution*. Computational Materials Science, 2017. **126**: p. 479-490.
7. Mani, M., et al., *A review on measurement science needs for real-time control of additive manufacturing metal powder bed fusion processes*. International Journal of Production Research, 2017. **55**(5): p. 1400-1418.
8. Tapia, G. and A. Elwany, *A Review on Process Monitoring and Control in Metal-Based Additive Manufacturing*. Journal of Manufacturing Science and Engineering, 2014. **136**(6).
9. Lane, B. and E.P. Whinton, *Calibration and measurement procedures for a high magnification thermal camera*. 2015, National Institute of Standards and Technology.
10. Du, H. and K.J. Voss, *Effects of point-spread function on calibration and radiometric accuracy of CCD camera*. Applied Optics, 2004. **43**(3): p. 665-670.
11. Abel, N.H., *Oeuvres Completes*. Vol. 1. 1881, Christiana (Oslo): Imprimerie de Grondahl & Son.
12. Pretzier, G., *A New Method for Numerical Abel-Inversion*, in *Zeitschrift für Naturforschung A*. 1991. p. 639-641.
13. Killer, C., *Abel Inversion Algorithm*. 2013, MATLAB Central File Exchange.
14. Hecht, E., *More on Geometrical Optics*, in *Optics*. 2002, Addison Wesley, 1301 Sansome St., san Francisco, CA9411. p. 243-265.
15. Han, L., F.W. Liou, and S. Musti, *Thermal Behavior and Geometry Model of Melt Pool in Laser Material Process*. Journal of Heat Transfer, 2005. **127**(9): p. 1005-1014.
16. Lane, B.M., et al. *Performance Characterization of Process Monitoring Sensors on the NIST Additive Manufacturing Metrology Testbed*. in *Solid Freeform Fabrication Symposium*. 2017. Austin, TX.
17. Lai, F., et al., *Thermal image enhancement through the deconvolution methods for low-cost infrared cameras*. Quantitative InfraRed Thermography Journal, 2018. **15**(2): p. 223-239.
18. Lane, B.M., et al., *Uncertainty of temperature measurements by infrared thermography for metal cutting applications*. Metrologia, 2013. **50**(6): p. 637-653.
19. Babu, S.S., et al., *Additive Manufacturing of Nickel Superalloys: Opportunities for Innovation and Challenges Related to Qualification*. Metallurgical and Materials Transactions A, 2018. **49**(9): p. 3764-3780.
20. Seidel, A., et al., *Additive Manufacturing of Powdery Ni-Based Superalloys Mar-M-247 and CM 247 LC in Hybrid Laser Metal Deposition*. Metallurgical and Materials Transactions A, 2018. **49**(9): p. 3812-3830.
21. Panwisawas, C., Y.T. Tang, and R.C. Reed, *Metal 3D printing as a disruptive technology for superalloys*. Nature Communications, 2020. **11**(1): p. 2327.
22. Mills, K., et al., *Calculation of thermophysical properties of Ni-based superalloys*. ISIJ International, 2006. **46**(5): p. 623-632.

## 6. SPATIOTEMPORALLY RESOLVED QUANTITATIVE THERMOGRAPHY IN POWDER BED FUSION PROCESS REPLICATION

---

In this chapter a high-speed thermographic instrument, with the highest spatial sampling rate of any work found in the field, was characterised and used in an entirely unique additive manufacturing test rig. The test rig is designated the Laser Additive Manufacturing Process Replicator mark two (*LAMPRIi*). Characteristics of the instrument are presented. A method to account for the tilt of the optical axis is implemented and its validity is assessed. A correction to the measurement of the spatial transfer function is introduced and applied. Sources of uncertainty in measurement of the thermal fields using this instrument, in this environment, are discussed and quantified in an uncertainty budget. Confounding factors in the experimental setup on the test rig are introduced and their impact is discussed. Finally, standard metrics are extracted from exemplar data gathered using the instrument on the additive manufacturing process replicator.

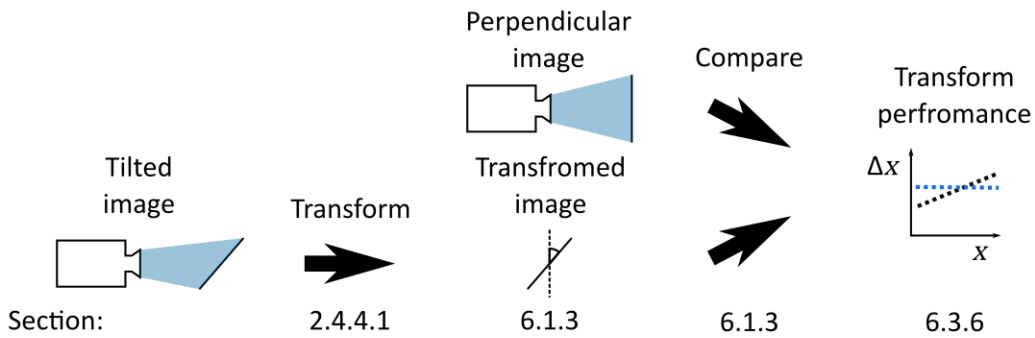
This chapter illustrates the best implementation of thermography in Additive Manufacturing of Metals (*AM/M*) achieved during the authors PhD experience. The metrological characteristics which can be ascertained from characterisation of the thermographic instrument are presented and their relevance to data captured during the *AM/M* process is explored. The experimental setup used during this chapter is given in section 3.3.3. The *IFOV* of 3  $\mu\text{m}$  in these experiments is the highest spatial sampling frequency thermography of an *AM/M* process, when compared with examples found in literature. The speed of the laser was slower than the work in chapter 5, in order to enable measurements using the x-ray facilities. The laser used was a continuous wave laser rather than the pulsed system used in chapter 5, further improving the temporal resolution issues outlined in section 5.5.

Original contributions to the field in this chapter are:

- The most highly spatially sampled thermography of the *AM/M* process.
- A validated accurate projection algorithm to create an orthographic projection of a tilted scene.
- A quantitative assessment of the uncertainty of the thermographic measurements in *AM/M*.
- A method for determination of the measurement field of view for thermographic instrument with poor size of source effect.

Aim: Accuarate spatiotemporally resolved thermal field measurements

Objective: Validate geometric transform



Objective: Convert NIR process replicator images to quantitative thermal field measurements

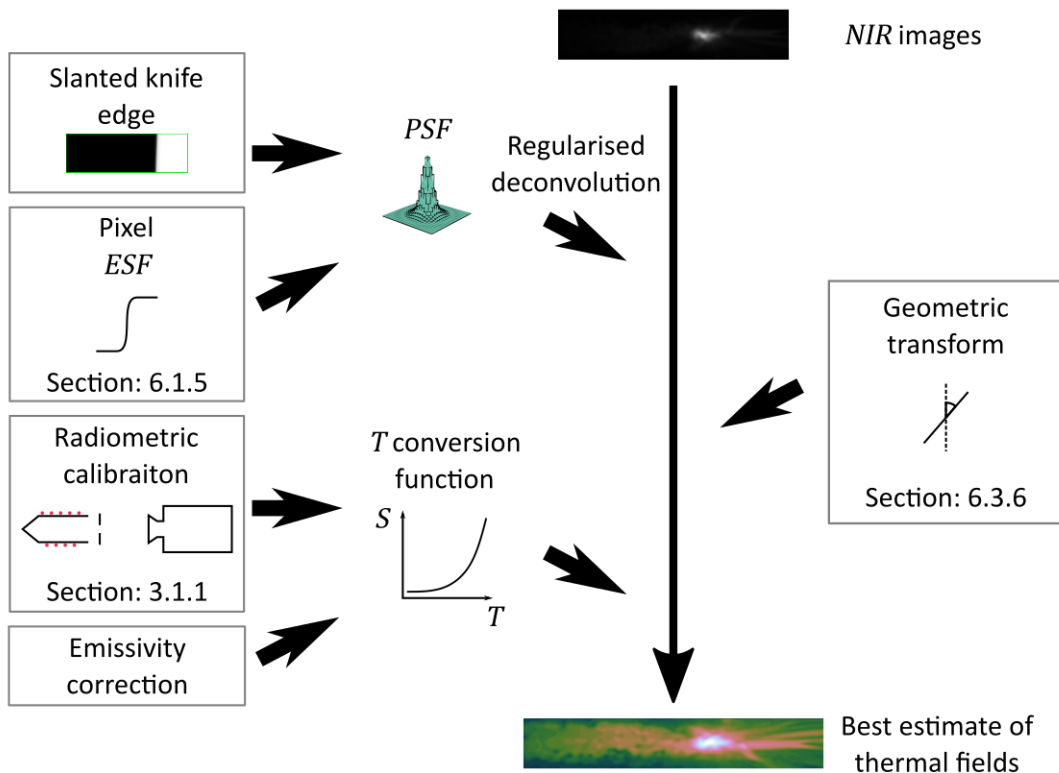


Figure 6-1 Schematic of the main objectives of this chapter.

A simplified description of the processes involved in this chapter is shown in Figure 6-1. In addition to this the main sources of uncertainty present in the measurement of thermal fields are examined and quantified where possible, and some consequences of the spatial response function measurement are explored.

## 6.1 CHARACTERISATION ANALYSIS

### 6.1.1 Spectral characteristics

The spectral characteristics of the instrument shown in Figure 6.1-1 were taken from instrument and filter datasheets and do not constitute a measurement in the laboratory. A power-characterised variable monochromatic illumination source (monochromator) could have been used to undertake this measurement, but the experimental effort required to create an imageable surface of sufficient radiance and known relative monochromatic radiance was considered impractical for this work.

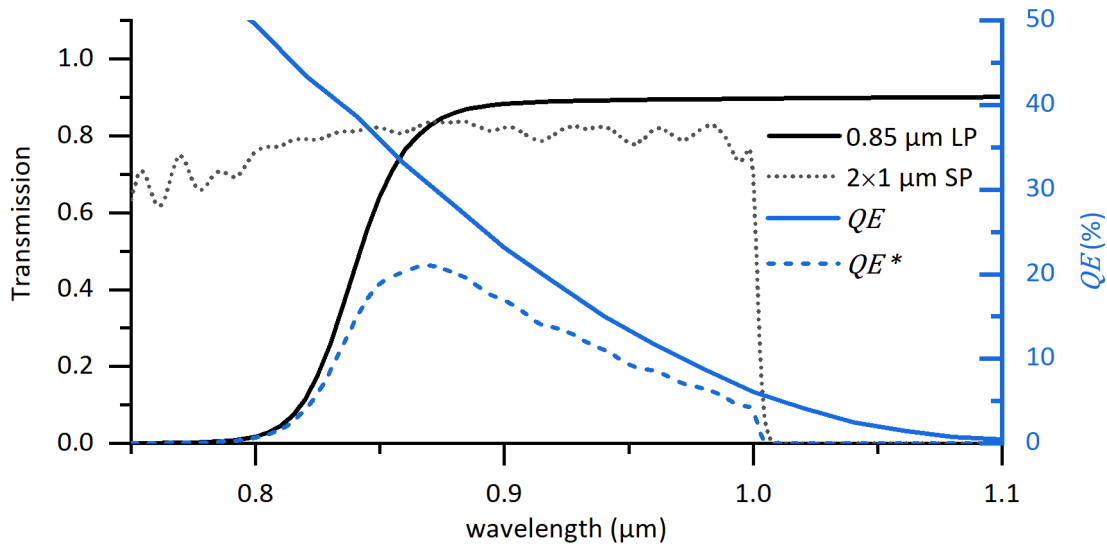


Figure 6.1-1 Three (two identical short pass and one long pass) spectral filters were used in the instrument with transmission characteristics plotted on the left hand axis. The Spectral sensitivity characteristics of the instrument, as taken from manufacturer datasheets, are plotted on the right-hand axis in terms of a Quantum Efficiency percentage.  $QE^*$  is the effective quantum efficiency of the spectrally filtered instrument.

### 6.1.2 Noise

The temporal (frame to frame) noise in the signal obeys a square root dependence as predicted by the theory presented in section 2.3.3. The square root dependence can be seen in Figure 6.1-2. The noise is plotted for a variety of temperatures and exposure times. The relation:

$$\sigma_S \approx 1.5\sqrt{S} \quad \text{Eq 6.1-1}$$

is a good approximation for the temporal noise in the signal, independent of the exposure time or temperature. The noise is solely a function of the number of absorbed photons (signal).

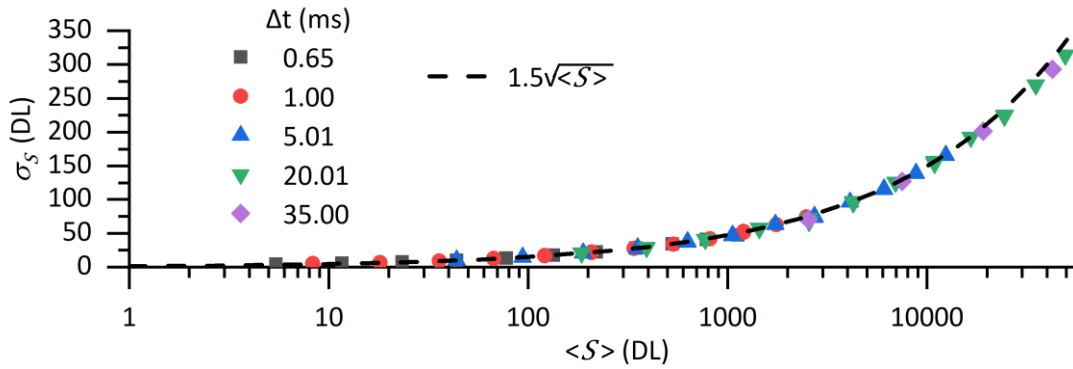


Figure 6.1-2 The square root dependence of the temporal noise on the signal is independent of temperature and exposure time ( $\Delta t$ ).  $\langle S \rangle$  is the mean signal.

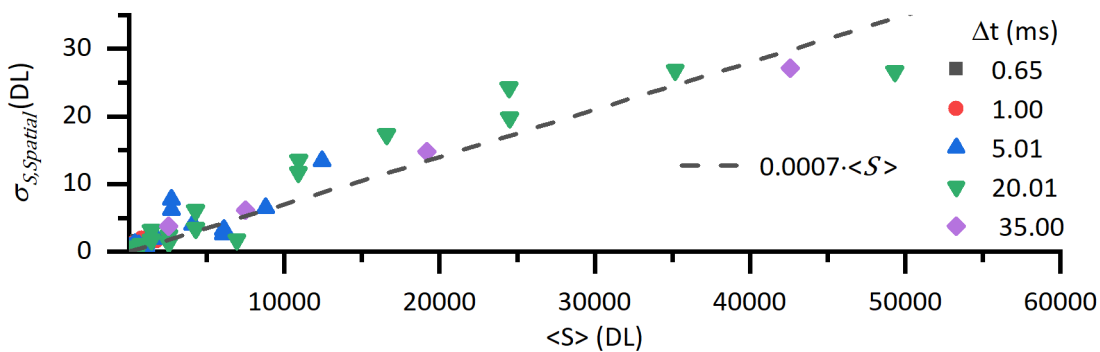


Figure 6.1-3 Estimate of spatial noise. Spatial noise is expected to be linearly proportional to signal.

The spatial variations depicted in Figure 6.1-3 are partly due to local inhomogeneities in the  $QE$  of the detector and amplification circuitry, and partly due to dust and imperfections in the optical system. A linear scaling in terms of signal was assumed. This factor approximates the expected spatial variation across the sensor.

$$\sigma_S \approx 7 \times 10^{-4} \cdot S \quad \text{Eq 6.1-2}$$

The two noise components in terms of temperature shown in Figure 6.1-4 are calculated from the derivative of the SH-Fit, truncating the Taylor series at the first term.

$$\sigma_{T_{BB}} = \frac{dS_{SH}^{-1}}{dT} \cdot \sigma_S \quad \text{Eq 6.1-3}$$

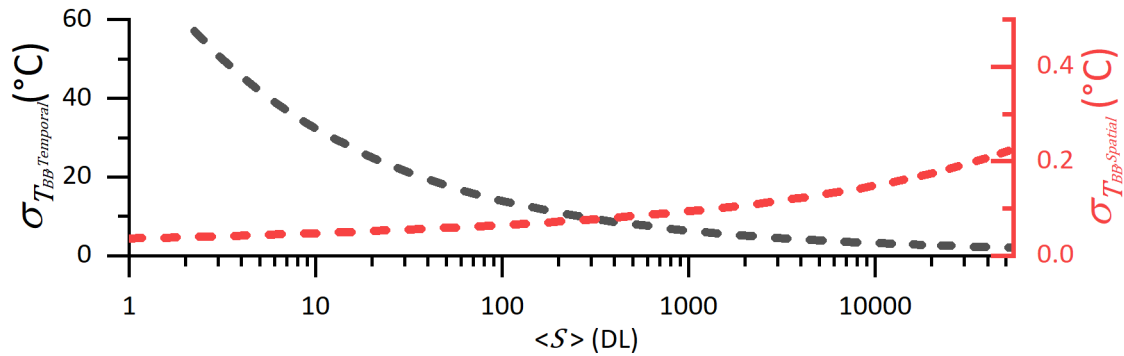


Figure 6.1-4 The magnitude of the spatial and temporal components of noise in terms of temperature.

The temporal noise component two orders of magnitude larger than the spatial component but it can be reduced by averaging, but the spatial component of noise must always be assumed to be present in the measured image.

### 6.1.3 Geometric transforms

The large angle between the optical axis and the surface normal of the print, imposed by the geometry of the process replicator (see section 3.3.3), means that the images must be transformed to allow dimensional measurements. The theory of the transform applied is described in section 2.4.3.1. The transform was validated by use of the printed checkerboards described in section 3.2.4. Images of the checkerboard are shown in Figure 6.1-5. The performance of the geometric transforms was assessed by how well the transform converted the image of a tilted checkerboard to have the same measured dimensions as the checkerboard imaged perpendicularly.

The working distances (geometric approximation) required for the transformation ( $r_{WD}$  &  $r_{im}$ ) were calculated using the measured magnification ( $M_{ag}$ ) and the known focal length ( $f_L$ ) of the lens, using Eq 2.1-9.  $M_{ag}$  was calculated by the ratio of the measured  $IFOV$  with the known pixel size. The dimensions of the printed checks were unknown and were assumed constant across the Total Field Of View ( $TFOV$ ). The checker size across the scenes in Figure 6.1-5 were measured by fitting a sine wave to the centre of each vertical row of checks. The inverse of the fitted angular frequency ( $\times 2\pi$ ) was used as the measure of the checker size to test the performance of the geometric transform.

The reciprocal of the mean spatial frequency of the horizontal rows was measured to compare the magnitude of the transform perpendicular to the axis of rotation. The results for both the horizontal and vertical measurements are presented in section 0.

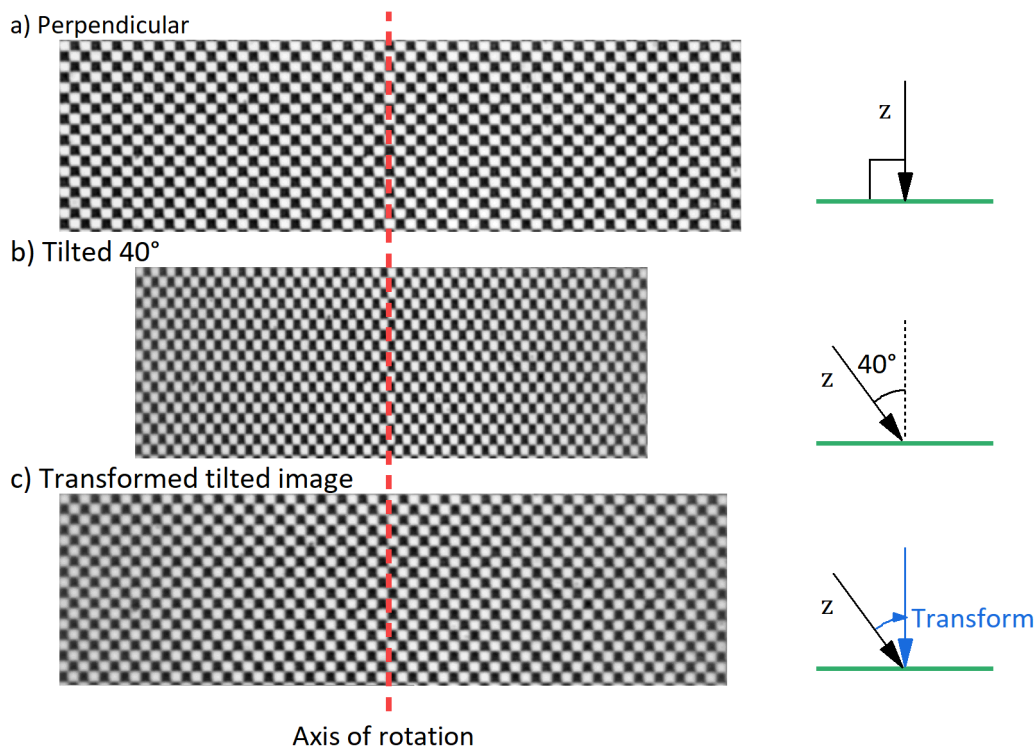


Figure 6.1-5 a) Is an image of a checkerboard taken with the checkerboard perpendicular to the optical axis. b)- is an image of the same checkerboard rotated by  $40^\circ$  to the optical axis. The image was cropped to include the same number of checks as a). c) Is the same image as b) transformed to be a perpendicular orthographic projection of the checkerboard.

The position of the focal plane (axis of rotation) for the *ESRF2* data was determined from the position of peak signal in the images. Saturated data was ignored, the horizontal position of the maximum (in time) signal position (in space) was fitted with a second order polynomial. The position of the peak was determined from this fit. The focal plane position for the *ESRF1* dataset was more difficult to determine than *ESRF2* because the path of the laser was more complicated (multiple passes) and did not pass through the full *TFOV*, making the peak signal position a poor metric of the best focal position. The best focal position for the *ESRF1* dataset was determined qualitatively manually from the illuminated images. The geometric transform is relatively insensitive to the chosen position of the focal plane, because the change in *IFOV* (magnification) is small across the *TFOV*.

#### 6.1.4 Scatter effect, *SSE*

The optical system suffered from a noticeable problem with scatter, the problem manifests as a significant Size of Source Effect (*SSE*). This can be seen by looking at the response of the system to a series of large diameter apertures in Figure 6.1-6 a-c. The scatter effects cause a large cone shaped defect in the centre of the image. It is believed that this effect is mainly caused by inter reflections between the curved surfaces of the optical elements.

A consequence of this problem can be seen in Figure 6.1-6 d. The data shown in this sub-figure is taken using all three aperture sets described in section 3.2.3. The problem with the shape of the curve of central pixel value against aperture diameter is that there is no real plateau in the signal level, this makes it difficult to quantify the Measurement Field of View (*MFOV*) of the instrument (see section 2.4.2 & 2.4.3.4).

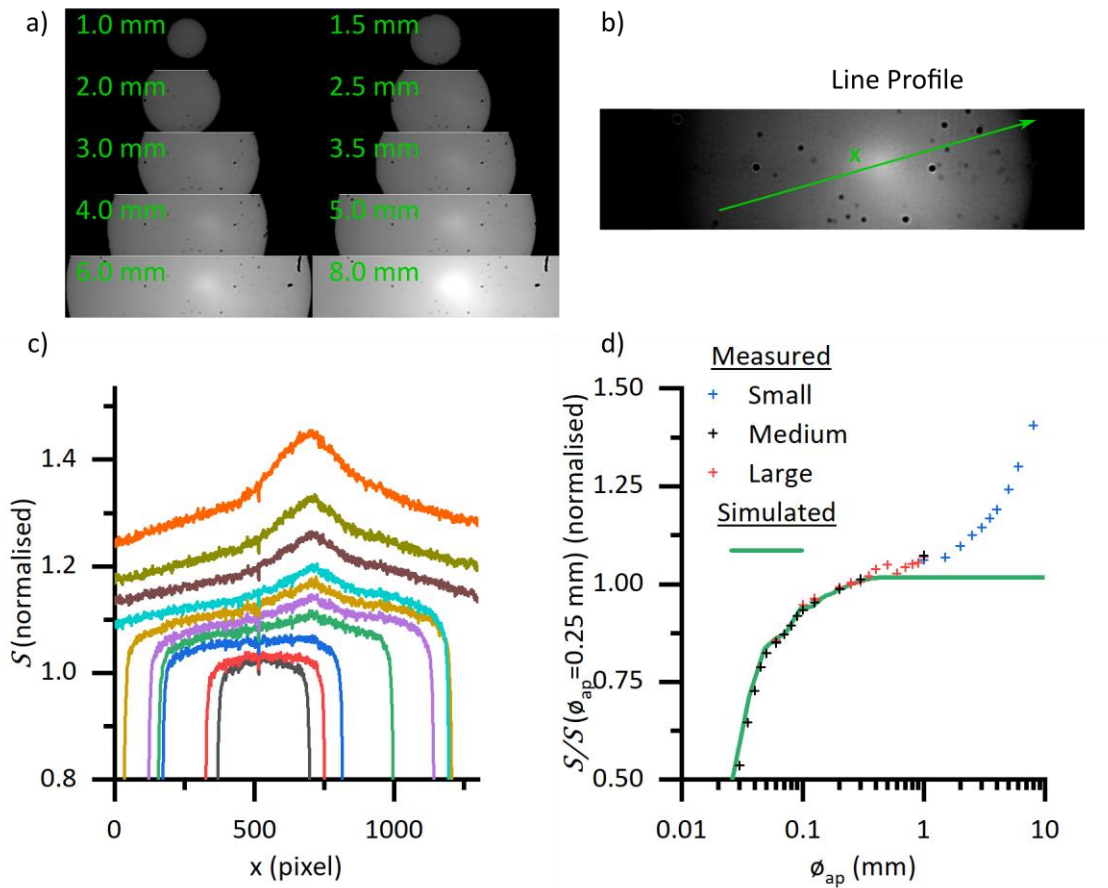


Figure 6.1-6 a) Shows mean images of the different diameter apertures from the large aperture set. The bright feature near the centre of the image can be seen to stay in the same place even when the apertures move within the TFOV. b) Shows the position of the line profile for the plot in c. c) The bright feature can be seen to be apparently 1.4 times as radiant as the 1 mm diameter aperture. d) Shows how the signal at the central pixel is affected by the aperture diameter, the expected plateau in signal level is never reached. The 'Simulated' curve is explored in section 6.1.5.

### 6.1.5 Correcting for the pixel *ESF*

A source of error in the determination of the Point Spread Function (*PSF*) is the inherent spread in the measured Edge Spread Function (*ESF*) caused by averaging across the pixel area. This phenomena is not taken into account in Lane & Whintenton (2015)[1]. If the optics were ideally geometric, the *PSF* would be a Dirac delta. The slanted knife edge measurement of the *ESF* would still not be a step function, due to averaging as the knife edge passes across the pixel.

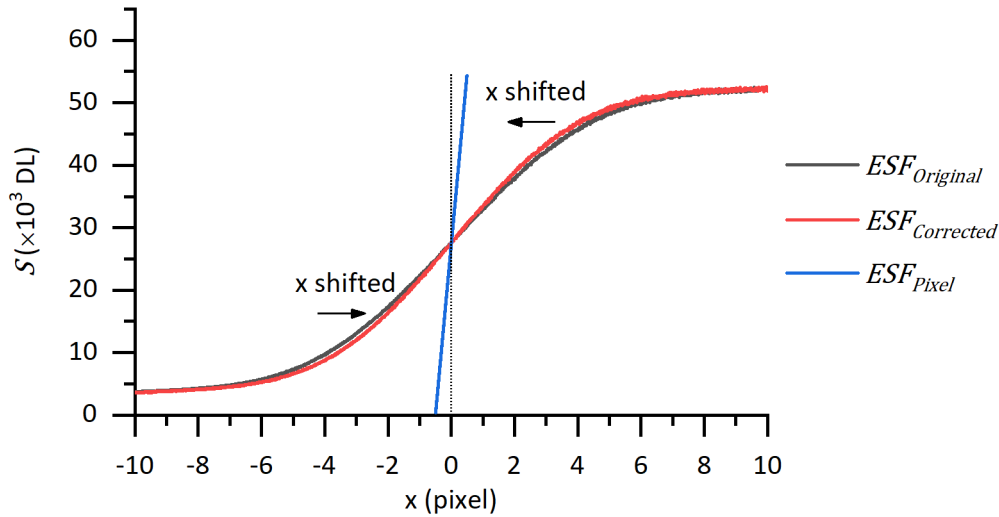


Figure 6.1-7 Correction for the averaging effect of the pixel area and the affect correcting for it has on the system ESF.

The pixel  $ESF$  function ( $ESF_{Pixel}$ ) is calculated using the equations in appendix 8.2. The corrected ESF ( $ESF_{Corrected}$ ) is calculated from the original ESF ( $ESF_{Original}$ ) by shifting the  $x$  coordinate of each measured data point ( $x_0$ ) in the  $ESF_{Original}$ , to a new position  $x_C$ .

$$\begin{aligned} S_0 &= ESF_{Original}(x_0) \\ S_C &= ESF_{Corrected}(x_C) \\ S_P &= ESF_{Pixel}(x_P) \end{aligned} \quad Eq\ 6.1-4$$

$$x_C = x_0 - ESF_{Pixel}^{-1}(S_0)$$

The  $x_0$  coordinate of the original function is shifted by the  $x_P$  value of the  $ESF_{Pixel}$  function at that same signal level ( $S_0 = S_P$ ). The  $ESF_{Pixel}$  function was generated in the bounds 0 to 1, the function was then scaled and shifted to align with the averages of the extreme ends of the  $ESF_{Original}$  function. For  $S_0$  values outside the range of  $S_P$ , the  $x_P$  values at the extremes of the  $ESF_{Pixel}$  function are used to shift the  $x$  coordinate.

### 6.1.6 Measurement field of view (MFOV)

The  $MFOV$  of a pixel can be measured directly by a series of expanding apertures [2]. The  $SSE$  problems with the optics of the instrument outlined in section 6.1.4 make the use of this method problematic. Instead, the measured  $PSF$  can be used to determine the  $MFOV$ . Two methods of achieving this, described in section 2.4.2, were trialed: pixel convolution (depicted in Figure 6.1-8) and aperture simulation (depicted as the *Simulated* line in Figure 6.1-6 d). The enclosed energy ( $EE$ ) determines how strictly the  $MFOV$  is defined. In an ideal situation using an  $EE$  of 100% would give an  $MFOV$  equal to the  $IFOV$  of the instrument, for this to be the case the  $PSF$  would have to be a Dirac delta. The  $IFOV$  of the instrument is a square with an area of  $9\ \mu\text{m}^2$ .

The  $f_{weight}$  function is approximately rotationally symmetric, because of the oversampled nature of the instrument. The less oversampled the instrument the closer the  $f_{weight}$  (and therefore the  $MFOV$ ) will come to resemble the shape and size of the  $IFOV$  (square).

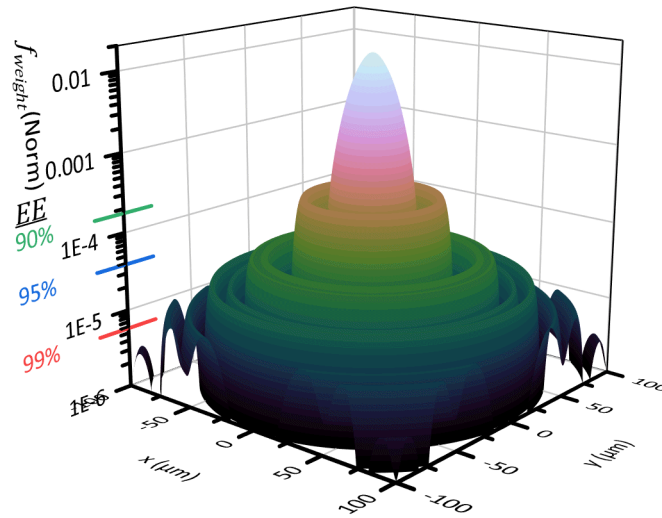


Figure 6.1-8 Depicts the weighting function  $f_{weight}$ , which shows the weighting distribution of the scene surrounding the IFOV of a pixel. The magnitude is normalized to make the total integral of the volume equal to unity. The y axis is on a log scale to show the detail of the distribution, on a linear scale only the central spike is clearly observable.

## 6.2 UNCERTAINTY

The guide to the expression of uncertainty in measurement [3] advocates the construction of an *uncertainty budget*, this is a quantisation of all the known sources of uncertainty and their effect on the measurand (sensitivity). The measurand, in this work, is the surface temperature of the scene. Some components of the uncertainty are straight forward to quantify, such as the noise in the instrument, characterised in section 6.1.2. Other components are much more difficult to quantify, the most relevant one to this work being the spatial transfer function of the instrument. Correlations between the different components determine how the components are combined. If the components are uncorrelated, their effect on the measurand is orthogonal to all other effects on the measurand and the components can be added together in quadrature. If the components are entirely correlated, the individual components must be added linearly to provide the final uncertainty in the measurand. The correlations in this work are in general not well known. It is assumed that there are no correlations between any of the components in Table 6.2-1. Components of uncertainty are combined [3] by:

$$\text{Uncorrelated} \quad U_T = \left( \sum_i (\kappa_i \cdot U_i)^2 \right)^{1/2} \quad \text{Eq 6.2-1}$$

$$\text{Fully correlated} \quad U_T = \sum_i \kappa_i \cdot U_i \quad \text{Eq 6.2-2}$$

Table 6.2-1 Components of uncertainty

Component	$U_i$ Standard uncertainty (k=2)	$\kappa_i$ Sensitivity factor
Spatial noise (Spatial)	$1.4 \times 10^{-3} \cdot S$ (DL)	$\partial f_{BB,SH}^{-1}(S, \varepsilon) / \partial S _S$
Temporal noise (Temporal)	$3\sqrt{S}$ (DL)	$\partial f_{BB,SH}^{-1}(S, \varepsilon) / \partial S _S$
Calibration function fit (Cal fit)	Eq 6.2-3	$\partial f_{BB,SH}^{-1}(S, \varepsilon) / \partial S _S$
Transfer standard uncertainty (IRT)	$4$ ( $^{\circ}\text{C}$ ) <sup>1</sup>	1
Emissivity	$0.05 \cdot S / \varepsilon$ (DL)	$\partial f_{BB,SH}^{-1}(S, \varepsilon) / \partial S _S$
Spatial transfer function	Scene dependent	-

<sup>1</sup>maximum uncertainty in range from most recent UKAS accredited calibration.

The sensitivity factors in Table 6.2-1 are used to convert an uncertainty in terms of radiance (signal) to terms of the measured temperature. This is done by first order Taylor expansion of the function linking signal and temperature (see section 3.1.1). (The  $|_S$  notation means evaluated at  $S$ )

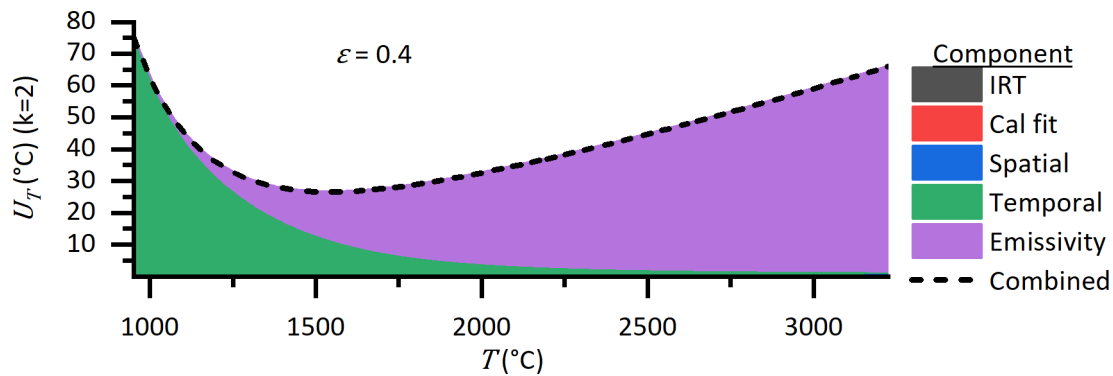


Figure 6.2-1 This figure shows the relative contributions of the different components of the uncertainty to the final combined uncertainty. The components were assumed to be uncorrelated. These curves were generated using the ESRF2 calibration and an assumed emissivity of 0.35.

Figure 6.2-1 shows that, out of the uncertainty components considered in Table 6.2-1, only the temporal noise (at the low end of the range) and the emissivity (at the high end of the range) contribute significantly to the combined uncertainty in the measurand ( $T$ ).

### 6.2.1 Calibration function uncertainty

The Standard Estimate of Error ( $SEE$ ) was used to quantify the uncertainty over the calibration interpolation range. The uncertainty was then linearly expanded, proportional to the radiance (signal), beyond the calibration range.

$$\begin{aligned}
 U_S(T < 1500 \text{ }^{\circ}\text{C}) &= SEE \text{ (Table 6.3-1)} \\
 U_S(T > 1500 \text{ }^{\circ}\text{C}) &= U_S(T = 1500 \text{ }^{\circ}\text{C}) \cdot \frac{S(T)}{S(T=1500 \text{ }^{\circ}\text{C})}
 \end{aligned}
 \tag{Eq 6.2-3}$$

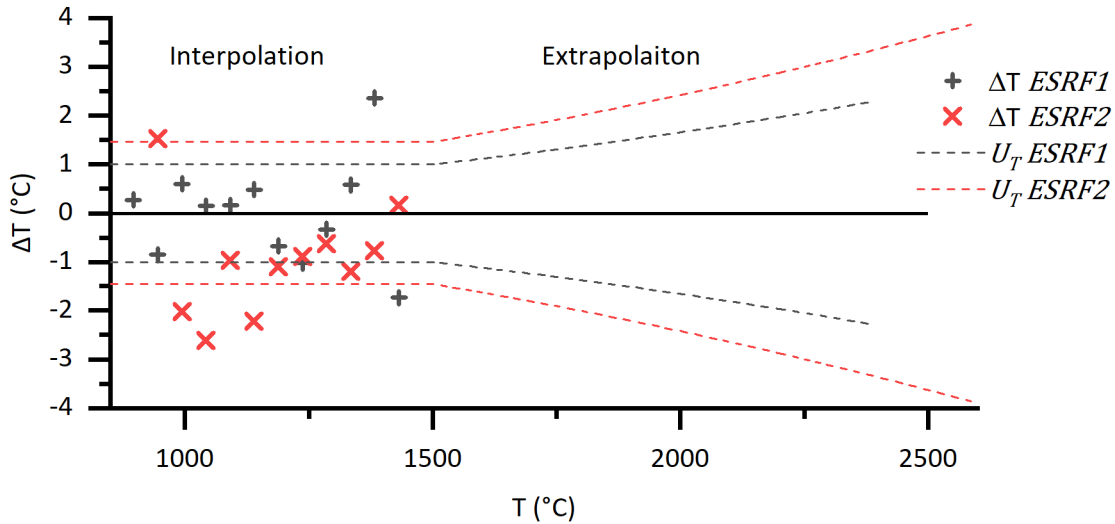


Figure 6.2-2 Calibration curve fitting uncertainty. the extrapolated uncertainty is the fractional uncertainty at the top end of the calibration range scaled by the increase in signal, see Eq 6.2-3.

### 6.2.2 Scene dependent uncertainty

The finite transfer function of the instrument means that the scene is not reproduced perfectly as an image. The spatial transfer function can be partially accounted for by deconvolution, but this process is not perfect. It is very difficult to quantify the effect that the transfer function has on the measured temperature because it depends on the scene itself. One way to attempt to quantify this component is to model the entire scene and probe how variations in different components of the scene would affect the measurement of temperature in all other components. This approach would yield uncertainties for a tightly controlled/reproducible scene. The scenes encountered in *AM* are varied, and only some simplified situations are amenable to this kind of analysis. The variations in the thermal fields on the length scales resolvable in this work (melt pool 10- 100  $\mu\text{m}$ ), make any model require a large amount of inbuilt random variation to capture the true behaviours of the scene. This was deemed unachievable in the time frame of a PhD.

### 6.2.3 Spatial measurement uncertainty

The method used for determining the *IFOV* (see section 5.4.1), and therefore spatial measurements of the scene, has its own, relatively small (<1%) uncertainty attached. Due to the relatively large uncertainty in the viewing angle (see section 3.3.3), an extra component in the uncertainty of spatial measurements in the horizontal (in the image) direction was included. This was modelled using the first order Taylor expansion of the orthographic projection approximation (Eq 2.4-23). The fractional uncertainty in a measured length in the horizontal direction (in the image) is given by:

$$\frac{U_{\Delta\tilde{x}}}{\Delta\tilde{x}} = \tan \theta \cdot U_{\theta} \approx 7.3\% \quad \text{Eq 6.2-4}$$

Where:  $\theta$  is  $40^\circ$  &  $U_{\theta}$  is  $5^\circ$  ( $k=2$ ).

#### 6.2.4 Components not considered

Table 6.2-1 does not form an exhaustive list of the sources of uncertainty in the final measurand. Some factors which affect the uncertainty of a radiometric measurement of temperature are not included in the uncertainty budget. This is because of a combination of the difficulty in quantifying the contribution and a judgment that the contribution is small compared to the overall uncertainty. Some of the main unconsidered components are listed in Table 6.2-2.

Table 6.2-2 Some components of uncertainty not considered.

Component	Mitigation / justification
Spectral discrepancy of calibration furnace	Operating wavelength of transfer standard was within 1 $\mu\text{m}$ of thermographic instrument, minimising difference.
<i>SSE</i> , ghosting & scatter	The thermal fields observed were usually smaller than the <i>MFOV</i> , making <i>SSE</i> problems irrelevant. The scatter and ghosting issues are mitigated by manual selection of the <i>ROI</i> during data analysis.
Reflections from sample surface	The room temperature diffusely reflecting enclosure mitigates the problem of reflections back onto the surface. Manual selection of the <i>ROI</i> also mitigates this problem because reflections can be avoided if they are identified.
Drift in calibration of instrument	The instrument is temperature stabilised and has shown no signs of significant drift between calibrations.
Short term drift	The temperature stabilisation of the instrument ensures that any drift is small enough to be indistinguishable from source drift of the furnace.
Blackbody calibration source $\epsilon$	This includes the spectral component caused by the non-isothermal nature of the walls. This is mitigated by utilisation of an <i>IRT</i> to measure the radiance temperature and using that as the transfer standard.
Different solid angle of collection for transfer standard ( <i>IRT</i> ) & thermographic instrument	Both instruments had a long working distance and a defining aperture was used in front of the calibration furnace, thus both instruments will have been collecting light from a very similar position on the back wall of the furnace.
Spectral emission & absorption lines in the plume	There is no evidence from the images that the plume either attenuates or provides a brighter region round the laser position. Further spectral investigation of the highest temperature region would be useful though.
Attenuation by particulates in the chamber	There is no evidence in the images or by visual observation that 'smoke' is present in the optical path, but further investigation would be needed to rule this out.

## 6.3 CHARACTERISATION RESULTS

### 6.3.1 Radiometric calibration

The Thermographic instrument was calibrated using a 250  $\mu\text{m}$  diameter aperture, from the medium aperture set (see sections 3.2.3), placed in the focal plane of the instrument. A fourth term ( $A_3$ ) was included in the Sakuma Hattori (S-H) fit of the calibration data to account for the relatively large spectral width of the band pass (see section 2.2.4.4).

Table 6.3-1 Calibration coefficients for thermographic instrument (see section 2.2.4).

Spectral fit coefficients		value	
	$A_1$	$9.298 \times 10^{-7}$	
	$A_2$	$-7.815 \times 10^{-5}$	
	$A_3$	$2.665 \times 10^{-2}$	
	$\lambda_{Wien}$	$8.687 \times 10^{-7}$	
Scaling fit coefficients			SEE
ESRF1	$A_0$	$1.490 \times 10^7$	1.00 °C
	$A_{Wien}$	$1.533 \times 10^7$	0.47 °C
ESRF2	$A_0$	$2.601 \times 10^7$	1.46 °C
	$A_{Wien}$	$2.716 \times 10^9$	1.08 °C
Optical throughput in spectral band @ 1000 °C			
ESRF1	$E_{te} \cdot \beta$	$7.1 \times 10^{-6} \text{ sr m}^2$	
ESRF2	$E_{te} \cdot \beta$	$1.2 \times 10^{-5} \text{ sr m}^2$	

The solid angle of collection ( $\Omega_{FS}$ ) and the transmission of the optics ( $\beta$ ) was unknown. They can be estimated from the assumed spectral characteristics shown in Figure 6.1-1 and Eq 2.2-7. The results are shown in Table 6.3-1 in terms of the etendue of the optical system, this can be calculated because the field stop is also known ( $A_{FS}$ ). The assumed spectral characteristics of the instrument do not match the calibrated signal as a function of temperature; therefore, some other unknown spectral components of the optical system must be participating in the optical train. Thus, the calculated throughput is temperature (spectral content) dependent, the calculated values are at 1000 °C.

### 6.3.2 IFOV

The IFOV perpendicular to the optical axis was found to be  $3.00 \pm 0.05 \mu\text{m}$  ( $k=2$ ), using the same methodology as that outlined in Chapter 5. The projected IFOV of each pixel (not for the geometrically transformed image as per section 6.1.3) is no longer square, the vertical IFOV is still  $3.00 \pm 0.05$  ( $k=2$ ), but the horizontal (in the image) IFOV is  $3.92 \pm 0.07$  ( $k=2$ ) at the focal plane.

### 6.3.3 PSF

The same procedure as in section 5.1.2 was used to measure the PSF of the thermographic instrument used in this chapter, with the addition of a correction for the pixel ESF, described in section 6.1.5, implemented in between stage 5.1.1.1 & 5.1.1.2. The parameters used to process the slanted knife edge images to the z dependent PSF are shown in Table 6.3-2. The measured PSF for this instrument can be compared with that measured for the instrument used in Chapter 5. The PSF can be seen to have fallen fractionally less for this instrument at a given radius, meaning the instrument is more oversampled [4]. Thus, the optics are limiting the measurable spatial frequencies more severely than the instrument used in chapter 5. The magnification of the instrument used in this chapter is more than double that used in chapter 5, making the extra oversampling predictable if the system is diffraction limited.

Table 6.3-2 Parameters used to process knife edge images to PSF.

$W_0$	0.4 Pixel <sup>-1</sup>
$W_\sigma$	0.1 Pixel <sup>-1</sup>
$N_{\text{Abel}}$	200

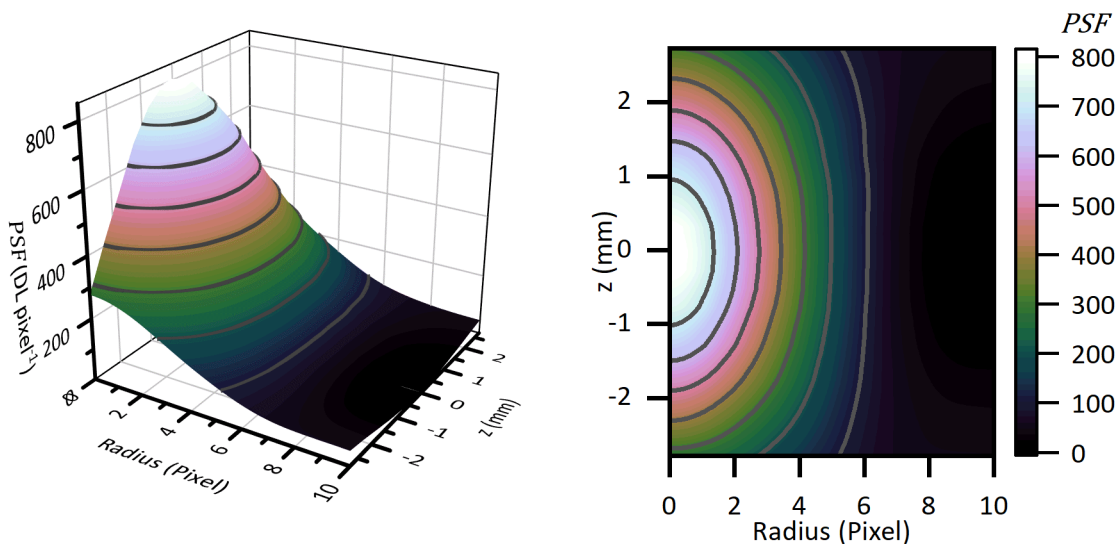


Figure 6.3-1 Measured *PSF* for small radii. The pixel *ESF* correction has been applied to this data.

### 6.3.3.1 Effect of pixel *ESF* correction on *PSF*

The correction for the finite *ESF* of the pixel area (described in section 6.1.5) alters the calculated *PSF* by reducing its width as exemplified in Figure 6.3-2. The 0.71 pixel reduction at half the maximum value (*FWHM*) constitutes a ~15% reduction in the width of the *PSF*.

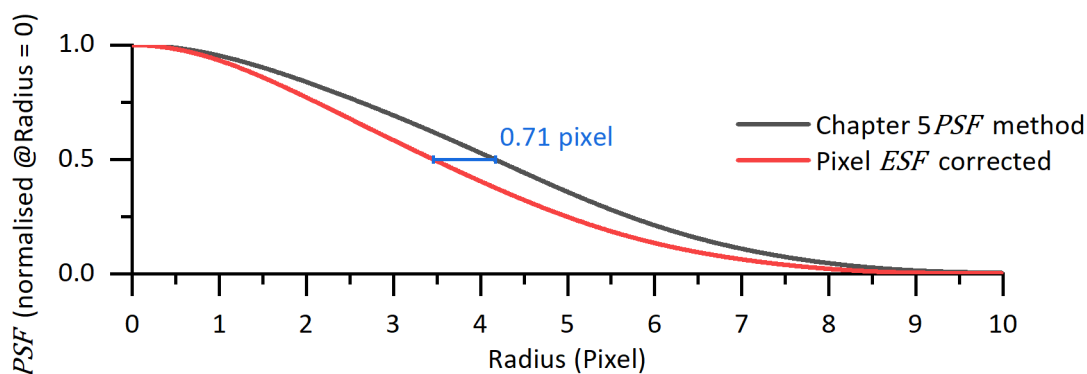


Figure 6.3-2 Effect of Pixel *ESF* correction on calculated *PSF*. The pixel *ESF* correction reduces the *FWHM* of the *PSF* by 1.42 pixels.

### 6.3.4 MFOV and Measurement resolution

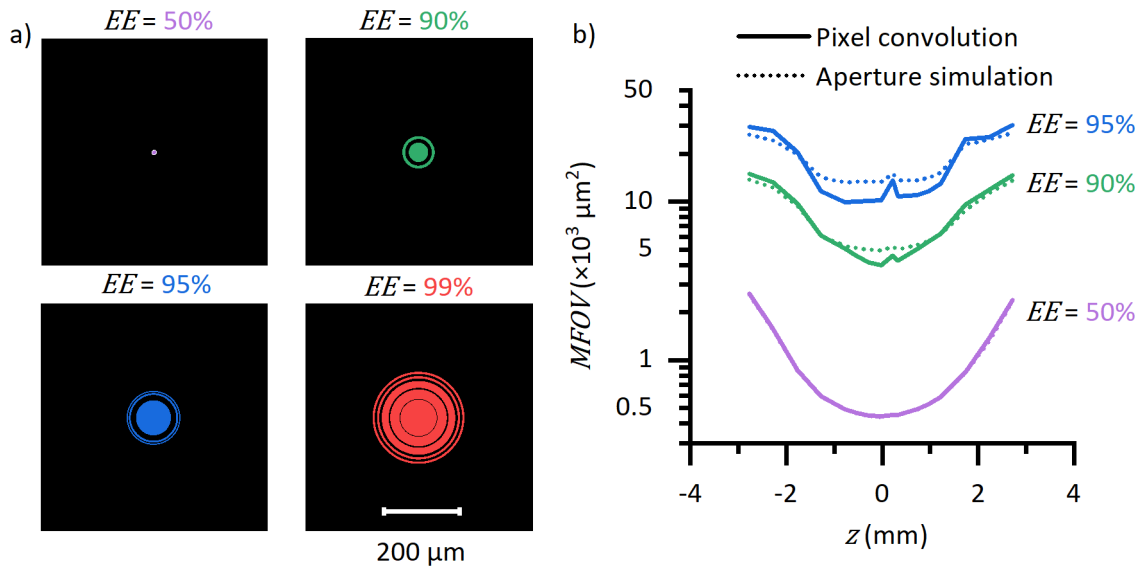


Figure 6.3-3 a) Shows the shape of the MFOV for enclosed energy (EE) fractions. b) Shows the  $z$  dependence of the MFOV area, the two methods broadly agree on the area if not the shape of the MFOV.

The MFOV was measured by two methods, the results of which are shown in Figure 6.3-3. For comparison both measurements are shown in terms of an area, but the aperture simulation method actually returns a circle diameter. The pixel convolution method returns a shape which is not necessarily contiguous, it is therefore more informative to express it as an image or as an area. At  $z=0$  (best focus) the IFOV of a pixel is only the originating area for 1.54 % of the total signal incident on the corresponding pixel (from a uniform source), this can be compared with the instrument used by Du & Voss (2004)[5], where 39.6 % of the signal originates in IFOV of the central pixel. This is a stark representation of the importance of consideration of the MFOV and not just the IFOV of a thermographic system. The MFOV at  $EE = 95\%$ , by the aperture simulation method at best focus is a circle of 130  $\mu\text{m}$  diameter. Figure 6.3-4 shows the MFOV and measurement resolution of the instrument expressed in scene units.

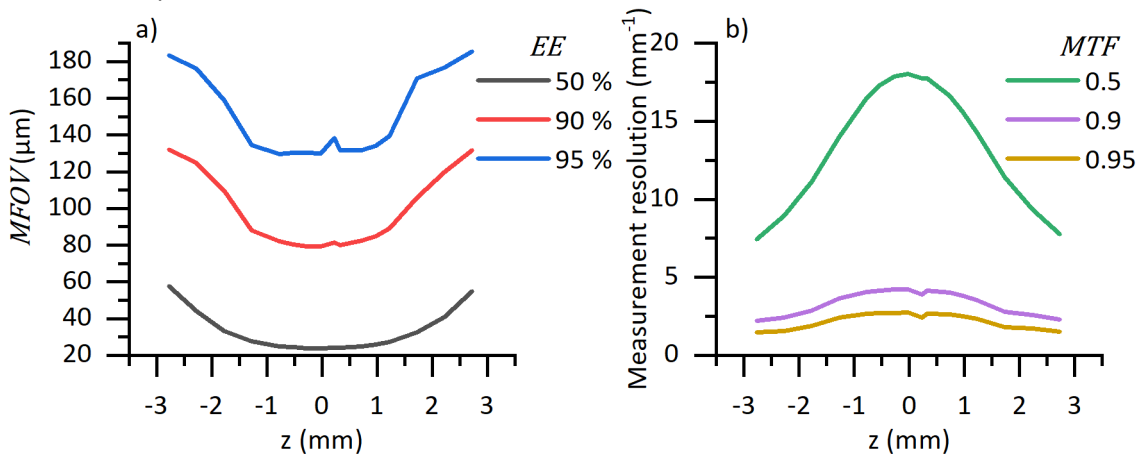


Figure 6.3-4 a) Is the Measurement field of view expressed as the diameter of a circle for three Enclosed Energies (EE). b) Is the measurement resolution for three Modulation Transfer Function (MTF) levels, expressed as one dimensional spatial frequencies in the scene plane.

### 6.3.5 Direct measurement of a normal distribution

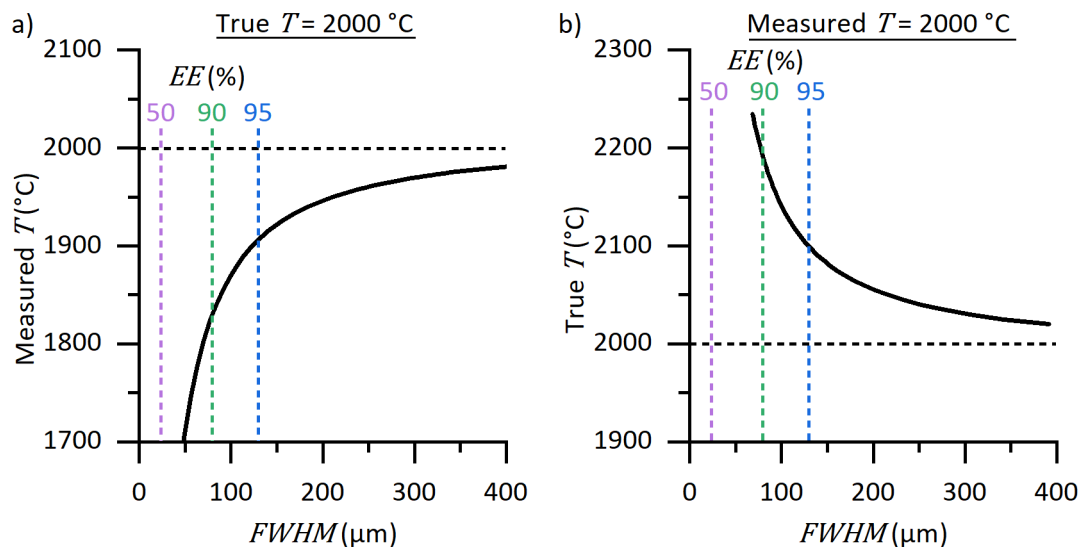


Figure 6.3-5 a) Shows how the central pixel of the thermographic instrument used in this chapter (@best focus), will measure the temperature of 2d Gaussian distribution in  $T$  ( $\epsilon = 0.35$ ), which has a 'True  $T$ ' of 2000 °C. b) Shows pairs of peak temperature and FWHM which would give a peak 'Measured  $T$ ' of 2000 °C (in the central pixel, using the direct method).

One metric that is sometimes of interest to the study of  $AM/M$  is the peak temperature that the liquid reached. The peak temperature is important because it will instruct whether some (different vaporisation temperatures), or all, of the alloy components have evaporated during the process. Measurement of the peak temperature is challenging because of the very high spatial thermal gradients around the laser. Figure 6.3-5 shows two representations of how a thermographic instrument can incorrectly measure the peak temperature of gaussian temperature distribution, due to the  $PSF$  of the instrument.

There is often an indent (cavity) present in the liquid metal surface at the location of the laser caused by vaporisation of the surface layer of metal this vapour often causes the spatter of partially melted particles [6]. When this indent becomes large the phenomenon is termed keyholing, which can lead to the laser melting a long distance into the previous layers of the build, possibly causing void defects [7]. The cavitation creates multiple reflection from surface to surface which not only makes the keyholing process self-reinforcing (by increasing the absorptivity of the laser). The indent also increases the surface emissivity of the part making the assumed surface emissivity invalid. A cavity will make the estimate of the emissivity too low meaning that the device will measure a temperature that is higher than reality. This makes accurate measurements of the peak temperature even more uncertain than the exposed (feely radiating) liquid or solid surfaces. It is very difficult to deconvolve this phenomenon from the localised high temperature (& therefore radiance) region around the laser. More work needs to be done on this aspect before the peak temperature can be considered accurately measured.

### 6.3.6 Geometric transform

The Geometric transforms laid out in Section 6.1.3 were implemented on a series of aerosol jet printed checkerboards. Reconstruction of the spatial dimension of the vertical component of the image is shown in Figure 6.3-6. The flattening of the measured checkerboard sizes shows that the algorithm has successfully corrected the change in magnification across the *TFOV*.

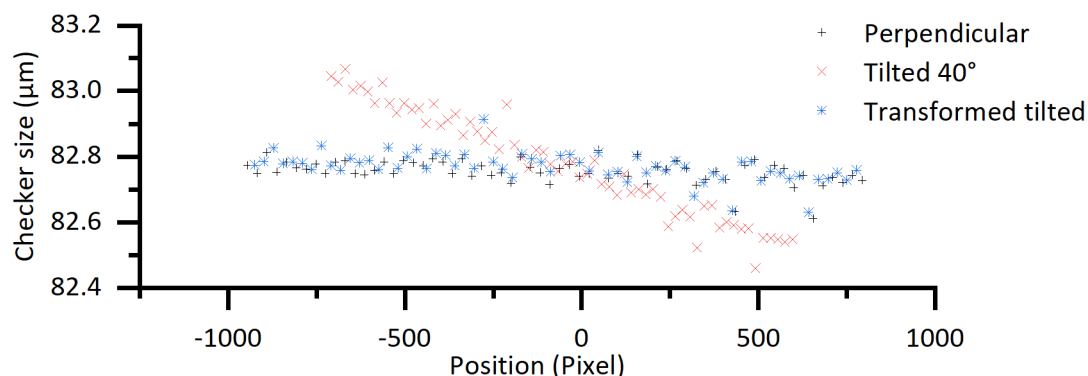


Figure 6.3-6 The measured checker size across the *TFOV* was constant for a perpendicularly imaged plane, as expected. The change in measured checker size seen in the image of the tilted plane is corrected by the application of the geometric transform.

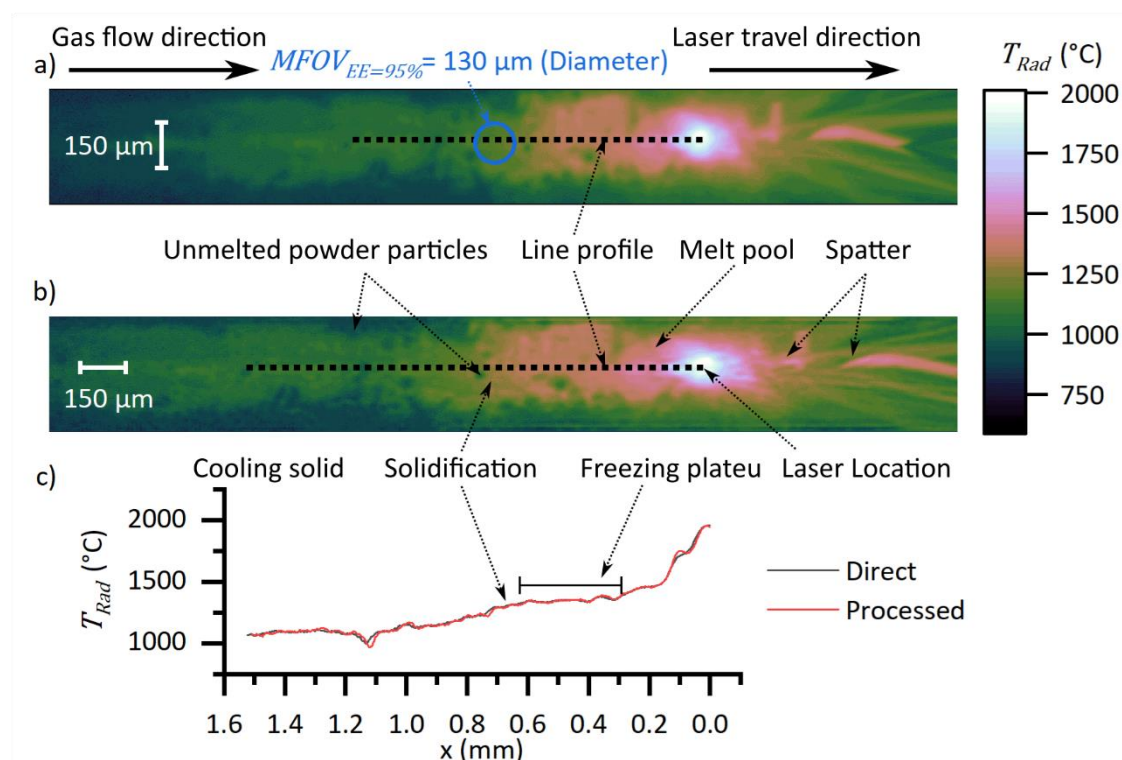
Results of the geometric transform in the horizontal dimension are shown in Table 6.3-3. The transform of the image brings the measurement of the dimensions of the checkerboard much closer to the checker dimensions measured in the perpendicular image. The 2% discrepancy between the transformed and original perpendicular measurement may be caused by the difficulty in ensuring the initial image was truly perpendicular. Alternatively, the discrepancy may have been caused by the interpolation required in the reconstruction.

Table 6.3-3 Geometric transform results.

Checker size (horizontal)	
<i>Perpendicular</i>	82.75 µm
<i>Tilted 40°</i>	62.13 µm (25% change)
<i>Transformed tilted image</i>	81.11 µm (2% change)
Measured geometric image characteristics	
<i>IFOV</i>	3.00±0.05 µm pixel <sup>-1</sup> (Perpendicular)
<i>r<sub>WD</sub></i>	263 mm (Geometric approximation)
<i>r<sub>im</sub></i>	570 mm (Geometric approximation)
Position of focal plane in image	
<i>ESRF1</i>	1100±50 (pixels)
<i>ESRF2</i>	1102±7 (pixels)

The *ESRF2* data was amenable to this method of analysis because the laser traverse crossed through the full *TFOV*, and in both directions, Thus the mean position of the maximum signal is an acceptable estimate of the focal plane position. The manual qualitative determination of the focal plane position for the *ESRF1* data set makes the uncertainty large. See Table 6.3-3 for focal position used in the geometric transforms.

## 6.4 THERMOGRAPHY OF *AM/M* REPLICATOR RESULTS



### Print Parameters

Material	Ti-6-4	Layer thickness	100 μm
Experimental session	ESRF2	Layer number	8
Laser velocity	200 mm s <sup>-1</sup>	Emissivity used	0.35[8]
Laser power	200 W		

Figure 6.4-1 a) Is an example image, processed by conversion to radiance temperature only. The MFOV of the instrument is shown for illustration. 95% of the light incident on the central pixel originates from inside the circle. b) The same image as a, but with deconvolution and geometric transform applied. c) Line profile of a & b with the line profile from a stretched by  $1/\cos 40^\circ$  (Eq 2.4-24) for ease of comparison. The process parameters of the build are shown in the above table.

There are many usable IR datasets in the two experimental sessions of interest (ESRF1 & ESRF2, see section 3.3.3). The in-depth analysis of this data is primarily the concern of the materials scientists studying the *AM/M* process. The aim of this work was to provide processing of the raw images to a degree where they could be used as measurements of the thermal fields in the experiments.

In this section some example datasets have been used to exemplify the kind of metrics that can be extracted from this rich dataset.

The majority of the ESRF1 dataset consists of multiple passes of the laser within a single layer (hatching), this makes analysis more complicated because there can be no approximation of steady state. The ESRF2 dataset is all single passes of the laser, as the x-ray diffraction probing of the process requires the assumption of steady state. The single pass steady state data is easier to interpret and analyse.

The *freezing plateau* depicted in Figure 6.4-1 is a consequence of the latent heat in the phase change (solidification). If a constant heat flow out is assumed then the temperature drops proportional to the heat flow until the phase change, when the energy flow out is provided by the latent heat. Therefore, the temperature of the region around the phase transition pauses (plateaus) in temperature. The cooling continues once the phase change is finished.

### 6.4.1 Spatter

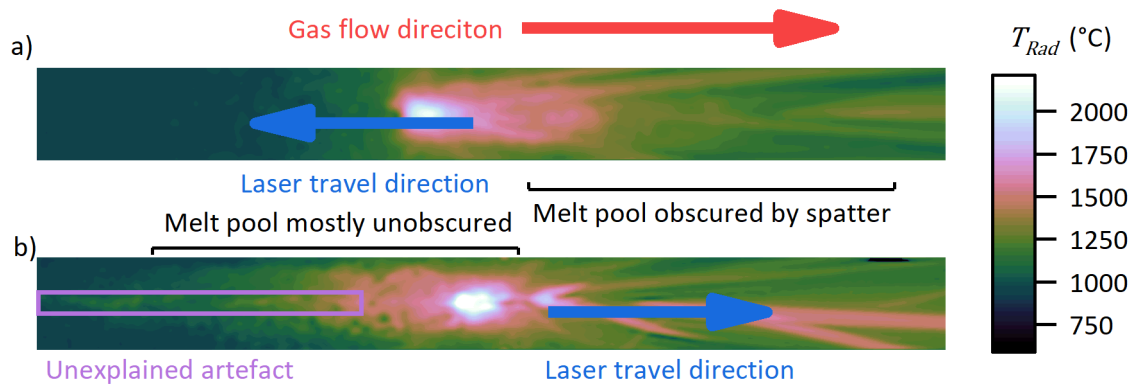


Figure 6.4-2 The Argon gas flow means that the ejected spatter always moves from left to right (in the image), as the laser travels from right to left the spatter obscures many useful measurements of the melt pool.

The richest thermographic data comes from the region directly behind the laser spot. This is where the detail of the melt pool and the cooling process can be observed. Quantification of the thermal fields during this cooling phase is of the highest importance to materials scientist studying the *AM/M* process. The ejection of hot ‘spatter’ particles obfuscates accurate radiometric measurements of this trailing melt pool. Unfortunately, ~95% *ESRF2* dataset is taken in the wrong direction.

An unexplained phenomenon is present in some frames of the data. The phenomenon manifests as a rough horizontal line of bright pixels along the centre of the image. This could be caused by specular reflections of the very bright melt pool from the build chamber back onto the part or be an artefact of scatter inside the lens. No evidence for such an artefact was found in lab tests.

### 6.4.2 Signal to noise ratio and exposure time

The highest speed that the laser moves in these experimental sessions is  $400 \text{ mm s}^{-1}$  which equates to 64 pixels per exposure. The modal speed used is  $100 \text{ mm s}^{-1}$  ( $16 \text{ pixels exposure}^{-1}$ ). The exposure time used during these experiments is  $633 \mu\text{s}$  with a frame rate of ~1600 fps. The motion of the laser during the exposure leads to attenuation of the signal (motion blur) and underestimation of the peak temperature this would require simultaneous spatial and temporal deconvolution of the images. This means that temporal resolution is still a problem (though much reduced from chapter 5) in this experimental setup. The camera used is not capable of implementing a shorter exposure time using a *TFOV* which captures the whole thermal field. Other higher speed Si cameras are available which may help this problem, but reduced exposure time has consequences for signal to noise ratio.

The freezing plateau of Ti-6-4 occurs at ~1000 DL ( $1473 \pm 22 \text{ }^\circ\text{C}$  ( $k=2$ )). To measure the initial solid cooling rate, temperatures cooler than this must be measurable, in this work temperatures down to ~20 DL (~960 °C) were used. Using quadrature addition of the spatial (Eq 6.1-2) and temporal (Eq 6.1-1) noise, The signal to noise ratio at 20 DL is approximately 3. This does not leave much scope for decreasing the exposure time while maintaining the ability to measure the solid cooling rate, using a similar Si device. Therefore, to operate faster, the etendue of the optical system or the  $QE^*$  or the operational wavelength (spectral radiance @ 960 °C) must increase to be able to lower the exposure time. These options come at the expense of spatial resolution. increasing the  $QE^*$  or the operating wavelength band would require changing the detector material, detectors other than Si cannot match the pixel density available here. Increasing the Etendue (decreasing the  $F\#$  see section 2.1.3) will decrease the measurement resolution due to aberrations in the optics.

### 6.4.3 Cooling rates (temporal)

#### Print Parameters

Material	Ti-6-4	Layer thickness	100 $\mu\text{m}$
Experimental session	ESRF2	Layer number	2-16
Laser velocity	200 $\text{mm s}^{-1}$	Emissivity used	0.35[8]
Laser power	200 W		

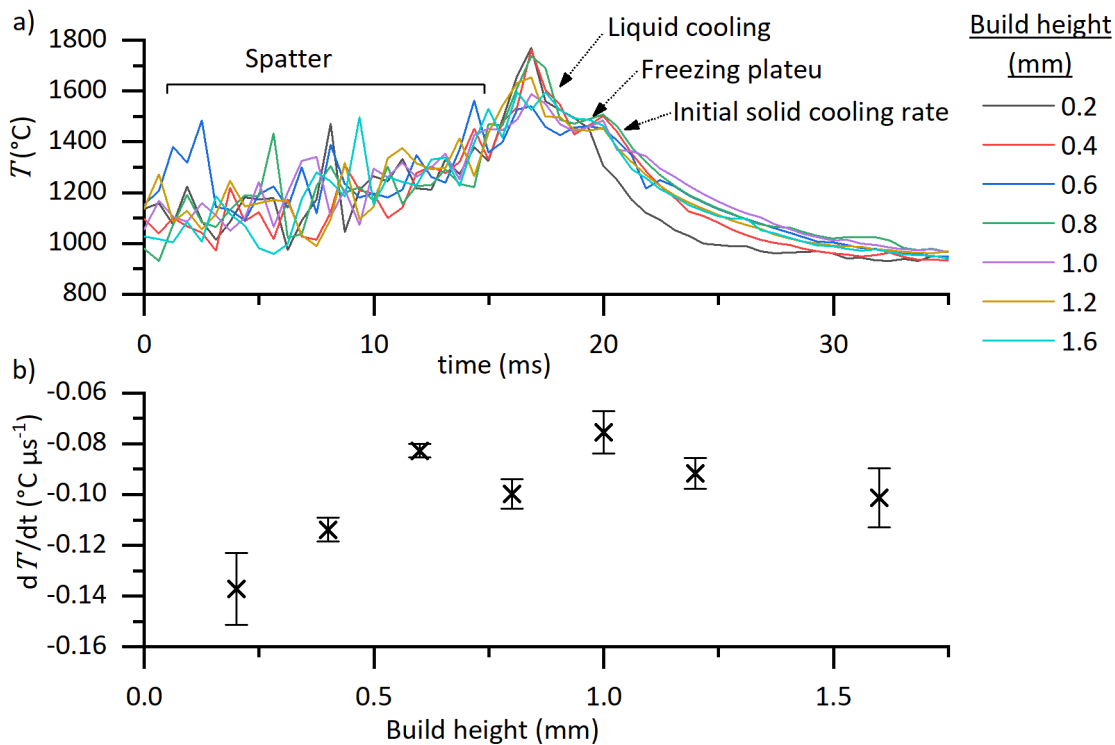


Figure 6.4-3 a) Time series of the temperature, just to the side of the laser travel vector, for 7 layers of a build. b) Cooling rate for the first 2.5 ms after solidification, the error bars are the combination of the uncertainty at temperature and the fit error of the linear cooling rate approximation. Some evidence exists for the decrease in cooling rate at higher build heights due to decrease in the conductive cooling through the build plate. There was a significant time delay  $t$  between each layer allowing the entire system to cool to close to ambient in between each layer.

The initial solid cooling rate is important [9-11], because this determines the solid-state phase transformations, the crystal structure formation (grain coarsening) and the residual stress in the part. Usually slower cooling rates equate to larger spacings between grain boundaries. Figure 6.4-3 shows how the initial solid cooling rate is affected by build height. The solid cooling rate is sensitive to the thermal conduction down the part, which decreases with build height. This is because the build is thinner than the substrate, reducing the cross-sectional area for thermal conduction down into the base plate.

Fisher et al (2017)[12] measured solid cooling rates of Ti-6-4 in *PBF-EB/M* of  $0.05 \text{ }^\circ\text{C } \mu\text{s}^{-1}$ . This is a little lower than measured in this work. This might be expected because *PBF-EB/M* usually use a preheated bed which will reduce the conductive cooling through the part.

#### 6.4.4 Thermal gradients (spatial)

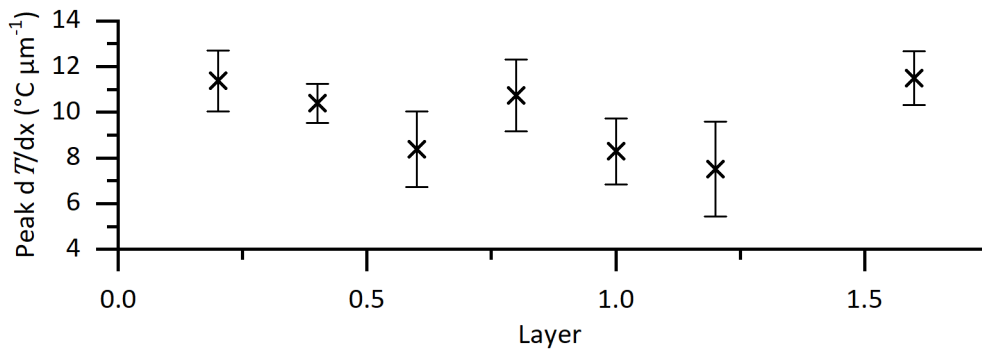


Figure 6.4-4 The peak spatial thermal gradients measured in the melt pool of Ti-6-4 do not seem to be dependent upon the build height.

Spatial thermal Gradients [10] around the laser (in the liquid) were measured on a 16 layer Ti-6-4 build the results are shown in Figure 6.4-4. There is no evidence for the maximum spatial gradient in the melt pool being dependent upon build height. The average peak thermal gradient is  $9.7 \pm 0.8$   $^{\circ}\text{C } \mu\text{m}^{-1}$ . This compares with the spatial thermal gradient measured by Hooper (2018)[13] in the range 5-20  $^{\circ}\text{C } \mu\text{m}^{-1}$  for Ti-6-4 in a modified commercial *PBF-LB/M* machine. Hooper (2018)[13] measured the peak thermal gradient as 20  $^{\circ}\text{C } \mu\text{m}^{-1}$  for the standard bulk print. This increase is probably due to the 2d (thin wall) nature of the *LAMPRII* prints reducing the thermal conductivity down the part. This reduction in conductive cooling will reduce the thermal gradients below those measured in a commercial 3d print.

## 6.5 CONCLUSIONS

In this chapter a high speed, high spatial sample rate, thermographic instrument was characterised and used in a unique additive manufacturing testbed. The instrument and testbed application are unique and entirely novel and provide insights into the *AM/M* process previously inaccessible. A correction for the spatial transfer function of the pixels was made in the measurement of the spatial transfer function of the system. The geometric projection method explained in section 2.4.4.1 was tested and assessed. The main sources of uncertainty and those not considered were discussed and quantified where possible. The spatial transfer function was used to determine the measurement field of view of the instrument. The effect of the spatial transfer function on the measurement of a small continuously varying thermal field was simulated and discussed. Finally, the quality of the data acquired from the test bed was critically appraised, and standard metrics used in additive manufacturing literature were extracted and compared to other examples in the literature.

The correction of the pixel *ESF* in the *PSF* measurement makes a ~15% difference to the width (*FWHM*) of the *PSF* which is a significant difference. This effect will become more pronounced for systems which are not as over sampled as the one used here (bigger pixels or higher resolution optics).

The results of the checkerboard projection tests show that the geometric transform accurately corrects for the tilt in the optical axis. This is assuming that the assumption of a planar (flat) build plane is valid.

Construction of an uncertainty budget is of the upmost importance for a measurement to be considered quantitative. It is not expected that the uncertainty budget presented here is entirely complete and the quantisation of the uncertainty in emissivity is poorly justified. It is expected that the uncertainty is an underestimate of the true uncertainty in the final measurement of the surface temperature. However, as many examples in literature make no attempt to quantify the uncertainty, the approximations used here are ahead in the field. The scene dependent uncertainty caused by the spatial transfer function of the instrument required further work to quantify.

Characterisation of the *MFOV* of a pixel is critical to know how sensitive the system is to inhomogeneities in the thermal field. Ideally quantitative measurement of temperature would only be undertaken when the scene can be assumed to be of uniform radiance over this *MFOV*. The classic aperture measurement of *MFOV* was shown to be unsuitable for this thermographic system due to scatter in the optical system. Use of the measured *PSF* to determine the *MFOV* of the system was shown to be a significant improvement over the classic aperture measurement for this instrument.

The *PSF* measurement allows a clear representation of the error that the direct method will incur when viewing a non-uniform (gaussian) temperature distribution. Even when using the relatively strict requirement that the gaussian width (*FWHM*) is the same size as the 95% enclosed energy *MFOV*, the measured peak temperature is undermeasured by ~ 100 °C @ 2000°C ( $\varepsilon = 0.35$ ). This and the motion blur which is likely to add a similar level of error, makes the peak temperature in data measured using the *LAMPRII* setup an underestimate of the true peak temperature.

The thermographic system developed for the *AM/M* application has the smallest *IFOV* of any instrument found in literature, thus these experiments have the highest spatial sampling quantitative thermography of an *AM/M* process. The data captured from the *LAMPRII* system in conjunction with the simultaneous x-ray data, presents an entirely novel measurement of the *AM/M* process. This level of detail in the process has not been seen before. Future publications plan to use this data to inform the material science of *PBF-LB/M*.

## 6.6 REFERENCES

1. Lane, B. and E.P. Whitemton, *Calibration and measurement procedures for a high magnification thermal camera*. 2015, National Institute of Standards and Technology.
2. ASTM International, E1256-17, *Standard Test Methods for Radiation Thermometers (Single Waveband Type)*, 2017
3. BIPM, et al., *GUM: Guide to the expression of Uncertainty in Measurement*, 2008
4. Bijl, P. and M. Hogervorst, *Sensor performance as a function of sampling (d) and optical blur (Fλ)*. SPIE Defense, Security, and Sensing. Vol. 7300. 2009: SPIE.
5. Du, H. and K.J. Voss, *Effects of point-spread function on calibration and radiometric accuracy of CCD camera*. *Applied Optics*, 2004. **43**(3): p. 665-670.
6. Leung, C.L.A., et al., *The effect of powder oxidation on defect formation in laser additive manufacturing*. *Acta Materialia*, 2019. **166**: p. 294-305.
7. King, W.E., et al., *Observation of keyhole-mode laser melting in laser powder-bed fusion additive manufacturing*. *Journal of Materials Processing Technology*, 2014. **214**(12): p. 2915-2925.
8. Boivineau, M., et al., *Thermophysical properties of solid and liquid Ti-6Al-4V (TA6V) alloy*. *International journal of thermophysics*, 2006. **27**(2): p. 507-529.
9. Gan, Z., et al., *Benchmark Study of Thermal Behavior, Surface Topography, and Dendritic Microstructure in Selective Laser Melting of Inconel 625*. *Integrating Materials and Manufacturing Innovation*, 2019. **8**(2): p. 178-193.
10. Ding, L., et al., *Investigation on Ti-6Al-4V Microstructure Evolution in Selective Laser Melting*. *MDPI Metals*, 2019. **9**(12): p. 1270.
11. Lia, F., et al., *Thermal and microstructural analysis of laser-based directed energy deposition for Ti-6Al-4V and Inconel 625 deposits*. *Materials Science and Engineering: A*, 2018. **717**: p. 1-10.
12. Fisher, B.A., et al., *Consequences of Part Temperature Variability in Electron Beam Melting of Ti-6Al-4V*. *JOM*, 2017. **69**(12): p. 2745-2750.
13. Hooper, P.A., *Melt pool temperature and cooling rates in laser powder bed fusion*. *Additive Manufacturing*, 2018. **22**: p. 548-559.

## 7. SUMMARY & CONCLUSIONS

---

### 7.1 SUMMARY

This thesis has studied the development and use of three Near-Infrared-Radiation (*NIR*) thermographic instruments, and their application to the additive manufacturing of metals (*AM/M*). The work has shown the importance of characterisation of the thermographic instrument, and how that characterisation can improve the accuracy of measurements of the thermal fields in *AM/M*. The field of quantitative thermography and its application to *AM/M* was reviewed.

In chapter 2, the theoretical basis for radiometric determination of surface temperature by collection of light on to a detector was explained. The principles of an instrument transfer function in normal and reciprocal space and the application of these ideas to the spatial transfer function of a thermographic instrument were described. Geometric optics were used to construct a transformation from an image to the orthographic projection of a tilted surface. The principles of convolution and deconvolution were explained, and two methods for calculating the Measurement Field of View (*MFOV*) from the Point Spread Function (*PSF*) were presented:

- *Aperture simulation*, which simulates the idealised results of the circular aperture experiments without the obfuscating Size of Source Effects (*SSE*).
- *Pixel convolution*, which provides the spatial distribution of weights for energy incident on a pixel, which can be thresholded to provide an area of a given enclosed energy.

In chapter 3, the experimental equipment and principles used in this work were presented. It described the important experimental considerations required to perform reliable radiometric measurements and thermographic instrument characterisations in the laboratory. Three methods of mapping the image to the thermal fields were explained:

- *Direct* method, where each pixel signal is assumed to map directly onto the scene.
- *Regularised deconvolution*, where the scene is assumed to vary smoothly.
- *Model deconvolution*, where a parameterised thermal field model is fit to the measured data.

In chapter 4, a low-cost, accessible, smart-phone-sensor based system (PiCam) was converted into a functioning high-temperature thermographic instrument. A standard transfer function target was used to characterise the spatial transfer function of the device. The modulation depth measurement was modified to fit into the Fourier framework. The modification made a significant difference to the calculated *measurement resolution* of the instrument. The noise equivalent temperature difference, as a function of temperature, was measured and found to be of an acceptable level across the temperature range. The instrument was used in a laser-based directed energy deposition of metals (*DED-LB/M*) application, where it measured the melt pool size. It was shown that the device could discriminate between the melt pool sizes of four linear power densities, covering a range of 6 to 18 J mm<sup>-1</sup>.

In chapter 5, a high-performance thermographic system was used for continuous monitoring of a modified commercial laser-based powder bed fusion of metals (*PBF-LB/M*) process. A novel numerical method for measuring the spatial transfer function of the instrument, based on a slanted knife edge, was devised and implemented. A method for quantitatively assessing and validating the performance of the three thermal field mapping methods was devised and implemented. The *model deconvolution* thermal field reconstruction method was the most accurate in the object size range 40 to 80 µm, which is the same size range as the heated zones observed in the *PBF-LB/M* application. The two thermal field reconstruction techniques applied resulted in a ~300 °C difference to the

measured peak effective temperature of the process. The *regularized deconvolution* provided a sharper peak with a higher peak temperature ( $\sim 60$  °C) than the *model deconvolution* solution. The limitations of the experimental setup and the data gathered were discussed. The lack of temporal resolution in the data precludes true quantitative thermography using this setup and process parameters.

In chapter 6, the characterisation and use of a high speed, high spatial sampling rate, and high dynamic range thermographic instrument used in a custom test bed facility is described. The transformation of the image to an orthographic projection of the build plane was assessed, and found to reproduce an accurate orthographic projection of the plane, with less than 2% error in spatial measurements in the scene plane, perpendicular to the tilt axis. Two methods for determining the *MFOV* from the *PSF* presented in section 2.4.2 were implemented and discussed. Both were found to produce similar results, with the *aperture simulation* method providing what is probably the most useful output, which is a circle of 130  $\mu\text{m}$  diameter at the focal plane, rather than an image of the distribution provided by the *pixel convolution* method. The sources and quantification of uncertainties in thermal fields measured with the instrument were discussed. The uncertainty in a measurement of a thermal field uniform over the *MFOV* was found to be  $\pm 30\text{-}70$  °C ( $k=2$ ), over the dynamic range of the camera. Thermal field metrics, important to the *PBF-LB/M* process, were extracted from exemplar data acquired from the test bed. Solid cooling rates of  $0.06$  to  $0.14$  °C  $\mu\text{s}^{-1}$  and maximum thermal gradients in the melt pool of  $6$  to  $12$  °C  $\mu\text{m}^{-1}$  for material Ti-6-4 were measured. These are similar in magnitude to values reported in literature.

Original contributions to the field include

- A deconvolution method which utilises a thermal field model as the basis for the reconstruction.
- Conversion of a PiCam system to a functioning thermographic instrument.
- Modification of a standard resolution test method to fit into the Fourier framework of transfer function measurement.
- Use of a PiCam system to measure melt pool characteristics in an *AM/M* application.
- Use of numerical methods to convert the measured edge spread function to the point spread function.
- A thermal field mapping method, which uses a thermal field model as the basis for the deconvolution rather than allowing the thermal field to take any shape.
- Quantitative assessment of the accuracy of thermal field mapping, by use of known thermal fields of similar size and distribution to the thermal fields found in *AM/M* processes.
- The most highly spatially sampled thermography of the *AM/M* process.
- A validated accurate projection algorithm to create an orthographic projection of a tilted scene.
- A quantitative assessment of the uncertainty of the thermographic measurements in *AM/M*.
- A method for determination of the measurement field of view and measurement resolution for thermographic instruments with poor size of source effect (*SSE*).

Each item in the list above represents a potential advancement in the field of radiometric thermography and/or its application to the *AM/M* process.

## 7.2 CONCLUSIONS

### 7.2.1 On quantitative thermography

It has been demonstrated that truly quantitative thermography is a challenging aim. A significant source of error in the measurement of radiance, using a focal-plane-array-based thermographic system, was found to be the spatial transfer function of the instrument. Error caused by the spatial transfer function can be split into two categories:

- Short range underfilling of the *MFOV* of each pixel.
- Long range *SSE* effects.

Characterisation of the spatial transfer function of the instrument by measurement of the *PSF* provides a lot of information about the performance of the imaging system, including the *MFOV* and the Modulation Transfer Function (*MTF*). There is no standardised definition of the *MFOV* of a thermographic instrument, so a percentage of the enclosed energy (similarly to single pixel infrared radiation thermometers) was used. Measurement of the *PSF* allows use of deconvolution to correct the error introduced by underfilling of the *MFOV*. The slanted knife edge method is an accessible and accurate method for determining a spatially averaged measure of the *PSF*. Use of numerical methods to convert the knife edge images to radial *PSF* measurements, allow for the detail of the *PSF* to be conserved without the need for an a priori assumption of the form. The *MTF* calculated from the *PSF* can be used to determine the measurement resolution of the instrument.

Underfilling of the *MFOV* is a source of error that is often ignored in thermographic applications. It is the opinion of the author, based on this work, that all thermographic applications should consider and report the *MFOV* or the measurement resolution of the system, not just the Instantaneous Field of View (*IFOV*) or spatial sampling frequency. This information allows for an assessment of the ability of the instrument to accurately measure the radiance (and hence temperature) of the scene. Calculation of the uncertainty introduced to the measurement of thermal fields by underfilling of the *MFOV* is difficult to quantify because it depends upon the radiance distribution in the scene, and not necessarily the image.

Accurate measurement of the *PSF* does not necessarily allow for complete, and accurate, reconstruction of the scene. Deconvolution is an ill posed problem which can have multiple solutions. Use of known-radiance validation targets, which closely resemble the expected scene, was found to be the most reliable way to test the performance of deconvolution methods. This kind of validation provides a clear measure of the expected reduction in error for a given scene.

Model deconvolution was found to significantly reduce the error in known scenes. This was mainly due to the removal of ringing errors found in the regularised deconvolution method. Model deconvolution is a useful tool, which could give more accurate measurements of the thermal fields, if the model fully captures the shape of thermal fields in the scene. Model deconvolution requires knowledge of the thermal field before the measurement, and can require significant computational resources, making it unsuitable for some thermographic measurement scenarios.

The errors caused by *SSE* and other long-range imaging defects are more problematic to correct. These sources of error should be minimised with careful optical design. This work has shown that reflections from the optical elements can lead to a large error for some scenes and instruments. This error can be minimised by using anti-reflective coatings on all scene-facing surfaces of the optics. Designing the optical system so that the *PSF* does not vary across the total field of view would validate the shift invariance assumption of the *PSF* required for deconvolution. There are examples in literature which attempt to measure the whole position dependent optical transfer function of the instrument and use this measurement to account for all stray light (defects) in the imaging system [1,

2], but these methods are difficult to implement and do not have traction in quantitative thermography.

Ideally deconvolution would be unnecessary. This would be achieved by ensuring that the image projected onto the focal plane array had sufficient modulation depth ( $MTF > 0.95$ ) at all spatial frequencies present in the scene. This is unlikely to be achieved in the general case, due to discontinuities in the thermal fields (edges). A good design requirement for the optics in radiometric thermographic instruments would be that the  $MTF$  is greater than 0.95 (or better) at the sample frequency of the focal plane array. This would make the  $MFOV$  close in size and shape to the  $IFOV$  of the instrument. Then the measurement resolution would be close to the sampling frequency, thus reducing ambiguity in the spatial resolution performance of the instrument. All these questions about the performance of a thermographic instrument can be answered by taking images of a slanted knife edge.

The PiCam system is a versatile instrument for distributed applications, such as remote volcano research and monitoring, where its low cost and the accessibility of the operating system make it a desirable tool. The very high spatial frequency measurements available with miniature smart phone sensors, such as the PiCam, are capable of producing very high spatial resolution thermographic measurements, if a suitable lens system is designed. The use of such sensors in microscope applications would lead to very highly sampled images, which could have useful applications.

The lack of temporal resolution of the thermographic instrument used in chapter 5 presents a similar problem to spatial deconvolution, except that instead of a gradual roll off of sensitivity at higher frequencies, the exposure time and frame rate cause the sampling frequency cut-off to be below the temporal frequencies present in the scene. Without the application of a super sampling regime, the data acquired will always be limited.

Using Si based sensors in the  $NIR$  portion of the spectrum has many advantages, which have been laid out throughout this thesis. The main advantages being:

- High sensitivity to temperature, therefore relatively low sensitivity to linear scaling factors such as emissivity.
- Maturity of Si technology allows for a high performance to cost ratio.
- Most standard visible-light optical elements can be used at these wavelengths.
- Reflected ambient (30 °C) background radiation is insignificant.

The main drawbacks of using Si detectors at  $NIR$  wavelengths can be summarised as:

- Relatively high minimum resolvable temperature  $\sim 600$  °C.
- Wavelengths are close to many atomic transition energies, which are mostly in the visible part of the spectrum, thus adversely affecting emissive properties.
- Highly non-linear radiance as a function of  $T$  means that a large dynamic range system is required to cover a useful  $T$  range.

This thesis has shown that tight control and proper design of the optical transfer function of a thermographic instrument allows direct mapping of the scene, resulting in more reliable measurements of thermal fields. Underfilling the  $MFOV$  makes a significant difference to the measured thermal field, especially for oversampled systems (most likely with Si based systems). Characterisation of the  $PSF$  of the thermographic system can correct the error caused by underfilling of the  $MFOV$ .

### 7.2.2 On thermography in additive manufacturing

The high-resolution measurements of thermal fields generated by this work will assist a deeper understanding of the *PBF-LB/M* process. The levels of detail exposed in the data generated for the experiments in chapter 6 are unprecedented.

Truly quantitative thermography in any field is a challenging undertaking. Thermography in *AM* of metals poses some specific challenges which remain to be solved. The continued challenges mainly relate to the radiative properties of the printed material and the strict spatiotemporal resolution requirements for a thermographic instrument to be effective. Specific metrics or process parameters can be extracted from thermographic data, but large-scale thermal field measurements across the entire powder bed in commercial machines are not currently possible with the types of setup we have used. Quantitative thermal field measurements in custom designed rigs, such as the *LAMPRII*, allow for quantitative measurements.

The peak instantaneous temperature of the process remains a challenging metric to extract from the data, because of the sensitivity of this metric to both the spatial and temporal sampling of the scene. It is expected that careful two-colour measurements have the best chance of succeeding at quantifying this metric accurately, but consideration must be given to the differences in *PSF* between the two colours used.

Si allows the full range of temperatures, pertinent to the process, to be measured, excluding solid state low temperature phase transitions important to some metals. Details of the un-melted powder in the melt pool and other features identified in the *LAMPRII* data would be obscured by systems with a lower spatial sampling rate, making analysis of their effect very difficult to implement. Expected improvements to high speed data transfer and handling technology will further improve the ability of Si sensors to provide higher spatial and temporal resolution data.

The low frame rate of the PiCam means that the (relatively high speed) *DED-LB/M* process would be poorly sampled by this instrument. Some smart phones which use similar sensors can stream very high frame rate data which may solve this problem in future iterations of the PiCam.

The results of the thermographic measurements in the *LAMPRII* rig show that the thermal fields measured are similar to those found in literature. Similar cooling rates and spatial thermal gradients measured in the *LAMPRII* rig imply that the system produces a good approximation of the process in commercial *PBF-LB/M* machines.

Researchers interested in the thermal fields present in *AM/M* include three groups: thermal metrologists, materials scientists and process modellers. Each group has its own specific requirements detailed in Table 7.2-1. The materials scientists, who operate the machines usually have their requirements met foremost, as they determine the build parameters. This kind of experimental work is always improved by multiple iterative attempts, which are difficult to implement when access to the equipment is restricted.

Table 7.2-1 Competing requirements (pressures) on experimental sessions

<b>Researcher: Thermal metrologist, aim: accurate thermal field measurement</b>
Slow process, to minimise temporal resolution issues.
Small build area, to allow maximum spatial resolution.
Short in experiment duration, to minimise data storage / transmission / processing problems and to allow many parameters to be tested in a short period of time.
Hot environment, to minimise cooling rates and provide maximum signal to noise ratio.
Steady state process, to allow for averaging.
Large melt pool, to minimise spatial resolution issues.
<b>Researcher: Materials scientist, aim: good material properties</b>
High speed, to represent industrial application.
Extended build area, to represent a full part build.
Data covering the full build of a part (many hours), to allow for correlation of part defects with thermal data.
Whatever thermal history produces good part performance.
Successful build, to further the understanding of which build parameters work.
<b>Researcher: Process modeller, aim: representative models</b>
Simplified situation. Model validation does not necessarily require validation for the complicated part geometries and thermal histories in parts and is simpler / more reliable to implement on simplified prints (lines and dots).
Simplified situation is as close as possible in speed and power to normal process.
Well defined boundary conditions, spatially and temporally.

This thesis has shown that the spatial transfer function of the thermographic instrument is important for accurate measurement of the thermal fields in *AM/M*. It has been shown that probing the detail of the thermal fields, around the heat source, to the level required to create accurate models of the process, cannot be achieved simultaneously with whole part/powder bed monitoring. The two applications (detailed laser/powder interaction monitoring and whole bed monitoring) cover five orders of magnitude in length (1  $\mu\text{m}$  (laser power variation) to 10 cm (part)). It has been shown that the high temperature imaging available with Si is more suited to monitoring the melt pool detail, because of the high spatiotemporal sampling rates available and the high temperatures present there. An alternative lower temperature technology could be applied to whole-bed monitoring applications, where the bulk temperature and slower cooling rates are important. The custom test rig with the limited area of interest has provided very useful thermographic data which will help inform the future of *AM/M*.

### 7.3 FURTHER WORK

Replacing the binary deconvolution targets with continuously varying scenes of known radiance (transmission), would allow direct assessment of the instrument on scenes which match the measurement scene. This would provide much greater confidence in the ability of the instrument to accurately reproduce the measurement scene, either natively, or with deconvolution. Being able to print these scenes, using a tool like the Optomec aerosol jet printer, would allow rapid assessment of a variety of thermographic instruments and scenes.

Ideally, better optics with lower *SSE* problems and better measurement resolution (smaller *MFOV*) would be used in custom test rig application, as used in chapter 6. Model validation can be best achieved in a simplified experimental setup which closely matches the real process. This simplified process (lines or spots) could be examined in detail by a thermographic system using microscope optics optimised for *NIR* use.

Development of a parameterised model to describe the extended thermal fields measured in the work in chapter 6, would allow the model deconvolution method to be applied to steady state, single line data, providing a more reliable alternative to the regularised deconvolution method used. The tilt in the optical axis was corrected geometrically, but the defocus caused by the limited depth of field was not corrected. The planar nature of the *PBF* process, means that the Scheimpflug principle[3] could be used to make the build plane coplanar with the focal plane, despite the tilt in the optical axis imposed by the heat source.

Using multiple PiCam systems in the build chamber would allow rapid processing of a 3d thermal field model (albeit sparsely sampled), which may allow for online defect detection in future work. The very high spatial pixel density, available in smart phone sensors, provides opportunities for very high-resolution microscopy of the process.

The design of a small portable high temperature blackbody which could be inserted into the build chamber, similar to Rodriguez (2015)[4], would allow for in-situ calibration of the thermographic instrument.

### 7.4 REFERENCES

1. Zong, Y., et al., *Simple matrix method for stray-light correction in imaging instruments*. 2008.
2. Envall, J., et al., *Spatial Scatter Effects in the Calibration of IR Pyrometers and Imagers*. International Journal of Thermophysics, 2009. **30**(1): p. 167-178.
3. Scheimpflug, T., *Improved method and apparatus for the systematic alteration or distortion of plane pictures and images by means of lenses and mirrors for photography and for other purposes*, in *GB patent*. 1904.
4. Rodriguez, E., et al., *Approximation of absolute surface temperature measurements of powder bed fusion additive manufacturing technology using in situ infrared thermography*. Additive Manufacturing, 2015. **5**: p. 31-39.

## 8. APPENDICES

---

### 8.1 ESTIMATING ERROR BY TAYLOR EXPANSION

It is useful to be able to estimate the magnitude of change in a function based on the magnitude of the change in one of its dependent variables. To estimate this the Taylor expansion can be used. The Taylor expansion is a series, with an infinite number of terms, that reproduces any continuous function of  $x$ . The Taylor expansion of  $f(x)$  about some point  $a$  is:

$$f(x)|_a = f(a) + f'(a)(x - a) + f''(a)\frac{(x - a)^2}{2!} + f'''(a)\frac{(x - a)^3}{3!} + \dots \quad \text{Eq 8.1-1}$$

The use of primes denotes the order of a derivative evaluated at the point  $a$ :

$$f'(a) = \left. \frac{df}{dx} \right|_a \quad f''(a) = \left. \frac{d^2f}{dx^2} \right|_a \quad \text{etc} \quad \text{Eq 8.1-2}$$

Truncation of the series means that the function  $f(x)$  is only accurately reproduced near the point  $a$ . The fewer terms included, the smaller the quantity  $(x - a)$  must be for the approximation to be accurate. The more non-linear  $f(x)$  is, the worse the approximation, or the tighter the requirements for a small  $(x - a)$  to reproduce the function at  $x$ . The expansion of a function  $f(x + \Delta x)$  about the position  $x$  is:

$$f(x + \Delta x)|_x = f(x) + f'(x)(x + \Delta x - x) + f''(x)\frac{(\Delta x)^2}{2!} + \dots \quad \text{Eq 8.1-3}$$

The first term and the subsequent terms (which include  $\Delta x$ ) can now be considered separately. Any change in the function  $f(x)$  caused by the change in the dependent variable  $x$ , can be encapsulated in the quantity  $\Delta f(x)$ :

$$f(x) + \Delta f(x) = f(x) + f'(x)\Delta x + f''(x)\frac{\Delta x^2}{2} + \dots \quad \text{Eq 8.1-4}$$

Removing  $f(x)$  from both sides gives:

$$\Delta f(x) = f'(x)\Delta x + f''(x)\frac{\Delta x^2}{2!} + f'''(x)\frac{\Delta x^3}{3!} + \dots \quad \text{Eq 8.1-5}$$

Assuming that the change in magnitude of the function is small compared with the value of the function ( $\Delta f(x) \ll f(x)$ ), then the series in Eq 8.1-5 can be truncated to a single term. The non-linearity of  $f(x)$  and the relative magnitude of  $\Delta f(x)$  affect the validity of the truncation.

### 8.2 AREA OF SECTION CREATED BY A LINE INTERSECTING WITH A RECTANGLE

A knife edge illumination passing across a pixel at an angle will illuminate a fraction of the pixel.

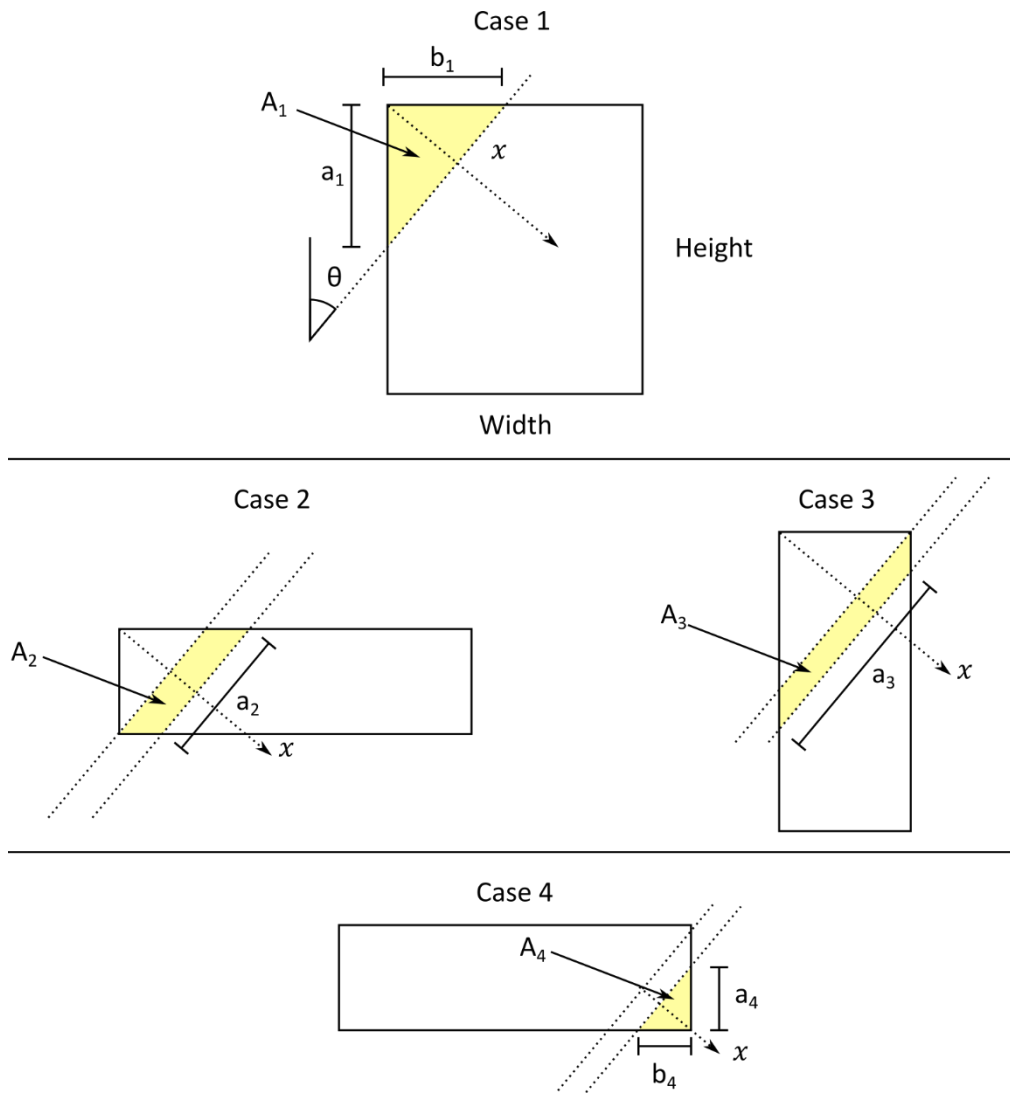


Figure 8.2-1 Area illuminated by a perfect undistorted knife edge moving across a rectangular pixel.

The fraction of the pixel illuminated is given by  $2A/(\text{Height} \times \text{Width})$  as the line moves across the pixel. There are four distinct regimes for calculating the enclosed area  $A(x)$ .

**Case 1:**  $0 < x < \text{Width} \cdot \cos \theta$  or  $\text{Height} \cdot \sin \theta$

$$A(x) = A_1 = \frac{x^2}{2} (\cot \theta + \tan \theta) \quad \text{Eq 8.2-1}$$

The limits where case 1 are valid is from  $x = 0$  to  $x = \text{Width} \times \cos \theta$ , or  $x = \text{Height} \times \sin \theta$ , whichever is smaller. Then, depending whether the line intersected with the bottom left corner (Case 2) or the top right corner (case 3) first, the enclosed area will be given by:

**Case 2:**  $\text{Height} \cdot \sin \theta < x < \text{Width} \cdot \cos \theta$

$$A(x) = \frac{\text{Height}^2}{2} \cdot \tan \theta + A_2 \quad \text{Eq 8.2-2}$$

$$A_2 = (x - (\text{Height} \cdot \sin \theta)) \cdot \frac{\text{Height}}{\cos \theta}$$

**Case 3:**  $\text{Width} \cdot \cos \theta < x < \text{Height} \cdot \sin \theta$

$$A(x) = \frac{\text{Width}^2}{2} \cdot \cot \theta + A_3 \quad \text{Eq 8.2-3}$$

$$A_3 = (x - (\text{Width} \cdot \cos \theta)) \cdot \frac{\text{Width}}{\sin \theta}$$

**Case 4:**  $\text{Width} \cdot \cos \theta$ , &  $\text{Height} \cdot \sin \theta < x < \text{Width} \cdot \cos \theta + \text{Height} \cdot \sin \theta$

The final section is similar to Eq 8.2-1 where  $x$  is replaced with the distance from the end of the traverse, and the enclosed area is the area of the rectangle minus this small triangle.

$$A(x) = \frac{(\text{Width} \cdot \text{Height})}{2} - A_4 \quad \text{Eq 8.2-4}$$

$$A_4 = \frac{((\text{Width} \cdot \cos \theta + \text{Height} \cdot \sin \theta) - x)^2}{2} (\cot \theta + \tan \theta)$$

### 8.3 TWO WAVELENGTH SYSTEMS, COLOUR/RADIANCE TEMPERATURE AND EFFECTIVE WAVELENGTH

The two colour method employs two distinct wavelength bands, and relies on the differences in  $\partial L_{BB}(T)/\partial T$  at the two wavelengths ( $\lambda_1$  &  $\lambda_2$ ) to produce a measurand which is sensitive to temperature. The measurand  $R(T)$  is:

$$R(T) = \frac{S(T, \lambda_1)}{S(T, \lambda_2)} \quad \text{Eq 8.3-1}$$

If it can be assumed that both wavebands are sufficiently well modelled by the Wien approximation, then the measurand is given by:

$$R(T) = \frac{B_1 \cdot A_{Wien1} e^{\frac{-c^2}{\lambda_{Wien1} T}}}{B_2 \cdot A_{Wien2} e^{\frac{-c^2}{\lambda_{Wien2} T}}} \quad \text{Eq 8.3-2}$$

Where the subscripts 1 & 2 denote the two waveband instruments, and  $B_1$  &  $B_2$  are any factors which scale the signal measured by the two distinct systems, such as emissivity. If it is assumed that only the emissivity is changing, all other scaling factors can be combined into one constant  $A_r$ . With some rearrangement, Eq 8.3-2 can be expressed as:

$$R(T) = \varepsilon_r A_r \exp\left(\frac{c_2}{T} \left(\frac{1}{\lambda_{Wien2}} - \frac{1}{\lambda_{Wien1}}\right)\right) = \varepsilon_r A_r \exp\left(\frac{c_2}{\Lambda T}\right) \quad \text{Eq 8.3-3}$$

Where the effective wavelength ( $\Lambda$ ) is:

$$\Lambda = \frac{\lambda_1 \lambda_2}{\lambda_2 - \lambda_1} \quad \text{Eq 8.3-4}$$

It can be observed that Eq 8.3-3 is a similar format to the single waveband radiometer equation using the Wien approximation (Eq 2.2-20). The sensitivity factor can be calculated by identical means:

$$\frac{\Delta R}{R} \cdot \frac{1}{\Delta T} = \frac{c_2}{T^2 \Lambda} \quad \text{Eq 8.3-5}$$

The effective wavelength allows a simple comparison of the sensitivity to temperature of single and multi-band systems. The effective wavelength of systems with more than two wavebands can be calculated [1], but is not necessary for this work.

1. Coates, P., *Multi-Wavelength Pyrometry*. Metrologia, 1981. **17**(3): p. 103.